

2

NSWC TR 83-526

# **MACH-10 HIGH REYNOLDS NUMBER DEVELOPMENT IN THE NSWC HYPERVELOCITY FACILITY**

BY ROBERT A. KAVETSKY

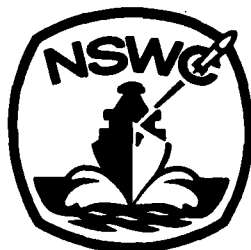
STRATEGIC SYSTEMS DEPARTMENT

13 FEBRUARY 1984

Approved for public release, distribution unlimited

DTIC  
ELECTE  
MAR 14 1985  
S E D

DTIC FILE COPY



**NAVAL SURFACE WEAPONS CENTER**

Dahlgren, Virginia 22448 • Silver Spring, Maryland 20910

85 03 06 014

UNCLASSIFIED

SECURITY CLASSIFICATION OF THIS PAGE (When Data Entered)

REPORT DOCUMENTATION PAGE		READ INSTRUCTIONS BEFORE COMPLETING FORM
1. REPORT NUMBER	2. GOVT ACCESSION NO.	3. RECIPIENT'S CATALOG NUMBER
NSWC TR 83-526	AL51 241	
4. TITLE (and Subtitle)		5. TYPE OF REPORT & PERIOD COVERED
MACH-10 HIGH REYNOLDS NUMBER DEVELOPMENT IN THE NSWC HYPERVELOCITY FACILITY		Final
7. AUTHOR(s)		6. PERFORMING ORG. REPORT NUMBER
Robert A. Kavetsky		
9. PERFORMING ORGANIZATION NAME AND ADDRESS		8. CONTRACT OR GRANT NUMBER(s)
Naval Surface Weapons Center White Oak (Code K23) Silver Spring, Maryland 20910		
10. PROGRAM ELEMENT, PROJECT, TASK AREA & WORK UNIT NUMBERS		
		1731319, Y3HR, 0, 0, 0
11. CONTROLLING OFFICE NAME AND ADDRESS		12. REPORT DATE
		13 February 1984
		13. NUMBER OF PAGES
		318
14. MONITORING AGENCY NAME & ADDRESS (if different from Controlling Office)		15. SECURITY CLASS. (of this report)
		UNCLASSIFIED
		15a. DECLASSIFICATION/DOWNGRADING SCHEDULE
16. DISTRIBUTION STATEMENT (of this Report)		
Approved for public release, distribution is unlimited.		
17. DISTRIBUTION STATEMENT (of the abstract entered in Block 20, if different from Report)		
18. SUPPLEMENTARY NOTES		
19. KEY WORDS (Continue on reverse side if necessary and identify by block number)		
Hypervelocity Facility      Structural Analysis Reynolds Number              Expansion Wave Mach Number                  Flow Restrictor Gas Dynamics                  Particle Separator Run Time                      Control Valve		
20. ABSTRACT (Continue on reverse side if necessary and identify by block number)		
The present NSWC hypervelocity facility has two Mach number capabilities (10 and 14) which operate over a range of Reynolds numbers. The Mach-10 leg had a maximum Reynolds number capability of $5.4 \times 10^6$ /ft. The Reynolds number region of interest for Mach-10, encompassing the reentry flight regime, has been established as 0 to $100 \times 10^6$ . Using oversized models in the present 5-foot diameter test cell, this Reynolds number regime scales down to a 0 to $20 \times 10^6$ /ft. Requirement in the hypervelocity facility. The potential		

DD FORM 1473  
1 JAN 73EDITION OF 1 NOV 65 IS OBSOLETE  
S/N 0102-LF-014-6601

UNCLASSIFIED

SECURITY CLASSIFICATION OF THIS PAGE (When Data Entered)

(Cont.)

10 to 100 6th power

UNCLASSIFIED

SECURITY CLASSIFICATION OF THIS PAGE (When Data Entered)

for a new, marketable testing capability, and the need to maintain a state-of-the-art facility, justified a major design effort to remove the constraints limiting the facility to the  $5.4 \times 10^8$ /ft Reynolds number. This report documents this design effort, and subsequent performance of the new configuration.

Original - English - Reynolds  
Unclassified

S/N 0102- LF-014-6601

UNCLASSIFIED

SECURITY CLASSIFICATION OF THIS PAGE (When Data Entered)

## FOREWORD

The purpose of this report is to document the Mach-10 High Reynolds Number (HIRE) Program recently completed in the NSWC Hypervelocity Wind Tunnel Facility. The report describes, chronologically, the HIRE program from its inception in January 1980, through its successful completion in July 1983. Included in the report is the analytical work performed which addressed the technical issues involved in developing the HIRE testing capability. Also included are the results of the test series used to shakedown the new hardware system.

The author wishes to acknowledge several individuals for performing analytical work which is documented in this report: Mr. Jacques A. F. Hill, the HIRE Program Manager, for his work in Appendices A, I, M, and P, Mr. Jeffrey F. Waldo for Appendices C, D, L, and O, Mr. Michael M. Metzger for Appendices G and P, Mr. Charles S. Rozanski for Appendices K and N, and Mr. Robert H. Waser for Appendix H. The author also wishes to acknowledge Mr. Roland Schlie who encouraged the writing of this manuscript.

Approved by:

*T. Clare*

T. CLARE, Head  
Strategic Systems Department

Accession For	
NTIS GRA&I	<input checked="" type="checkbox"/>
DTIC TAB	<input type="checkbox"/>
Unannounced	<input type="checkbox"/>
Justification	
By	
Distribution/	
Availability Codes	
Dist	Avail and/or Special
A-1	





## CONTENTS

	<u>Page</u>
INTRODUCTION . . . . .	1
TUNNEL OPERATION DESCRIPTION . . . . .	1
FACILITY HARDWARE LIMITATIONS . . . . .	3
HIRE INITIAL DESIGN CONFIGURATION . . . . .	6
CONTROL VALVES . . . . .	6
HEATER INSULATION PACKAGES . . . . .	6
OUTER JACKETS . . . . .	7
INSULATION MATERIAL . . . . .	7
INNER LINERS . . . . .	7
HEATER ELEMENT BASE . . . . .	8
DIAPHRAGM AREA . . . . .	8
NOZZLE THROAT . . . . .	8
PARTICLE SEPARATOR . . . . .	9
DIAPHRAGMS . . . . .	9
PRESSURE CONTAINMENT COMPONENTS . . . . .	9
THERMAL LINERS . . . . .	9
THROAT BLOCK INSERT CARRIER . . . . .	10
MECHANICAL VALVE . . . . .	10
NOZZLE, TEST CELL, AND VACUUM SPHERE . . . . .	11
INITIAL CONFIGURATION SUMMARY . . . . .	11
COLD SHAKEDOWN OF THE MECHANICAL VALVE . . . . .	11
COLD SHAKEDOWN SUMMARY . . . . .	13
ANALYSIS AND REDESIGN . . . . .	13
FLOW RESTRICTOR AND ABLATORS . . . . .	13
CONTROL VALVES . . . . .	15
QUICKPROOF TEST SERIES . . . . .	16
PRESSURE PULSE ANALYSIS AND HEATER PACKAGE REDESIGN . . . . .	17
QUICKPROOF PHASE TWO . . . . .	18
HARDWARE ANALYSIS AND DESIGN . . . . .	19
INSTRUMENTATION PACKAGE . . . . .	19
T <sub>0</sub> THERMOCOUPLES . . . . .	20
PARTICLE SEPARATOR EXHAUST . . . . .	20
MAIN HEATER INSULATION PACKAGE . . . . .	20
TEST CELL TEMPERATURE PROBE . . . . .	20
CONTROL VALVES . . . . .	21

## CONTENTS (Cont.)

	<u>Page</u>
CALIBRATION TEST SERIES . . . . .	21
HEATER ELEMENT AND CONTROL VALVE ANALYSIS . . . . .	22
DEMONSTRATION TEST SERIES . . . . .	23
OPERATIONS SUMMARY . . . . .	23
PROJECT SUMMARY . . . . .	25
REFERENCES . . . . .	70
APPENDIX A--INITIAL FEASIBILITY STUDY . . . . .	A-1
APPENDIX B--INITIAL HIRE DESIGN CONFIGURATION ANALYSES . . . . .	B-1
APPENDIX C--DEPRESSURIZATION TEST SERIES . . . . .	C-1
APPENDIX D--NOZZLE THROAT ANALYSIS . . . . .	D-1
APPENDIX E--PARTICLE SEPARATOR DESIGN AND ANALYSIS . . . . .	E-1
APPENDIX F--DIAPHRAGM AREA COMPONENTS' ANALYSIS . . . . .	F-1
APPENDIX G--THROAT BLOCK INSERT CARRIER ANALYSIS . . . . .	G-1
APPENDIX H--VERIFICATION OF SMALL DISTURBANCE FORMULA . . . . .	H-1
APPENDIX I--ABLATOR FUNCTION MODEL . . . . .	I-1
APPENDIX J--FLOW RESTRICTOR ANALYSIS . . . . .	J-1
APPENDIX K--ABLATOR STRUCTURAL ANALYSIS . . . . .	K-1
APPENDIX L--BLOWDOWN COMPUTER MODEL . . . . .	L-1
APPENDIX M--PRESSURE PULSE ANALYSIS AND NEW CONTROL VALVE OPERATION . . . . .	M-1
APPENDIX N-- $T_0$ PROBE DESIGN AND ANALYSIS . . . . .	N-1
APPENDIX O--M-10 HIRE TOTAL TEMPERATURE PROBE DESIGN . . . . .	O-1
APPENDIX P--HEATER ELEMENT BUFFETING AND BAFFLE PLATE DESIGN . . . . .	P-1

## ILLUSTRATIONS

<u>Figure</u>		<u>Page</u>
1	REYNOLDS NUMBER EXTRAPOLATION . . . . .	26
2	(a) SCHEMATIC OF TUNNEL NO. 9 FACILITY . . . . .	27
	(b) TUNNEL-9 VERTICAL HEATER AND FLOW PASSAGE ARRANGEMENT . . . . .	28
3	TYPICAL TUNNEL RUN . . . . .	29
4	MACH 10/14 DIAPHRAGM SECTION . . . . .	30
5	FATIGUE LIFE VERSUS OPERATING PRESSURE (DRIVER VESSELS) . . . . .	31
6	MACH-14 FLOW RESTRICTOR DESIGN . . . . .	32
7	(a) HEATER VESSEL INSULATION PACKAGES . . . . .	33
	(b) RAREFACTION WAVE MOVING BACK THRU VERTICAL FLOW PASSAGE . . . . .	34
8	MACH-10 HIRE DIAPHRAGM AREA . . . . .	35
9	THROAT INSERT FINITE ELEMENT MODEL . . . . .	36
10	MACH-10 PARTICLE SEPARATOR . . . . .	37
11	MECHANICAL VALVE . . . . .	38
12	AERODYNAMIC FORCE ON MECHANICAL VALVE . . . . .	39
13	ABLATION MODEL . . . . .	40
14	ABLATOR PERFORMANCE; THEORY AND EXPERIMENT . . . . .	41
15	HOT GAS USED IN ABLATION . . . . .	42
16	MACH-10 HIRE FLOW RESTRICTOR . . . . .	43
17	ABLATOR FINITE ELEMENT MODEL AND LOADING CONDITIONS . . . . .	44
18	BLOWDOWN MODEL . . . . .	45
19	SERVO CONTROLLER PERFORMANCE . . . . .	46
20	HEATER INSTRUMENTATION PACKAGE . . . . .	47
21	PRESSURE PULSE IN HEATER . . . . .	48
22	$P_o$ AND $T_o$ VERSUS TIME FOR QUICKPROOF . . . . .	49
23	VALVE DISPLACEMENT VERSUS TIME, NEW MODE OF OPERATION . . . . .	50
24	PRESSURE PULSES IN HEATER ANNULUS, $P_A - P_{H\text{BOT}}$ FOR OLD AND NEW VALVE MOTION . . . . .	51
25	NEW HEATER INSTRUMENTATION PACKAGE . . . . .	52
26	NEW $T_o$ THERMOCOUPLE DESIGNS . . . . .	53
27	PARTICLE SEPARATOR MUFFLER DESIGN . . . . .	54
28	MAIN HEATER INSULATION VOIDS . . . . .	55
29	TOTAL TEMPERATURE PROBE DESIGN . . . . .	56
30	RADIAL MACH NUMBER DISTRIBUTION AT TWO AXIAL STATIONS . . . . .	57
31	HEATER PACKING RING . . . . .	58
32	HEATER ELEMENT FAILURE LOCATIONS . . . . .	59
33	BAFFLE PLATE DESIGN . . . . .	60
34	LAMINAR TO TURBULENT TRANSITION ON MODEL . . . . .	61
35	TRANSITION ONSET VS REYNOLDS NUMBER . . . . .	62
36	TYPICAL SUPPLY PRESSURE HISTORY . . . . .	63
37	NUMBER OF ACTIVE VALVES VS NUMBER OF OPEN HOLES IN FLOW RESTRICTOR . . . . .	64

## ILLUSTRATIONS (Cont.)

<u>Figure</u>		<u>Page</u>
38	NOZZLE SUPPLY PRESSURE, $P_o$ , VS. NUMBER OF HOLES IN FLOW RESTRICTOR . . . . .	65
39	REYNOLDS NUMBER VS. RUN TIME . . . . .	66
40	STATIC PRESSURE, $P_\infty$ , DYNAMIC PRESSURE, $q_\infty$ , PITOT PRESSURE, $P_T$ VS SUPPLY PRESSURE . . . . .	67
41	MACH NUMBER VERSUS SUPPLY PRESSURE . . . . .	68

## TABLES

<u>Table</u>		<u>Page</u>
1	EXPANSION WAVE STRENGTH IN VARIOUS HEATER SECTIONS . . . . .	69
2	OUTER JACKETS' PRESSURE CAPABILITIES . . . . .	69
3	INNER LINERS' PRESSURE CAPABILITIES . . . . .	69

## INTRODUCTION

It is a well documented fact that the key to reentry vehicle flight simulation is duplication of the principal similarity parameters, i.e., Mach number and Reynolds number. The present NSWC Hypervelocity Facility has two Mach number capabilities (10 and 14) which operate over a range of Reynolds numbers. The Mach-10 leg had a maximum Reynolds number capability of  $5.4 \times 10^6/\text{ft}$ . The Reynolds number region of interest for Mach-10, encompassing the reentry flight regime, has been established as 0 to  $100 \times 10^6$ . Using oversized models in the present 5 foot diameter test cell, this Reynolds number regime scales down to a 0 to  $20 \times 10^6/\text{ft}$ . requirement in the Hypervelocity Facility. The potential for a new, marketable testing capability, and the need to maintain a state-of-the-art facility, justified a major design effort to remove the constraints limiting the facility to the  $5.4 \times 10^6/\text{ft}$  Reynolds number. The intent of this report is to document this design effort, which will hereafter be termed HIRE (Higher REynolds number), and subsequent performance of the new configuration.

Figure 1 is a graph of Reynolds number versus nozzle supply pressure,  $P_0$ , again for Mach-10 operation. The data plotted represent the  $P_0$  testing capability prior to HIRE. Depending upon the method of extrapolation used, attaining the  $20 \times 10^6/\text{ft}$ . Reynolds number at Mach-10 would require a  $P_0$  between 15,000 psi and 20,000 psi. The maximum  $P_0$  attainable prior to the HIRE program was 5,000 psi, constrained by structural limitations of a number of tunnel hardware items.

## TUNNEL OPERATION DESCRIPTION

The original design concept for the NSWC Hypervelocity Facility entailed having three distinct Mach number capabilities, Mach-10, Mach-15, and Mach-20, as shown in Figure 2(a). Each Mach number capability, or "leg" of the facility, would have its own heater vessel to store hot gas, and its own nozzle. The three legs of the facility would share the "driver vessels," and the test cell. The Mach-15 capability was first brought on line, and subsequently changed to Mach-14 due to problems experienced in obtaining gas temperatures required for Mach-15 testing. The Mach-14 leg has now operated successfully for 8 years, and a total of 750 tunnels runs. The Mach-20 leg of the facility is considered a future capability due to its test gas temperature requirement of  $5000^\circ\text{F}$ . The Mach-10 leg of the facility originally used the horizontal heater vessel shown

in Figure 2(a). However, problems with the heater vessel (described herein) necessitated moving Mach-10 operations to the Mach-14 leg of the facility. This could be done by simply interchanging the Mach-14 and Mach-10 nozzles, an operation requiring about one-half of a day. The reason for moving Mach-10 operations to the Mach-14 leg was to take advantage of the proven performance of the vertical heater vessel. Before proceeding with details of Mach-10 testing using the vertical heater vessel, it is appropriate to describe a typical tunnel run in order to highlight several important hardware components.

In operation, nitrogen at room temperature is used to fill the heater (see Figure 2(b)) to a pressure on the order of 1/4 of the desired test pressure. Electrical power (up to a megawatt) is then applied to a graphite heater element which heats the gas and, at the same time, pressurizes it at a constant volume. The nitrogen is contained in the heater by a dual diaphragm assembly as shown. A run is begun by overpressurizing the inter-diaphragm volume. The hot test gas is driven at constant pressure through the nozzle throat by cold nitrogen initially stored at a higher pressure in the driver vessels. The flow of this gas is modulated by control valves located between the driver vessels and the heater vessel. An inlet manifold upstream of the valves distributes the flow from the driver vessels to the inlets of the valves. An outlet manifold downstream of the valves distributes the flow to the heater inlet pipe. The gas from the driver vessels proceeds down through the annular gap between the heater vessel I.D. and insulation package O.D. to the bottom of the heater. This cold gas then turns and pushes the hot test gas up, in a piston-like fashion, out of the heater, through the diaphragm area, and down the nozzle, eventually dumping into a large vacuum sphere.

While nine control valves are available, this number of valves is required only at Mach-10, where the nozzle throat diameter is largest. The control valves are driven by an electrohydraulic servo, which acts to drive the rate of change of heater pressure to zero.

The driver vessel pressure is raised to 26,000 psi by compressors. The pressure is then raised to its final value (<40,000 psi) by constant volume heating.

A typical tunnel run, from diaphragm burst to flow breakdown, lasts 1.5 seconds, during which .8 seconds of "good" flow is obtained, i.e., flow that is condensation free, as shown in Figure 3.

From a gas dynamics point of view, a tunnel run has two important regimes; the initial transient condition which occurs during the first 100 msec after diaphragm burst, and the steady-state regime during which "good" flow is established and data taken.

The transient condition is characterized by an expansion wave, resulting from diaphragm burst, which moves back into the heater. The pressure oscillations experienced by various heater internal components, resulting from the effects of this wave, can be of a large magnitude. In particular, the survival of heater insulation packages (shown in Figure 2(b)) during this period is a major concern.

The steady-state flow regime is characterized by uniform flow through the vertical flow passage. Primary concerns during this time are pressure drops across the insulation packages (arising from flow friction losses in the annular gaps around the insulation liners), and pressure drops across various diaphragm area components.

#### FACILITY HARDWARE LIMITATIONS

It was noted in the Introduction that Mach-10 testing using the vertical heater vessel was limited in Reynolds number capability due to a number of hardware constraints. Originally Mach-10 testing was conducted using a horizontal heater vessel with a maximum pressure capability of 15,000 psi. Problems were encountered in trying to keep the pressure vessel's inner diameter cool while the test gas was heating. A decision was made to conduct Mach-10 testing utilizing the Mach-14 heater vessel. It was felt that the demonstrated operability of the Mach-14 heater vessel assembly would eliminate the heatup problem encountered in the horizontal vessel. However, due to internal volume differences between the Mach-10 horizontal vessel (87 ft<sup>3</sup>) and the Mach-14 vertical vessel (30 ft<sup>3</sup>), and the difference in nozzle throat diameters between Mach-10 (2.4 inches) and Mach-14 (1 inch) run time would be greatly reduced. It was felt though, that the penalty of reduced run time was worth the hoped for increase in operability.

The diaphragm area assembly which was a result of the decision to mate the Mach-10 nozzle and the Mach-14 heater vessel is shown in Figure 4. It contained a mixture of Mach-10 and Mach-14 components. The reason for the mixture was that it was necessary to use the Mach-14 "flow restrictor" to keep the strength of the expansion wave moving back into the heater to Mach-14 levels, thus ensuring the survivability of the Mach-14 heater insulation packages, and the graphite heating element. (A critical groundrule set down before Mach-10 testing would be permitted in the vertical heater vessel was that Mach-14 operations must not be adversely affected). Because a number of Mach-14 components had to be used, the resulting flow passage through the diaphragm area was smaller than Mach-10 testing usually employed. Thus, a large pressure drop through the diaphragm area was induced which resulted in the reduced nozzle throat pressure,  $P_0$  referred to in the Introduction. Calculations indicated that due to the smaller flow restrictor opening present in the Mach-14 restrictor, flow would be choked at both the nozzle throat and Mach-14 flow restrictor. Reference 1 contains analyses of critical Mach-14 components, under Mach-10 loading conditions. In addition, Reference 2 contains the results of the test series that first used the combination of the Mach-10 nozzle and the Mach-14 heater vessel. That test series demonstrated that Mach-10 testing could be conducted in the Mach-14 tunnel leg, but that Reynolds number capability would be limited due to the reduced flow passage area.

While the above-noted configuration was a bonafide Mach-10 facility, with a Reynolds number capability of  $5.4 \times 10^6/\text{ft}$ , proven out by numerous tunnel runs, it would never be able to attain the more desirable higher Reynolds numbers of interest. In order to ascertain what Reynolds numbers were



obtainable using the vertical heater vessel, an engineering study was performed in-house. This effort entailed matching the facility's operability and safety constraints to desired HIRE performance characteristics. The basic guidelines/limitations the study worked within were:

- a. The driver vessel pressure must not exceed 40,000 psi.
- b. The heater vessel pressure must not exceed 22,000 psi, its current operating pressure limit.
- c. The heater element must not be stressed to a level greater than that experienced in Mach-14 testing.
- d. The insulation packages should be designed to withstand a full strength rarefaction wave.

A few words concerning these items are in order. For Mach-14 testing the maximum driver vessel pressure required is 34,000 psi. However, Mach-10 HIRE with its larger mass flow rates, would require somewhat higher pressures. A limit of 40,000 psi was selected for two reasons. First, in a number of runs made early in the initial shakedown of the facility, operability problems were experienced at pressures over 40,000 psi. Secondly, acceptable fatigue life could be realized at the 40,000 psi pressure level. Figure 5 is a graph of fatigue life versus maximum operating pressure (based on calculations in Appendix A).

The heater vessel pressure limit of 22,000 psi was based strictly on fatigue life considerations. A study performed in Reference 3 determined that modifications had to be made to the large closure nuts which bolt the ends of the vessel shut, in order to increase their available fatigue life. The modification made to the closure nuts resulted in a decrease in maximum pressure capability from 47,000 psi to 22,000 psi.

Structural analysis of the graphite heater element, shown in Figure 2(b), is difficult due to its unusual geometry and the nature of the loading conditions placed upon it. In order to ensure operability of the HIRE configuration, it was decided to keep the strength of the expansion wave to its Mach-14 value, which the heater element had demonstrated it could withstand. Appendix A contains the calculations on which decisions about expansion wave strength were made.

As noted earlier, when the diaphragms rupture, an expansion wave moves upstream through the diaphragm area into the heater, where it damps out quickly. The flow restrictor mentioned earlier contains a number of components, as shown in Figure 6. The plastic "ablator" inserts are what actually reduce the strength of the wave to an acceptable level. Once the wave has passed through the ablators, hot gas begins to wash out the ablators, thus opening up the flow passage to an area 1.4 times the throat area. This has been found to be the minimum area required for good flow recovery.

Because of the potential for ablator structural failure, it was decided that the new heater insulation packages should be able to withstand a "full strength" expansion wave, i.e., one based on the final open area in the flow

restrictor, not on the initial ablator area, which the heater internal components should normally experience. Thus, if an ablator structural failure were to occur, the costly heater insulation packages would not need to be replaced. (The question that naturally arises then is, if the heater insulation packages were to be designed to withstand the largest possible expansion wave load, why bother with ablators in the first place? The basic reason ablators were needed was to protect the heater element. However, even if the heater element could have been designed to survive the full strength expansion wave, there are two secondary reasons why ablators were needed. First, the prediction of the magnitude of the expansion wave strength was based on small disturbance formulae, the accuracy of which had not been verified at the time of the insulation package design effort, thus leading to a measure of caution being injected into the overall system design. Secondly, even if the formulae were yielding accurate estimates of the expansion wave load, it would not be desirable to "hit" the insulation package with its design load in every tunnel run.)

It warrants mentioning that the above constraints were the result of a combination of operational experience at Mach-14, and the recommendations of a major safety study (Reference 4) which was performed in 1975.

Based on the limitations noted above, the preliminary study concluded:

- a. The maximum throat pressure,  $P_0$ , which could be expected was 18,000 psi. Due to the 22,000 psi pressure limit in the heater, and expected pressure drops through the diaphragm area, it was felt that 18,000 psi was the best the facility could be expected to yield. In addition, recall the observation that, depending on the method of extrapolation used, a  $P_0$  of 18,000 psi would probably translate into the  $20 \times 10^6/\text{ft}$ . Reynolds number desired.
- b. The amount of "good flow" time would be .25 seconds, as contrasted to a typical value of .8 seconds. It was felt that this shortened period would still enable the facility to conduct pitch sweeps for R/B stability testing (+4 to -4 degrees angle-of-attack).
- c. For Mach-10 HIRE, the present ablative type flow restrictor was too slow, i.e., used up valuable good flow time, and must be replaced.
- d. The driver vessels could match the .25 second run time, with a  $P_0$  of 18,000 psi, if their maximum operating pressure were increased to 38,000 psi. The detailed calculations on which the above conclusions were based are contained in Appendix A.

In short, the study concluded that Reynolds numbers up to  $20 \times 10^6/\text{ft}$ . were obtainable, with one important caveat: a new method of restricting the expansion wave moving back into the heater must be found. This was due to the conclusion that the ablators would be too slow-opening for HIRE operations. In addition, all the Mach-14 hardware which was used in the initial Mach-10 testing program would have to be replaced. This included the three heater insulation packages, and the Mach-14 diaphragm area components which had previously been used.

## HIRE INITIAL DESIGN CONFIGURATION

The entire calendar year of 1980 was devoted to generating and reviewing a preliminary design. This section will cover in some detail the preliminary design configuration, and the design and analysis work associated with this effort.

## CONTROL VALVES

Once the diaphragms rupture, gas begins to exit the heater. To maintain constant supply conditions at the nozzle throat, gas from the drivers must replace the gas discharging from the heater. The control valves located between the driver vessels act to drive the rate of change of heater pressure to zero. The valves themselves are electrohydraulic servo driven gas valves. The Rexroth servo drivers are capable of opening the valves fully in .230 seconds, which permitted the predicted useful run time of .250 seconds to be realized. The blowdown calculations on which this assessment was made are contained in Appendix A. Therefore, the decision was made to use the Rexroth controllers on hand.

## HEATER INSULATION PACKAGES

It was noted earlier in the report that the design criteria for the structural adequacy of the heater insulation packages was that they be able to survive an expansion wave that the ablators failed to mitigate. Calculations were made to ascertain the strength of the expansion wave in various sections of the heater. Typically, three areas were examined, as shown in Figure 7(a); the main heater section where the heating element is located, the vertical elbow section just above the main heater section, and the horizontal elbow section leading into the diaphragm area. The strength of the expansion wave in each section was calculated using small disturbance formulae, and the assumption that the expansion wave is similar to that in a Ludwig tube. Reference 5 contains the initial calculations performed for the Mach-14 leg. Appendix B contains similar calculations for the three areas noted above, assuming Mach-10 conditions. The results are summarized in Table 1.

There are a total of three insulation packages in this area, one for each of the sections noted above. Each insulation package consists of a carbon steel outer liner, a thickness of insulating material (Lo-Con felt for the initial design), Inconel mesh screen, and a perforated inner liner fabricated from Hastelloy. In addition, the main heater package contains a top plate and support ring (not shown). The expansion wave moving back through the heater places an oscillating pressure load on the insulation packages, as shown in Figure 7(b). There is a region of undisturbed gas just ahead of the wave at pressure  $p$ , while the gas behind the wave is at  $p - \Delta p$ , the  $\Delta p$  being the value given in Table 1 for different areas of the heater. Recall now the design criteria that the insulation packages be able to withstand this pressure load situation.

### Outer Jackets

All of the insulation packages' outer jackets were fabricated from low carbon steel. Due to the quasi-static nature of the load placed on the jackets, two pressure capabilities were ascertained for each outer jacket. Pertinent calculations are contained in Appendix B. The first was a static pressure drop capability, across the jacket. The second was a buckling capability, assuming the stresses stayed within the elastic limit of the material. The values given in Table 2 represent the most conservative estimate of load carrying capability of the outer liners, i.e., the smaller of the two values noted above. Also given in Table 2 are the pressure drop numbers obtained earlier for each section of the heater. As can be seen, all the outer jackets met the design criteria noted above.

The strength of the top cover plate of the main heater insulation package was also obtained, and is listed in Table 2. As can be seen, this component was also structurally adequate.

### Insulation Material

Due to the reduced run times anticipated under Mach-10 HIRE conditions, it was necessary to maximize the volume of hot gas available during a run, while insuring that the heater pressure vessel bore stayed below 500°F. To that end, calculations were made (Appendix B) to determine the thickness of insulation material required in the main heater insulation package. A final thickness of 1.13 inches was selected. It then became necessary to ascertain various insulator's ability to withstand the depressurization which occurs when the expansion wave moves down through the heater. A test series was conducted to that end, the results of which are summarized in Appendix C. The combination of Lo-Con felt and a layer of mesh screen resulted in the largest depressurization rate capability. As determined in Appendix B, the highest depressurization rate for an ablator failure condition occurs in the horizontal elbow section, and is equal to  $9.6 \times 10^6$  psi/msec which is much less than the depressurization capability of the combination noted above.

### Inner Liners

All of the inner liners of the various insulation packages were fabricated from perforated Hastelloy sheet, rolled and welded to shape. As was done for the outer jackets, a pressure drop capability was obtained, and is listed in Table 3. The pressure load each inner liner experiences however, is much less than that felt by its respective outer jacket, due to the perforations in the liner which facilitate the depressurization occurring in the insulation volume behind the liner. However, the holes tend to weaken the liner from a structural viewpoint. Calculations were performed in Appendix B which account for both effects, and the results listed in Table 3. As can be seen from the values given, all of the inner liners had adequate strength.

## HEATER ELEMENT BASE

The heater element base, shown in Figure 2(b), connects the heater element to electrodes supplying electrical power to the element. In order to maximize available hot test gas, it was desirable to shorten the heater element base. Calculations contained in Appendix B indicated that a reduction in length from 23.5 inches to 14 inches was possible while ensuring that the power input/volume ratio would not exceed that used in Mach-14 operations (recall that Mach-14 gas temperature is 3000°F versus 1500°F required for Mach-10). Further reductions in length would necessitate other geometric changes whose effect would be difficult to gauge. It was therefore decided that geometric changes other than a reduction in length to 14 inches would be foregone.

## DIAPHRAGM AREA

The diaphragm section of the Mach 10 leg is located between the heater vessel and the nozzle, as shown in Figure 2(b). This section houses the nozzle throat, particle separator, flow restrictor, diaphragms, and diaphragm separator bodies, all of which are shown in Figure 8. To prevent leakage of the gas flowing through this section of the tunnel, the entire diaphragm area is "locked up" by means of a hydraulically pressurized ring. The pressure containment components in the diaphragm area are subjected to lockup loads, and the flow of high pressure, high temperature nitrogen. In particular, the loads imposed due to the high mass flow rates present under HIRE conditions necessitated a great deal of new hardware being designed in this section.

## Nozzle Throat

The existing Mach-10 nozzle throat was fabricated from 17-4 PH stainless steel, and had been used successfully for tunnel runs where the throat pressure,  $P_0$ , has reached 6,400 psi. Mach-10 HIRE conditions would result in a  $P_0$  of 18,000 psi. To ascertain the suitability of the existing throat for Mach-10 HIRE operations, a thermostructural finite element analysis of the throat was performed (Appendix D). The throat model, shown in Figure 9, was subjected to the high pressure noted above, and a transient heat transfer condition, due to the hot gas flowing through the throat. The analysis indicated that a small thickness of material along the bore of the throat would yield in compression. This gave rise to concerns about setting up a mechanism for a fatigue type failure of the component. An additional analysis was performed, using the  $P_0$  of 6,400 psi, which the throat had successfully withstood for 50 runs. This analysis also indicated that a very small region of material (.1 inches in the radial direction) would yield in compression. Comparison of the two analyses determined that the stress field at the bore was dominated by the temperature gradient through the component at any given cross section. The difference in this gradient between the 6,400 psi and 18,000 psi condition was minimal. It was decided that the existing throat insert piece could be used for Mach-10 HIRE operations, with the stipulation that the bore of the component be periodically checked for dimensional stability.

### Particle Separator

The particle separator acts as a filter in that it removes debris from the gas flow. Separation is effected by turning the flow through the separator, while dislodging particles from the flow stream by bouncing them along the annular gap between the separator and the particle separator housing liner, as shown in Figure 10. In essence, the inertia of the particle itself is used to separate it from the flow stream. It was determined that the existing particle separator used in Mach-10 operations would have to be redesigned for two reasons; first, the pressure drop across the separator had to be reduced for HIRE operations in order to maximize  $P_0$ , and second, aerodynamicists working in the facility had expressed a desire to "clean up" the Mach-10 flow, based on their observations of pitting occurring on models located downstream in the test cell. An analysis was performed (Appendix E) which utilized a flow model to optimize both particle separation effectiveness, and pressure drop performance. The improved performance was achieved by, primarily, two modifications to the old design; a nose section was added to reduce the pressure drop occurring across the front of the separator, and a larger number of smaller holes were employed to increase efficiency of the separation mechanism. The new design is shown in Figure 10. The analysis predicted the new separator would have a 25% decrease in pressure drop across it, and be able to remove particles 20 microns in diameter and larger, versus the old separator's 40 micron and larger capability.

### Diaphragms

The diaphragms used for Mach-10 operations were fabricated from 304 stainless steel, and act to separate the high pressure and low pressure sides of the tunnel. The diaphragms are scored to give a particular burst pressure capability. Mach-10 HIRE operations would utilize the existing diaphragm design.

### Pressure Containment Components

The pressure containment components noted in Figure 8 are subjected to both the lockup load, and the high internal pressure present when a tunnel run is occurring. Appendix F contains calculations which determined the fatigue life of these components. New pressure containment components were fabricated for HIRE due to the number of geometry changes required in this section.

### Thermal Liners

To protect the pressure containment components noted above from being subjected to the hot gas flow and resulting high thermal stresses at the bore, thermal liners were used throughout the diaphragm section, as shown in Figure 8. These liners simply act as a buffer between the hot gas and the pressure containment components. Appendix F contains pertinent analyses of the thermal liners. Operational procedures dictate that the thermal liners be periodically inspected for signs of cracking. The benefit of using liners is that they can be replaced cheaply and easily when cracking does occur.

### Throat Block Insert Carrier

A finite element analysis (Appendix G) of the throat block insert carrier, shown in Figure 8, was performed to determine its ability to withstand HIRE loading conditions. The analysis indicated that the existing carrier, fabricated from 304 stainless steel, was structurally inadequate. The analysis also determined that a geometrically similar throat block insert carrier, fabricated from 4340 steel, would be adequate. A new carrier was fabricated from 4340 to be used for all Mach-10 operations.

### Mechanical Valve

The flow restrictor design used in both Mach-14 and Mach-10 operations prior to HIRE utilized ablative inserts with small holes (see Figure 6). This design has proven to be highly reliable and has been utilized in more than 700 tunnel runs, over a wide range of conditions. For Mach-10 operations using the combination of Mach-14 and Mach-10 components, a typical tunnel run included about .200 seconds of ablation time.

As noted earlier in the limitations section, the maximum run time that was predicted for the HIRE configuration was .250 seconds. An ablation time of .200 seconds would be unacceptable in that it would consume too much valuable run time. Several schemes were investigated to determine if the .200 second ablation time could be reduced. The end result was the decision to design a hydraulically driven mechanical flow restrictor valve to replace the ablative type design. In fact, the initial design of the facility incorporated a mechanical valve design, but it was intended to replace both the flow restrictor and diaphragm functions. The mechanical valve suggested for use in HIRE replaced only the flow restrictor function, thus greatly reducing the complexity of the design problem. A short description of the valve operation will now be given.

The mechanical valve consisted of an upstream coverplate containing seven holes, a downstream slideplate containing seven holes, a piston to move the slideplate and an air to oil cylinder, as shown in Figure 11. The valve was designed to work off a pressure difference that existed across the slideplate. Up until the time of diaphragm rupture the diaphragm area, from the upstream diaphragm to the elbow section, was under the heater pressure of 22,000 psi. Initially the slideplate was set in the down position. In this position there was an open area created by the .020 inch gap between the upstream coverplate and the slideplate. Upon diaphragm rupture, gas began to move through the flow restrictor as the rarefaction wave passed back through the small initial open area. As the gas passed through the restrictor, a pressure drop was induced across the slideplate. This pressure drop was sensed by the gas to oil piston with the upstream (higher) pressure on one side, and downstream (lower) pressure on the other side. This pressure difference drove the piston, which in turn moved the slideplate upward. When the slideplate reached the end of its travel, the seven holes in the upstream coverplate were in line with the seven holes in the slideplate, thus producing the larger areas needed for HIRE operations. The desired "time to open" for the mechanical flow restrictor valve was 50 milliseconds. This value of opening time was selected to keep the frequency of any expansion wave resulting from the valve opening (20 Hz for a 50 millisecond

opening time) some distance away from the measured frequencies of the rarefaction wave (40 Hz to 100 Hz) resulting from diaphragm burst. In addition to its faster opening time, the mechanical flow restrictor had the advantage of removing a potential source of debris (the ablator material) from the tunnel flow.

#### NOZZLE, TEST CELL, AND VACUUM SPHERE

The nozzle, test cell, and vacuum sphere are all on the low pressure side of the tunnel. Mach-10 HIRE conditions were not expected to require redesign or modification of these components.

#### INITIAL CONFIGURATION SUMMARY

To recapitulate briefly, Mach-10 operation required a predicted throat pressure capability between 15,000 psi and 20,000 psi. This requirement, and its attendant increased mass flow rates, necessitated reevaluation of the entire Mach-10 leg of the Hypervelocity Facility. This reevaluation resulted in several major hardware developments:

- a. Three new insulation packages, which protect the heater vessel from the hot test gas, were designed which were capable of withstanding a full strength rarefaction wave.
- b. A new particle separator was designed which was more efficient from a particle separation standpoint, and had a 25% decrease in pressure drop.
- c. A mechanical flow restrictor valve capable of opening in 50 milliseconds was designed to replace the ablative type flow restrictor.

In addition, a new throat block insert carrier, pressure containment components, and thermal liners were designed. It was decided to manufacture and cold test the mechanical valve by February 1981, with hot testing to be started in late 1981.

#### COLD SHAKEDOWN OF THE MECHANICAL VALVE

There were actually two series of cold pressure tests run with the mechanical valve, totalling 17 runs, in 1981. In addition to checking out the feasibility of using a mechanical flow restrictor, the tests had two other purposes:

- a. Determine if the assumption that the magnitude of the expansion wave could be calculated using small disturbance formulae was valid.



b. Observe servo valve performance with respect to maintaining a constant heater pressure.

Both of the above issues required resolution before procurement of additional hardware could proceed.

The first test series (in February) consisted of 3 tunnel runs. In this test series numerous problems were experienced in trying to make the mechanical flow restrictor function properly. In fact, the valve never opened fully in any of the tests, usually sticking open at about 40% of its stroke. Analyses after the test series was completed indicated two primary sources of resistance to the slideplate moving completely open. First, the dry lubricant used on the contact surface was not performing as expected, and secondly, aerodynamic forces resulting from the flow being turned through a partially opened valve resulted in large forces opposing the valve opening motion (see Figure 12). A second test series was planned to determine forces required to completely open the valve.

Two runs made in the first test series were dedicated to obtaining information regarding the strength of the expansion wave in the heater, and the accuracy of the methods used to calculate it. In these two runs pressure transducers were mounted in the bottom of the heater to measure variations in pressure. The mechanical flow restrictor valve was successively blocked half open, and then full open, so that a correlation between flow restrictor open area and expansion wave strength could be obtained. The results of the two tests (Appendix H) indicated that the formulae used to calculate expansion wave strength (in Appendix B) were accurate within 10%. Thus, heater insulation packages designed to withstand pressures obtained using the small disturbance formulae should have a high probability of successfully withstanding a full strength expansion wave resulting from an ablator failure.

The second series of tunnel tests, conducted in June 1981, consisted of nine runs. In these tests, the gas side of the free piston was connected to the driver vessels, thus resulting in a larger upstream pressure to drive the mechanical valve. Insofar as opening the valve completely was concerned, the testing was successful. However, numerous operational problems were again experienced with respect to obtaining consistent run-to-run performance.

Following the second series of cold runs, a great amount of analytical work was performed on the mechanical valve to determine if it should still be considered a viable concept in its present form. It was decided that there were too many unknowns remaining to rely on the mechanical valve for Mach-10 HIRE operations. The two principal areas of concern were: one, the force required to open the valve was greater than that capable of being supplied by the initial mode of operation (i.e., the pressure drop existing across the valve) and two, it was not known how the valve would perform under hot conditions, the area of concern here being how the lubricant used between the sliding surfaces would hold up when exposed to the 1500°F nitrogen.

In addition to the mechanical valve problems, the second series of cold shakedown runs demonstrated that the servo valves were not able to maintain a constant heater pressure. This led to concern about the existing Rexroth servo controller's ability to open the control valves fast enough to meet Mach-10 HIRE mass flow rate requirements.

## COLD SHAKEDOWN SUMMARY

The principal conclusions drawn from the results of the two series of cold shakedown runs were:

a. The operability of the mechanical flow restrictor valve under Mach-10 HIRE flow conditions was questionable. Due to uncertainties in how the dry film lubricant would perform when exposed to hot test gas, and uncertainties in what was actually happening aerodynamically when the flow was passing through a partially opened valve, it was felt that the mechanical flow restrictor valve was not a viable option.

b. The use of small disturbance formulae to ascertain expansion wave strength was valid. This conclusion was based on measurements made at the bottom of the heater, with the flow restrictor blocked both half open and full open. It is important to note that this conclusion furnished a data point to compare to the design strength of the insulation packages.

c. The performance of the Rexroth servo controllers on hand was inadequate. These servo controllers seemed to be incapable of meeting the demands of the large mass flow rates required to obtain HIRE conditions.

Between September and November of 1981, numerous schemes were evaluated to replace the mechanical valve. It was decided that ablators should be reinvestigated to see if there might be a configuration which would ablate faster, thus allowing for adequate run time under HIRE conditions.

## ANALYSIS AND REDESIGN

## FLOW RESTRICTOR AND ABLATORS

Recall that the ablators, shown in Figure 6, act to break up the expansion wave moving back into the heater by presenting a small initial opening (.17 in total initial open area) to the wave. The ablators then vaporize, thus opening up a flow passage sufficient for the mass flow rate required. For the Mach-10 HIRE case, this final open area was 6.33 in<sup>2</sup>.

To reexamine the possibility of using ablators, it was decided to perform an analysis of the ablator function itself. The analysis, contained in Appendix I, utilized a mathematical model of the ablation process, and the corresponding changing efflux of gas from the heater as the ablators opened up, as depicted in Figure 13. The mathematical model generated was exercised using previous Mach-10 runs as a data base. As shown in Figure 14, the model accurately predicted the rise of gas pressure passing through the nozzle throat, as a function of time. An important operational point is contained in this figure. As can be seen, there is a finite amount of time before actual test conditions at the nozzle throat are reached, i.e., before maximum pressure and temperature conditions are obtained. This time lag is a result of two phenomena. First, there is a volume of gas contained in the horizontal elbow which is at a

temperature somewhat below the hot gas temperature. This is due to the 7° dogleg present in this section, which acts to stratify the hot and cold regions of gas. This gas must be expelled before the hot gas reaches the nozzle throat. Secondly, it takes a certain amount of heat input to warm up the diaphragm area components, such as the particle separator, to a temperature that will allow for proper gas conditions at the throat. The end result of these observations is that if the ablators could open up in this time period, then no hot gas would be wasted in the ablation process. (Recall that the initial concern about using ablators was that they would consume useful run time.)

Based on the results of the analysis, it was felt that the best way to decrease ablation time was to use a large number of small ablators, maintaining the initial and final open areas noted earlier. Accordingly then, the ablation model was exercised for a number of different ablator configurations. The analysis determined that at least 100 small ablators would have to be used in order to reduce the amount of hot gas wasted to an acceptable level (less than 20% of the total hot gas available). Figure 15 is a graph of hot gas wasted versus number of ablators generated by the ablation model. As can be seen from this figure, if 200 or more ablators could be used, the mass of hot gas wasted would fall below 10%.

The initial design decision then was to select the number of ablators. To do so required analyzing the flow restrictor plate which the ablators are seated against, to determine the maximum number of holes that could be put in such a plate, while maintaining the plate's structural integrity under the HIRE pressure and temperature loading conditions. In addition, there were physical constraints with respect to how large an area could be used in which to situate the ablators. The results of the flow restrictor analysis (Appendix J) indicated that by using a 2.8 in. thick flow restrictor plate, 241 ablators could be accommodated in a pattern as shown in Figure 16. Referring again to Figure 15, this translates into 20 lbs of hot gas wasted, or 8% of the total mass of hot gas available, which was an acceptable loss. It thus appeared, based on the results of the analyses noted above, that ablators could indeed perform as required.

(The question naturally arises at this point, why weren't these analyses performed earlier, thus eliminating the development time used to test out the mechanical valve? The answer is at the time the mechanical valve concept was first proposed, its development appeared to be direct and straightforward. In addition, the valve would help to "clean up" the flow by eliminating small pieces of ablator material which enter the flow rather than sublimating. It was thus decided to forgo alternate flow restrictor concepts at that time and pursue only the mechanical valve option.)

After selecting the number of ablators to be used, attention turned to the design of the ablators themselves. Due to the unusual loading conditions placed upon them, analysis by itself was not an adequate basis on which to make design decisions concerning ablator material and geometry. As a result, a combination of analysis and testing was employed to ensure that the ablators would perform successfully. In the case of HIRE, a finite element analysis of the ablators was performed, using the finite element mesh and static loading conditions shown in Figure 17. Actually two analyses were performed. In the first, the existing Mach-14 ablator geometry was analyzed to use as a baseline for comparison. Then

the proposed HIRE ablator was analyzed, and the results compared. The Mach-10 analysis, contained in Appendix K, indicated that the HIRE ablator was stronger for the loading condition analyzed than the existing Mach-14 ablator.

Following the analytical work, 4 prototype HIRE ablators were manufactured and tested in a depressurization chamber. The entire chamber was heated to 140°F to ensure that the ablator test would simulate a worst-case loading situation. (The tunnel has a protective abort system which will automatically fire the tunnel if the temperature of the gas in the diaphragm area goes above 300°F. Temperature measurements have indicated that at the 300°F gas temperature, the ablators attain a temperature of 140°F.) The results of the testing indicated that the ablators could withstand an expansion wave 1.2 times as strong as that anticipated under HIRE operating conditions. (A brief aside is appropriate here to illustrate the typical problems one encounters in a facility development program such as HIRE. In the initial depressurization tests performed, the ablators failed miserably. This was cause for great concern due to the importance of obtaining a usable ablator design. Analyses were revisited, and initial calculations checked. In the end, the culprit turned out to be the material supplier. The HIRE ablator design called for DELRIN 150, an acetal resin, in the white condition. The supplier delivered DELRIN 500, an acetal resin, also in the white condition. The two materials are virtually indistinguishable, even by chemical testing. Once the proper material was obtained the HIRE ablators performed as expected.)

#### CONTROL VALVES

Recall that after the cold shakedown runs, it was determined that the Rexroth servo controllers on hand were performing inadequately. While the flow restrictor analyses were being performed, the performance of the control valves was being addressed. It was decided that the Rexroth controllers should be replaced by previously obtained Moog controllers. The Moog servo controllers on hand are capable of much faster valve opening speeds (80 milliseconds versus the Rexroths' 250 milliseconds) due to their larger oil flow capacity (200 GPM versus 40 GPM for the Rexroths). To ensure that the Moogs would in fact achieve desired performance, tests were run in which a synthetic valve command was given to the Moog controller, and valve motion was recorded. The synthetic command was generated using calculations of driver vessel blowdown performance. The blowdown calculations (contained in Appendix L) were performed using a computer model of the tunnel blowdown system, as depicted in Figure 18. This model replaced the tedious, and less accurate, hand calculations used to obtain blowdown performance such as those described in Appendix A.

Figure 19 is a trace of valve motion superposed on the synthetic command. As can be seen, the existing Moog controller allows the valve to follow the command nicely. An existing Rexroth controller was also tested to ensure that the synthetic command was accurately reflecting required valve performance. The Rexroth controller's performance was unsatisfactory in this test, as indicated by its curve on Figure 19.

The use of the Moog controllers on hand would present a temporary operational limitation. As a result of their larger oil flow capacity, they inherently possessed a larger leak rate. Tests run on the Moogs indicated that

the leak rate per valve was eight GPM. The existing hydraulic supply unit was capable of 50 GPM at a 3000 psi supply pressure. This would accommodate the use of only 6 valves, whereas HIRE required 9 valves to supply the requisite mass flow rate. The lead time associated with obtaining a new hydraulic unit was about one year. It was decided that while the new hydraulic supply unit was being obtained, a test series should be run to test out the existing Moog controllers' performance in actual wind tunnel testing. Furthermore, it was decided that this test series could be used to test out the new ablator design, and the heater insulation packages' performance.

The test series, named "QUICKPROOF", was designed to be a "proof-of-principles" test in which the HIRE goal of  $20 \times 10^6$ /ft. Reynolds number would be reached. The tunnel would be run using only 6 control valves, which would result in a reduced run time. However, this limitation would be offset by the valuable information obtained concerning the new ablator design, the new heater insulation packages, and the Moog servo controllers on hand. QUICKPROOF would be run in July of 1982, allowing time for manufacture and assembly of the above-noted components.

At this time two additional test series were planned. The first would be a calibration test in which the Mach-10 HIRE flow field would be calibrated in the test cell, primarily checking Mach number uniformity across the core flow. The second test series would be a demonstration test in which predictions of laminar to turbulent flow transition on a body would be validated.

#### QUICKPROOF TEST SERIES

The QUICKPROOF test series required two tunnel entries. In the first test entry, two runs were made with a heater pressure of 10,000 psi and a driver pressure of 24,000 psi. A number of operational problems were experienced, as chronicled below.

1. A larger than expected pressure drop was experienced between the discharge manifold and the bottom of the heater. Apparently overlooked when accounting for the pressure drop expected between the discharge manifold and the bottom of the heater was the restriction due to the "plug valve" which is used to mechanically isolate the driver vessels from the heater vessel between runs. Calculations indicated the plug valve could be modified to reduce the pressure drop across it.

2. The instrumentation package which is used to monitor temperatures throughout the heater vessel was damaged. (The instrumentation package is located in the annular gap around the main heater insulation package, as shown in Figure 20). This was due to the high dynamic pressures associated with the HIRE mass flow rates ripping the instrumentation from the side of the main heater insulation package's outer jacket. This instrumentation package would have to be redesigned before testing could continue.

3. The thermocouples which measure gas temperature in the diaphragm area were reading incorrectly, and were bent over by the high loads imposed due to the HIRE mass flow requirements.

4. The particle separator exhaust system, which empties into the tunnel room, was damaging equipment around the nozzle throat area by venting a large mass flow rate of gas into the tunnel room.

5. A pressure pulse of 2,000 psi amplitude and 50 milliseconds duration was measured in the annular gap around the main heater's insulation package, as shown in Figure 21. The unexpected presence of this pulse precluded testing at higher heater pressures due to concerns about the survivability of the insulation packages.

On the positive side, in both runs the ablators opened up with little or no wasted hot gas. This is indicated in Figure 22 by noting that the gas pressure and temperature required for condensation-free flow are reached simultaneously. Thus, it appeared that ablators could be used to achieve HIRE conditions. Also, the Moog servo controllers on hand performed well, opening the control valves as predicted. Lastly, with the 10,000 psi heater pressure used, the measured Reynolds number was  $10 \times 10^6/\text{ft.}$ , about twice the previous limit.

Following the first two QUICKPROOF runs, it was decided that before additional testing could be performed the heater instrumentation package would have to be redesigned, and the pressure pulse situation resolved. QUICKPROOF was thus scheduled for resumption in November 1982, allowing 3 months for redesign and analysis. It was also decided that the other operational problems noted above should be resolved before the calibration test series was run.

#### PRESSURE PULSE ANALYSIS AND HEATER PACKAGE REDESIGN

An analysis of the pressure pulse phenomenon was performed, and is contained in Appendix M. Results of the analysis indicated that the rapidly opening control valves could be causing a wave to be formed which moved through the vertical flow passage, similar to that resulting from diaphragm burst. While the results of the analysis did not agree exactly with the measured values of pressure oscillation, they were close enough to believe that phenomenologically the pressure pulse could be explained by the quick opening of the control valves. The simple solution to the problem was to slow the control valve opening. However, this operational change was not without potential repercussions. (Recall that in the cold pressure tests run with the mechanical valve, poor heater pressure control resulted when the valves were opened too slowly). The analysis noted above indicated that the valve opening speed should be limited to a value pertaining to an oil flow rate of 40 GPM, which was the capacity of the existing Rexroths. The question which needed to be answered immediately was, could in fact the Rexroths on hand be used for Mach-10 HIRE?

When the decision was made to use the existing Moog controllers, it was because the Rexroths on hand could not follow the synthetic command generated which simulated required valve opening. This command incorporated a 35% initial stroke step function. An investigation was launched to determine if an alternate mode of valve operation could be found in which a much more gradual initial opening command would be required.

An analysis was performed (also contained in Appendix M) in which the initial valve opening commanded by the servo was related to the changing open area of the ablators. This could be done using one of the earlier QUICKPROOF runs as a database. An approximation of the valve motion required is shown in Figure 23. Also shown is the corresponding oil flow into the valve actuator. Note that it does not exceed 30 GPM. Following this analysis, a synthetic command was generated using the valve displacement curve shown in Figure 23. The Rexroths were tested using this command, and were able to follow it very well, as expected. It thus appeared that the Rexroths were capable of being used in HIRE testing, using this new mode of valve initial opening.

During this time the heater instrumentation package was redesigned and installed. Basically the redesign consisted of "beefing up" the package using additional support points along the length of the tubing, and covering the exposed wiring at the top of the main heater can.

#### QUICKPROOF PHASE TWO

The second QUICKPROOF test series, conducted in November, consisted of 6 runs. A number of important milestones were achieved in this series, as listed below:

- a. The pressure pulse in the heater annulus was eliminated. Figure 24 is a graph of the pressure pulse measured in the annular gap for runs 720 (using the Moogs) and 779 (using the Rexroths). As can be seen, the amplitude of the pressure oscillations was reduced by an order of magnitude.
- b. The ablator performance was confirmed for heater pressures up to 18,000 psi.
- c. A Reynolds number of  $20 \times 10^6/\text{ft.}$  was achieved.
- d. Actual run time was about 300 milliseconds, slightly longer than predicted.
- e. The heater pressure was stable within  $\pm 4\%$ , indicating acceptable control valve, and thus servo controller operation.

While the second series of QUICKPROOF runs were certainly encouraging, a number of nagging operational problems existed, as noted below.

- a. The heater instrumentation package again sustained damage. It was felt that the last redesign would be adequate for the maximum heater pressure of 22,000 psi. However, it appeared that there must be some sort of asymmetrical flow pattern in the annular gap which resulted in higher-than-expected loads being placed on the instrumentation components. This package would again require modification.
- b. During the last few runs a number of hot spots developed in the main heater section. The integrity of the insulation material under the repeated HIRE depressurization conditions was thus brought into question.

c. Although the servo controllers were able to maintain a fairly constant heater pressure, there was an initial drop in pressure (on the order of 15% of the total heater pressure). This might not be a problem to worry about due to the fact the  $20 \times 10^6/\text{ft.}$  Reynolds number was obtained for a heater pressure of only 18,000 psi. It is worth noting that the switch to the slower servo controllers was not responsible for the drop in heater pressure. The Rexroths were fast enough to follow the command generated. The only way to recover some of this lost pressure capability would be to increase the gain of the servo system itself.

d. The thermocouple measurements in the diaphragm area were still not entirely satisfactory. Redesign of the  $T_0$  probe was a necessity.

An additional phenomena that was noted during the tunnel runs was the tunnel flow appeared to be supercooled by 7 to 8°K. In order to confirm this, a total temperature probe would have to be designed to monitor gas temperature in the test cell.

In summary, QUICKPROOF accomplished what it was intended to, that is, demonstrate that Reynolds numbers up to  $20 \times 10^6/\text{ft.}$  were possible in the facility. At the same time, these tests indicated that operability of the new configuration was in question, and until operability was demonstrated, HIRE would not be a viable capability. The problems noted above, and those noted after the first QUICKPROOF test program, would all require attention before the calibration test series could be run. The calibration test was thus scheduled for February 1983 to allow time for the necessary analysis and design work to be accomplished.

## HARDWARE ANALYSIS AND DESIGN

### INSTRUMENTATION PACKAGE

During the last redesign of the instrumentation package efforts were made to ascertain the aerodynamic loads on the hardware. With the resulting failure of the package it became obvious that unusual flow conditions existed in the annular gap around the main heater insulation package, making it almost impossible to determine design loads for the hardware. Thus, a worst case situation was assumed and a new instrumentation package designed which was more than an order of magnitude stronger than the previous one. The new package incorporated tubing welded to the O.D. of the main heater outer jacket, protective covers for wiring that might come into contact with the gas flow, and flow deflectors to keep the gas flow away from areas containing instrumentation, as seen in Figure 25.



## T<sub>0</sub> THERMOCOUPLES

The basic design problem confronting the thermocouples to be used in the diaphragm area was that a tradeoff between structural integrity and measurement accuracy, with respect to the thermocouple wire, must be made. That is, the thermocouple wire should be as thick as possible to ensure its structural integrity, but as thin as possible to ensure adequate response time, which is critical in short duration runs. An analysis, contained in Appendix N, addressed the problems noted above. Figure 26 is an assembly drawing of the new T<sub>0</sub> probe design. The principal feature of the new design is the "backstop" which is used to slow down the gas flow past the thermocouple wire, thus preventing the wire from being bent over, while permitting adequate convection to the wire, thus ensuring adequate response time.

## PARTICLE SEPARATOR EXHAUST

It was decided that to eliminate the problem of the disturbances caused by the particle separator exhaust, a muffler system should be designed, with a primary goal of reducing the velocity of the gas exiting the particle separator. The new mufflers, shown in Figure 27, should reduce gas velocities exiting the particle separator by more than an order of magnitude.

## MAIN HEATER INSULATION PACKAGE

The disassembly of the main heater insulation package revealed that a number of the strips of tape which held the insulation against the inner liner during assembly had not melted away as planned, thus resulting in a number of voids between the insulation and the outer can (see Figure 28). This led to the conclusion that convection along the voids was resulting in hot spots on the outer jacket. In addition, the Lo-Con insulation material appeared to have lost resiliency. Information uncovered in Reference 6 indicated that under compression, fibers of Lo-Con can lose resiliency at temperatures as low as 1400°F. It was decided that graphite felt should be used as the insulation material. While this material is not quite as strong as the Lo-Con (see Appendix C) it has been used in Mach-14 testing for a number of years, with success. In addition, a new method of assembly was developed wherein rope was wrapped around the insulation blanket to compress the insulation material, then unwrapped as the outer jacket was pulled over the assembly, thus precluding the need for tape to hold the insulation together during assembly.

## TEST CELL TEMPERATURE PROBE

A total temperature probe was designed and analyzed (Appendix O) for use in the test cell. The probe, shown in Figure 29, incorporated a fine wire design inside a radiation shield. The purpose of the probe was to confirm the accuracy of temperature measurements made in the diaphragm area, thus verifying observations of supercooling in the nozzle.

## CONTROL VALVES

Investigation of the control valve position feedback circuit revealed a phase lag problem associated with the quick opening of the control valves required for Mach-10 HIRE. New LVDT's (linear variable displacement transducers) were installed which were capable of following the fast valve opening. This modification would result in somewhat better heater pressure control.

## CALIBRATION TEST SERIES

The calibration test series, conducted in March 1983, consisted of nine tunnel runs at various supply conditions. In this test series, operability up to a Reynolds number of  $15 \times 10^6/\text{ft.}$  was demonstrated. However, a major operational problem was encountered when four graphite heater elements failed during runs attempting to obtain maximum Reynolds number conditions. The failure of the heater elements thus limited demonstrated operability to runs in which a Reynolds number of  $15 \times 10^6/\text{ft.}$  was obtained. Despite this setback, a number of significant results were obtained in this test series, as detailed below.

- a. The ablators were qualified for operations up to the maximum heater pressure of 22,000 psi.
- b. The new diaphragm area thermocouples and total temperature probes used in the test cell survived all operational conditions run. In addition, the measurements obtained in the two different areas appeared to be consistent, thus verifying observations that supercooling was present in the Mach-10 nozzle.
- c. Flow uniformity was good, as indicated by the graph of Mach number versus radial position in the test cell shown in Figure 30.
- d. The new heater instrumentation package survived all operating conditions.
- e. The reworked main heater insulation package eliminated all the hot spots experienced during QUICKPROOF, and reduced the temperature of the heater vessel well below allowable temperature limits.
- f. The particle separator blowby muffler system eliminated the high velocity discharge problem.

In addition to the heater element problem, there were difficulties experienced in trying to obtain stable control of nozzle supply pressure. These difficulties were attributed to the erratic behavior of the valve command in that the difference between initial valve opening set, and the actual valve command was not repeatable. Also, the packing ring (Figure 31) which thermally protects the upper main heater vessel pressure seal, was damaged. It appeared

that the gas volume behind the ring was not vented properly, thus placing a large pressure drop across the packing ring. Minor modifications to the ring would eliminate the problem.

In summary, in the calibration test series a number of operational hurdles were overcome. However, the failure of the graphite heater element to survive the maximum heater pressure desired resulted in an Reynolds number limit of  $15 \times 10^6/\text{ft}$ . In addition, the performance of the control valve command system would need to be addressed in order to obtain stable, repeatable valve performance.

#### HEATER ELEMENT AND CONTROL VALVE ANALYSIS

The graphite heater element used in Tunnel 9 has had a somewhat erratic performance history. Heater element life has ranged from 1 to 150 tunnel runs. The primary reason for this large variation was material property inconsistency between various batches of graphite used. Numerous testing has been done in an attempt to characterize the graphite so that it can be determined a priori that a given batch of graphite should or should not be used to fabricate an element. At the present time the database generated is not large enough to draw conclusions, thus heater element reliability is somewhat a luck-of-the-draw situation.

The heater element failures noted above in the HIRE calibration test series were markedly different in nature from those that had occurred in previous testing. In the failures experienced in HIRE, the element fractured in a number of locations as indicated in Figure 32. In one case, the entire top portion of the element was blown off and eventually lodged itself in the diaphragm area. The most likely explanation for this new type of failure was that the heater element was being buffeted by turbulent gas flow. The turbulent flow was caused by the driver gas being turned at the bottom of the heater, and then bouncing between the heater element base and the inner insulation liner, as depicted in Figure 32.

To solve the buffeting problem, a baffle plate was designed to "straighten out" the driver gas flow. The baffle plate assembly, shown in Figure 33, had porous plates on the side and top, and was designed to induce a pressure drop of 50 psi in the gas flow (pertinent calculations are contained in Appendix P). The baffle plate installation required a slight modification to the heater element base, as shown in Figure 33. Appendix P contains pertinent flow calculations and structural analysis of the baffle plate.

With regards to the erratic nozzle supply pressure control, investigation of the control valve electronic circuitry indicated that minor modifications were required to rid the system of this inconsistent performance. The modifications were made, and tests run to compare initial opening set with initial command generated. The testing indicated that the modifications would be successful in eliminating the erratic pressure control problem.

It was decided to forego further calibration testing, and to use the baffle plate and modified servo controller electronics in the demonstration test series. Thus, the demo test series would demonstrate operability at a Reynolds number of  $20 \times 10^6/\text{ft.}$ , and obtain aerodynamic data on natural transition.

#### DEMONSTRATION TEST SERIES

The demonstration test series was run in July 1983. This tunnel entry consisted of 15 runs during which data was taken at a number of nozzle supply pressures. This test series was a success from a facility operations and aerodynamic performance standpoint. The significant achievements are listed below.

a. The heater element buffeting problem was eliminated by the baffle plate design. In addition, inspection of the baffle plate after the demo test series indicated no structural problems with the baffle plate surviving the large mass flow rate.

b. The nozzle supply pressure control was good to  $\pm 4\%$  at the highest heater pressure. This was considered to be acceptable.

c. The initial program objective of obtaining a Reynolds number of  $20 \times 10^6/\text{ft.}$  was met. In addition, 4 good runs in which no operational problems were experienced demonstrated operability at this condition.

d. At the maximum Reynolds number, a run time of 300 milliseconds was obtained, which was slightly more than initially predicted.

The aerodynamic data obtained verified predictions of natural transition on a reentry vehicle afterbody. Figure 34 is a graph of Stanton number (a measure of heating rate) versus axial position along the model. The knee in the curve represents the transition point from laminar to turbulent flow. Figure 35 is a graph of Reynolds number versus transition point. Shown plotted are actual flight data and the data obtained in the HIRE demo test. The agreement between flight test data and wind tunnel data appear to be excellent. The conclusion of the demonstration test series effectively marked the end of the HIRE project. The initial goal of obtaining an operable  $20 \times 10^6/\text{ft.}$  Reynolds number capability at Mach-10 had been met.

#### OPERATIONS SUMMARY

The final hardware design configuration, and mode of operation to obtain Mach-10 HIRE conditions, was somewhat different than that initially proposed in 1980. A brief recapitulation of the major design changes, and resulting operational system is in order.

Initially it was predicted that Mach-10 HIRE would require a driver vessel pressure of 38,000 psi to maintain constant heater pressure during the run. What finally resulted, following a design change to the plug valve to remove a restriction in the discharge manifold, was a 36,000 psi maximum driver vessel pressure requirement. This lower maximum pressure resulted in increased fatigue life, and longer periods between maintenance operations on seals and compressors.

Proceeding downstream, the operation of the servo-driven gas valves was changed twice. The first change was brought about by a perceived need to open the valves more quickly. The second change resulted from the valves opening too quickly, thus creating a pressure pulse in the heater vessel. It was determined that the valves did not require a large initial opening command to be effective, and that by opening the valves a little early, excellent pressure control could be achieved. An additional side benefit of the control valve work was the generation of a computer model of the high pressure gas supply system. This model will be used in the future to select driver vessel conditions for various heater supply conditions.

The vertical elbow and horizontal elbow insulation packages did not undergo any changes during the HIRE program. The main heater insulation package, in contrast, underwent substantial changes. The instrumentation package located on the main heater outer jacket underwent several changes before a successful design was obtained. Due to the high mass flow rates passing through the annular gap between the main heater's outer jacket and the heater vessel's I.D., all instrumentation required protective covering. The insulation material was changed from Lo-Con to graphite due to breakdown of the Lo-Con under the severe temperature environment.

To solve the problem of heater element buffeting, a baffle plate was installed in the bottom of the heater to breakup the flow of driver gas entering the heater.

The diaphragm area underwent several generations of design changes. The biggest change resulted from the decision to switch from the mechanical valve to ablators. The mechanical valve was shelved when it appeared that its initial operating concept might not prove out under hot test conditions. The ablators have, to date, been used in about 70 HIRE runs, with success.

It was predicted that the new particle separator would result in a 25% decrease in pressure drop across the separator system. Pressure measurements indicated that the decrease was on the order of 20%.

The nozzle throat insert was measured after 80 runs. Some movement of material was observed. Additional analysis of this phenomena is presently underway. It should be emphasized that this observation does not preclude the ability to do testing at HIRE conditions. It does mean that periodic inspection of the insert is important.

Figure 36 is a graph of a typical supply pressure history that occurred during the demonstration test series. There was an initial pressure peak right after diaphragm burst which was followed by a flat pressure "plateau" during which the gas flowing through the ablators was not hot enough to produce ablation. When the hot gas arrived, the ablators opened up very rapidly and

condensation free flow was achieved very soon after the pressure reached maximum value. This pressure trace was used to synchronize a number of tunnel events, as depicted in Figure 36. The control valves were given a small initial opening command (3%), after which they operated in a closed-loop system, responding to changes in heater pressure. The data acquisition system was started when the ablation process commenced, which was at a pressure of about 20% of the maximum supply pressure. The model pitch system was triggered so that the pitch sweep of interest occurred during condensation-free flow time.

During the course of the HIRE calibration and demonstration test series, operational characteristics of the new assembly were obtained. Figure 37 is a plot of the number of control valves required for a given number of open holes in the flow restrictor. Figure 38 shows the relationship between the number of open holes in the flow restrictor and the resulting supply pressure. As can be seen from Figure 38, the flow through the flow restrictor up to a  $P_o$  of 10,000 psi is choked, as expected. Also, there is not much increase in  $P_o$  as the number of open holes is increased beyond 133. Figure 37 and 38 are to be used by tunnel operators to determine the number of open holes needed in the flow restrictor to obtain a certain supply pressure, and to select the proper number of control valves so that good heater pressure control is obtained.

Figure 39 is a graph of Reynolds number versus run time for the HIRE configuration. This curve is very important, in that it defines the tradeoff available to customers of the facility between Reynolds number and run time. At the highest Reynolds number condition, pitch sweeps of at least 10 degrees are possible. (During the HIRE program a new pitch system controller was installed which enabled the pitch system to increase its operating speed, thus allowing longer pitch sweeps than previously anticipated. A major project is now underway in the facility to upgrade the model pitch system. Part of the upgrade will be to further increase the speed of the pitch system to allow for more data gathering during the short duration HIRE runs). As can be seen from Figure 39, a run time of 300 milliseconds was obtained at the maximum Reynolds number condition. This was slightly longer than the predicted 250 millisecond run time predicted in the initial feasibility study. An interesting point is that a nozzle supply pressure of only 13,500 psi was required to obtain the  $20 \times 10^6/\text{ft}$ . Reynolds number, versus the predicted requirement of 18,000 psi. This turned out to be fortuitous due to the unexpected pressure drops which occurred in the heater vessel which precluded obtaining a higher supply pressure than 13,500 psi.

Figure 40 is a graph showing the variation of static pressure, dynamic pressure, and pitot pressure with  $P_o$ , which is supplied for purposes of test planning. Lastly, Figure 41 depicts the variation of Mach number with supply pressure, which is within  $\pm 3\%$ .

#### PROJECT SUMMARY

The HIRE program required about 3 1/2 years to complete. Five tunnel entries were made consisting of a total of 49 runs. The attainment of the HIRE capability was an excellent example of the capabilities possessed by NSWC wind tunnel personnel to develop, in-house, state-of-the-art wind tunnel capabilities in response to predicted testing needs.

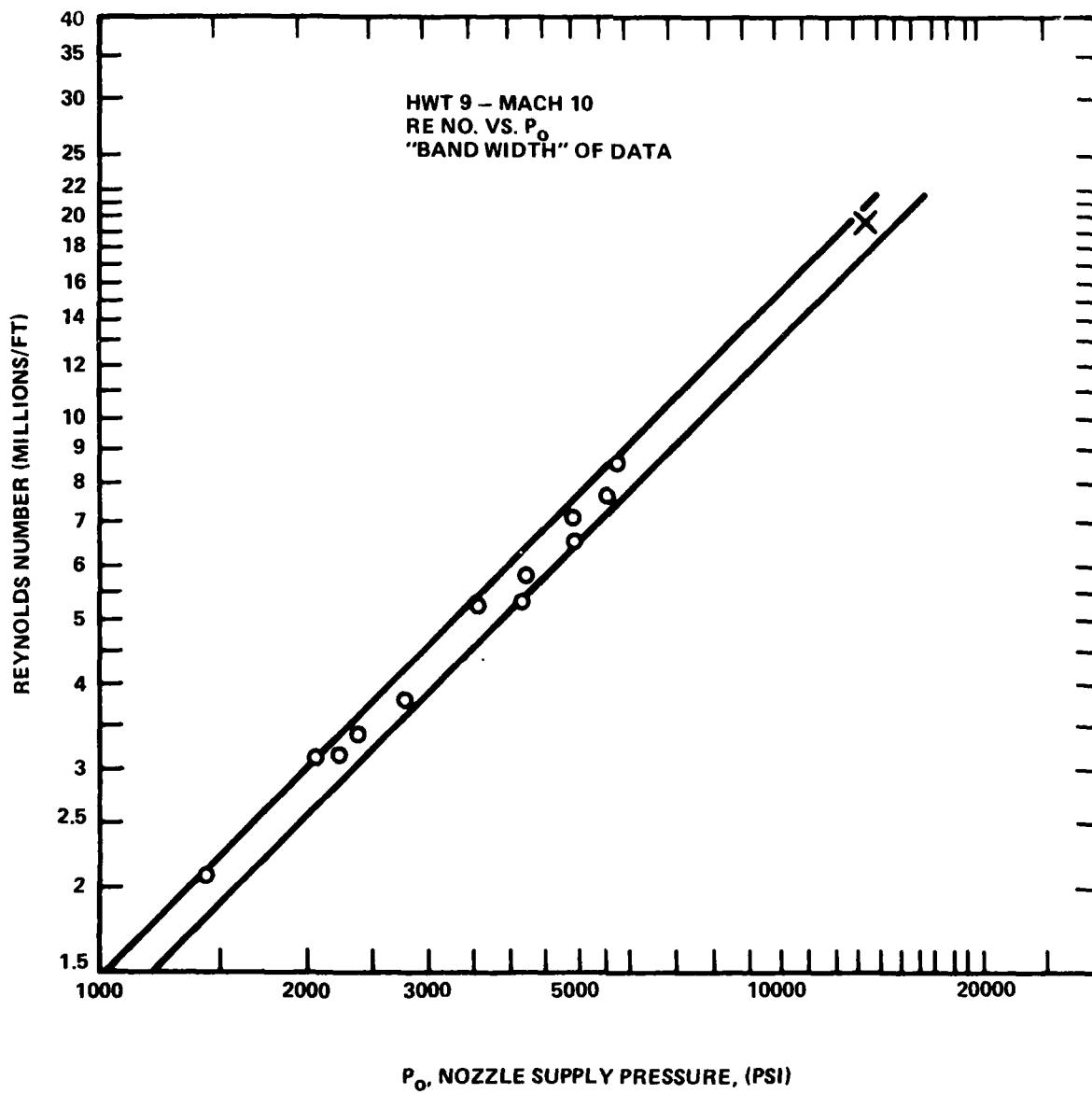


FIGURE 1. REYNOLDS NUMBER EXTRAPOLATION

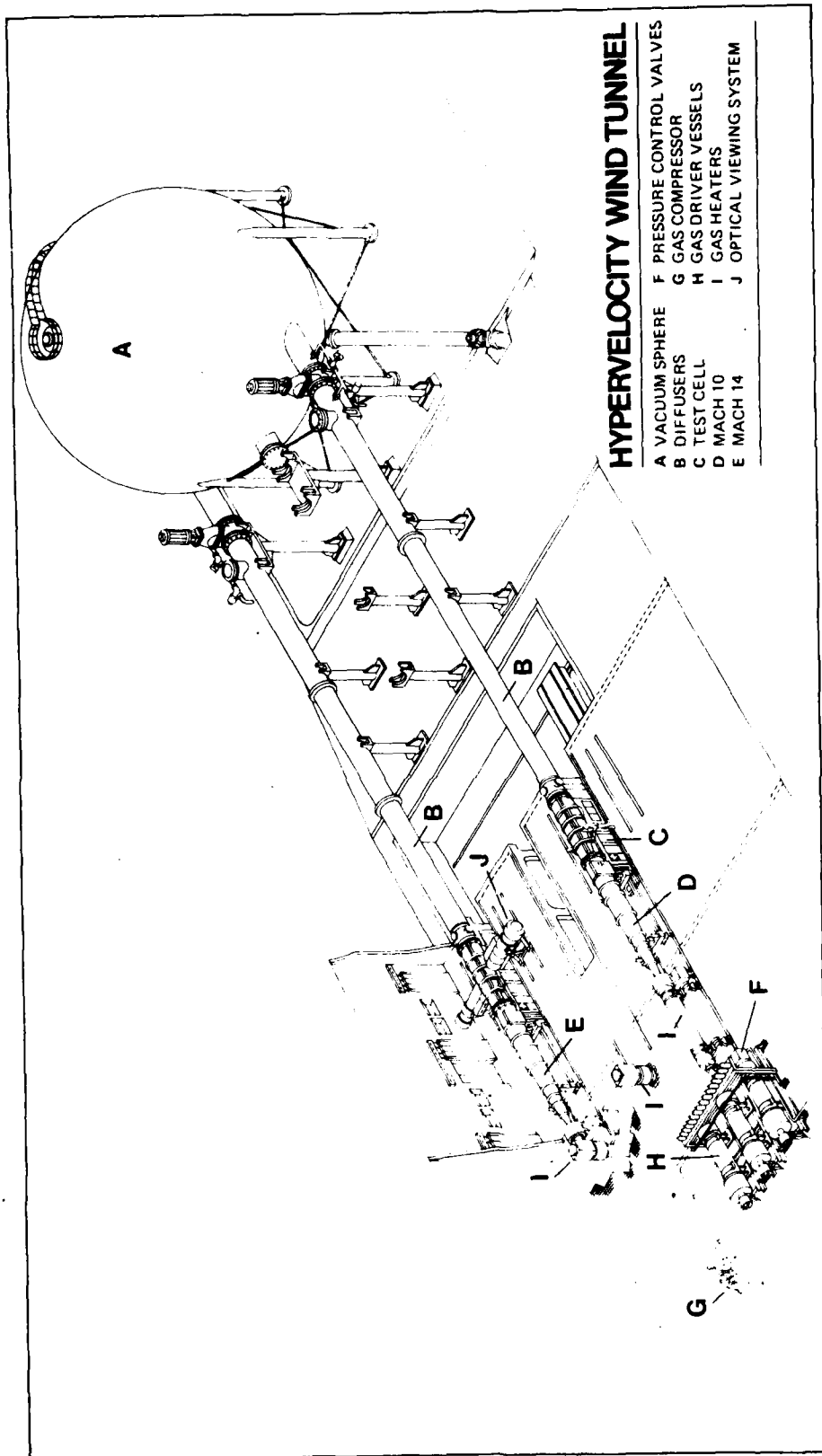


FIGURE 2a. SCHEMATIC OF TUNNEL NO. 9 FACILITY



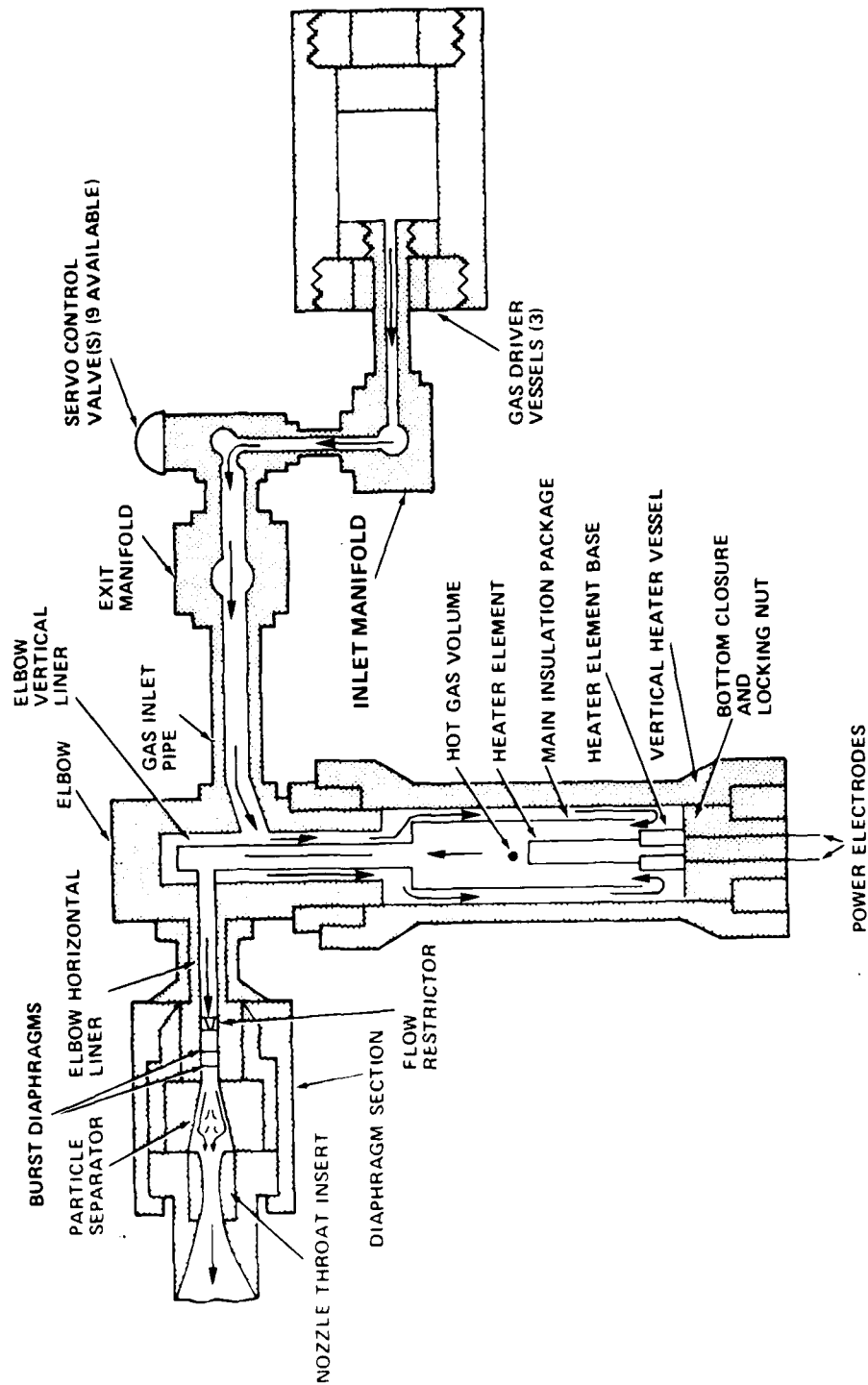


FIGURE 2b. TUNNEL 9 VERTICAL HEATER AND FLOW PASSAGE ARRANGEMENT

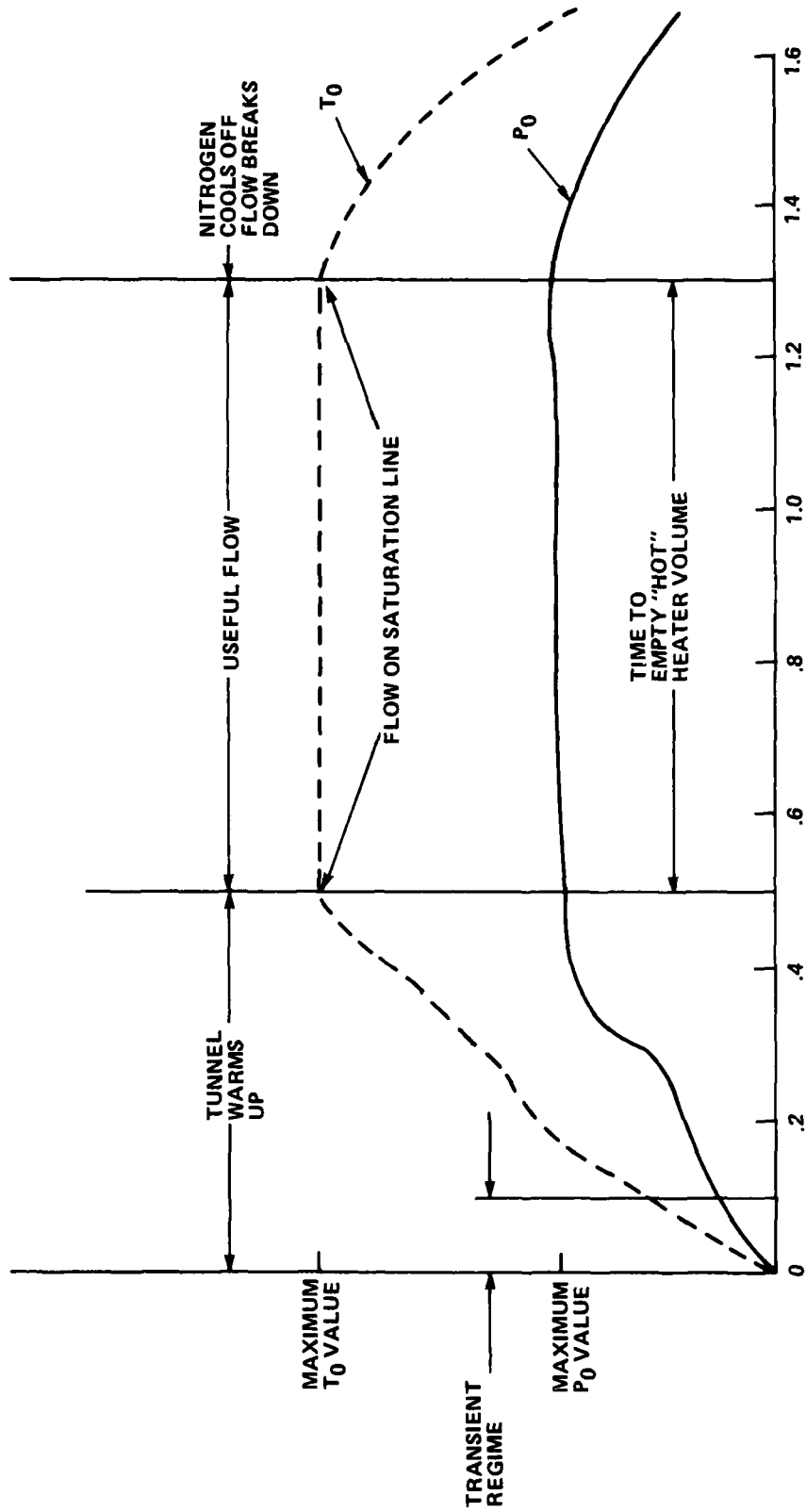


FIGURE 3. TYPICAL TUNNEL RUN

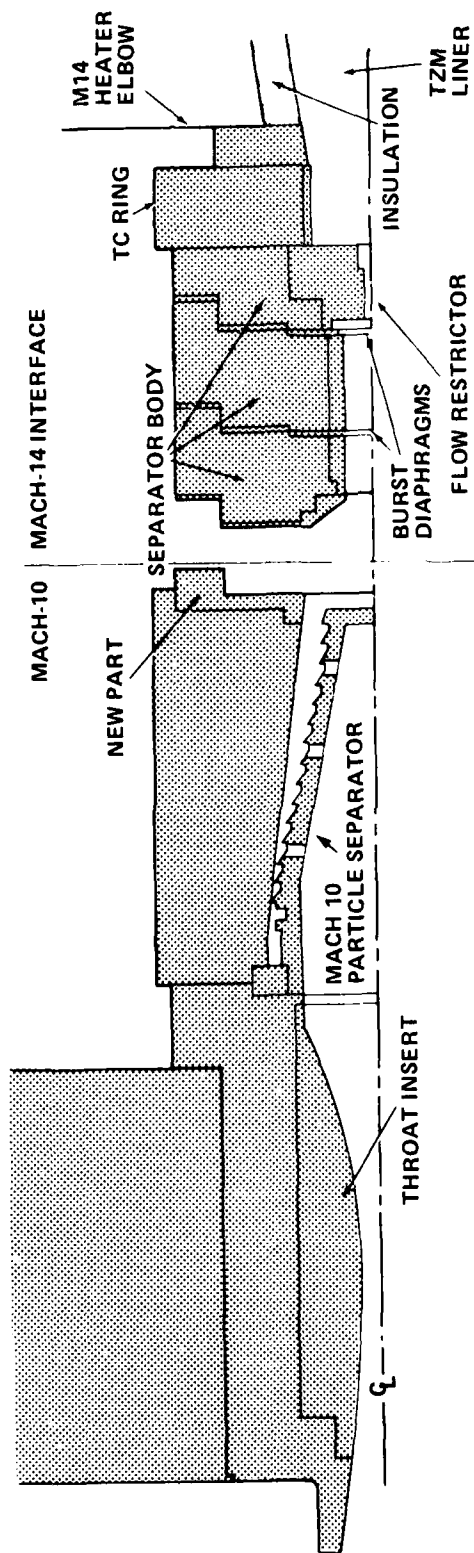


FIGURE 4. MACH 10/14 DIAPHRAGM SECTION

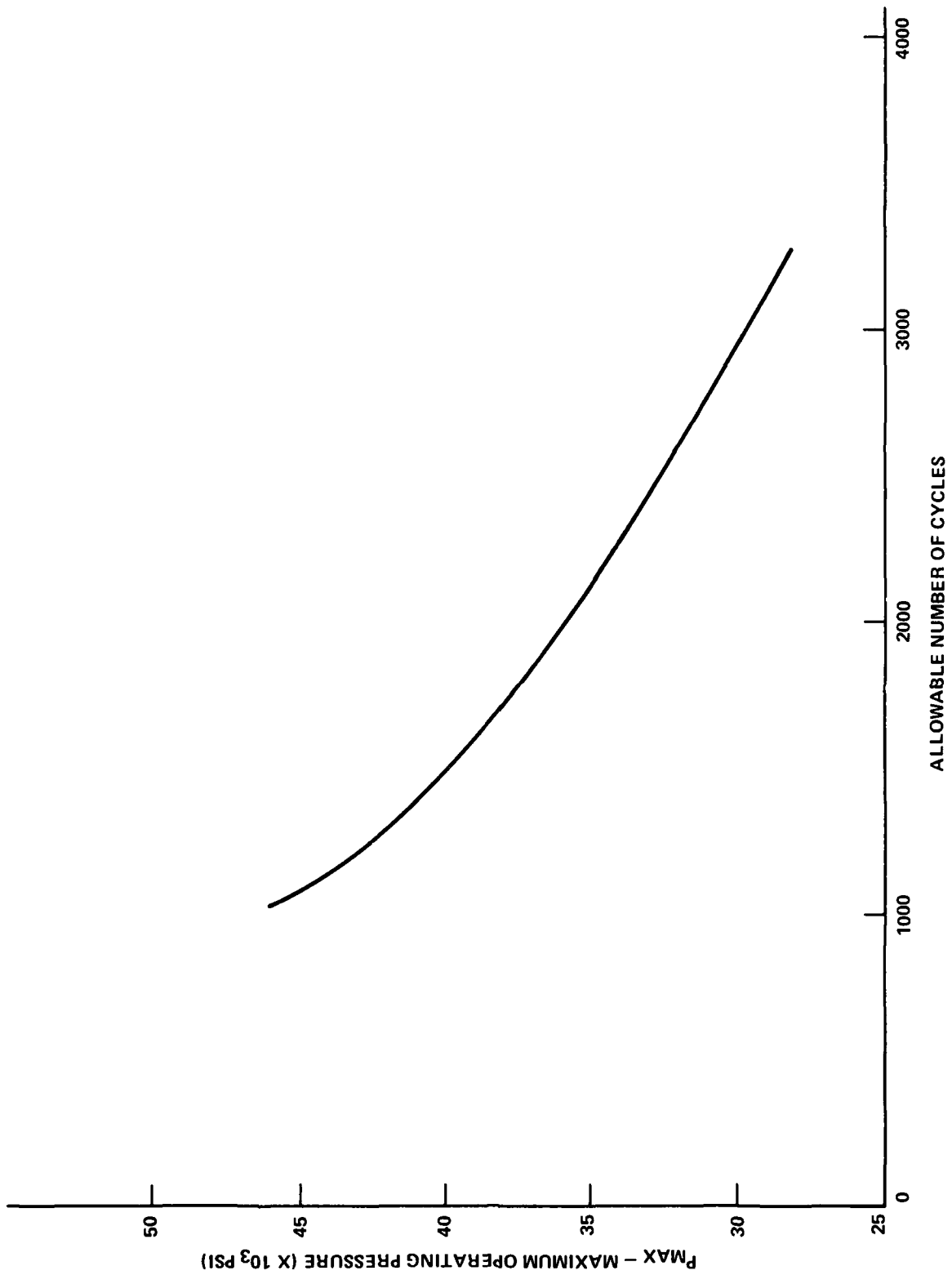


FIGURE 5. FATIGUE LIFE VERSUS OPERATING PRESSURE (DRIVER VESSELS)

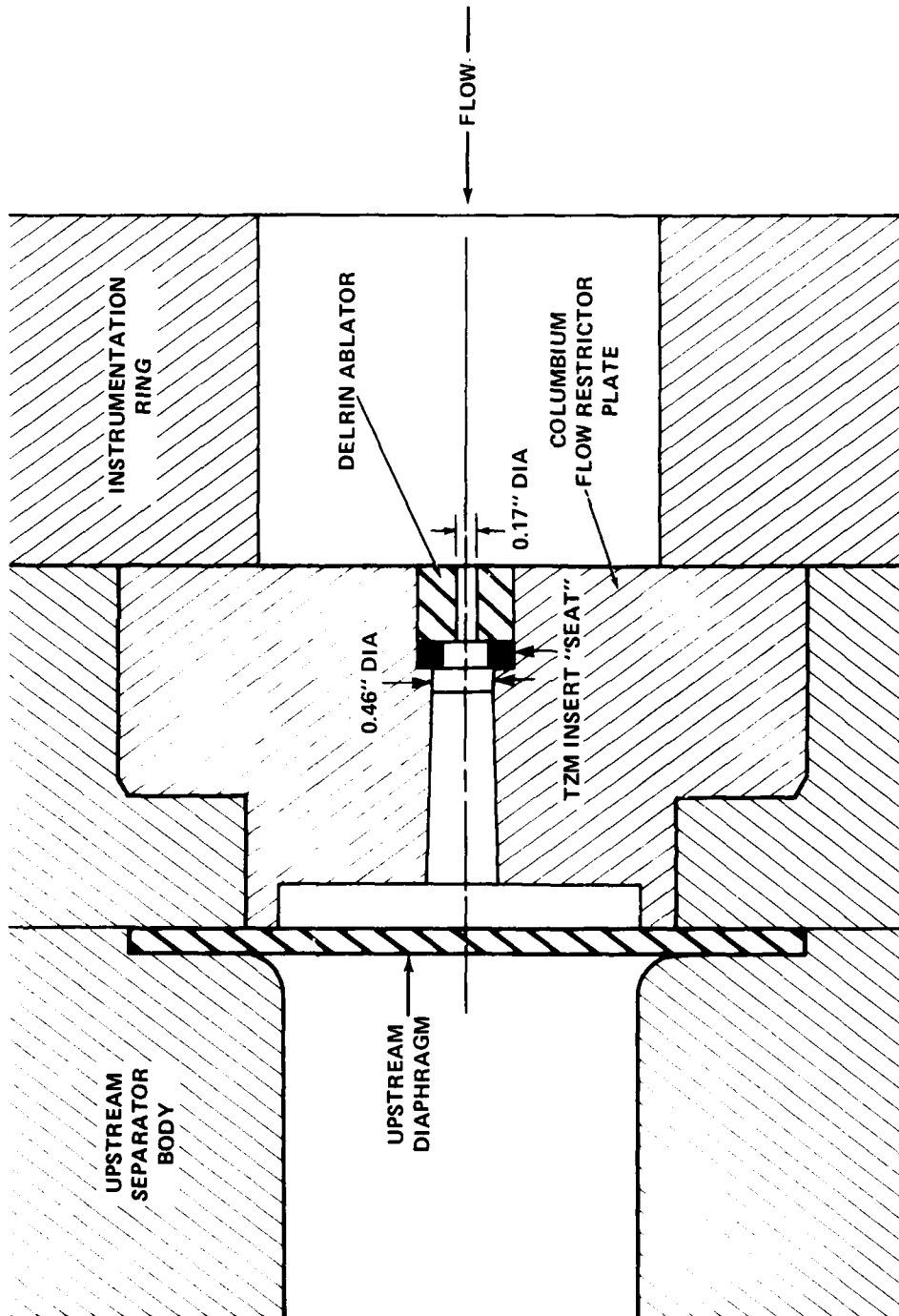


FIGURE 6. MACH-14 FLOW RESTRICTOR DESIGN

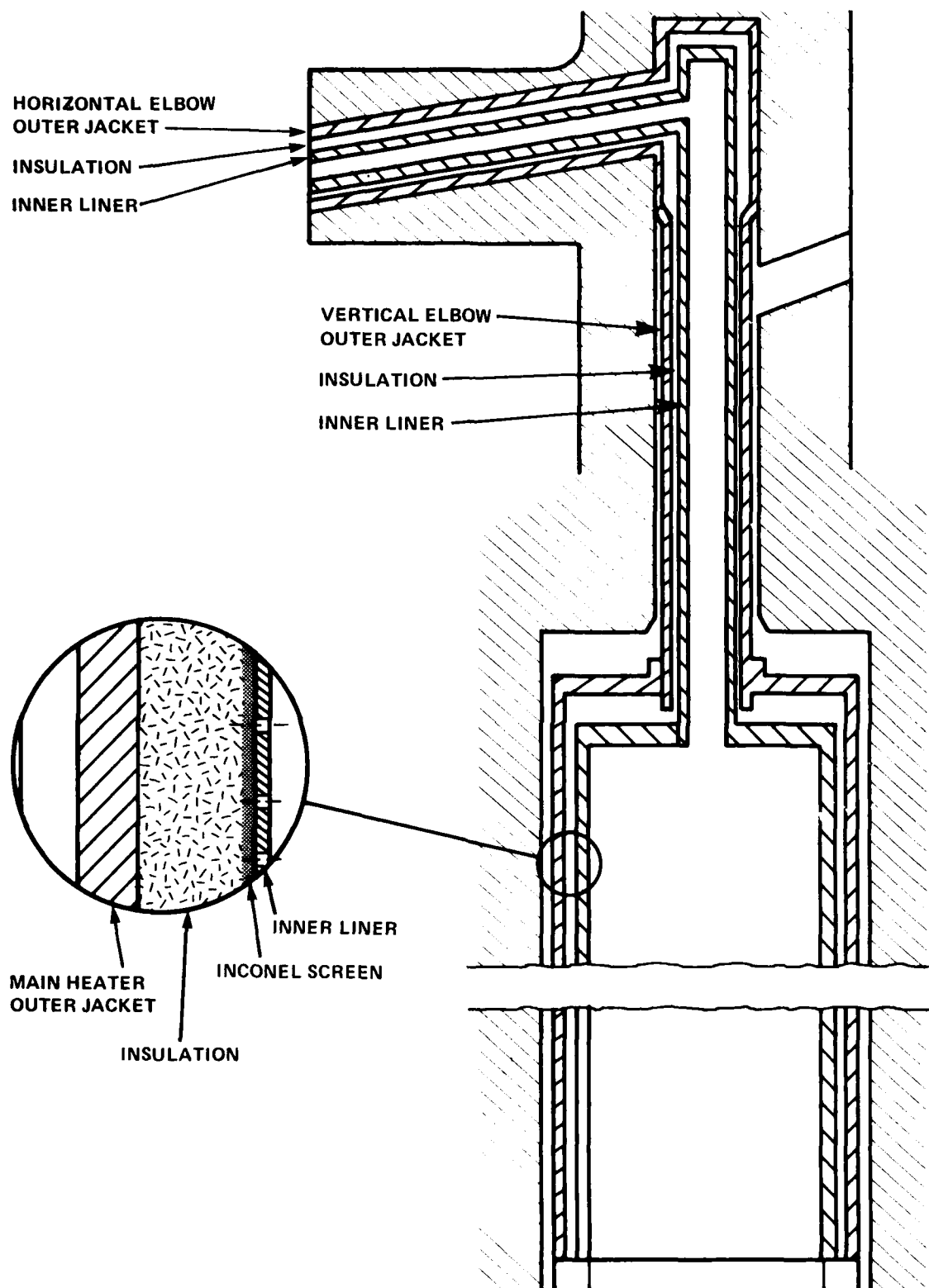


FIGURE 7a. HEATER VESSEL INSULATION PACKAGES

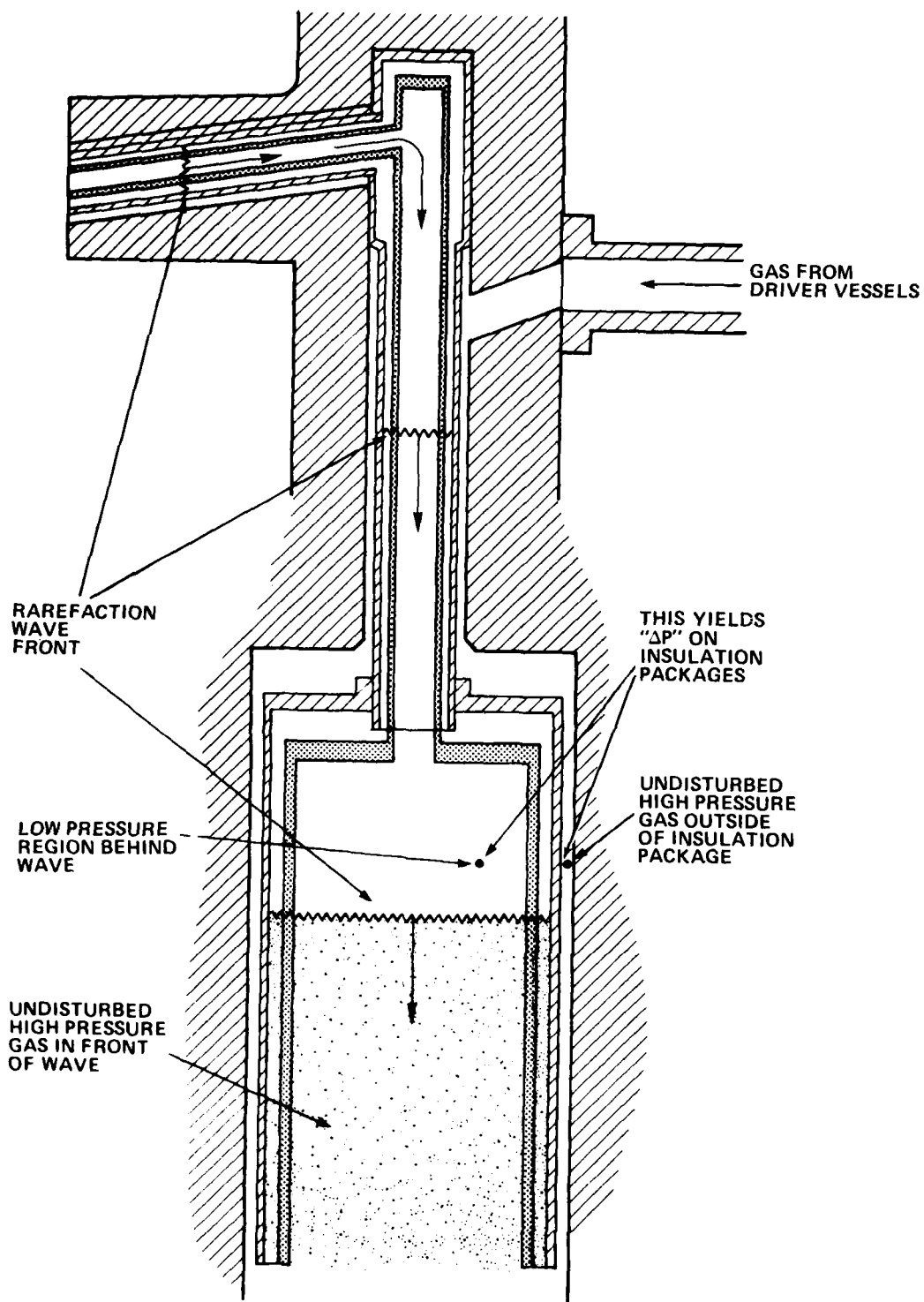


FIGURE 7b. RAREFACTION WAVE MOVING BACK THRU VERTICAL FLOW PASSAGE

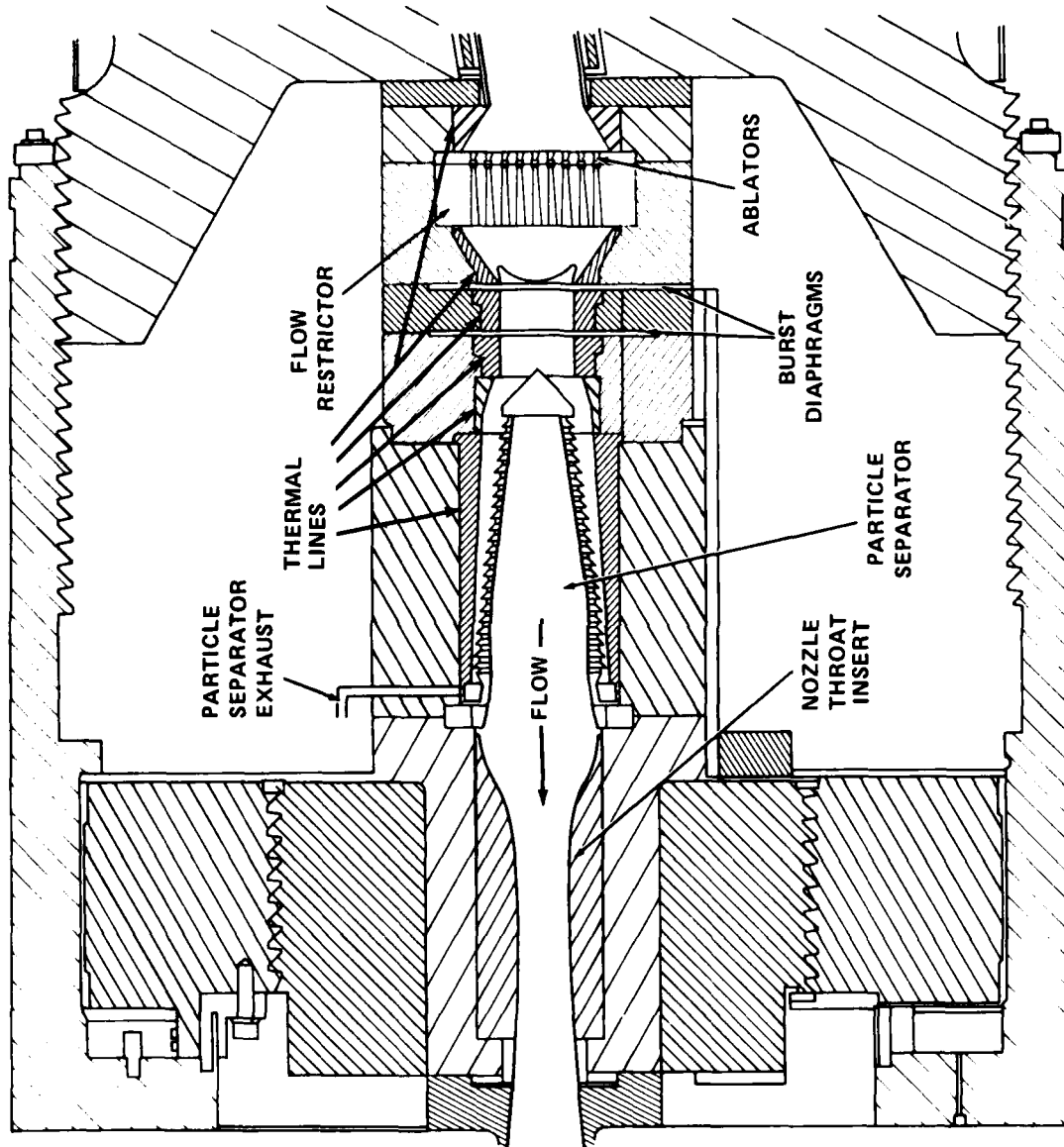


FIGURE 8. MACH-10 HIRE DIAPHRAGM AREA



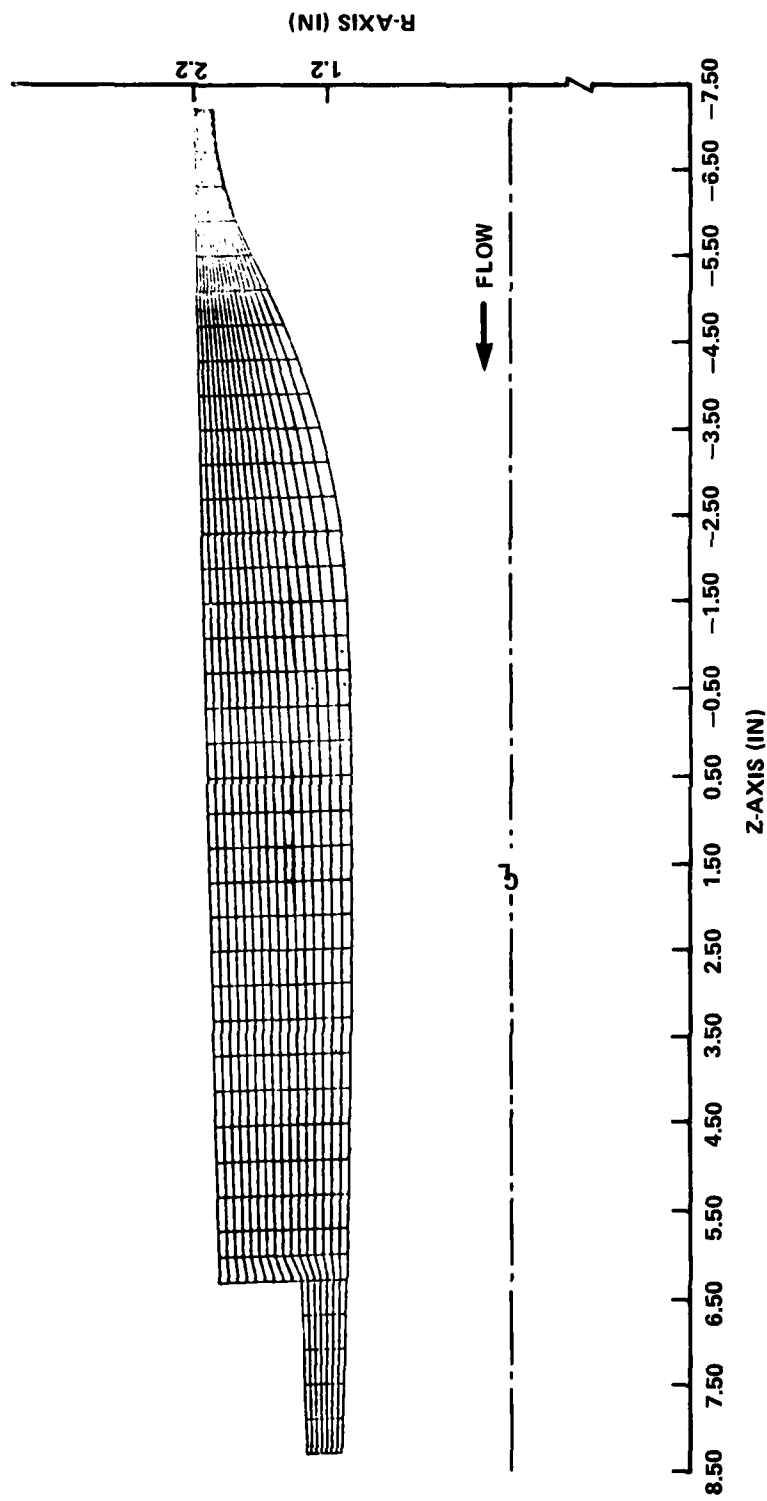


FIGURE 9. THROAT INSERT FINITE ELEMENT MODEL

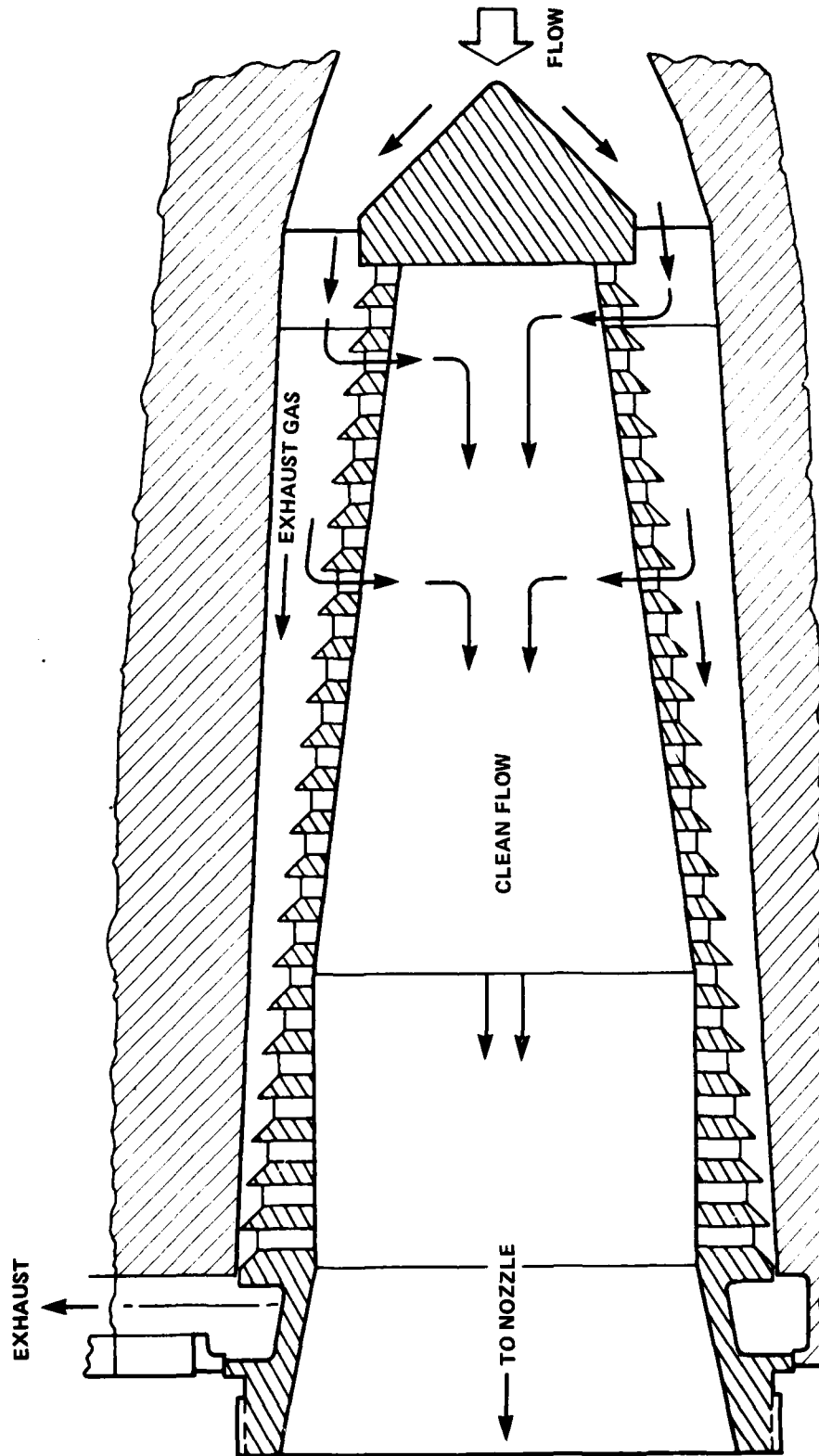


FIGURE 10. MACH-10 PARTICLE SEPARATOR

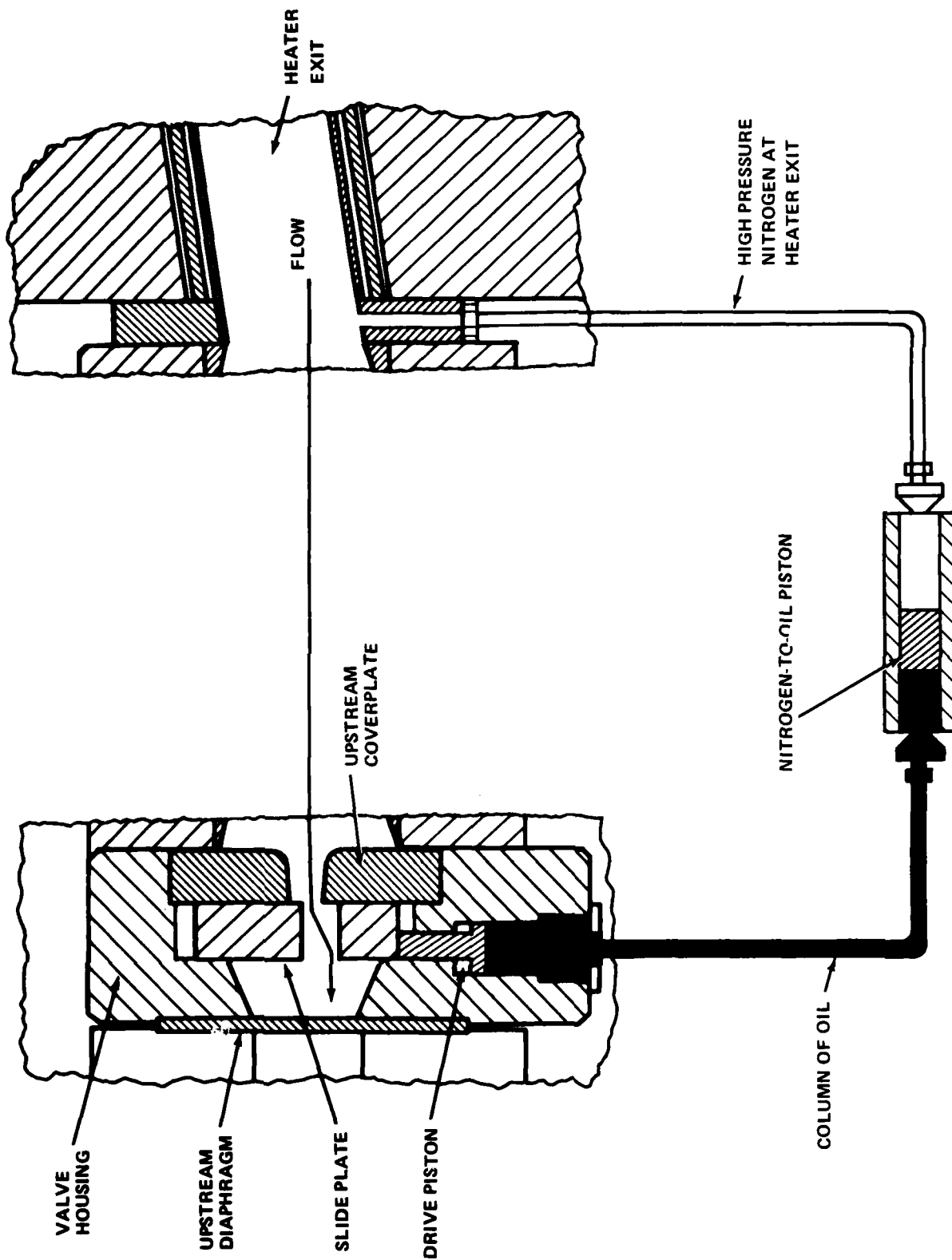


FIGURE 11. MECHANICAL VALVE

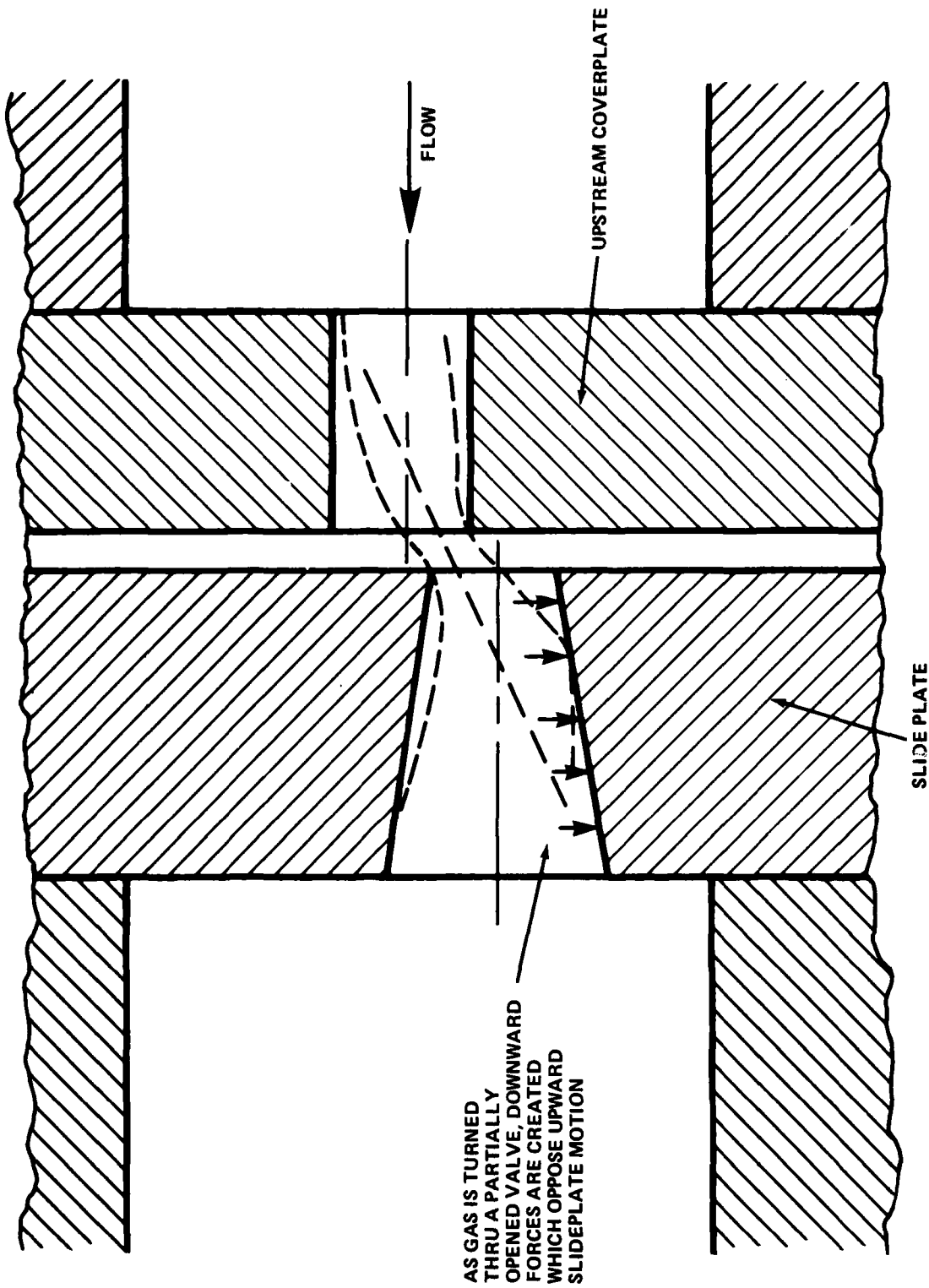


FIGURE 12. AERODYNAMIC FORCE ON MECHANICAL VALVE

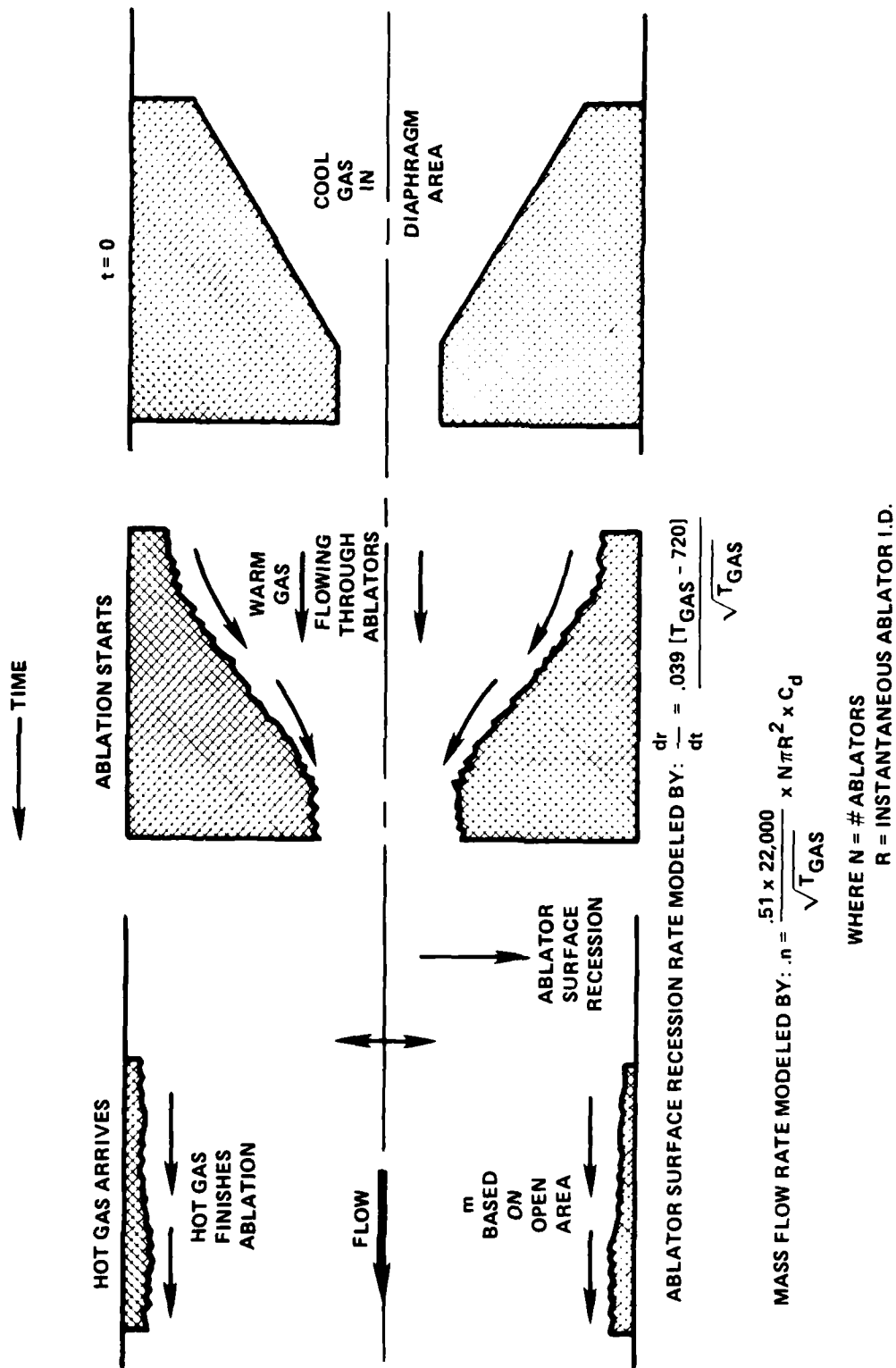


FIGURE 13. ABLATION MODEL

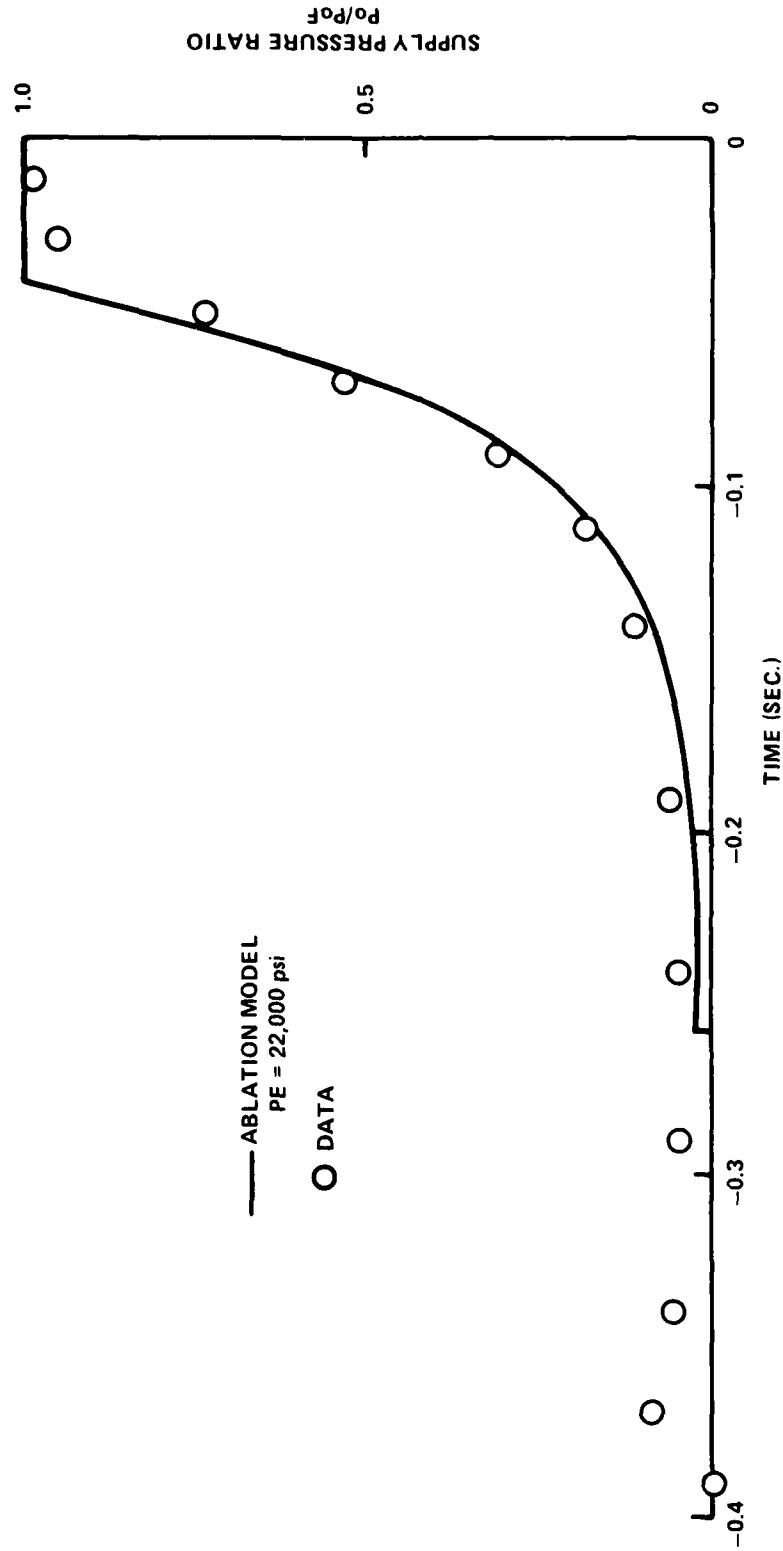


FIGURE 14. ABLATOR PERFORMANCE, THEORY &amp; EXPERIMENT

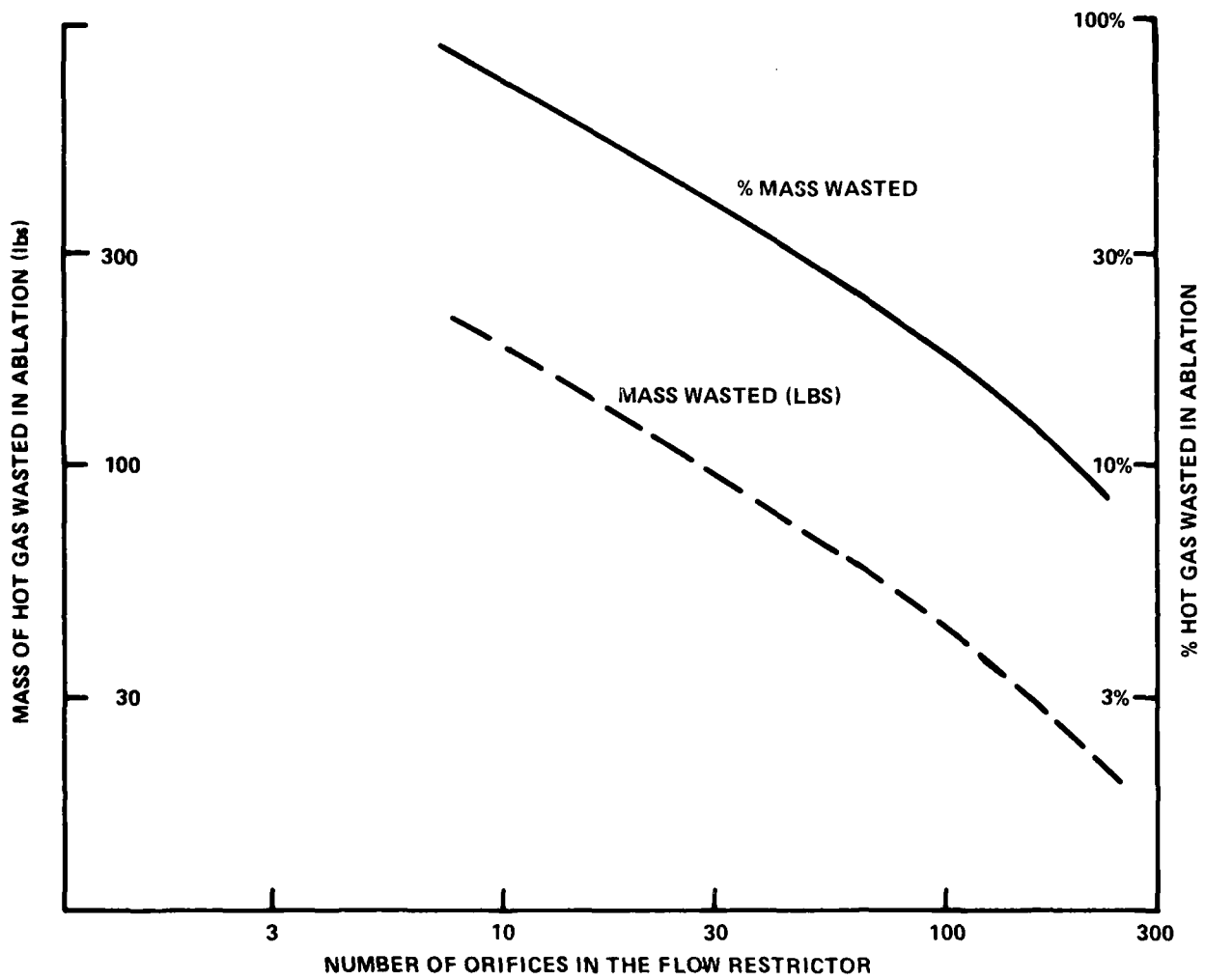


FIGURE 15. HOT GAS USED IN ABLATION

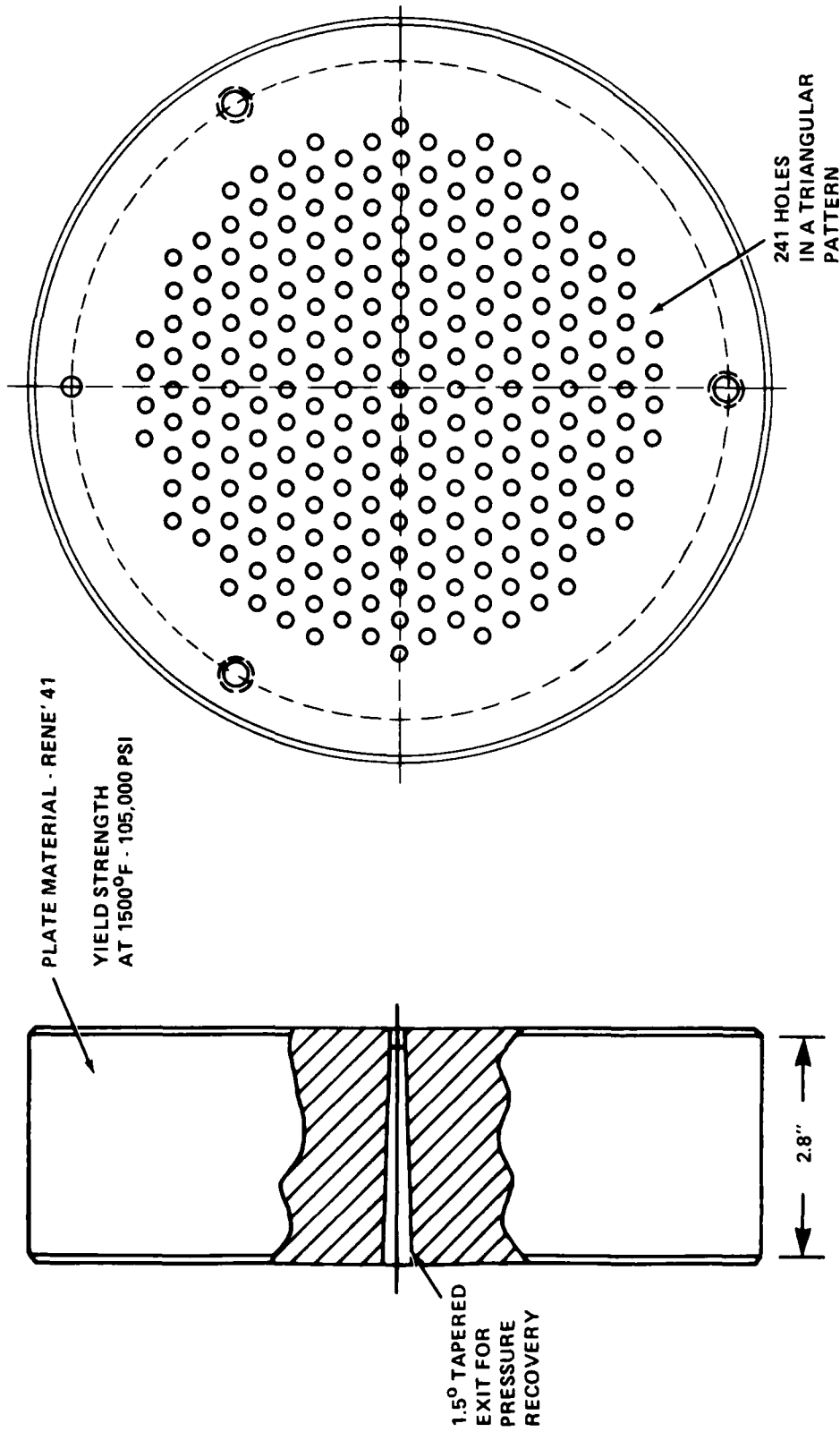


FIGURE 16. MACH-10 HIRE FLOW RESTRICTOR



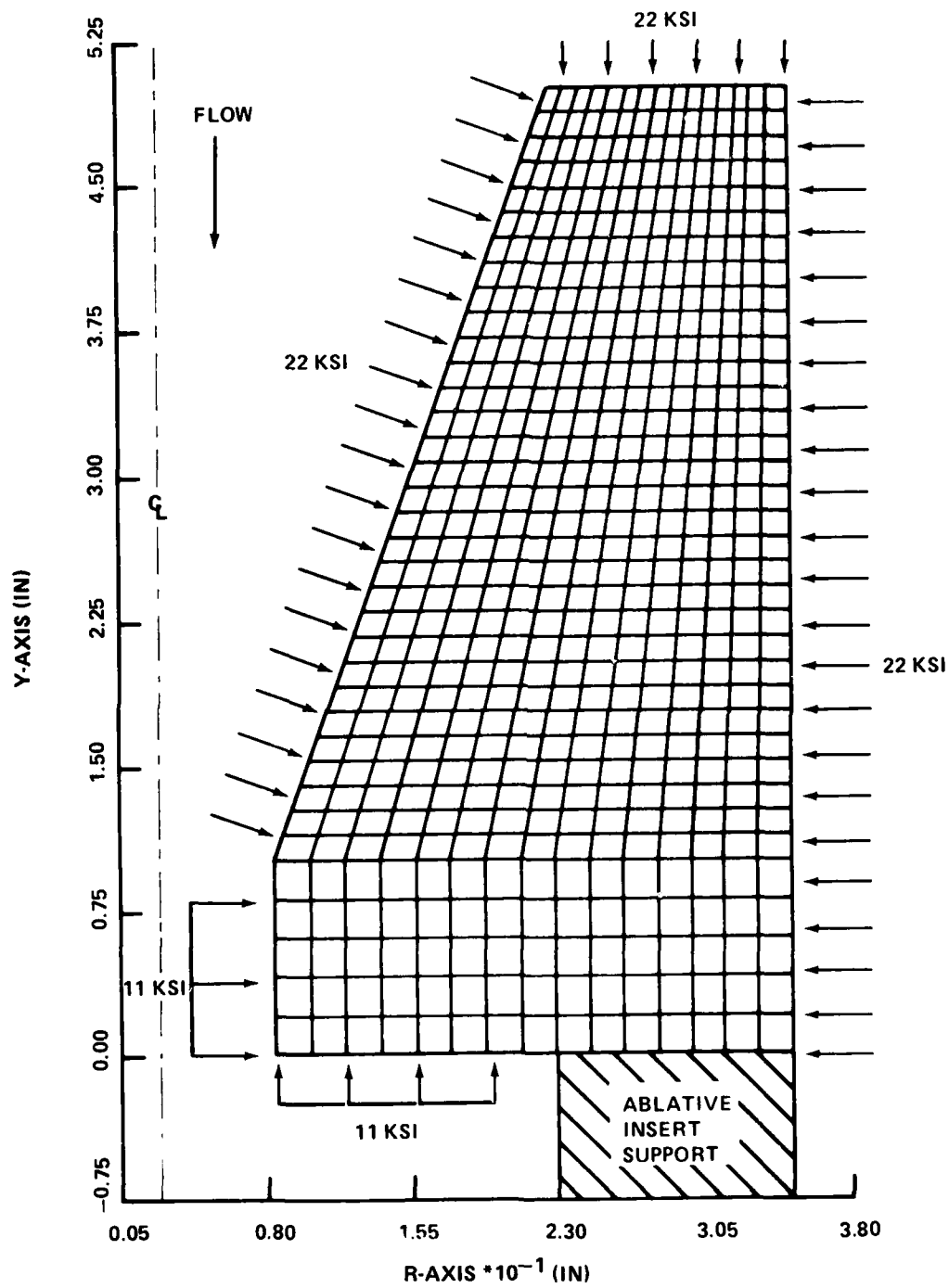


FIGURE 17. ABLATOR FINITE ELEMENT MODEL &amp; LOADING CONDITIONS

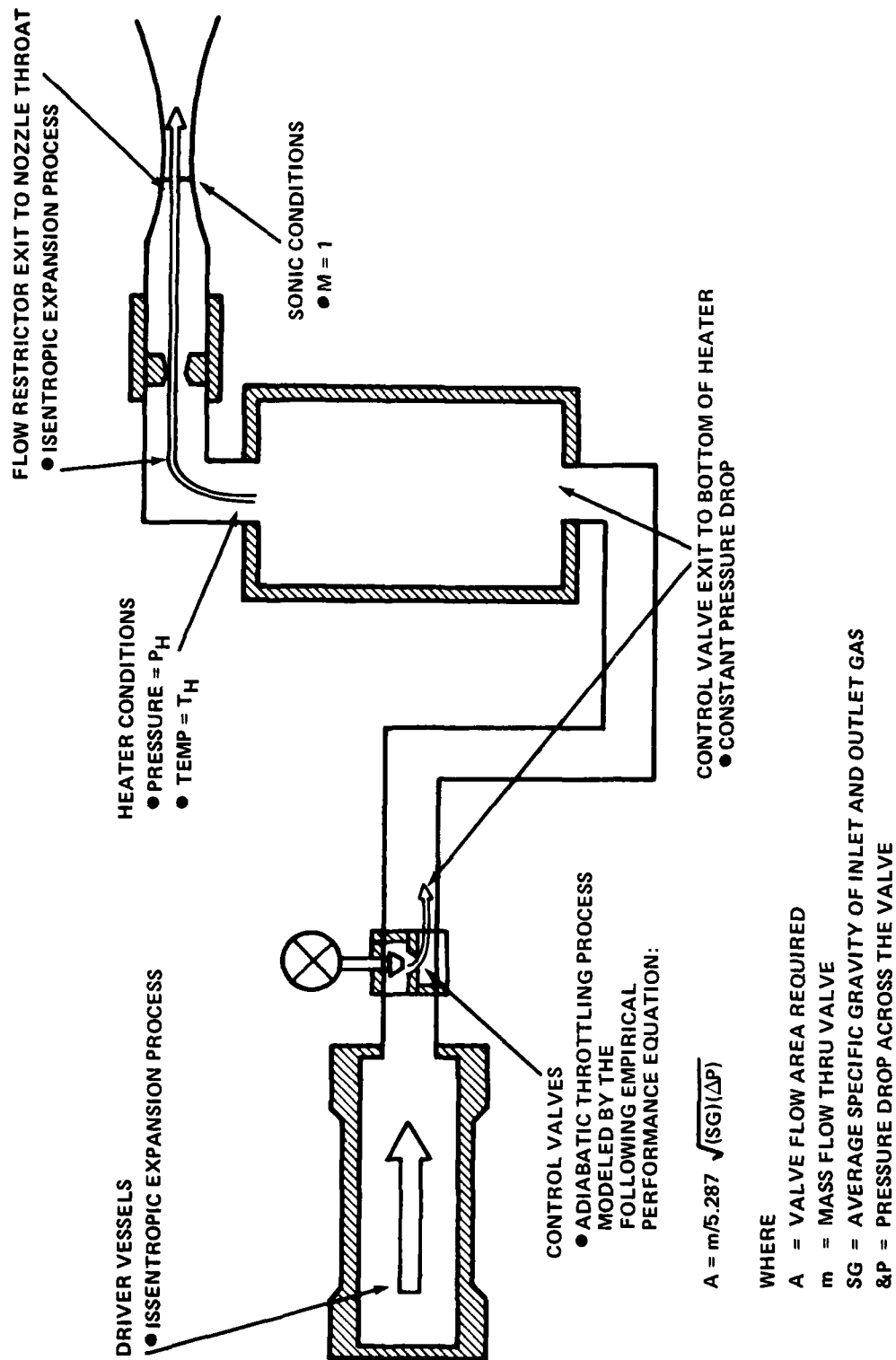


FIGURE 18. BLOWDOWN MODEL

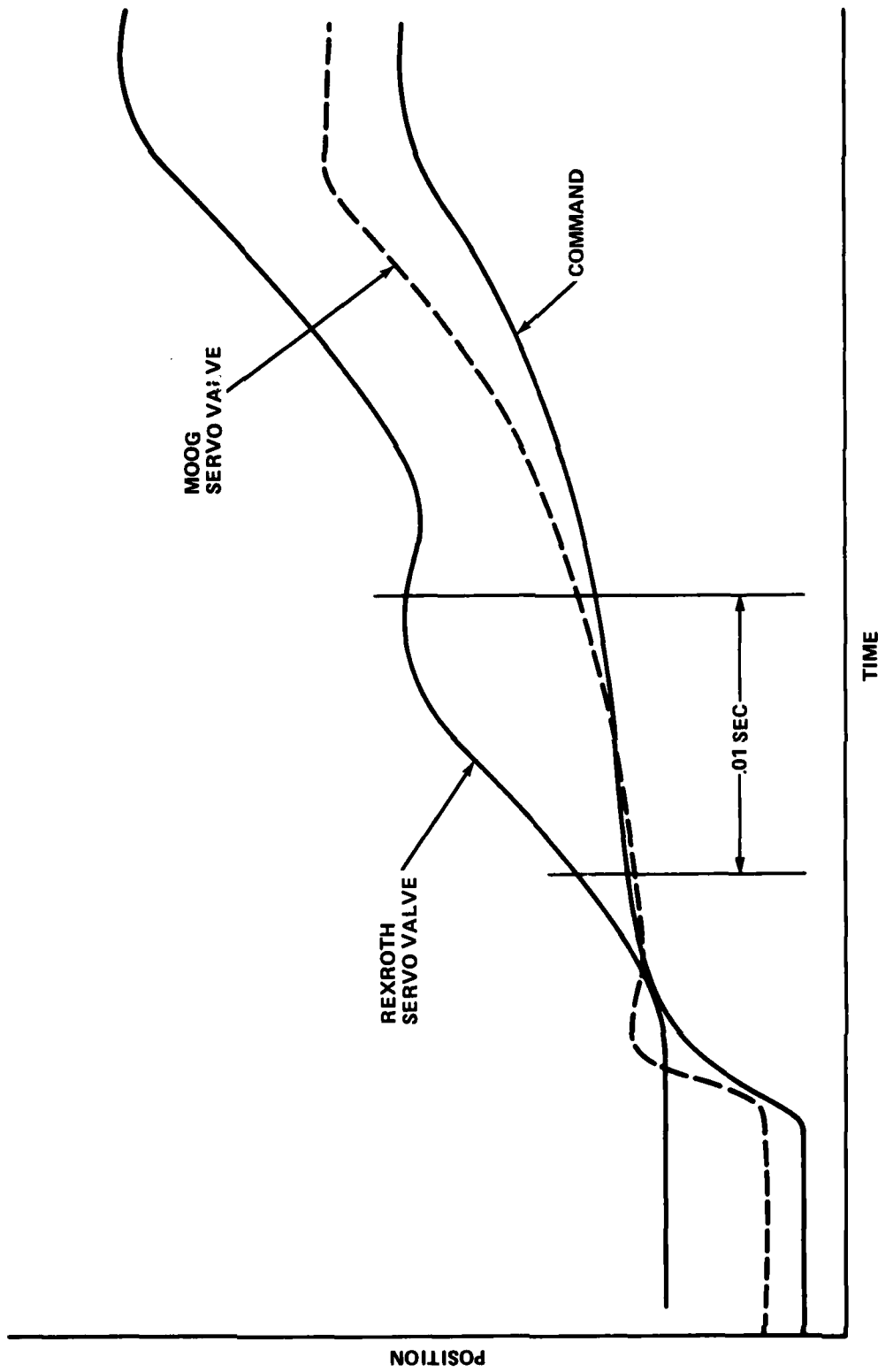


FIGURE 19. SERVO CONTROLLER PERFORMANCE

DURING QUICKPROOF,  
TIEDOWN STRAPS  
WERE RIPPED  
OFF THE OUTER  
JACKET, & THE  
PROTECTIVE  
TUBING WAS  
DISTORTED DUE  
TO FLOW OF  
DRIVER GAS  
THROUGH THE  
ANNULAR GAP  
IMPINGING ON  
THE HARDWARE

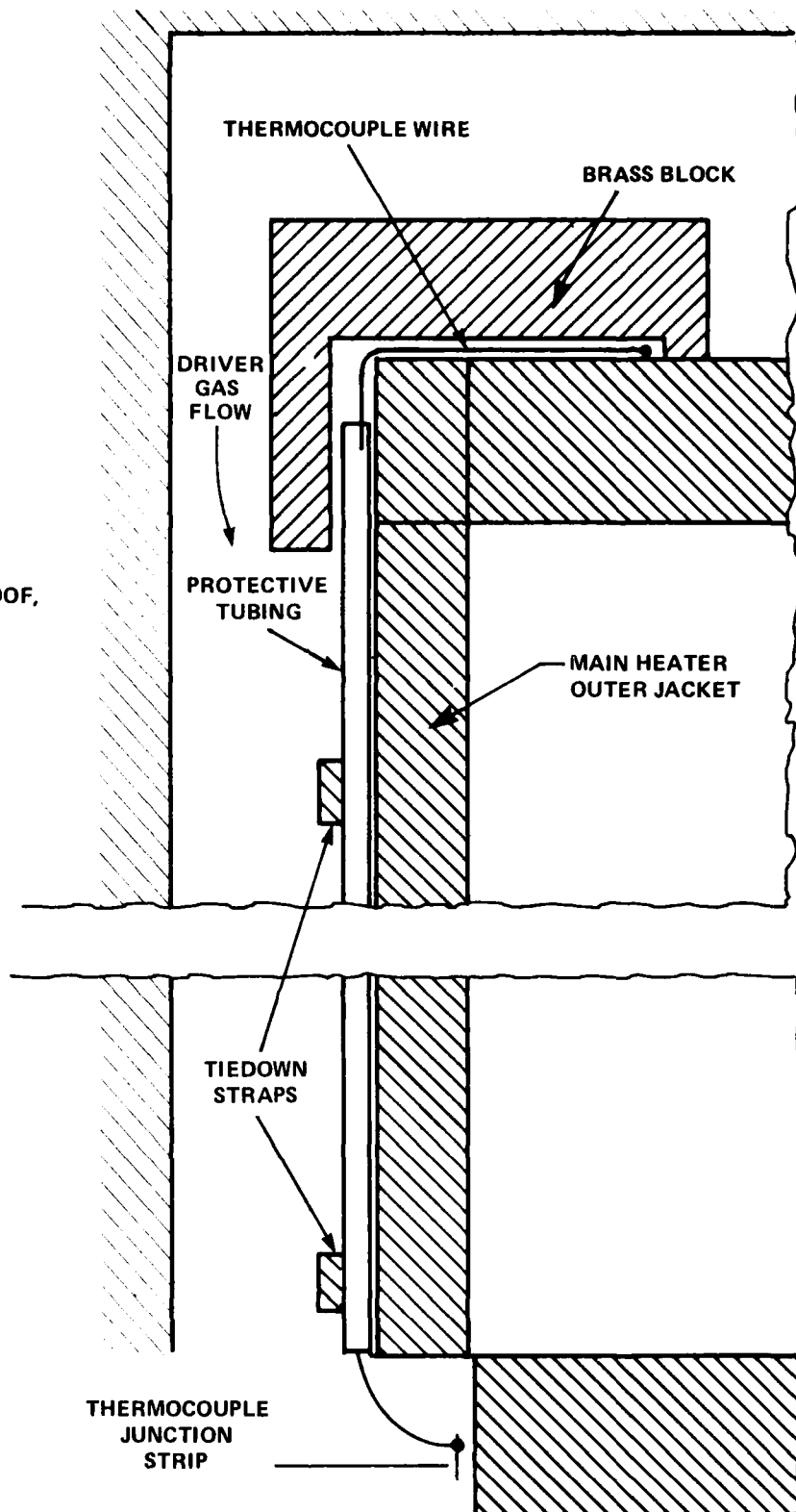
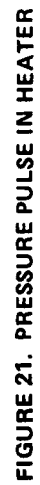
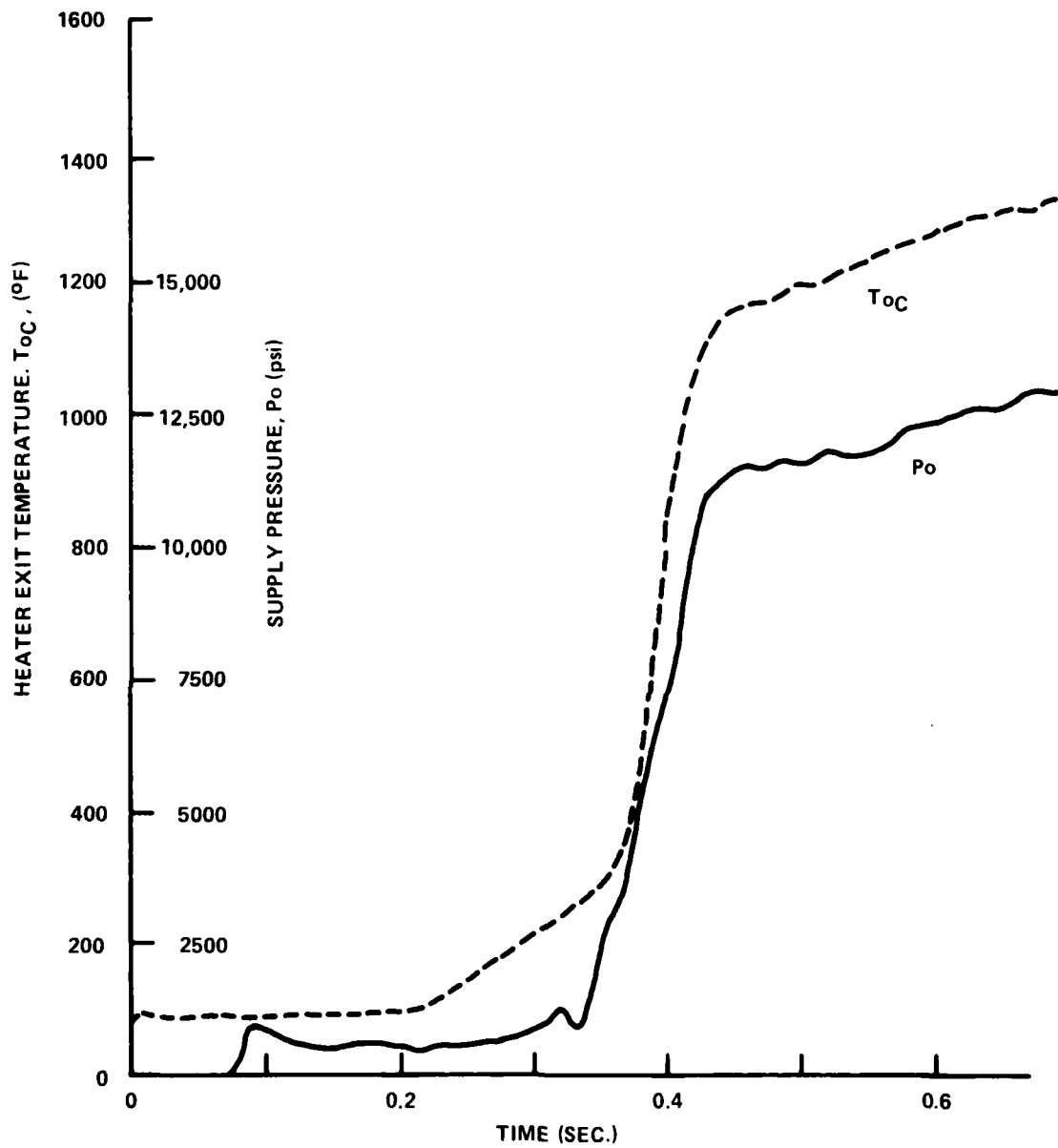


FIGURE 20. HEATER INSTRUMENTATION PACKAGE



FIGURE 22.  $P_o$  &  $T_o$  VERSUS TIME FOR QUICKPROOF

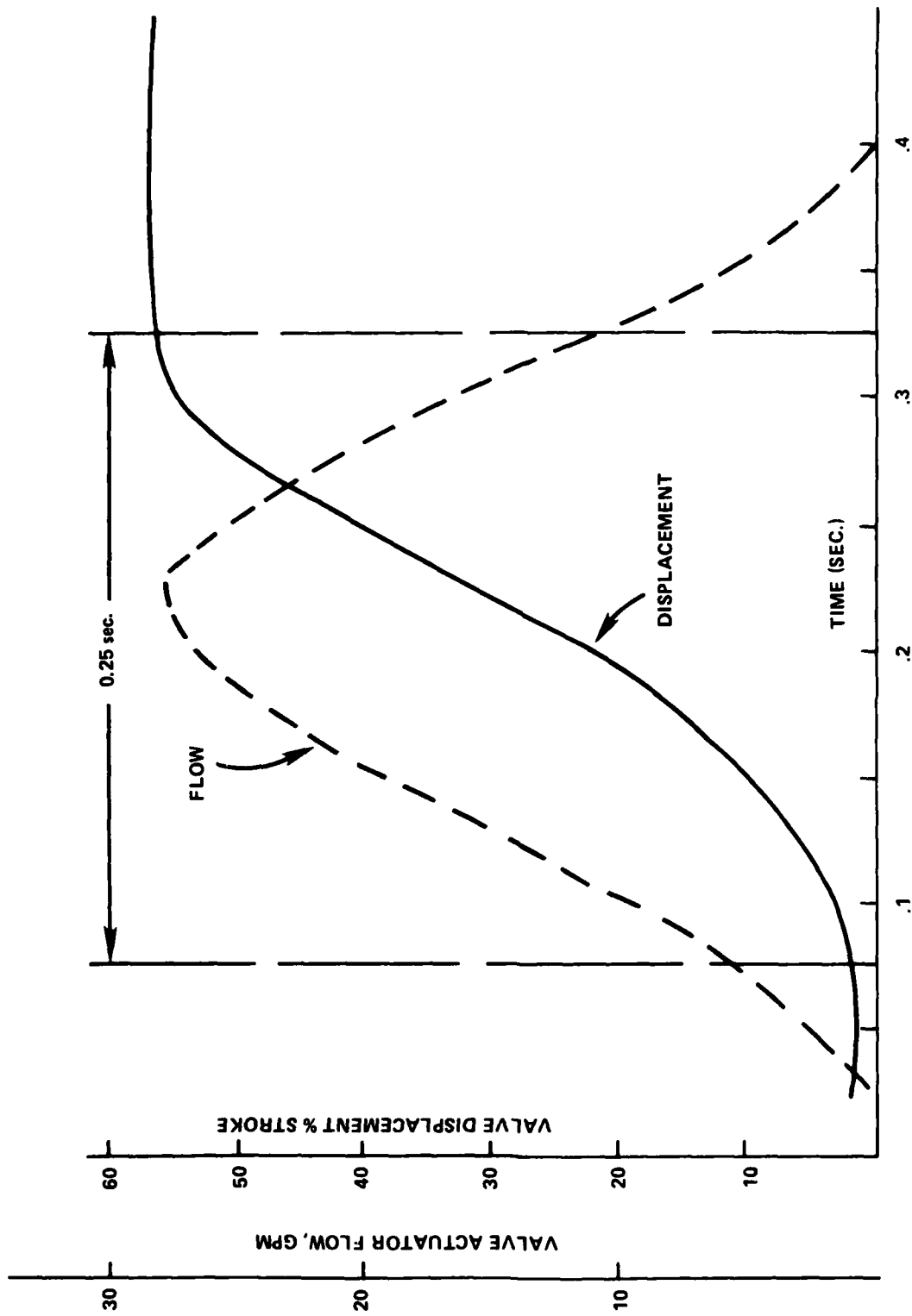


FIGURE 23. VALVE DISPLACEMENT VERSUS TIME-NEW MODE OF OPERATION

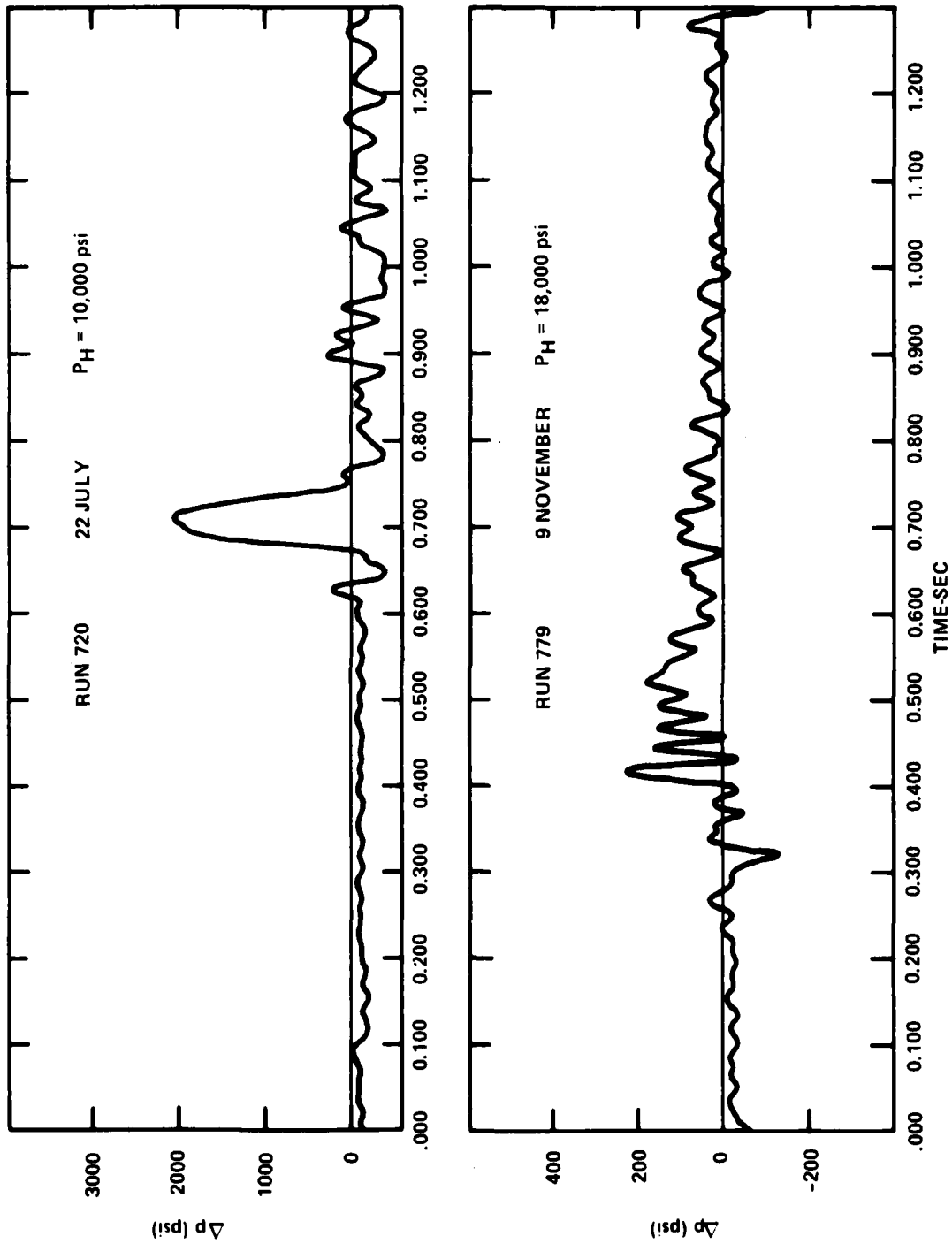


FIGURE 24. PRESSURE PULSE IN HEATER ANNULUS,  $P_A - P_{H\text{BOT}}$  FOR OLD AND NEW VALVE MOTION



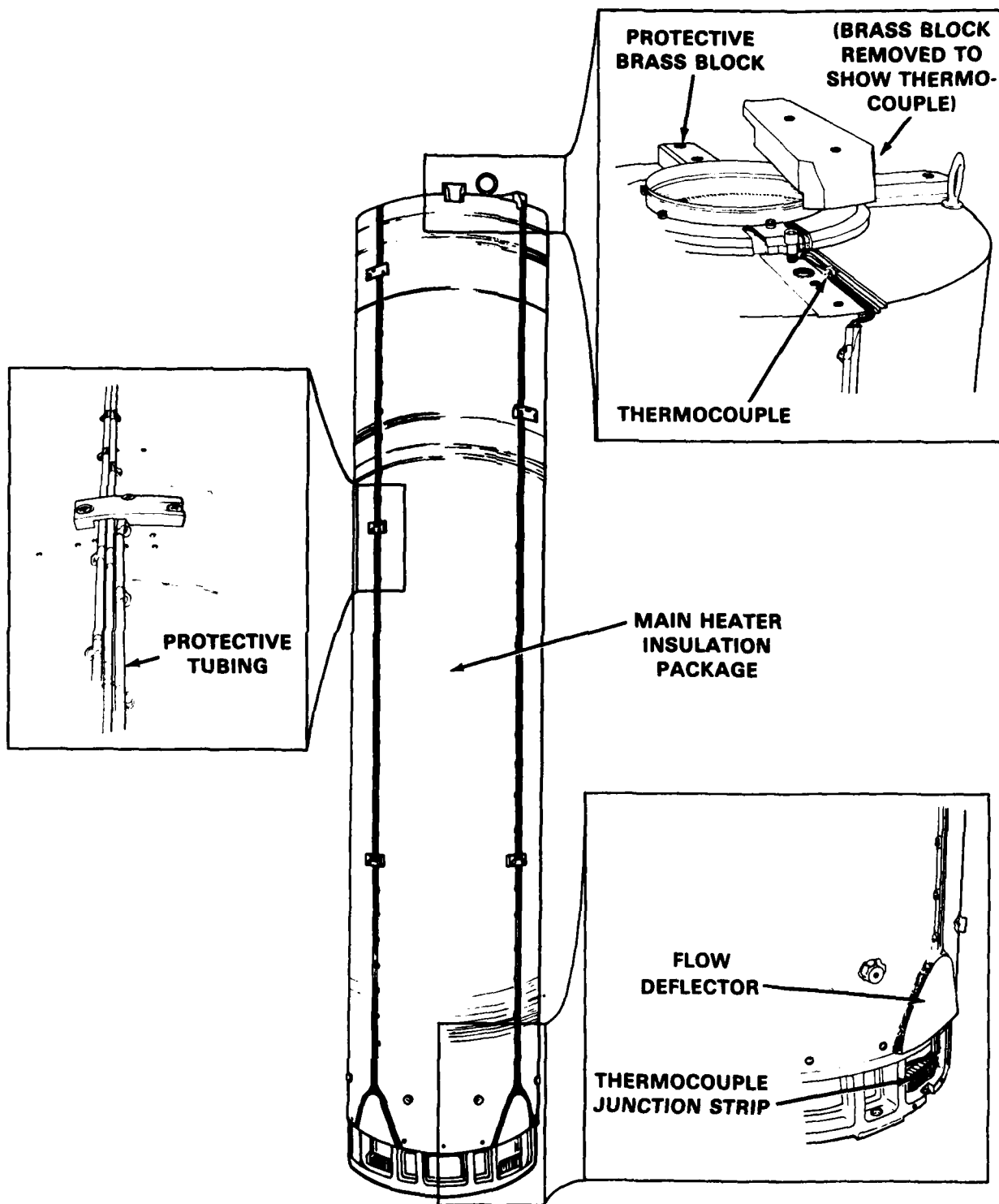


FIGURE 25. NEW HEATER INSTRUMENTATION PACKAGE

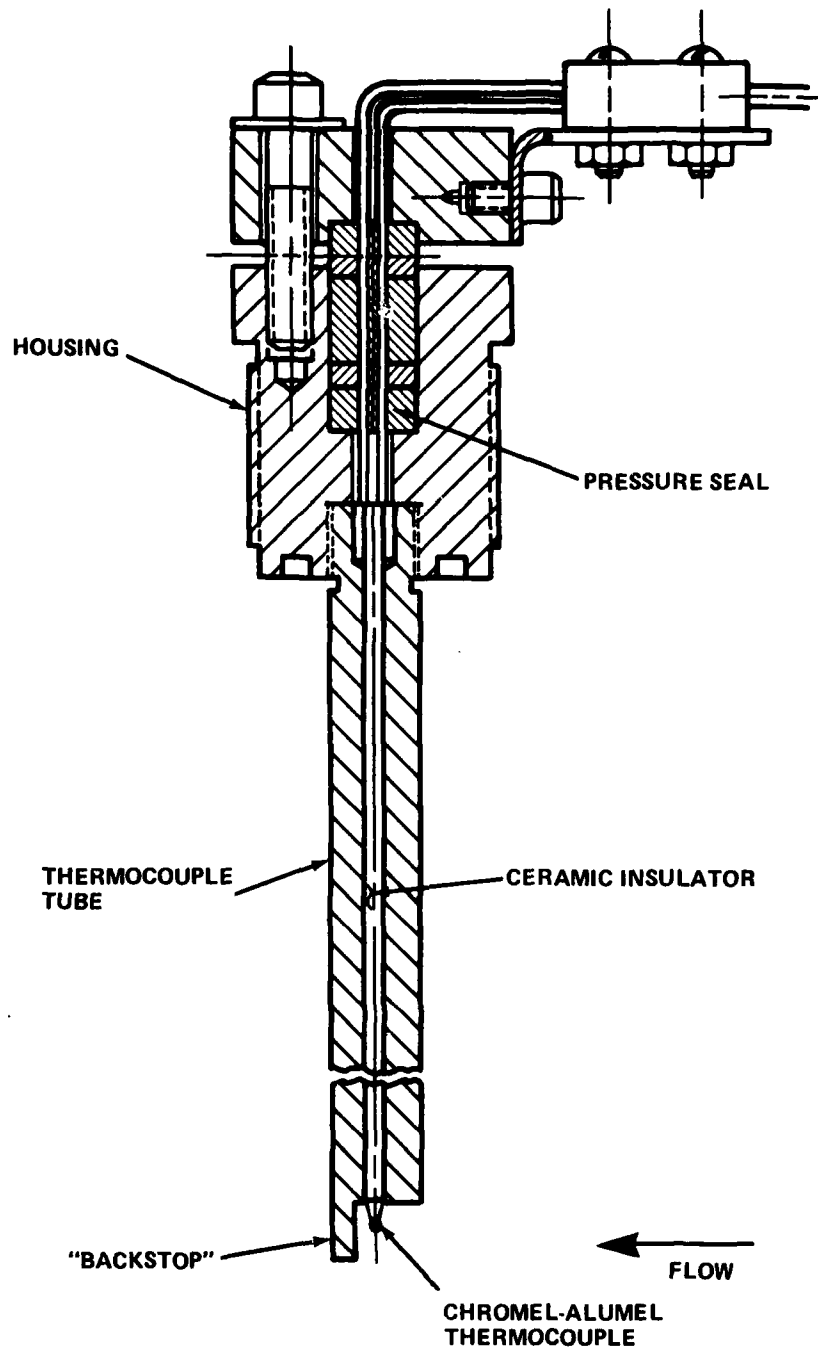


FIGURE 26. NEW  $T_0$  THERMOCOUPLE DESIGNS



FIGURE 27. PARTICLE SEPARATOR MUFFLER DESIGN

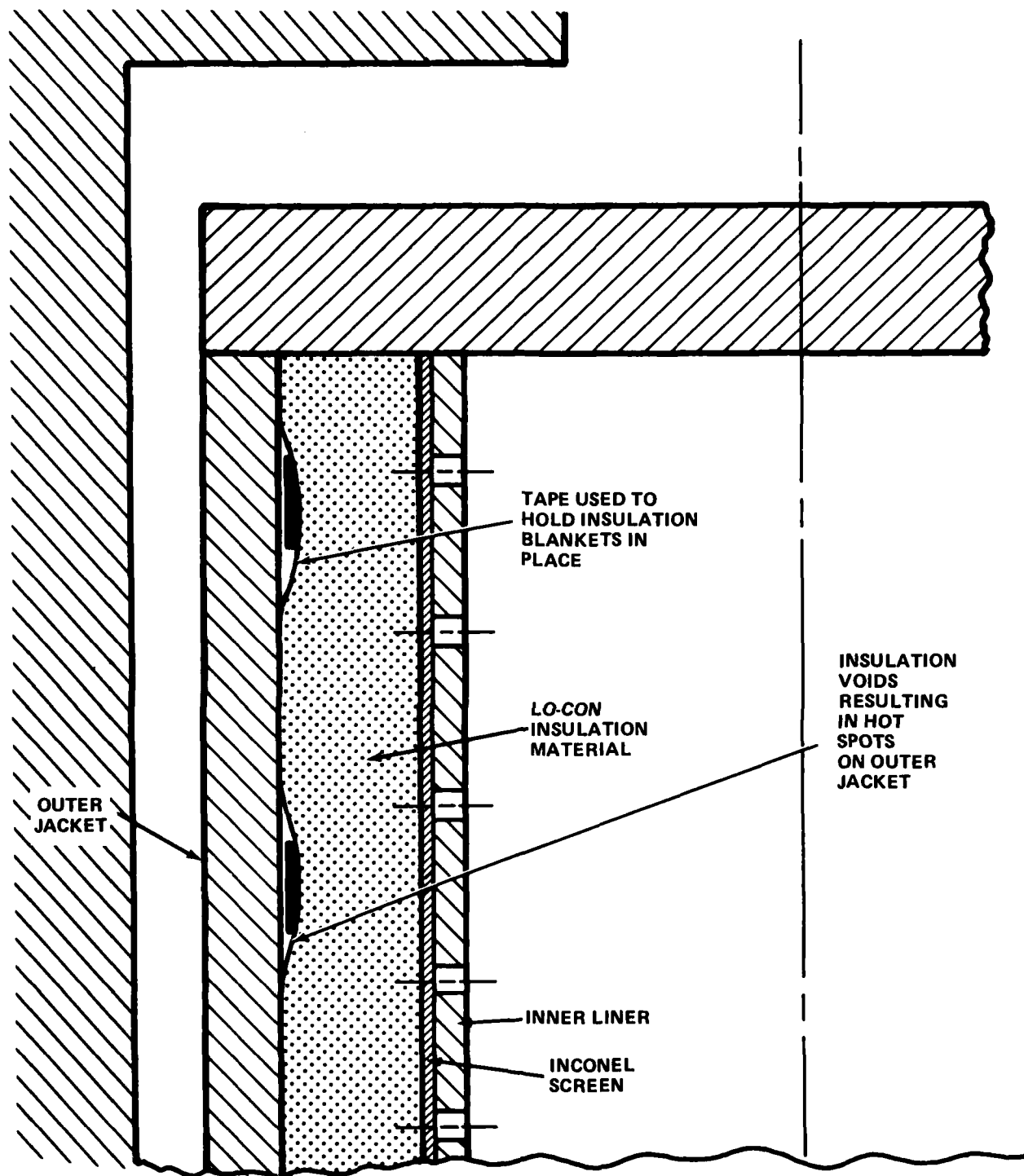


FIGURE 28. MAIN HEATER INSULATION VOIDS

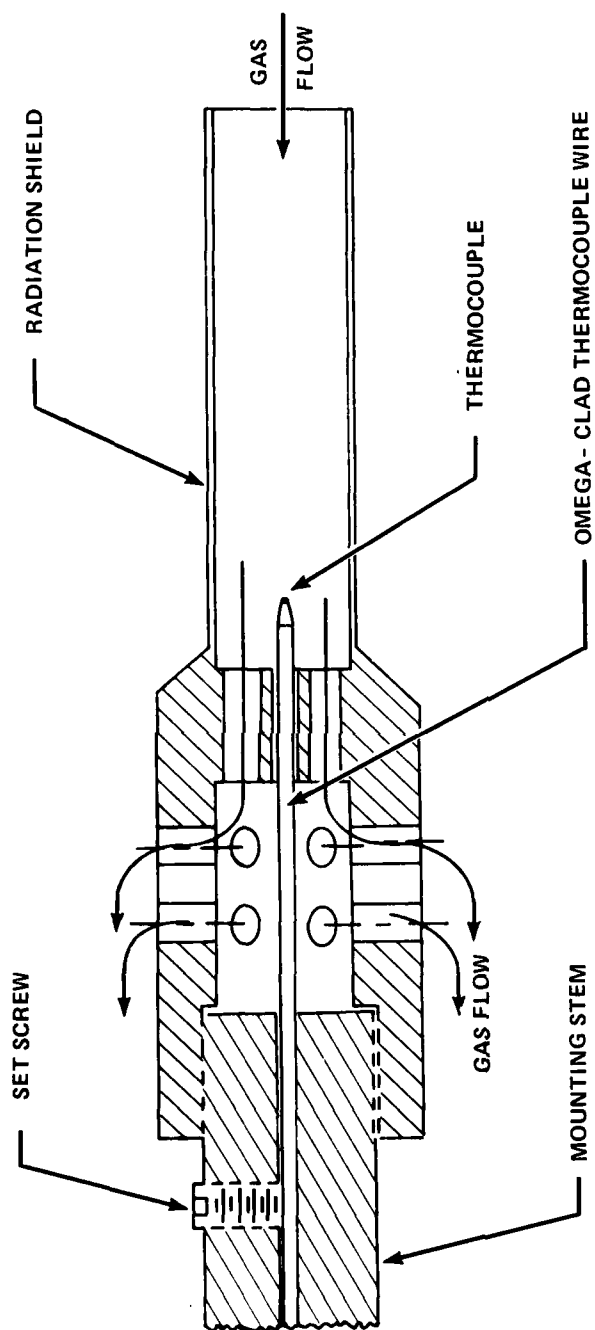


FIGURE 29. TOTAL TEMPERATURE PROBE DESIGN



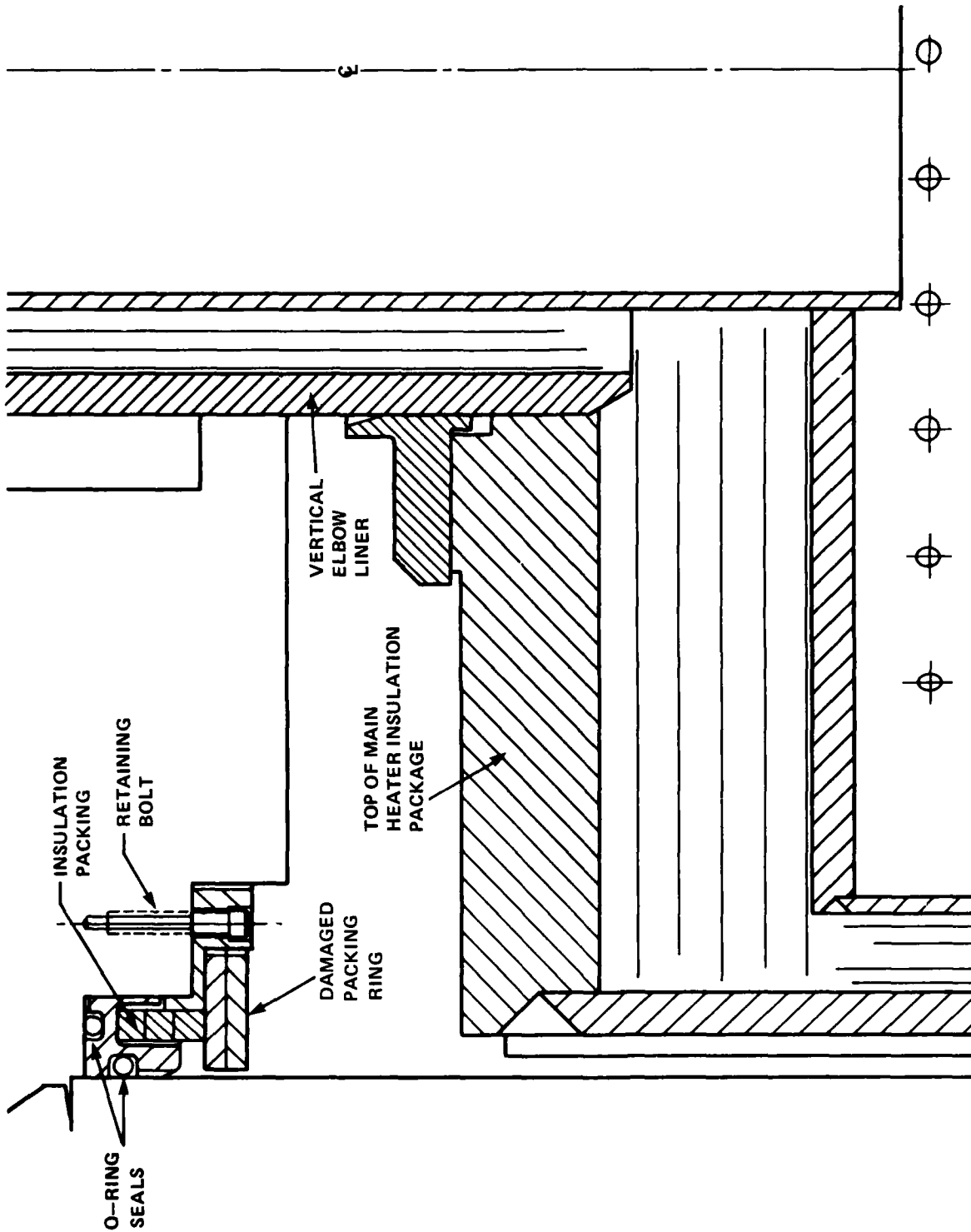


FIGURE 31. HEATER PACKING RING

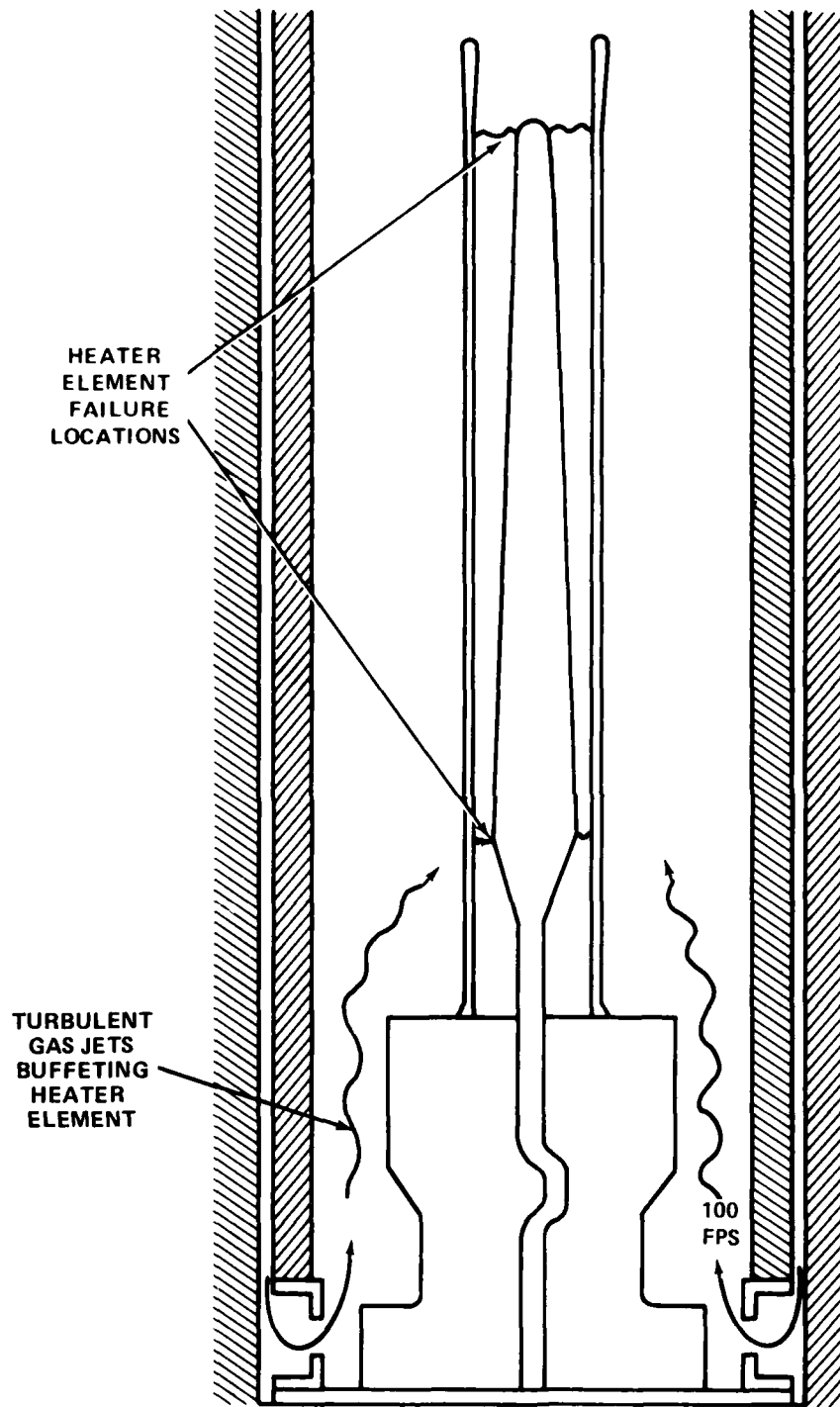


FIGURE 32. HEATER ELEMENT FAILURE LOCATIONS



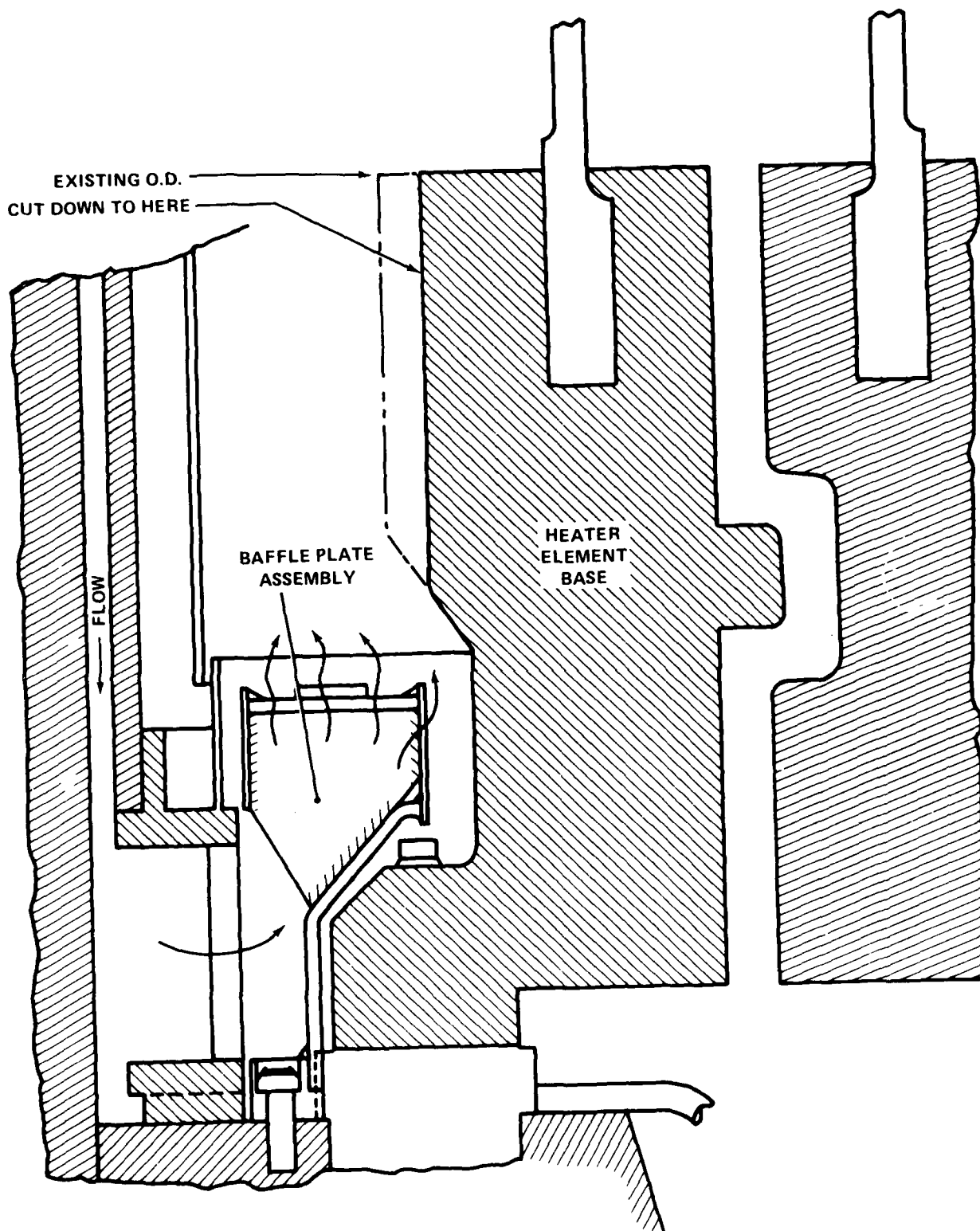


FIGURE 33. BAFFLE PLATE DESIGN

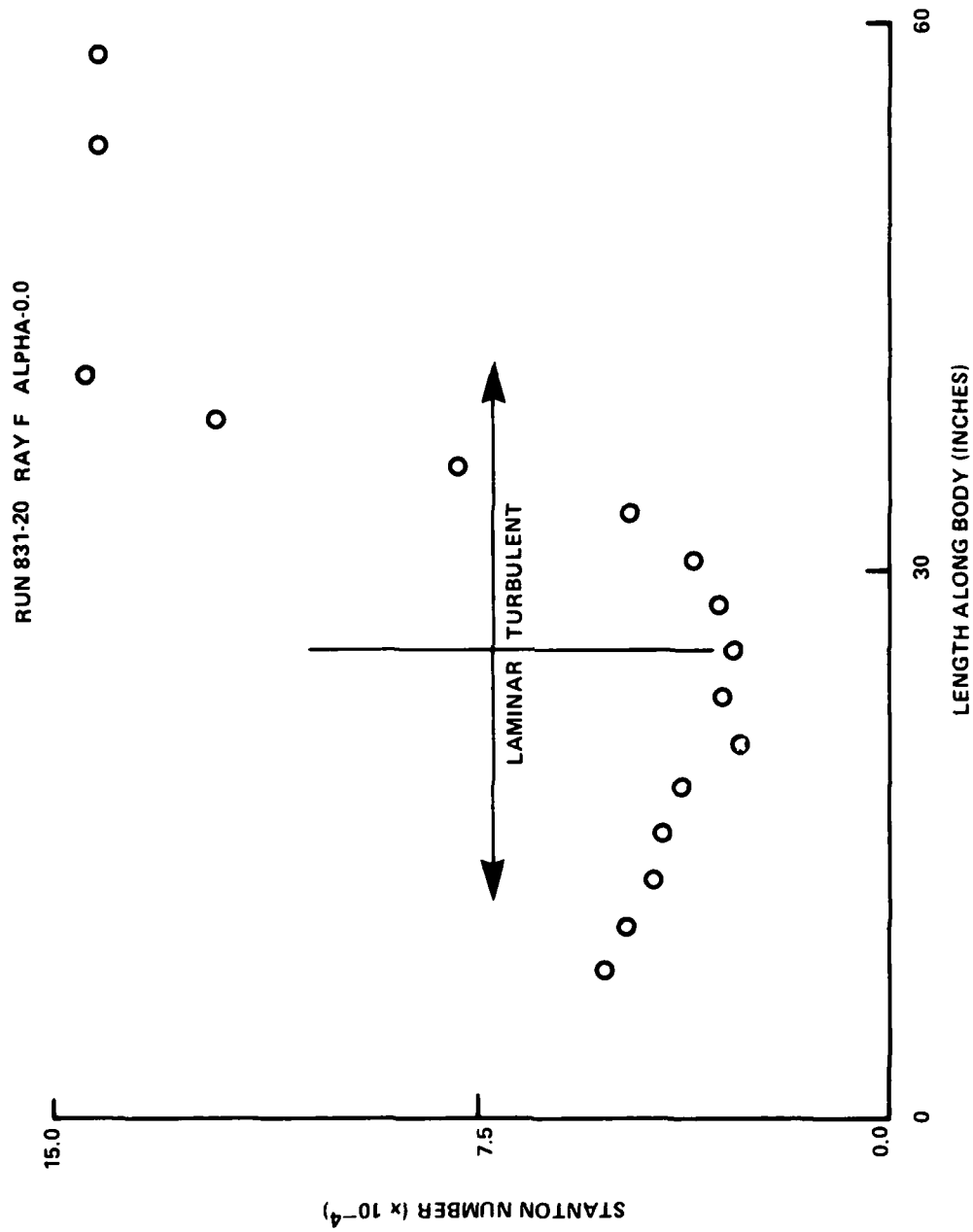


FIGURE 34. LAMINAR TO TURBULENT TRANSITION ON MODEL

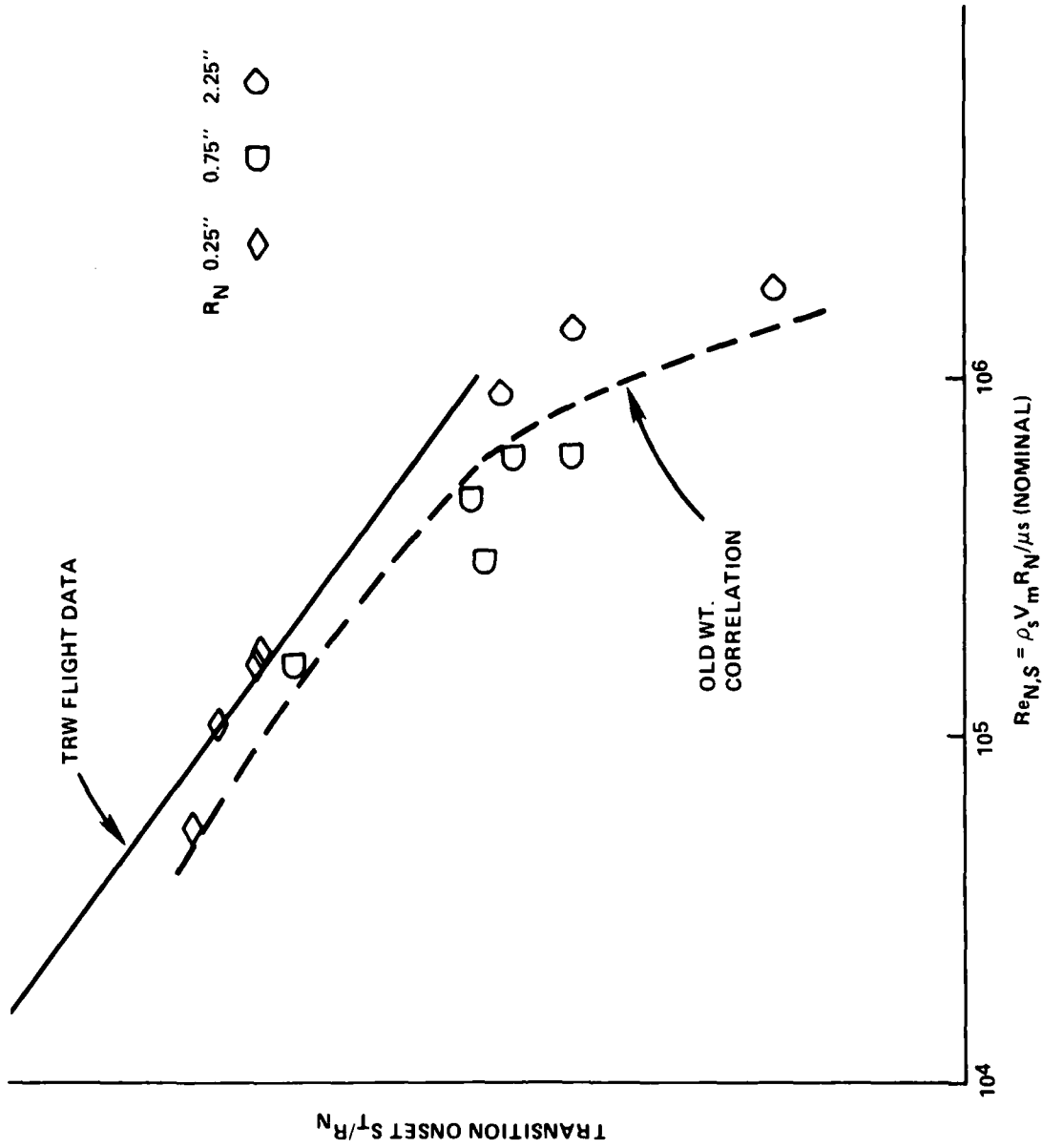


FIGURE 35. TRANSITION ONSET VS. REYNOLDS NUMBER

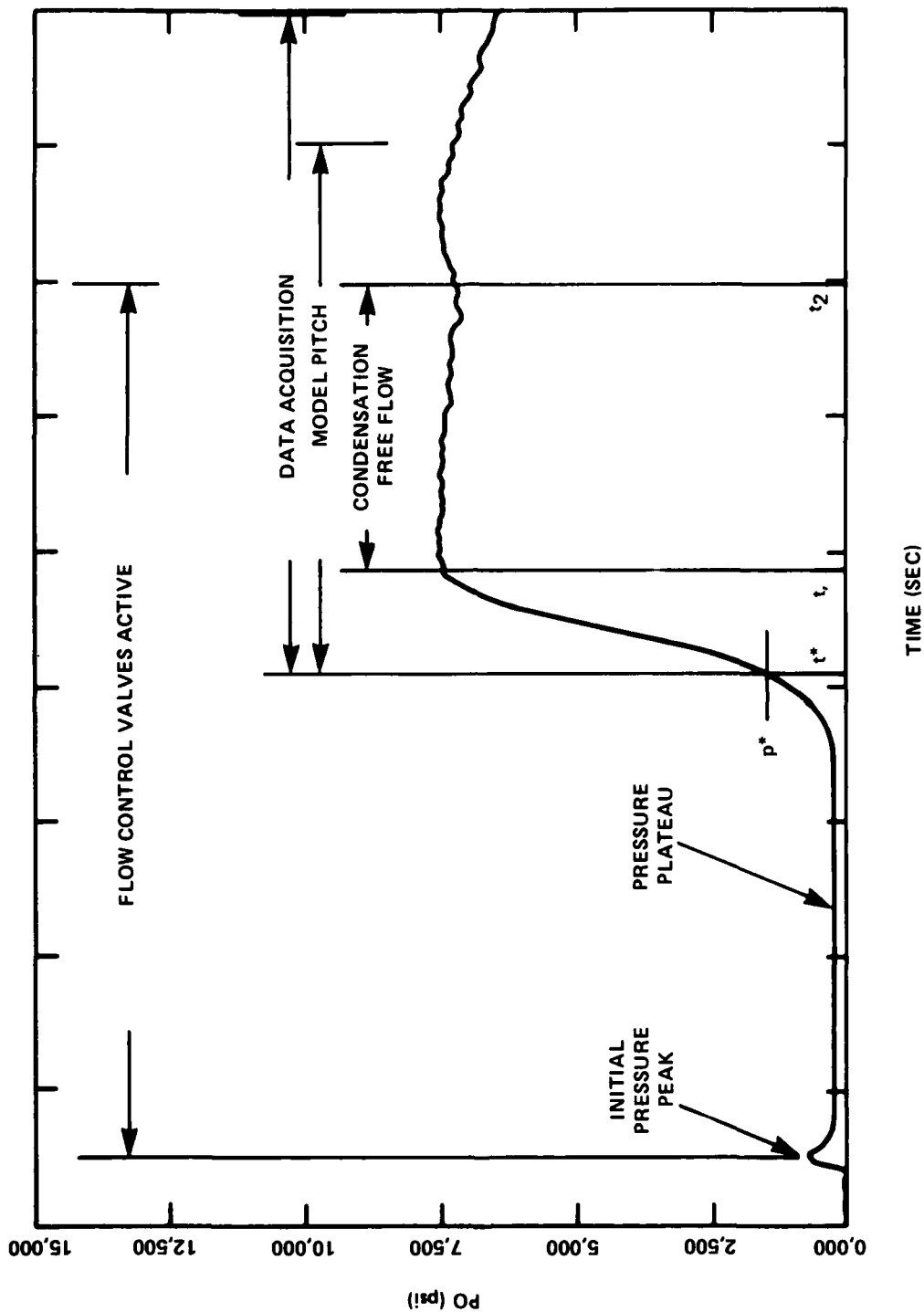


FIGURE 36. TYPICAL SUPPLY PRESSURE HISTORY

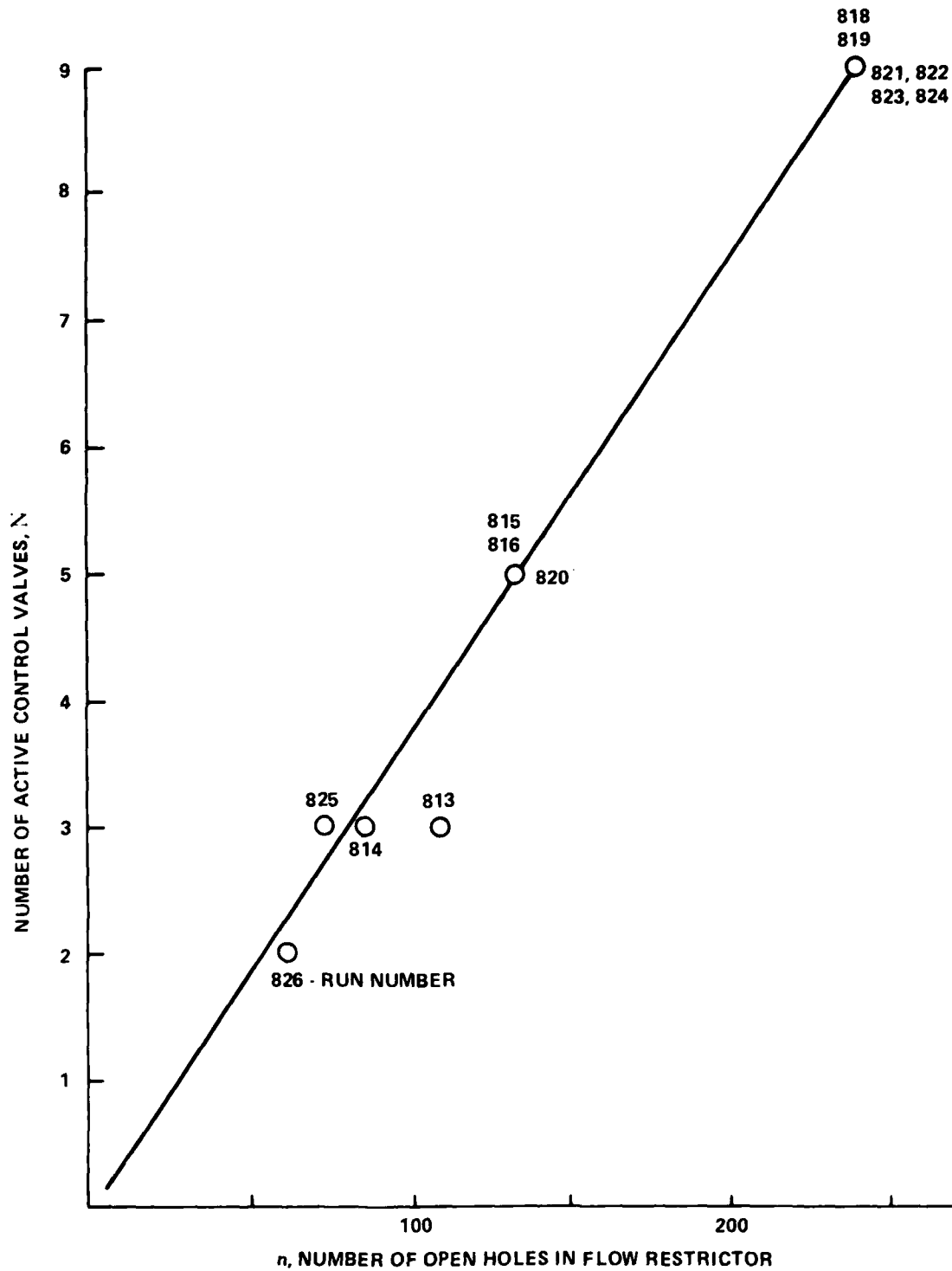


FIGURE 37. NUMBER OF ACTIVE VALUES VS. NUMBER OF OPEN HOLES IN FLOW RESTRICTOR

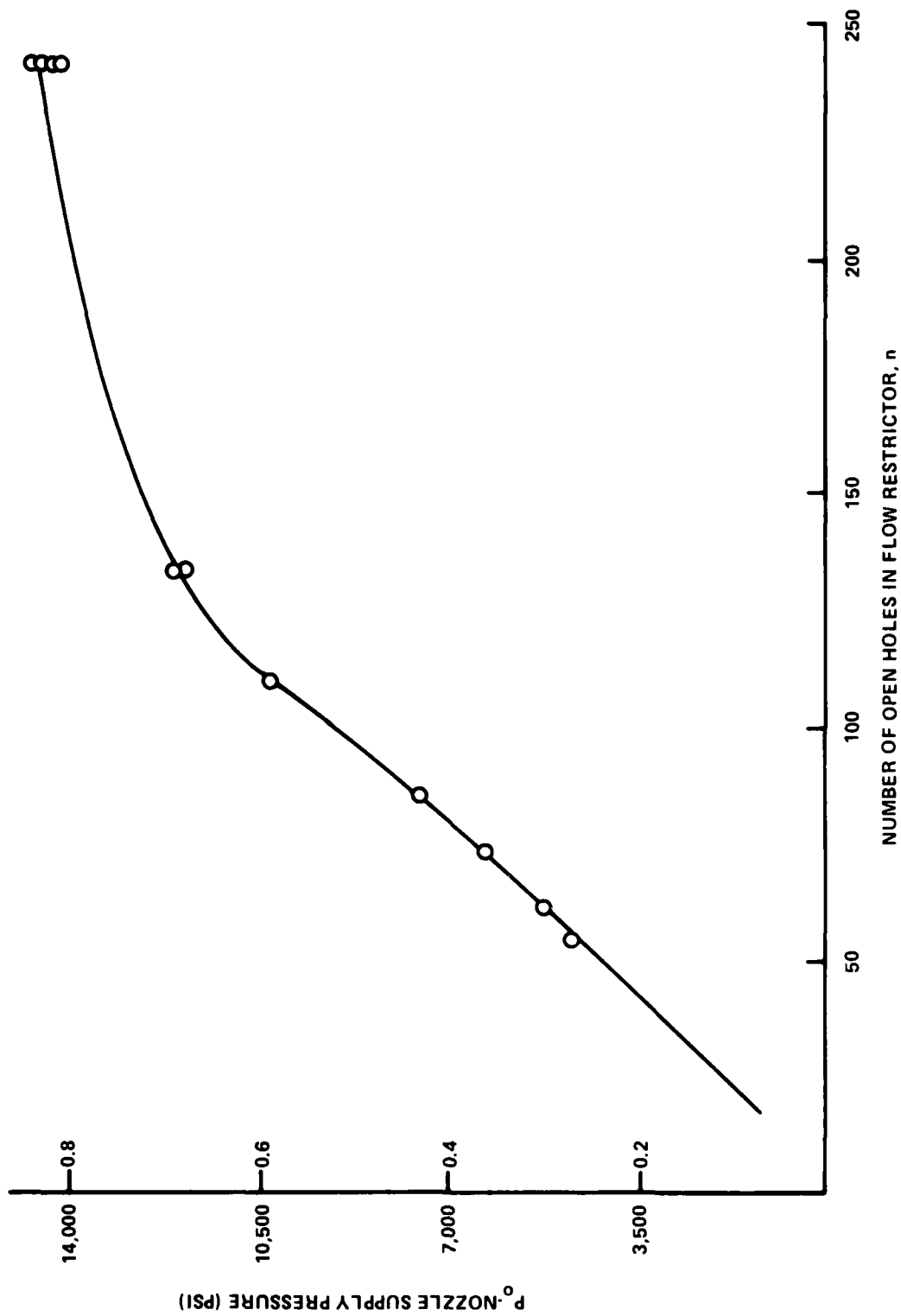


FIGURE 38. NOZZLE SUPPLY PRESSURE,  $P_o$ , VS. NUMBER OF HOLES IN FLOW RESTRICTOR

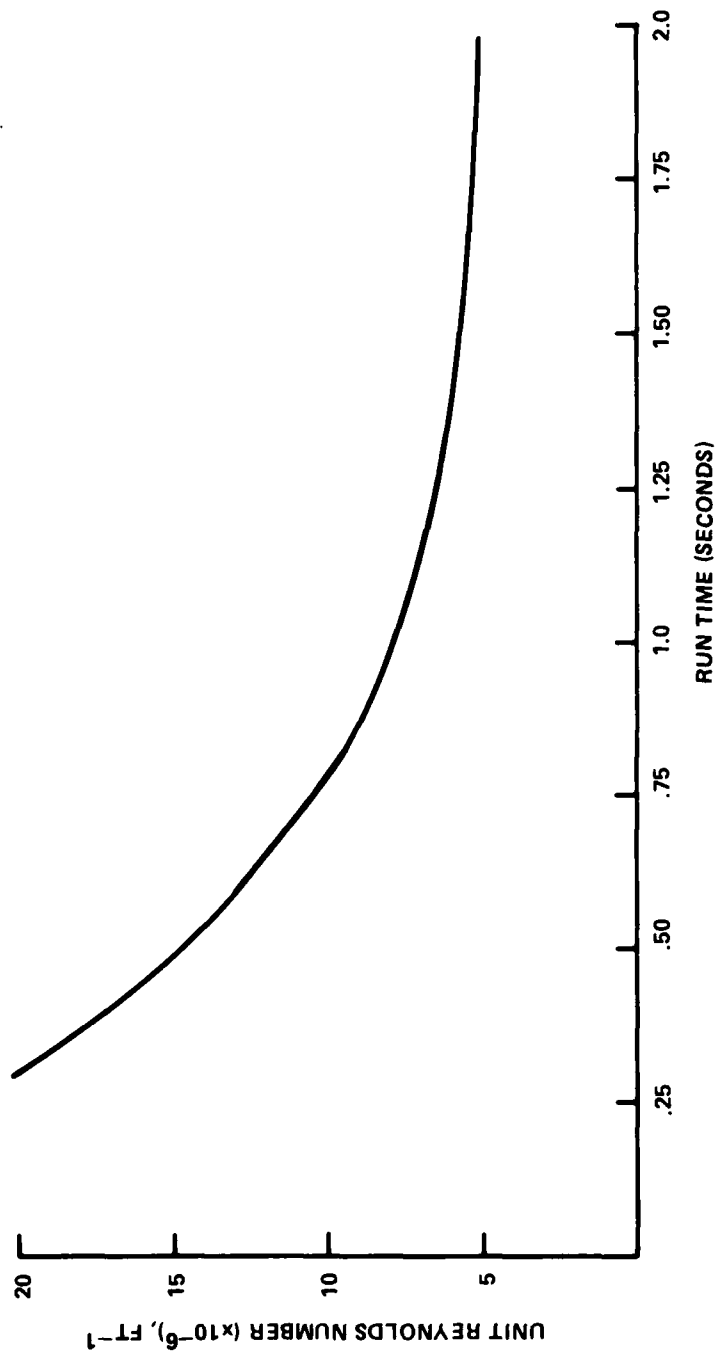


FIGURE 39. REYNOLDS NUMBER VERSUS RUN TIME

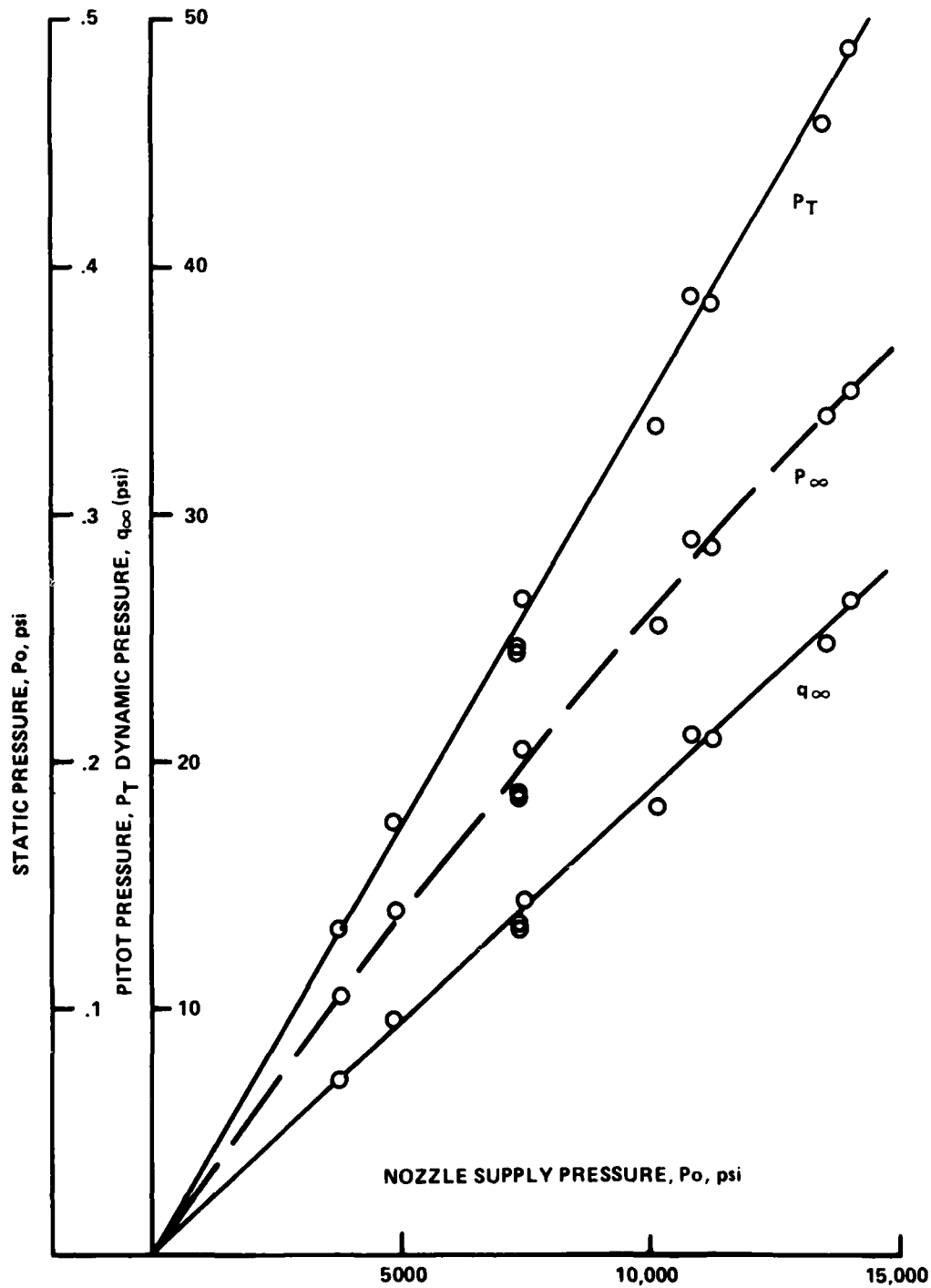


FIGURE 40. STATIC PRESSURE,  $P_o$   
DYNAMIC PRESSURE,  $q_o$   
PITOT PRESSURE,  $P_T$   
VS. SUPPLY PRESSURE



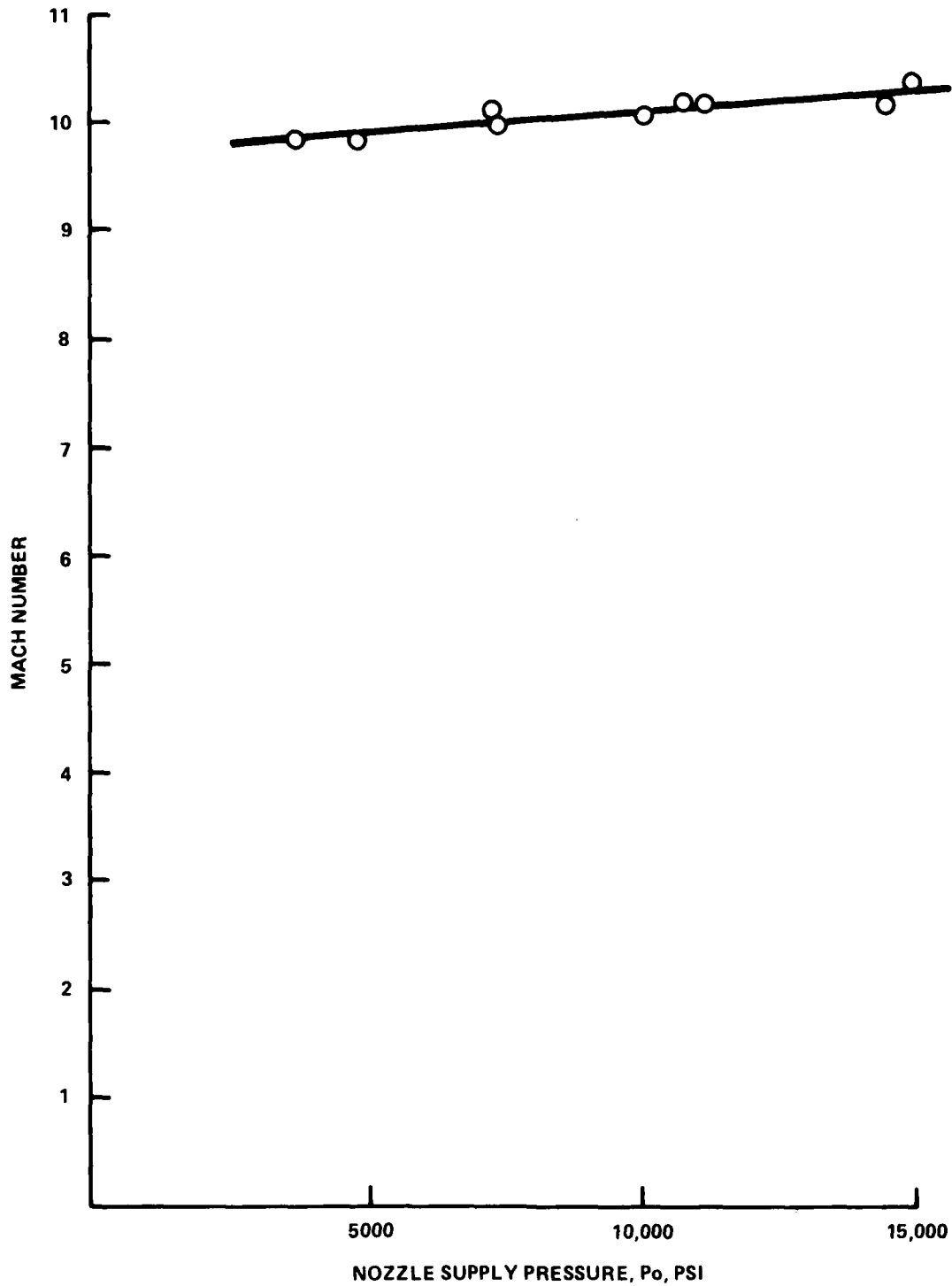


FIGURE 41. MACH NUMBER VS. SUPPLY PRESSURE

TABLE 1. EXPANSION WAVE STRENGTH IN VARIOUS HEATER SECTIONS

HEATER SECTION	EXPANSION WAVE STRENGTH (PSI)
HORIZONTAL ELBOW	15,428
VERTICAL ELBOW	8,431
MAIN HEATER	714

TABLE 2. OUTER JACKETS' PRESSURE CAPABILITIES

COMPONENT	PRESSURE CAPABILITY (PSI)	EXPANSION WAVE PRESSURE LOAD (PSI)
HORIZONTAL ELBOW OUTER JACKET	15,827	15,428
VERTICAL ELBOW LOWER OUTER JACKET	10,310	8,431
UPPER	9,260	
MAIN HEATER CAN OUTER JACKET	1,080	714
TOP PLATE	1,410	

TABLE 3. INNER LINERS' PRESSURE CAPABILITIES

COMPONENT	PRESSURE CAPABILITY (PSI)	EXPANSION WAVE PRESSURE LOAD (PSI)
HORIZONTAL ELBOW INNER LINER	1,347	138
VERTICAL ELBOW CAN INNER LINER	700	242
TOP PLATE	737	464
MAIN HEATER CAN INNER LINER	82	36
TOP PLATE	54	33

REFERENCES

1. Kavetsky, R. A., Mach 10/14 Operations in the NSWC Hypervelocity Wind Tunnel No. 9 (Vertical Heater Vessel Leg), NSWC TR 80-487, Jul 1982.
2. Ragsdale, W. C., Pershing II Static Stability and Pressure Test in the NSWC Hypervelocity Facility, NSWC MP 80-495 (Unpublished), Oct 1980.
3. O'Donnell and Associates, Inc., Hypervelocity Wind Tunnel Components Structural Evaluation-Final Report, May 1979.
4. WA-40 Safety Committee, Safety Review of the Hypervelocity Facility Wind Tunnel No. 9, Navy JAG Report, Mar 1976.
5. Hill, J. A. F., Initial Operation of the NOL Hypervelocity Tunnel, AIAA Paper No. 74-608, Jul 1974.
6. Bulletin of the Society of French Ceramics, NO. 118, 1978, p. 31-34.

# APPENDIX A

## INITIAL FEASIBILITY STUDY

### FATIGUE LIFE EVALUATION

A method outlined in Reference A-1 was used to obtain the allowable number of cycles shown in Figure 5 of the main report.

For a given pressure cycle from  $P_{\max}$  to a  $P_{\min}$  of 15,000 psi, an alternating stress and a mean stress are calculated from:

$$\sigma_{\text{alt}} = \frac{k(P_{\max} - 15,000)}{2} \quad (\text{A-1})$$

$$\sigma_{\text{mean}} = \frac{k(P_{\max} + 15,000)}{2} \quad (\text{A-2})$$

where  $k = 5.588$  (obtained from Reference A-1) is a factor relating stress to operating pressure. It takes into account load distribution to the component of interest, and material properties of the component.

Next, Peterson's cubic equation is used to obtain an equivalent alternating stress intensity ( $\sigma_{\text{eq}}$ ) that accounts for cycling about some value other than zero psi. Peterson's equation is:

$$\sigma_{\text{eq}} = \frac{7 \cdot \sigma_{\text{alt}}}{8 - \left[ 1 + \frac{\sigma_{\text{m}}}{\sigma_{\text{ult}}} \right]^3} \quad (\text{A-3})$$

where

$$\sigma_{\text{m}} = \sigma_{\text{y}} - \sigma_{\text{alt}} \quad (\sigma_{\text{y}} = 140,000 \text{ psi--material yield strength})$$

$$\sigma_{\text{ult}} = 150,000 \text{ psi--material ultimate strength}$$

Knowing the equivalent alternating stress intensity, Figure A-1 can be used to obtain a total number of cycles allowed for a given pressure excursion. The curve given in Figure A-1 was generated by Manson and is based on actual fatigue data. The curve has taken into account the required ASME code safety factors of two on  $\sigma_{eq}$ , or twenty on cycles, whichever is more conservative.

Using the above equations, an allowable number of cycles,  $n$ , was generated for several values of  $P_{max}$ , as given in Table A-1. Figure 5 of the main report was then generated, showing the variation in allowable number of cycles with  $P_{max}$ . For the HIRE pressure of 40,000 psi, 1495 cycles would be allowed.

TABLE A-1. DRIVER VESSEL FATIGUE LIFE PARAMETERS

$P_{max}$ (psi)	$\sigma_{alt}$ (psi)	$\sigma_{mean}$ (psi)	$\sigma_{eq}$ (psi)	N (cycles)
46,000	86,614	170,434	110,092	1020
40,000	69,850	153,670	101,052	1495
34,000	53,086	136,906	91,528	2305
28,000	36,322	120,142	80,383	4290

## EXPANSION WAVE STRENGTH

From continuity considerations, the flow rate through the heater is equal to the flow rate through the flow restrictor. In equation form:

$$m = \rho_H u A_H = K_N \rho_R a_R A_R \quad (A-4)$$

where the subscripts H and R refer to heater and restrictor area respectively, and  $\rho$  is density,  $K_N$  is a nozzle discharge coefficient, and A is area.

Solving for  $u$ , the velocity of a rarefaction wave, the following is obtained:

$$u = \frac{K_N \rho_R a_R A_R}{\rho_H A_H} \quad (A-5)$$

Recall Equation (1) from Reference A-2:

$$\Delta p = \rho_H a_H U \quad (A-6)$$

Substitution of Equation (A-5) into Equation (A-4) yields:

$$\Delta p = k_N \rho_R a_R \frac{A_R}{A_H} a_H \quad (A-7)$$

It can be seen from the above equation then, that for a given geometry ( $A_R/A_H$ ) and a given flow restrictor condition ( $k_N \rho_R a_R$ ),  $\Delta p$  is proportional to the  $a_H$ , the sound speed in the heater. Both Mach-10 and Mach-14 utilize the same heater geometry, and during the transient period, cold gas is moving through the flow restrictor area in both Mach-10 and Mach-14 operations. Thus, it can be written:

$$\frac{\Delta P_{M-10}}{\Delta P_{M-14}} = \frac{a_{H10}}{a_{H14}} \quad (A-8)$$

The sound speed may determined from:

$$a = \frac{\gamma p}{\rho} \quad (A-9)$$

where  $p$  is the gas pressure and  $\gamma$  is the isotropic gas coefficient.

But for Mach-10 and Mach-14 operations,  $p$  is the same. Substitution of Equation (A-9) into (A-8), and elimination of  $p$  results in the following:

$$\frac{\Delta P_{M-10}}{\Delta P_{M-14}} = \frac{\frac{\gamma}{\rho_{10}}}{\frac{\gamma}{\rho_{14}}}$$

For nitrogen at 1500°F (Mach-10),  $\gamma = 1.95$  and  $\rho = 19.5 \text{ lb/ft}^3$ . For nitrogen at 3000°F (Mach-14),  $\gamma = 1.61$ , and  $\rho = 12.7 \text{ lb/ft}^3$ . Substitution into Equation (E-7) yields:

$$\frac{\Delta P_{M-10}}{\Delta P_{M-14}} = \frac{\left(\frac{1.95}{19.5}\right)}{\left(\frac{1.61}{12.7}\right)} = .80$$

Thus the magnitude of the rarefaction wave strength in Mach-10 is about 80% of the Mach-14 value. This means that if the initial open area used in the Mach-10 flow restrictor is the same as that in the Mach-14 flow restrictor (.17 in<sup>2</sup>), the expansion wave impinging on the heater element will be slightly less in Mach-10 testing than it is in Mach-14 testing.

## ABLATIVE FLOW RESTRICTOR EVALUATION

One of the critical reviews which took place in the initial HIRE feasibility study was of the ablative flow restrictor. Due to the use of a fixed volume heater, concerns arose right from the onset of HIRE about the ability of the ablators to wash out fast enough to preclude wasting hot test gas. Figure A-2 is essentially the summary figure which resulted from an evaluation of past tunnel operational experience, and heater exhaust calculations. Generation of this figure led to the decision to design a mechanical valve to use as a flow restrictor device.

The useful run time available was defined as the difference between the amount of time it took to expell this "effective" heater volume ( $12.8 \text{ ft}^3$ ) and the larger of the tunnel warmup time or ablation time. The effective heater volume curve was based on expelling 80% of the total heater volume available. (The other 20% of the heater volume is used up by the insulation packages and other hardware in the heater.) The tunnel warmup time is roughly 500 milliseconds, independent of supply pressure. This curve was based on prior tunnel operating experience. The ablation time curve was an estimate based on a proposed HIRE ablation flow restrictor design, which incorporated 13 holes, and prior tunnel operating experience. As can be seen from Figure A-2, at supply pressures above 6,000 psi, the useful runtime is reduced due to the increased ablation time required. Again, it should be stressed that the prediction of ablation time was based solely on prior tunnel operating experience. Therefore, based on the prediction that the proposed HIRE ablative flow restrictors would use up a significant amount of the limited amount of hot test gas available, the decision was made to utilize a mechanical flow restrictor device for HIRE.

### Driver Vessel Blowdown Performance

To determine if the driver vessels could handle the very large (1050 lb/sec) HIRE mass flow rate requirement, "blowdown" calculations were performed which ascertained required driver vessel initial pressure. Figure A-3 is the model of the vertical flow passages which the blowdown calculations apply to.

The expected HIRE run time of .25 seconds was obtained as follows. With a fixed maximum heater pressure of 22,000 psi, and a calculated initial pressure drop in the heater of 2,800 psi (before the control valves could maintain constant conditions), and an expected pressure drop through the diaphragm area of 3,200 psi, a supply pressure of 16,000 psi was expected. Knowing the "effective" heater volume ( $12.8 \text{ ft}^3$ ) the amount of time to expel gas from the heater at a supply pressure of 16,000 psi was approximately .250 seconds.

To account for pressure losses between the driver vessels and heater vessel, a minimum pressure requirement of 5,000 psi plus the heater pressure was placed on the driver vessel pressure. Thus, the driver vessel pressure must not drop below 24,200 psi. A stepwise calculation was performed in which an initial driver vessel pressure was assumed. This gas was expanded isentropically while the heater gas was compressed isentropically, maintaining constant heater pressure. The driver vessel pressure was decreased until the lower cutoff limit (4,200 psi) was reached. The time the driver vessels took to blowdown to the lower limit was calculated. This procedure was repeated until the driver vessel

pressure was obtained which resulted in a blowdown time of at least .250 seconds, thus matching the predicted run time. Table A-2 contains the values for one such calculation, assuming a driver vessel pressure of 38,000 psi, which turned out to be the minimum driver vessel pressure which matched the predicted .250 second run time. Gas property values were obtained from the nitrogen gas tables (Reference A-3).



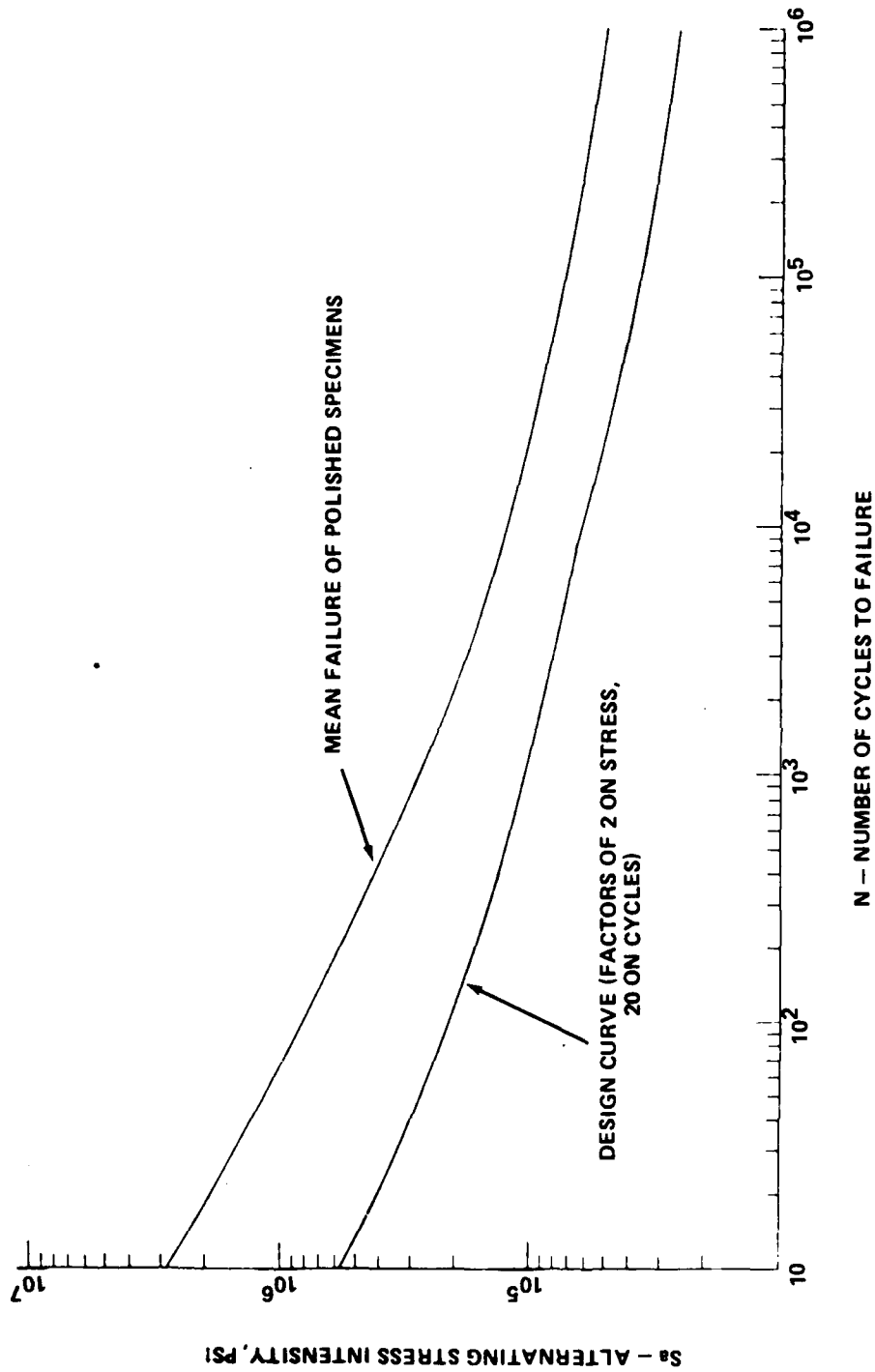
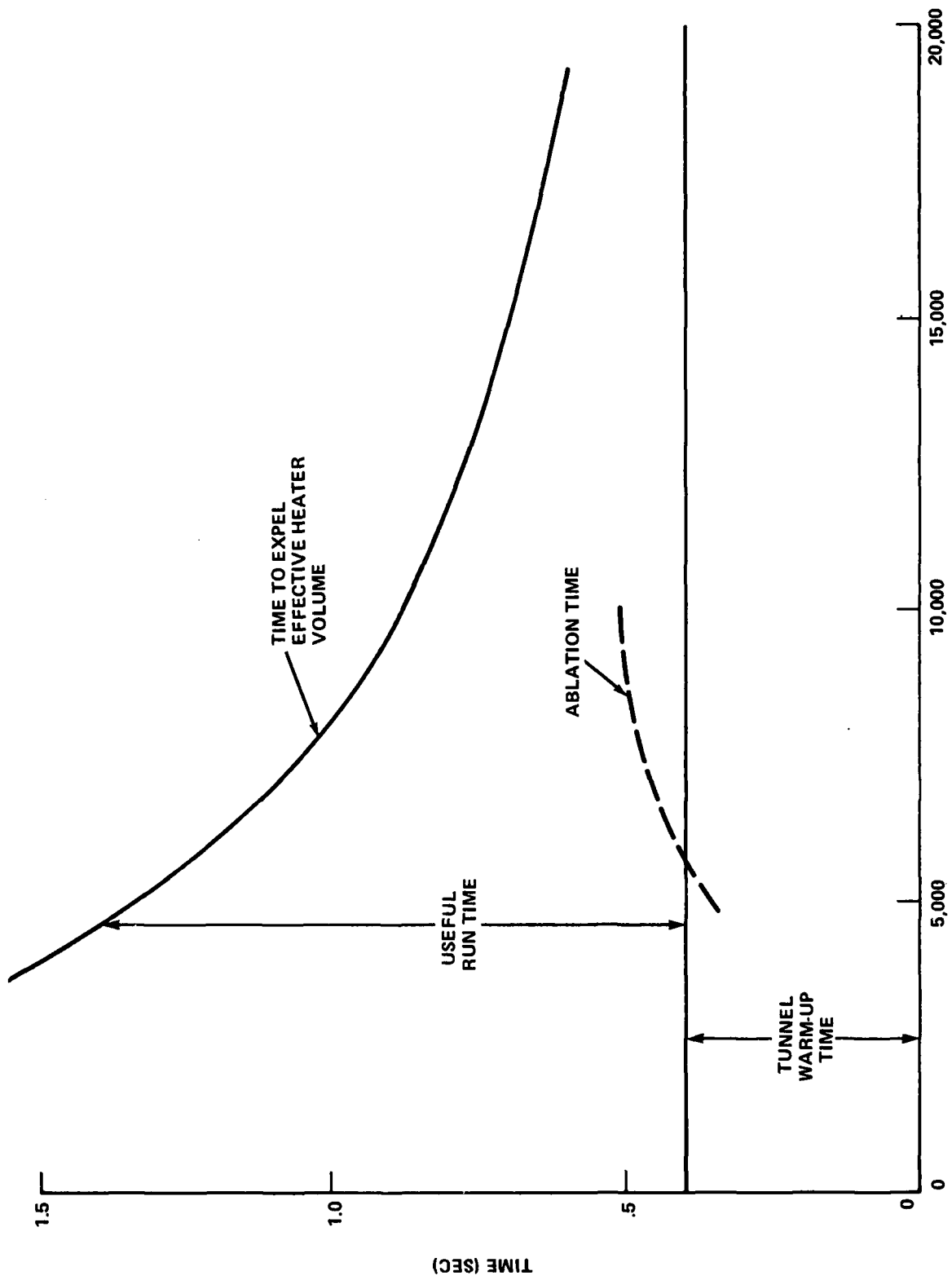


FIGURE A-1. DESIGN FATIGUE CURVE FOR AISI 4340 USED IN GAS STORAGE VESSEL (FROM MANSON)

FIGURE A-2. NOZZLE SUPPLY PRESSURE,  $P_o$  (PSI)

TIME (SEC)

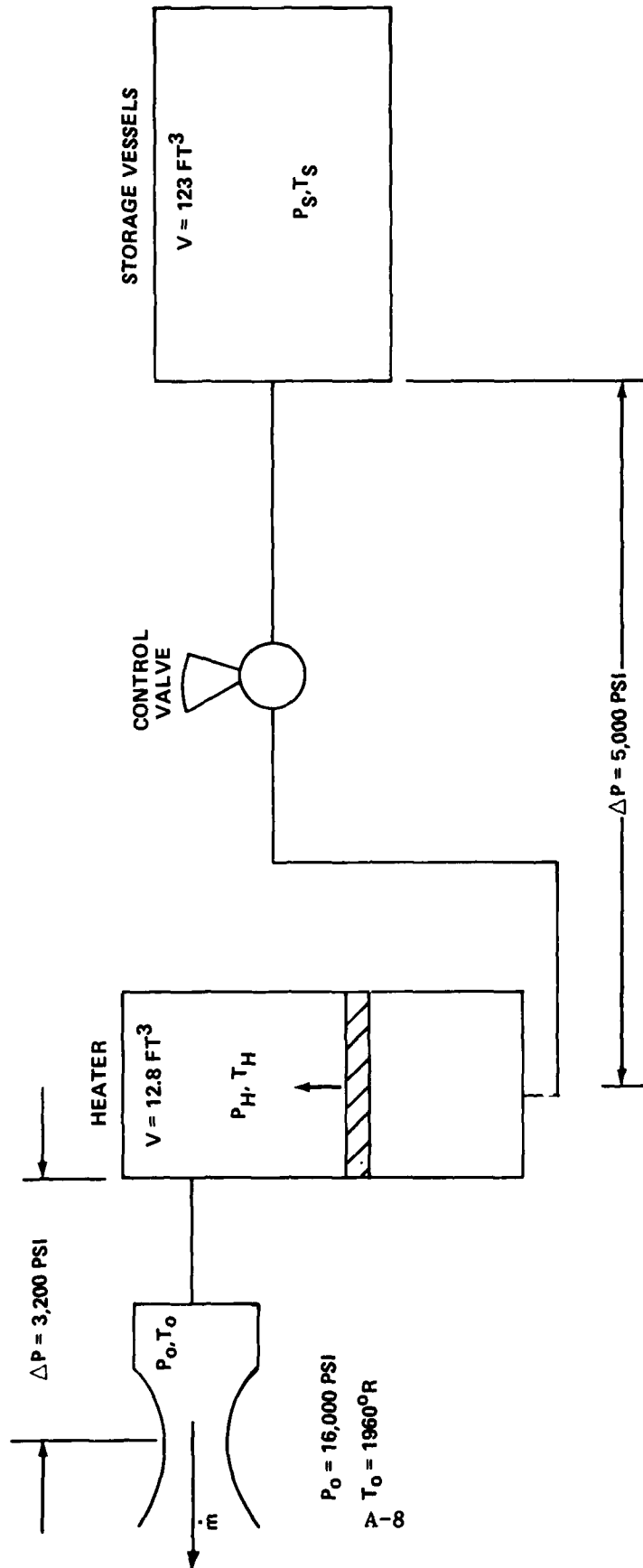


FIGURE A-3. DRIVER VESSEL BLOWDOWN SYSTEM

TABLE A-2. DRIVER VESSEL BLOWDOWN PERFORMANCE

$$V_H = 46.21 \frac{FT^3}{SEC} = \text{CONSTANT}$$

1	2	3	4	5	6	7	8	9	10	11	12
$\rho_S$ (PSI)	$T_S$ (°K)	$\rho_S$ (LB/FT <sup>3</sup> )	$\omega_S$ (LBS)	$P_H$ (PSI)	$T_H$ (°K)	$\rho_H$ (LB/FT <sup>3</sup> )	$\omega_H$ (LB/SEC)	$\Delta\omega_S$ (LBS)	$\rho_{S\text{AVG}}$ (LB/FT <sup>3</sup> )	$\Delta\theta$ (SEC)	$\Delta\theta_{\text{TOTAL}}$ (SEC)
38,000	425.0	43.007	5289.9	19,200	500	29.685	1371.7	—	—	—	—
36,000	417.4	42.319	5205.2	19,200	485	30.237	1397.3	84.7	42.7	0.043	0.043
34,000	409.9	41.643	5122.1	19,200	470	30.870	1426.5	83.1	42.0	0.043	0.086
32,000	402.3	40.977	5040.2	19,200	455	31.516	1456.4	81.9	41.3	0.043	0.129
30,000	394.7	40.415	4971.0	19,200	440	32.102	1483.4	69.2	40.7	0.037	0.166
28,000	387.2	39.768	4891.5	19,200	425	32.775	1514.5	79.5	40.1	0.043	0.209
26,000	379.6	39.132	4813.2	19,200	410	33.461	1546.2	78.3	39.5	0.043	0.252
24,000	372.0	38.507	4736.4	19,200	395	34.083	1574.9	76.8	38.8	0.043	0.295

$$\omega_C = 123 \cdot \rho_S$$

$$\omega_H = V_H \cdot \rho_H$$

$$\Delta\omega_S = \omega_{SN+1} - \omega_{S1}$$

$$\rho_{S\text{AVG}} = \frac{\rho_{SN+1} + \rho_{S1}}{2}$$

$$\Delta\theta = \frac{\Delta\omega_S}{\rho_{S\text{AVG}} \cdot V_H}$$

REFERENCES

- A-1. O'Donnell and Associates, Inc., Hypervelocity Wind Tunnel Components Structural Evaluation-Final Report, May 1979.
- A-2. Hill, J. A. F., Initial Operation of the NOL Hypervelocity Tunnel, AIAA Paper No. 74-608, Jul 1974.
- A-3. Brahinsky, H. S., and Neel, C. A., Tables of Equilibrium Thermodynamic Properties of Nitrogen, Volume IV, Aug 1969.

## APPENDIX B

## INITIAL HIRE DESIGN CONFIGURATION ANALYSES

## PRESSURE DROP CALCULATIONS

Several calculations were required to ascertain what pressure drop existed across the various insulation package components for an ablator failure condition. First, the pressure drop existing across the rarefaction wave moving through each section of the heater must be ascertained. This was done using the following equation, from Reference B-1:

$$\Delta p = P_H \gamma K_N \left( \frac{A_T}{A_D} \right) \quad (B-1)$$

where

$P_H$  = 22,000 psi--heater pressure

$K_N$  = product of the isentropic gas coefficient ( $\gamma$ ) and the nozzle discharge coefficient ( $K_N$ )

$A_T$  = 6.33 in<sup>2</sup>--maximum flow restrictor open area

$A_D$  = duct area through which the rarefaction wave is passing (in<sup>2</sup>)

Table B-1 contains values of  $K_N$  and  $A_D$  for various locations through the flow passage. The values listed for  $A_D$ --duct area, are based on the I.D. of the outer jacket at a particular location. Also given are values of  $\Delta p$ , used as the design values which the strength of the outer jackets must match.

Now a normalized rate of change of pressure in various sections of the heater can be estimated from:

$$\frac{1}{P_H} \frac{dp}{dt} \quad (B-2)$$

where

$P_H$  = 22,000 psi--heater pressure

$dp$  = initial pressure drop (from Table B-1)

$dt = .0016$ --time of initial pressure drop, from traces of pressure pulses obtained in earlier tunnel testing.

Substitution of values for  $dp$  from Table B-1 yield the values of  $1/P_H dp/dt$  given in Table B-2.

To estimate the effect perforating a liner will have on the pressure drop experienced by the liner, J. Hill, in a series of NSWC memos, concluded the pressure drop across a porous shell was equivalent to the dynamic head pressure of the gas moving through a vent hole.

In equation form:

$$\Delta p = \frac{1}{2} \rho V_h^2 \quad (B-3)$$

where

$\rho$  = density of gas in insulation volume (slugs/ft<sup>3</sup>)

$V_h$  = velocity of gas moving through a vent hole (ft/sec)

The velocity of gas moving through porous insulation is given as:

$$v = .9 \frac{V_i}{A} \frac{1}{\gamma} \frac{1}{P_H} \frac{dp}{dt} \quad (B-4)$$

where

$V_i$  = insulation volume (ft<sup>3</sup>)

$A$  = liner surface area (ft<sup>2</sup>)

$\gamma$  = isentropic exponent

For a perforated liner, the velocity at the hole is determined from:

$$V_h = \frac{v}{PC_D} \quad (B-5)$$

where

$P$  = porosity

$C_D$  = discharge coefficient = .6

Substitution of V from Equation (B-4) in Equation (B-5) yields:

$$V_h = .9 \frac{V_i}{A} \frac{1}{\gamma} \frac{1}{P_H} \frac{dp}{dt} \frac{1}{PC_D} \quad (B-6)$$

Now substituting for  $V_h$  in Equation (B-3) yields:

$$p = \frac{1}{2} \rho \left[ .9 \frac{V_i}{A} \frac{1}{\gamma} \frac{1}{P_H} \frac{dp}{dt} \left( \frac{1}{PC_D} \right) \right]^2 \left( \frac{1}{144} \right)^2 \quad (B-7)$$

The ratio of  $V_i/A$  is simply the insulation thickness. Thus having values of  $1/P_H dp/dt$ , the pressure drop across a given liner can be determined. Table B-2 contains values of  $\rho$ ,  $\gamma$ ,  $V/A$ , and  $p$ --porosity. The porosity value must be changed to account for the blockage effect of the Inconel screen, which is 46.2% porous that lies against the inner liner. The value of porosity used in Equation (B-7) is thus the net porosity shown in Table B-2.

Also given in Table B-2 are the values of pressure drop across various components. These are the values cited in the main report which are compared to component strength.

#### PRESSURE DROP CAPABILITY OF HEATER INTERNALS

##### Outer Jackets

Buckling pressure capabilities,  $P_{cr}$ , were calculated using the following equation from Reference B-2:

$$P_{cr} = .92 E \frac{R}{L} \left( \frac{t}{r} \right)^{\frac{5}{2}} \quad (B-8)$$

where

$E = 28 \times 10^6$  psi--Young's Modulus

$R$  = cylinder mean radius (in)

$L$  = cylinder length (in)

$t$  = cylinder wall thickness (in)



Table B-3 contains values of these parameters for the various outer jackets and the value of  $P_{CR}$  obtained. To ensure the values of  $P_{CR}$  are in the elastic range of the material, a buckling pressure  $P_E$ , corresponding to the yield strength of the material was calculated using:

$$P_E = \frac{\sigma_y \cdot t}{R} \quad (B-9)$$

where

$\sigma_y$  = yield strength (psi).

Also noted in Table B-3 are the pressure capabilities of the top cover plate of the main heater outer liner, and the support ring, which attaches the main heater insulation package to the bottom closure nut.

To determine the cover plate's pressure drop capability, the loading condition on the plate was approximated by the condition shown below. The plate is assumed to be simply supported on the outer edge and free on the inner edge. This loading condition is analyzed in Reference B-3. The following equation is used to determine the cover plate's  $P_E$ .

$$P_E = \frac{\sigma_y t^2}{k a^2} \quad (B-10)$$

where

$\sigma_y$  = yield strength of the material = 40,000 psi

$t$  = plate thickness = 1.75

$k$  = factor based on ratio of plate O.D. to I.D.  
(for O.D./I.D. = 23/8.75 = 2.6),  $k$  = .657

$a$  = outer radius = 11.5 in

Substitution yields:

$$P_E = \frac{40,000(1.75)^2}{.657(11.5)^2} = 1410 \text{ psi}$$

The top cover plate thus has a pressure drop capability of 1410 psi.

As can be seen from the values listed in Table B-3, there are instances where  $P_{cr}$  exceeds  $P_E$  for a given outer jacket. The values of buckling capability cited in the main report refer to the minimum value for a given outer jacket. That is, if  $P_E$  was less than  $P_{cr}$ , then  $P_E$  was used in the main report for comparisons to anticipated pressure loads.

#### Inner Liners

Equation (B-8) was also employed to calculate buckling capabilities of the inner liners. Recall that all inner liners were fabricated from Hastelloy, which has the following properties at 1800°F:

$$E = 20.7 \times 10^6 \text{ psi}$$

$$\sigma_y = 35,000 \text{ psi}$$

(1800°F is used as the inner liner temperature based on gas temperature measurements obtained in previous testing.)

The value of Young's Modulus was degraded 10% to account for the weakening effect of vent holes (Reference B-4). Thus, the value of Young's Modulus used in Equation (B-8) was  $18.6 \times 10^6$  psi.

Table B-4 contains pertinent parameters for the various inner liners. Also listed are values of  $P_{cr}$  and  $P_E$ . Note for the inner liners the minimum value of buckling capability cited in the main report is the  $P_{cr}$  value for each liner.

The vertical elbow and main heater inner liners also have top cover plates (perforated) whose strength must be ascertained. As was done for the main heater can's top plate, a pressure drop capability was calculated using Equation (B-10). The values for these components are also shown in Table B-4.

#### HEATER ELEMENT MODIFICATION

In order to maximize available hot gas, it was decided that the heater element base (recall Figure 33 from the main report) should be cut down. To assure operability of the component it was felt that the thermal input/material volume ratio should not be greater than that experienced in Mach-14 testing.

The thermal input is proportional to the power applied, and the length of time it is applied. In equation form:

$$TI \propto P \cdot T$$

(B-11)

For Mach-14, the power level is .6 megawatts and the time is 17 minutes. For Mach-10, the power level will remain .6 megawatts, but the heating time is only 10 minutes due to the lower gas temperature required.

The heater element volume is simply the cross sectional area times the length, or

$$V = A \cdot L \quad (B-12)$$

The cross sectional area remains the same for Mach-10 and Mach-14. The length of the Mach-14 heater element base is 23.5 inches. Combining Equations (B-11) and (B-12) and rearranging yields:

$$\frac{TI}{V} \propto \frac{PT}{AL} \quad (B-13)$$

or

$$\left[ \left( \frac{PT}{AL} \right) \right]_{\text{Mach-14}} = \left[ \left( \frac{PT}{AL} \right) \right]_{\text{Mach-10}} \quad (B-14)$$

Substitution of known values in Equation (B-14) determines the minimum allowable Mach-10 heater element base length.

$$\left[ \frac{.6(17)}{A(23.5)} \right]_{\text{Mach-14}} = \left[ \frac{.6(10)}{A \cdot L} \right]_{\text{Mach-10}}$$

$$L = 13.8 \text{ inches}$$

The actual length chosen was 14 inches.

TABLE B-1. PRESSURE DROP ACROSS RAREFACTION WAVE IN VARIOUS AREAS OF THE HEATER

LOCATION		$\gamma K_N$	$A_D$ (IN <sup>2</sup> )	$\Delta P$ (PSI)
HORIZONTAL ELBOW		2.29	20.67	15,428
VERTICAL ELBOW	LOWER	2.50	63.62	5,472
	UPPER	2.50	41.28	8,431
MAIN HEATER		1.95	380.65	714

TABLE B-2. PRESSURE DROPS ACROSS INNER LINERS

COMPONENT	$\frac{1}{P_H} \frac{dp}{dt}$ $\left(\frac{1}{\text{SEC}}\right)$	$\rho$ $\left(\frac{\text{SLUGS}}{\text{FT}^3}\right)$	$\gamma$	$\frac{V_i}{A}$ (IN)	POROSITY	NET POR. (POR. x 462)	$\Delta P$ (PSI)
HORIZONTAL ELBOW LINER	438	0.978	2.943	0.25	0.05	0.0231	138
VERTICAL ELBOW LINER	239	0.839	2.43	TOP 1.625	0.15	0.0693	242
				BOT 0.75	0.15	0.0693	52
VERTICAL ELBOW TOP PLATE	239	0.839	2.43	$\frac{2.25}{2}$ (4.5" DIA)	0.15 (ON SIDES)	0.0693	464
MAIN HEATER LINER	20	0.714	2.25	1	0.02	0.00924	36
MAIN HEATER TOP PLATE	20	0.714	2.25	2.5	0.052	0.0240	33

TABLE B-3. OUTER JACKET PRESSURE CAPABILITIES

COMPONENT		R (IN)	L (IN)	t (IN)	$\sigma_y$ (PSI)	P <sub>CR</sub> (PSI)	P <sub>E</sub> (PSI)
MAIN HEATER OUTER JACKET		11.25	106.5	0.49	40,000	1080	1740
VERTICAL ELBOW OUTER JACKET	LOWER	3.88	55.5	0.50	80,000	10,735	10,310
	UPPER	4.75	20.0	0.44	100,000	15,980	9260
HORIZONTAL ELBOW OUTER JACKET		2.78	42.0	0.44	100,000	16,990	15,827
TOP COVER PLATE		K = 0.657		1.75	40,000	—	1410

TABLE B-4. INNER LINER PRESSURE CAPABILITIES

COMPONENT	R (IN)	L (IN)	t (IN)	$\sigma_y$ (PSI)	$P_{CR}$ (PSI)	$P_E = \frac{\sigma_y t}{R}$ (PSI)	$\Delta P$
MAIN HEATER INNER LINER	9.97	100.0	0.187	16,000	82	300	36
	TOP PLATE	K = 0.75	0.5	16,000	NA	54	33
VERTICAL ELBOW INNER LINER	2.78	80.0	0.187	16,000	700	1076	242
	TOP PLATE	K = 0.75	0.5	16,000	NA	690	464
HORIZONTAL ELBOW INNER LINER	2.22	45.2	0.187	16,000	1730	1347	138

REFERENCES

- B-1. Hill, J. A. F., Initial Operation of the NOL Hypervelocity Tunnel, AIAA Paper No. 74-608, Jul 1974.
- B-2. Baker, E. H., Shell Analysis Manual, NASA Contractor Report CR-912, Apr 1968.
- B-3. Timoshenko, Y., Theory of Plates and Shells, Second Edition, (New York: McGraw-Hill, 1968).
- B-4. Horvay, "The Plain Stress Problem of Perforated Plates," Journal of Applied Mechanics, Volume 19, 1962.

## APPENDIX C

## DEPRESSURIZATION TEST SERIES

The inner liner of the main heater insulation package is perforated with many vent holes. These holes vent the insulation area behind the liner to the heater core. The venting must take place to prevent the collapse of the inner liner when the heater core is rapidly depressurized during a tunnel run. This depressurization and venting tends to blow insulation out through the vent holes into the heater core.

The tests described in this appendix involved the measurement of the pressure of a gas within a porous insulation specimen, contained inside a test apparatus. The test apparatus had been designed to simulate a unit volume of insulation being vented through a single hole. The objective of the test series was to obtain an estimate of the maximum pressure that could be discharged through a vent hole without causing damage to the insulation in the vented area.

Tests were conducted on Lo-Con Felt and Graphite Felt insulation types. The Lo-Con Felt insulation was also tested using a Nichrome Wire Fiber Cloth as a damage protector, between the insulation and the test apparatus vent hole, in one test series; and a Wire Screen as a damage protector in another test series.

## DEPRESSURIZATION SIMULATION

The heater depressurization effect which is being modeled will now be described. Figure C-1 shows a cross sectional view of the vertical heater for the Hypervelocity Wind Tunnel #9. The heater insulation and the insulation liners are shown more clearly in Figure C-2. This insulation-liner package consists of a perforated graphite inner liner, a graphite felt insulation, and a stainless steel outer liner. The insulation-liner package isolates the pressure vessel from the hot nitrogen gas in the heater core.

When the heater vessel is initially loaded with nitrogen, and the nitrogen is subsequently heated, the gas in the insulation is in pressure equilibrium with the heater core gas. In order to start a tunnel run, diaphragms are burst allowing the high pressure nitrogen gas to flow into an evacuated test cell. The bursting of the diaphragms causes a rarefaction wave to propagate back into the heater vessel. The rarefaction wave is mitigated by a flow restrictor. In the event of a flow restrictor failure, a severe rarefaction wave would be allowed to enter the heater vessel, causing a more rapid depressurization of the heater core.

High pressure gas from the driver vessels flows through a set of control valves to the bottom of the heater. This high pressure "Driver" gas pushes the heated gas out of the heater vessel and down the tunnel. At the end of a tunnel run the control valves close shutting off the supply of driver gas to the heater vessel. The closing of the control valves causes the heater core to be depressurized. In normal operation the control valves are closed slowly enough so that this depressurization is not too rapid. In the event of a control valve failure the valves might slam shut causing the heater core to depressurize rapidly. During this rapid depressurization of the heater core the high pressure gas in the insulation material must be vented to the heater core. The insulation material is typically 90 percent porous. The venting must take place to prevent the collapse of the inner liner due to external pressure, and to prevent the distortion of the insulation blanket as the escaping nitrogen gas flows through it. The inner liner vent holes are shown in Figure C-2. These vent holes are nominally .25 inches in diameter and spaced about 2 inches apart in a diamond pattern.

A primary concern was that the insulation may be pulled through the vent holes due to the depressurization. It is this depressurization of the insulation area through the vent holes that is being modeled. The test apparatus, described herein, attempts to model a single vent hole and the insulation volume vented by that hole.

A distinction is made between the "insulation porosity" and the "liner porosity." The insulation porosity is a ratio of the void volume to the total volume occupied by a given sample of insulation. A typical value for the insulations we are interested in is an insulation porosity of about 90 percent. For the heater vessel the liner porosity is the ratio of the total open area of all the vent holes to the liner surface area. In the case of the test apparatus, the liner porosity is the ratio of the open area of the single vent hole to the surface area of the seal piece, which acts as the insulation liner.

The testing apparatus we will be using to model the heater will use nitrogen gas at ambient temperature. Thus, in order to relate the hot gas in the heater to the cold gas in the testing apparatus a scaling relationship between the two is needed. This relationship was obtained between the densities of the gasses using Equations (B-1) then (B-6) from Appendix B. They resulted in the following relationship:

$$\rho_T = \rho_H \left( \frac{V_{h_H}}{V_{h_T}} \right)^2 \quad (C-1)$$

Since the test apparatus will have a ratio of atmospheric pressure to supply pressure less than .53, we can assume that the velocity of gas through the hole of the test apparatus,  $V_{h_T}$ , is the sonic velocity for choked flow, or approximately 1120 feet per second (based on nitrogen at atmospheric conditions).  $V_{h_T}$  can be calculated from Equation (B-6); and  $\rho_H$  can be obtained from nitrogen tables. Using these values for  $V_{h_T}$ ,  $V_{h_H}$ ,  $\rho_H$ , and Equation (C-1), the density of the gas through the hole of the test fixture,  $\rho_T$ , can be obtained.



In the test apparatus, a distinction is made between the properties of the gas at the vent hole and the properties of the gas in the insulation. Figure C-3 illustrates these two areas of test apparatus. The properties of the gas at the vent hole will be designated with a subscript "T", and the gas properties in the insulation designated with a subscript "S".

Assuming adiabatic flow from the insulation through the hole of the test apparatus, we have,

$$\frac{P_T}{P_S} = \left( \frac{\rho_T}{\rho_S} \right)^k = .53 \quad (C-2)$$

where

$p$  = pressure

$\rho$  = density

$k$  = specific heat ratio for nitrogen gas = 1.4

Knowing  $\rho_T$  from Equation (C-1), the density of the gas in the insulation can be obtained from Equation (C-2) as,

$$\rho_S = \frac{1}{.53^{1/k}} \rho_T \quad (C-3)$$

Now, using the ideal gas law, an expression for the pressure in the insulation is

$$P_S = \rho_S RT \quad (C-4)$$

where

$R$  = universal gas constant

$T$  = temperature of gas

In carrying out the tests described in this report, the pressure in the insulation was measured. Using this test pressure, and working backwards from Equations (C-4) through (C-1), a test apparatus pressure can be related back to physical characteristics of the hot gas located in the insulation material.

## TEST HARDWARE AND INSTRUMENTATION

Lo-Con Felt Insulation

Carborundum Fiberfrax ceramic fiber Lo-Con felt insulation; density of 6 lbs/ft<sup>3</sup>.

Graphite Felt Insulation

National Carbon Graphite felt insulation; grade WDF.

Nichrome Wire Fiber Cloth

Carborundum Fiberfrax cloth, type L-114T, 1/8" thick.

Wire Screen

20 x 20, 38 gauge (.016") wire, open area 46.2%.

The test apparatus used to simulate the venting of the heater vessel insulation is shown in Figures C-3 and C-4. While describing the test apparatus and its components, part numbers will be referred to. These numbers refer to the various parts of the test apparatus shown in Figure C-3.

The internal volume of the test apparatus was much greater than the unit insulation volume which was to be simulated, so a filler piece, 3, was inserted into the bore of the apparatus. This filler piece simply decreased the volume of pressurized nitrogen gas within the test apparatus. Nitrogen gas entered the base through an inlet pipe, 1, at one end of the filler piece. The gas then flowed between the outer diameter of the filler piece and the inner diameter of the apparatus main body, 2, into a chamber at the front of the filler piece. The insulation samples to be tested were located in this chamber. The size of the chamber could be changed by adding a volume change piece, 4. The volume change piece was inserted into the insulation test chamber to vary the volume of insulation vented. By changing this volume relative to the vent hole diameter, the liner porosity of each test could be changed. The insulation test chamber was 2-1/4 inches in diameter. By inserting the volume change piece the chamber diameter was decreased to 1-1/4 inches. The seal piece, 5, had two functions. First, the O-ring on its outer diameter sealed the nitrogen gas in the insulation chamber. Second, the hole in the center of the seal piece served as the liner vent hole for the insulation chamber. By using seal pieces with different diameter center holes, we had another way to vary the liner porosity for each test. The two seal pieces used had center holes of 1/4 inch and 3/8 inch diameter. By using the two seal pieces and the volume change piece liner, porosities of 1.2, 2.7, 4.0, and 9.0 percent were obtained. An O-ring and a thin diaphragm were used to seal the test gas at the center hole of the seal piece. The diaphragm, 8, was located between the seal piece, 5, and the diaphragm holder piece, 9. The diaphragms ranged from one layer of the aluminum foil to several layers of brass shim stock depending on the test pressure to be

sealed. The diaphragm holder piece, 9, was used to hold the diaphragm in place against the seal piece. The diaphragm holder was made sufficiently wide so that when the lock-up nut, 10, was threaded onto the main body, all of the various pieces were in compression. This compression held the diaphragm in place against the seal piece.

Figure C-5 shows a schematic of the insulation test apparatus set up. A needle valve was installed in a series with the test apparatus so that the pressure within the test apparatus could be increased in small increments. A pressure gauge installed near the needle valve indicated the pressure within the test apparatus. By increasing the pressure slowly with the needle valve and observing the pressure gauge the burst pressure of the diaphragm could be recorded.

#### PROCEDURE

The same test procedure was followed for all insulation tests. Four layers of insulation were placed in the test chamber. These four layers of insulation made up one insulation test specimen. Each layer of insulation was .50 inch thick. The test chamber was 1.44 inches deep. Thus, the insulation test specimen was compressed about 40% in the test chamber. This compression simulated the conditions which exist in the heater liner. If the test required a fiber cloth or wire screen protection it was compressed into the test chamber after the last sample of insulation. The O-rings on the seal piece were then lubricated with vacuum grease and the seal piece was inserted into the test apparatus. The seal piece covered the test chamber and insulation specimen. The diaphragm was then placed against the seal piece. The diaphragm was held temporarily in place by the vacuum grease until the diaphragm holder piece could be inserted to hold it. All of the pieces were held in place by a lock-up nut which was threaded into the end of the test apparatus.

The pressure in the test chamber was slowly increased until the diaphragm burst. The diaphragm burst simulated the venting of the insulation area in the heater vessel. The burst pressure for each test was recorded. This burst pressure became the test pressure for that particular insulation test specimen. The test apparatus was then disassembled in the reverse order of the above procedure, using the disassembly screws to remove the seal piece. The insulation samples were removed from the chamber and examined for damage. New insulation samples were fitted into the chamber and the procedure was started again.

The simulated liner porosity could be varied from 1.2% to 9.0% by replacing the seal piece with a seal piece having a different size vent hole. In addition, the volume change piece could be removed thereby allowing larger insulation specimens to be installed. This was done in order to increase the insulation volume being vented and thus change the simulated liner porosity.

#### DATA AND RESULTS

A log of the test pressures, the calculated heater depressurization rates and the results of the tests on the insulation are given in Tables C-1 through C-4. The run numbers in the first column of each table were for record keeping purposes.

Test runs marked with the symbol (\*) in Tables C-1 through C-4 indicate the the highest test pressure at which that insulation showed no damage, for that particular liner porosity. This maximum "no damage" data was used to plot "no damage" curves of depressurization rate versus porosity. The depressurization rates were obtained from the experimental test pressures according to the calculation shown in the Data Reduction section.

The curves of depressurization rate capability versus liner, i.e., "no damage curves," for all four insulation configurations are shown in Figure C-6. For the curves plotted in Figure C-6 the areas below and to the right of the curves represent combinations of values of liner porosity and depressurization rate that caused damage to test specimens.

## DISCUSSION

### Test Pressure Data

The maximum uncertainty of the pressure gauge used in the test series was measured at  $\pm 1/10$  percent error over the range of the gauge. The gauge used had a range of 5000 psia and was incremented at 5 psia per division.

The test pressures were measured at diaphragm burst. Due to slight differences from diaphragm to diaphragm it was impossible to burst the diaphragm at a desired pressure. The different test pressures were obtained by a "trial and error" method which consisted of changing the diaphragm size and material.

The plotted pressure data shown in Figure C-6 indicates that the Lo-Con insulation is the least resistant to depressurization effects. The safe "no damage" threshold limits vary from  $2.2 \times 10^6$  psi per second depressurization rate (85 psi) at 1.2% liner porosity to  $1.1 \times 10^7$  psi per second (40 psi) at 9.0% liner porosity.

Of the four insulation configurations tested, the Lo-Con Felt with steel screen protection appeared to be the most resistant to depressurization effects. The threshold limits ranged from  $2.71 \times 10^6$  psi per second (600 psi) at 1.2% liner porosity to  $1.52 \times 10^7$  psi per second (335 psi) at 9.0% liner porosity.

All four of the threshold curves shown in Figure C-6 seem to be "flattening out" near the maximum liner porosity. This indicates that a further increase in liner porosity would not yield an increase in depressurization rate. As the liner porosity is increased the diameter of the vent hole is increased relative to the diameter of the unit area of insulation that it is venting. As the diameter of the vent hole increases, the area of "unsupported" insulation also increases. "Unsupported" insulation is that insulation which covers the open vent hole area. This increased "unsupported" insulation seems more likely to be pulled through the vent hole (damaged) during depressurization, even though the liner porosity is increasing. For this reason, it should be noted that the tests described in this report, whose results are shown in Figure C-6 and Tables C-1 through C-4, are based on vent hole diameters of 1/4 inch and 3/8 inch to

obtain the various liner porosities. Applying these results to cases where the liner porosity is identical but the vent holes are larger or smaller is not recommended since the "unsupported area" of insulation changes.

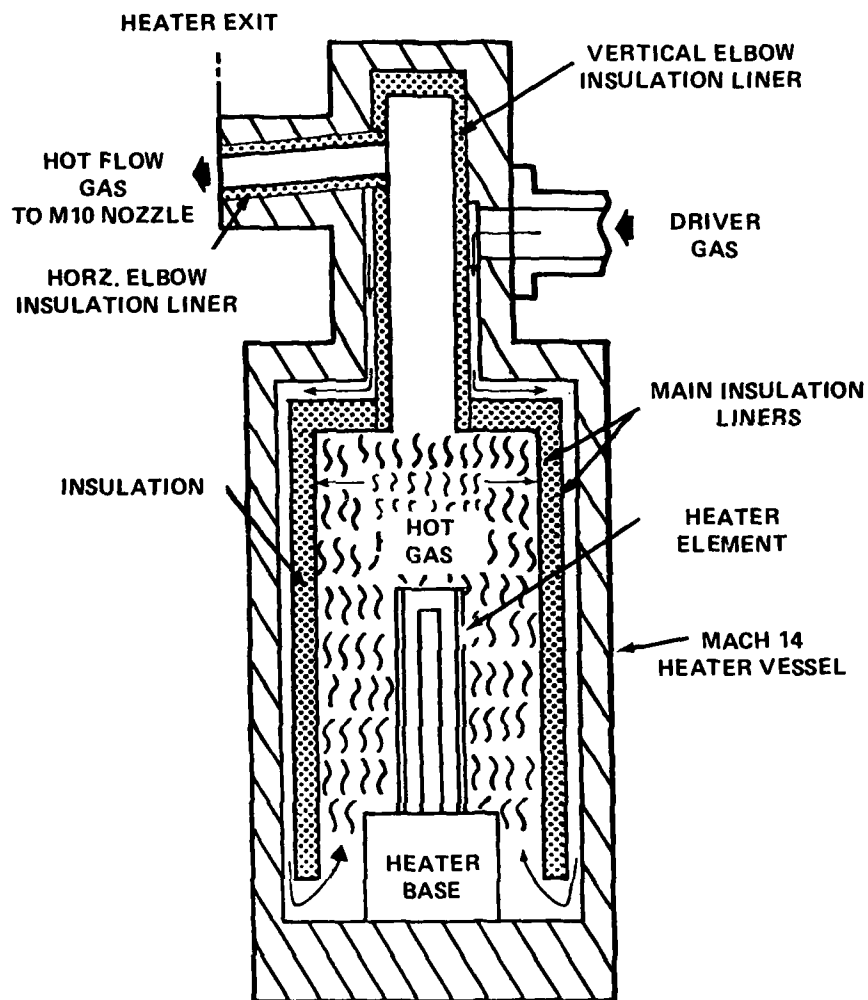
The Lo-Con Felt with wire screen protection configuration, shown in Figure C-6, has been tested at lower liner porosities than the other three insulation configurations. This difference is due to the wire screen present in this configuration. The wire screen used has an open area of 46.2 percent, thus reducing the linear porosity. This reduced liner porosity has been taken into account in Figure C-6, and also in calculating the depressurization rates for this configuration shown in Table C-3.

In addition to showing the expected depressurization capability versus liner porosity for the various insulation configurations tested, Figure C-6 also shows the anticipated Mach-10 HIRE operating conditions ( $2.4 \times 10^5$  psi/sec at 2% liner porosity). A worst case operating configuration for Mach-10 HIRE ( $9.6 \times 10^6$  psi/sec at 2% liner porosity) is also shown.

As can be seen from Figure C-6, all four of the insulation configurations tested appear to be capable of surviving the anticipated Mach-10 HIRE operating conditions. In addition, Figure C-6 shows that the Lo-Con with wire screen is the only configuration of those tested which is capable of surviving the worst-case operating conditions for Mach-10 HIRE.

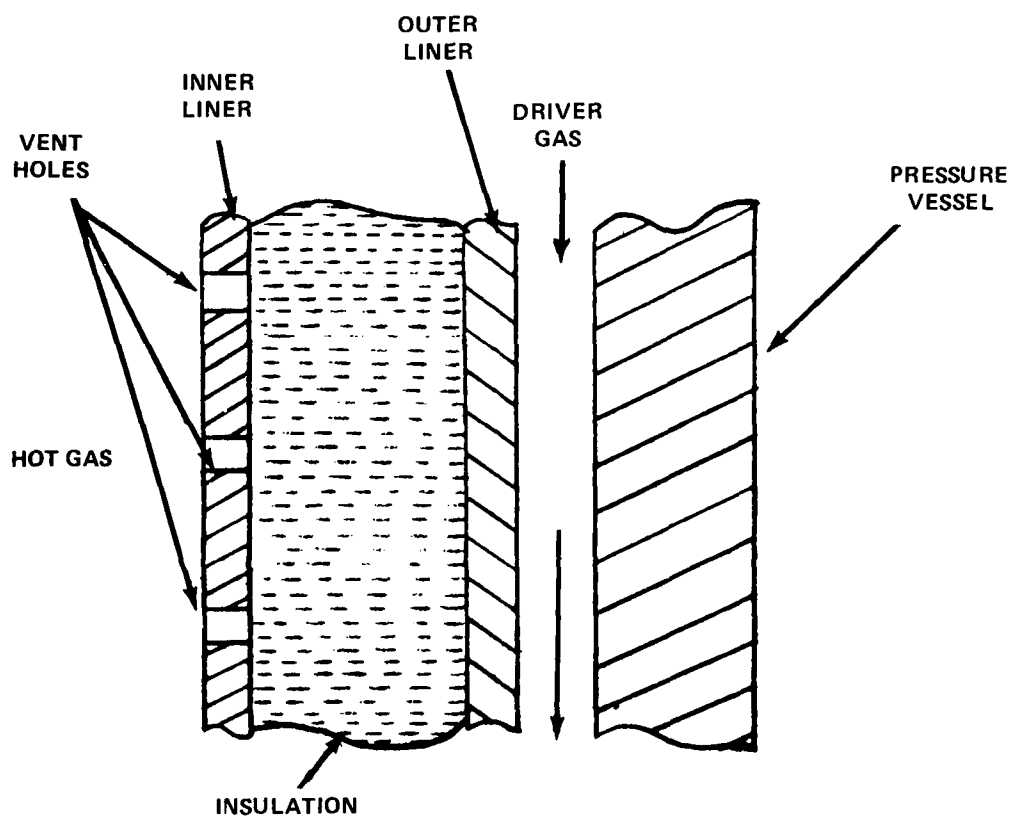
## CONCLUSIONS

The results of these tests indicate that the Lo-Con Felt insulation is the least resistant to depressurization damage. The "no damage" depressurization limits range from  $2.2 \times 10^6$  psi/sec at a 1.2% liner porosity to a limit of  $11.0 \times 10^7$  psi/sec at a 9.0% linear porosity. The test results also indicated that the Lo-Con Felt with steel wire screen protection was the insulation configuration that was most resistant to depressurization damage. The "no damage" depressurization limits for this configuration ranged from  $2.71 \times 10^6$  psi/sec at a 1.2% liner porosity to a limit of  $15.2 \times 10^6$  psi/sec at a liner porosity 9.0%.



HEATER VESSEL CROSS SECTION

FIGURE C-1. CROSS SECTION VIEW OF VERTICAL HEATER AND HEATER LINERS



INSULATION LINER CROSS SECTION

FIGURE C-2. CROSS SECTION VIEW OF VERTICAL HEATER AND HEATER LINES

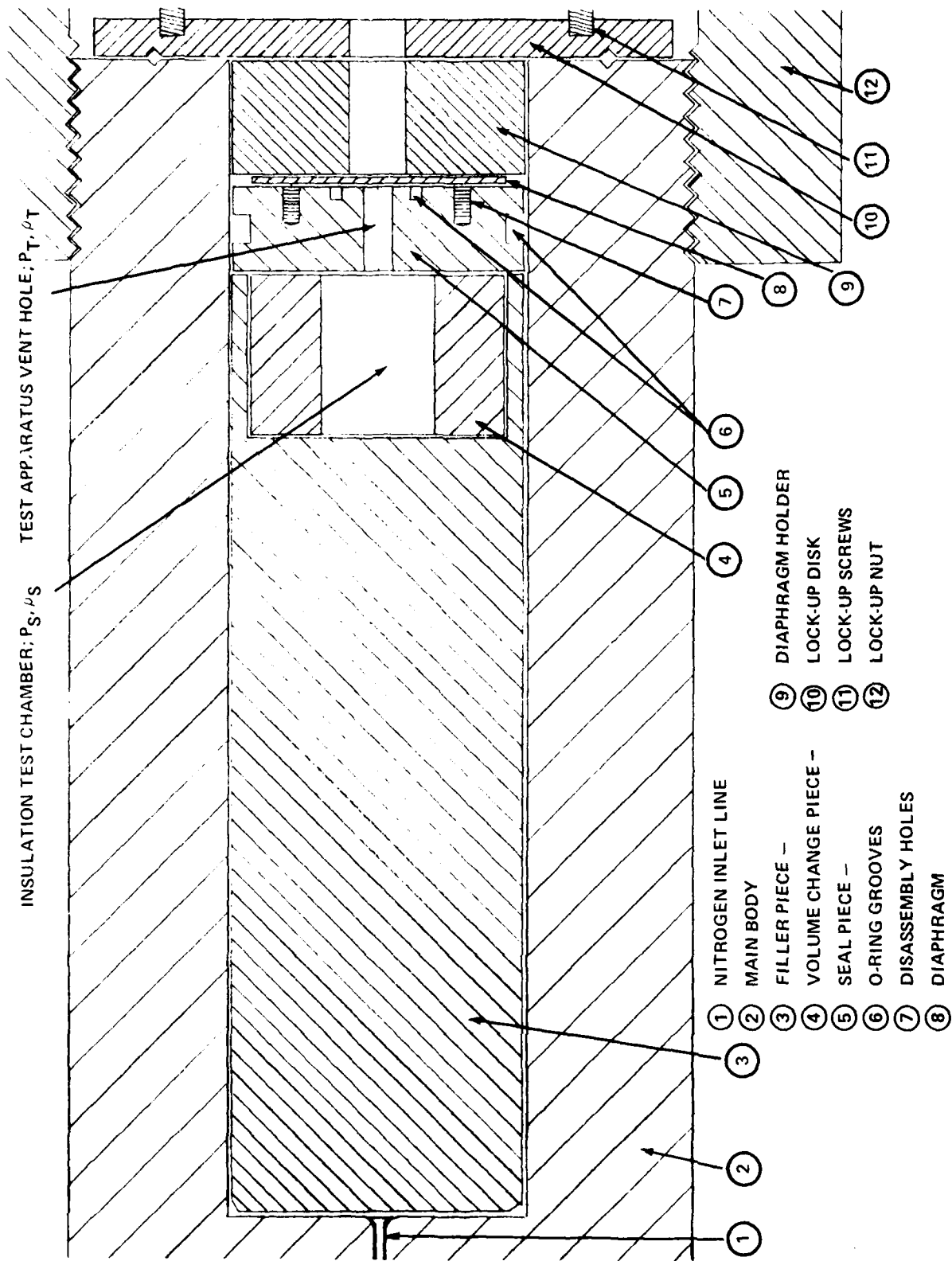


FIGURE C-3: CROSS SECTION VIEW OF INSULATION TEST APPARATUS



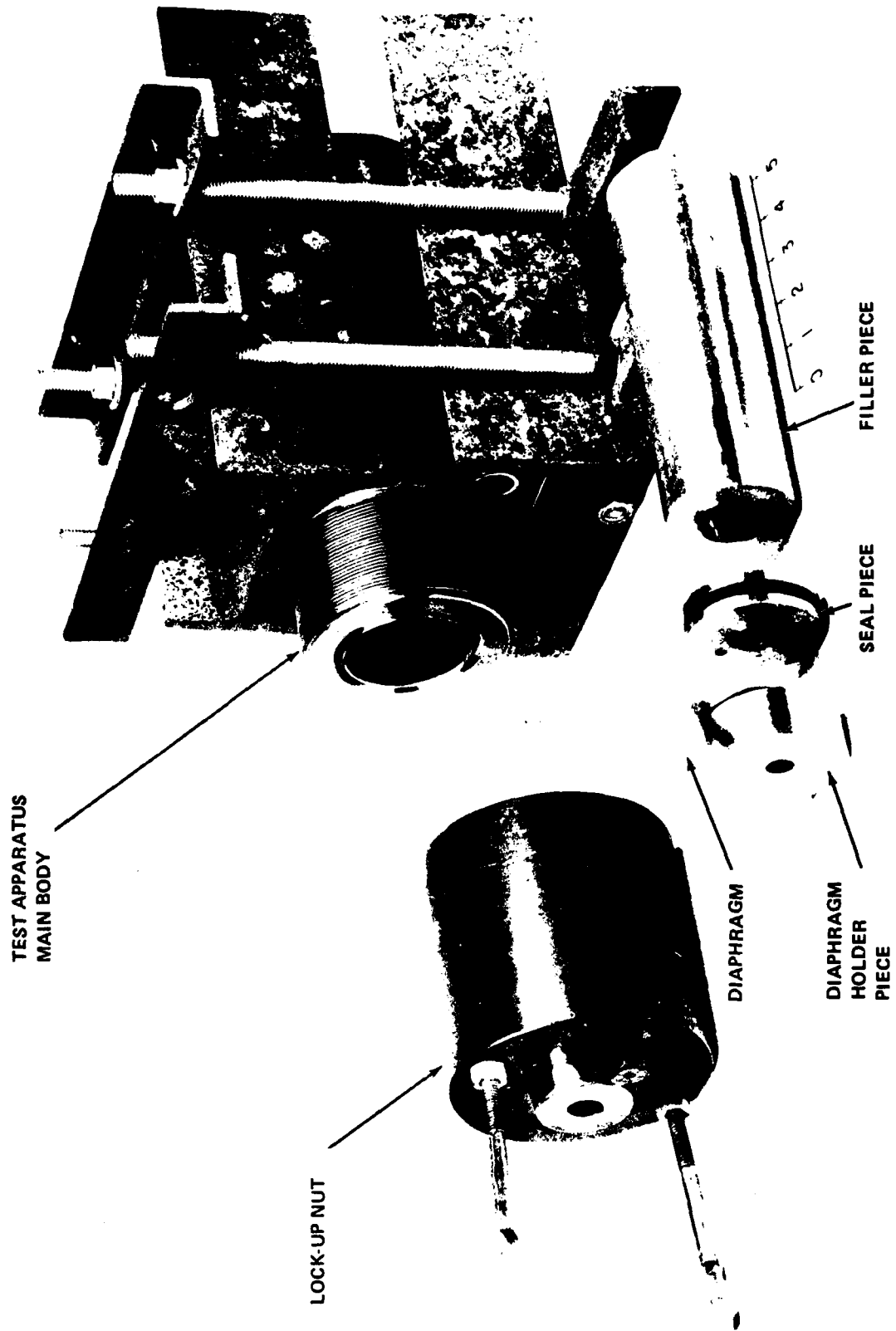


FIGURE C-4. INSULATION TEST APPARATUS

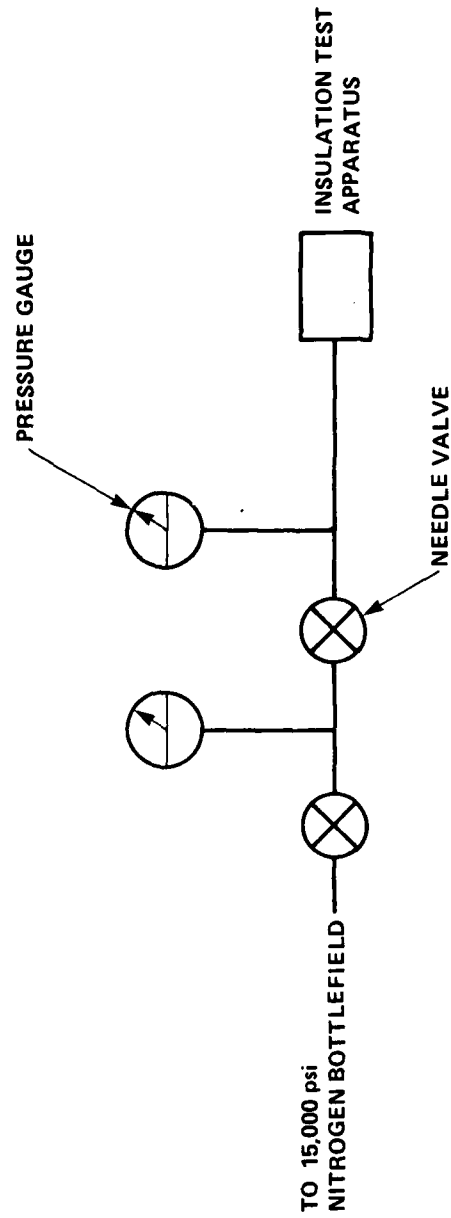


FIGURE C-5. INSULATION TEST APPARATUS SCHEMATIC

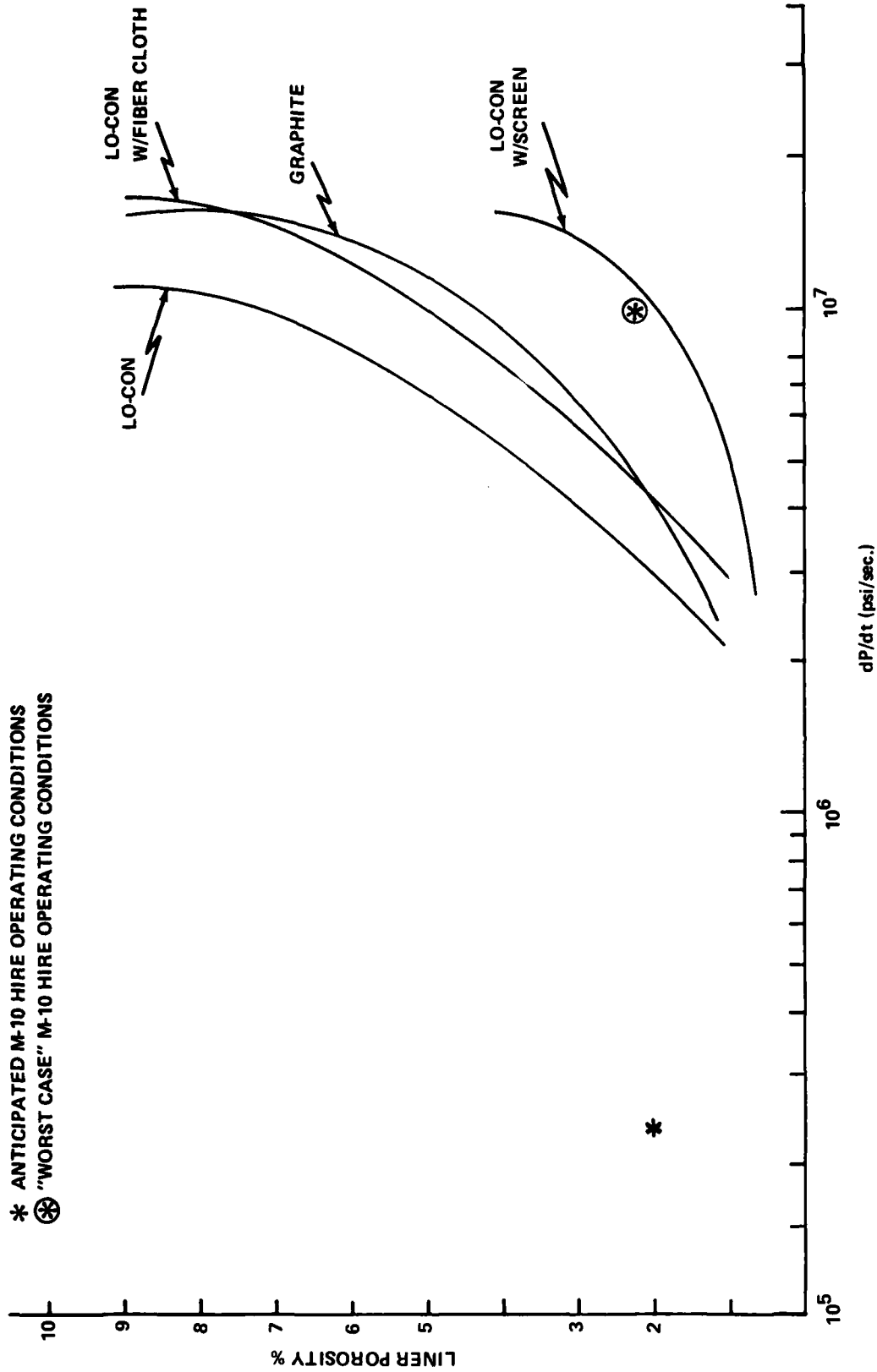


FIGURE C-6. MAXIMUM "NO DAMAGE" THRESHOLD PLOTS OF DEPRESSURIZATION RATE VS. LINER POROSITY

TABLE C-1. TEST DATA--LO-CON FELT INSULATION

RUN #	LINER POROSITY (%)	TEST PRESSURE (PSI)	DEPRESSURIZATION RATE (PSI/SEC)	INSULATION CONDITION AFTER TEST
5	1.2	30	$1.338 \times 10^6$	NO DAMAGE
6	1.2	85	$2.253 \times 10^6$	NO DAMAGE*
7	1.2	120	$2.677 \times 10^6$	DAMAGED
8	1.2	280	$4.089 \times 10^6$	DAMAGED
1	2.7	175	$7.275 \times 10^6$	DAMAGED
2	2.7	40	$3.478 \times 10^6$	NO DAMAGE*
9	4.0	20	$3.643 \times 10^6$	NO DAMAGE
10	4.0	45	$5.465 \times 10^6$	NO DAMAGE*
11	4.0	75	$7.055 \times 10^6$	DAMAGED
12	4.0	180	$1.093 \times 10^7$	DAMAGED
13	4.0	375	$1.577 \times 10^7$	DAMAGED
14	4.0	475	$1.775 \times 10^7$	DAMAGED
3	9.0	40	$1.159 \times 10^7$	NO DAMAGE*
4	9.0	245	$2.869 \times 10^7$	DAMAGE

\*INDICATES HIGHEST TEST PRESSURE AT WHICH INSULATION SHOWED NO DAMAGE

TABLE C-2 TEST DATA - LO-CON FELT INSULATION WITH NICHROME FIBER CLOTH PROTECTION

RUN #	LINER POROSITY (%)	TEST PRESSURE (PSI)	DEPRESSURIZATION RATE (PSI/SEC)	INSULATION CONDITION AFTER TEST
20	1.2	80	$3.361 \times 10^6$	NO DAMAGE*
21	1.2	250	$6.057 \times 10^6$	DAMAGED
22	2.7	265	$8.952 \times 10^6$	DAMAGED
23	2.7	100	$5.500 \times 10^6$	NO DAMAGE*
24	4.0	340	$1.502 \times 10^7$	DAMAGED
25	4.0	95	$7.940 \times 10^6$	NO DAMAGE*
26	9.0	105	$1.878 \times 10^7$	NO DAMAGE*
27	9.0	200	$2.581 \times 10^7$	DAMAGE

\*INDICATES HIGHEST PRESSURE AT WHICH INSULATION SHOWED NO DAMAGE

TABLE C-3. TEST DATA - LO-CON FELT INSULATION WITH STEEL SCREEN PROTECTION

RUN #	LINER POROSITY (%)	TEST PRESSURE (PSI)	DEPRESSURIZATION RATE (PSI/SEC)	INSULATION CONDITION AFTER TEST
100	0.5	295	$1.93 \times 10^6$	NO DAMAGE
101	0.5	365	$2.14 \times 10^6$	NO DAMAGE
102	0.5	480	$2.46 \times 10^6$	NO DAMAGE
103	0.5	750	$3.03 \times 10^6$	DAMAGED
104	0.5	600	$2.71 \times 10^6$	NO DAMAGE*
105	1.3	785	$7.06 \times 10^6$	DAMAGED
106	1.3	585	$6.09 \times 10^6$	DAMAGED
107	1.3	445	$5.26 \times 10^6$	DAMAGED
108	1.3	390	$4.89 \times 10^6$	NO DAMAGE*
15	1.8	465	$8.11 \times 10^6$	NO DAMAGE
16	1.8	785	$1.05 \times 10^7$	NO DAMAGE*
109	1.8	795	$1.04 \times 10^7$	DAMAGED
110	1.8	625	$9.24 \times 10^6$	NO DAMAGE
17	1.8	1,065	$1.22 \times 10^7$	DAMAGED
18	4.1	500	$1.88 \times 10^7$	DAMAGED
19	4.1	1,090	$2.79 \times 10^7$	DAMAGED
111	4.1	955	$2.60 \times 10^7$	DAMAGED
112	4.1	465	$1.81 \times 10^7$	DAMAGED
113	4.1	390	$1.61 \times 10^7$	DAMAGED
114	4.1	335	$1.52 \times 10^7$	NO DAMAGE*

\*INDICATES HIGHEST TEST PRESSURE AT WHICH INSULATION SHOWED NO DAMAGE

TABLE C-4. TEST DATA - GRAPHITE FELT INSULATION

RUN #	LINER POROSITY (%)	TEST PRESSURE (PSI)	DEPRESSURIZATION RATE (PSI/SEC)	INSULATION CONDITION AFTER TEST
7	1.2	275	$4.05 \times 10^6$	DAMAGED
8	1.2	95	$2.38 \times 10^6$	NO DAMAGE*
9	1.2	65	$1.97 \times 10^6$	NO DAMAGE
10	1.2	30	$1.36 \times 10^6$	NO DAMAGE
11	2.7	200	$7.74 \times 10^6$	DAMAGED
12	2.7	120	$6.05 \times 10^6$	NO DAMAGE*
1	4.0	30	$4.46 \times 10^6$	NO DAMAGE
2	4.0	70	$7.49 \times 10^6$	NO DAMAGE
3	4.0	165	$1.04 \times 10^7$	NO DAMAGE*
4	4.0	280	$1.36 \times 10^7$	DAMAGED
5	4.0	350	$1.52 \times 10^7$	DAMAGED
6	4.0	1,050	$2.64 \times 10^7$	DAMAGED
120	4.0	275	$1.32 \times 10^7$	DAMAGED
121	4.0	155	$9.96 \times 10^6$	NO DAMAGE
122	9.0	70	$1.5 \times 10^7$	NO DAMAGE*
123	9.0	120	$3.14 \times 10^7$	DAMAGED

\*INDICATES HIGHEST PRESSURE AT WHICH INSULATION SHOWED NO DAMAGE

## APPENDIX D

## NOZZLE THROAT ANALYSIS

## INTRODUCTION

The existing M-10 Nozzle Throat Insert has been proposed for use in the M-10 HIRE program at conditions of  $T_0 = 1500^\circ\text{F}$ ,  $P_0 = 20,000$  psi. The M-10 Nozzle Throat Insert was originally designed for use at nominal M-10 conditions of  $T_0 = 1500^\circ\text{F}$ ,  $P_0 = 7000$  psi. Concerns arose regarding the structural capability of the insert to handle the increased  $P_0$  and higher heating rates imposed on the insert under M-10 HIRE operating conditions. In response to these concerns a finite element thermostructural analysis was performed using the anticipated M-10 HIRE loading conditions. The results of this elastic analysis indicated compressive stresses exceeding the material yield strength in a narrow band along the inner radius of the insert during a 0.5 second period of a "simulated" tunnel run. Although it was felt that these extremely localized stresses would not cause any severe permanent plastic deformation of the nozzle insert wall, it was desired to see how these stresses compared to the stresses already experienced by the nozzle throat insert under prior M-10 use. Due to the need for further information, an elastic/plastic finite element thermostructural analysis has been performed utilizing the M-10 design conditions of  $T_0 = 1,500^\circ\text{F}$ ,  $P_0 = 7000$  psi. In addition, the M-10 HIRE case has been redone using an elastic/plastic analysis. This appendix summarizes and compares the results of these two analyses.

## METHOD OF ANALYSIS

Figure D-1 shows the finite element model with the boundary elements numbered. Nitrogen gas properties were obtained as a function of temperature and pressure at each time step during the "simulated" 2-second tunnel run. Figure D-2 shows the assumed variation of the gas temperature and pressure during the "simulated" M-10 run. Figure D-3 shows the variation for the "simulated" M-10 HIRE run. Using the gas properties, convective film coefficients were calculated as a function of time at the throat with the equation:

$$h = .023 \frac{k}{d} (Re)^{.8} (Pr)^{.4} \quad (D-1)$$



where

$k$  is the Thermal Conductivity of Nitrogen (BTU/in-sec-°F),

$d$  is the M-10 Throat Diameter (2.4 inches),

$Re$  is the Renyolds number,

$Pr$  is the Prandtl number.

Table D-1 shows a comparison of the convective film coefficients calculated using M-10 (Design) and M-10 HIRE conditions. The comparison shows the M-10 HIRE coefficients to be an average of 3.5 times greater than the M-10 design coefficients. The convective film coefficients at nozzle insert positions away from the throat were scaled by area. Thus, the film coefficients are a function of time and position. The convective film coefficients were input to a heat conduction computer code (OATS) to yield temperatures as a function of time at the nodes of the finite element model. Table D-1 shows the assumed gas temperature and the temperature predicted by the computer code at the throat wall. This table reinforces the intuitive result that the M-10 HIRE throat wall temperatures are higher due to increased heating rates from the higher mass flow rate. The temperatures predicted by the OATS computer code were used as input to a finite-element stress analysis code (DOASIS). Pressure boundary conditions for the M-10 design case of  $P_0$  equal to 7000 psi were used. The maximum pressure was applied statically in all cases. Using the pressure and temperature inputs to the stress analysis code it was possible to get results:

- a. Due to pressure loading only,
- b. Due to thermal loading only,
- c. Combined pressure and thermal loading.

In all cases where applicable elastic/plastic solutions were obtained. The elastic/plastic solution gives results which are much more realistic than elastic results only.

## RESULTS

A summary and comparison of the results obtained from the elastic/plastic DOASIS stress analyses are shown in Tables D-2 and D-3. For each case that was run the summary shows whether local yielding occurred, where it occurred (element numbers refer to the finite element model of Figure D-1), and the stress magnitude, location, yield strength of the particular finite element under greatest stress (max). The summary also shows results due to pressure loading only, thermal loading only (at time of maximum predicted wall temperatures), and combined pressure and thermal loading at particular times during a tunnel run.

Pressure Loading Only

As shown in Table D-3 the maximum stresses ( $\sigma_{max}$ ) due to pressure loading only are relatively small. No local yielding occurred due to pressure loading in either case. The maximum stress predicted in the M-10 HIRE case was  $\sigma_{max} = 31,897$  psi which was almost three times higher than the maximum stress in the design case. This prediction makes sense since  $P_0$  is approximately three times higher in the M-10 HIRE case. All of the stresses predicted were compressive.

Thermal Loading Only

The stresses due to thermal loading only were evaluated at the time the OATS heat conduction code predicted the highest wall temperature at the throat. This time occurred at 1.0 seconds for the M-10 design case and 0.5 seconds for M-10 HIRE case. In both cases local yielding occurred at most of the elements along the insert wall. Looking at the summary of the two cases in Table D-3 it can be seen that more elements yield in the M-10 HIRE case. Although the  $T_0$  is the same in both cases, the higher  $P_0$  in the M-10 HIRE case leads to higher mass flow rates, higher heating rates, and higher wall temperatures. The summary also shows the maximum stresses occurring in two very different areas between the two cases. This can probably be explained by the fact that the two temperature only cases represent different stages in their respective tunnel runs. Later in the combined loading results we see that the maximum stresses occur in the upstream end of the insert (element #1) at early run stages and move toward the downstream end (element #30) at later stages for both the M-10 design and M-10 HIRE cases.

Combined Pressure and Thermal Loading

Looking at the combined pressure and thermal loading results summary shown in Table D-3 it can be seen that local yielding occurs during a certain period of time in both cases. For the M-10 design case the local yielding occurs in the nozzle wall elements from time = .45 seconds to time = 1.7 seconds. In the M-10 HIRE case the local yielding occurs in several more elements along the nozzle wall but its time duration is much smaller, from time = .2 seconds to time = .8 seconds. The maximum stresses are an average of 7% above the yield strength in the M-10 design case and an average of 11% above yield for the M-10 HIRE case. Approximately 20% more material elements are subject to local yielding in the M-10 HIRE case. The ratio of maximum number of yielded elements to total number of elements is 6.4% for the M-10 design and 7.3% for M-10 HIRE. All of the stresses predicted by the stress analysis were compressive.

## CONCLUSIONS

Although stresses exceeding the material yield strength were indicated in the analysis it is felt that no severe permanent plastic deformation of the M-10 nozzle throat insert will occur due to operation at M-10 HIRE conditions for the following reasons:

- a. The extremely localized area over which the high stresses act.
- b. The very short time over which the M-10 HIRE stresses act.
- c. Dimensional measurements made on a M-10 nozzle throat insert after a number of tunnel runs at design conditions indicated no measurable deformation; the results of this analysis and comparison indicate only a slight increase in stress and local yielding along the wall of the insert when comparing the M-10 HIRE analysis to the M-10 design analysis, therefore, the performance of the M-10 nozzle throat insert at M-10 HIRE conditions should be comparable to previous performance at M-10 design conditions.

Due to the high compressive stresses the insert is likely to experience during M-10 HIRE operation it is possible that residual tensile stresses may be left along the bore of the insert after cooldown of the nozzle. After a number of tunnel operations, the cycling from high compressive to residual tensile stress may be severe enough to cause small fatigue cracks along the bore of the insert.

## RECOMMENDATIONS

Based on the results of this analysis it is recommended that the present M-10 nozzle throat insert be used, without modification, in tunnel operation at the proposed M-10 HIRE conditions of  $P_0 = 20,000$  psi and  $T_0 = 1500^\circ\text{F}$ . Also, due to the possible residual stress problem mentioned earlier, it is being recommended that the bore of the nozzle throat insert be inspected after each of the first ten HIRE runs and periodically thereafter.

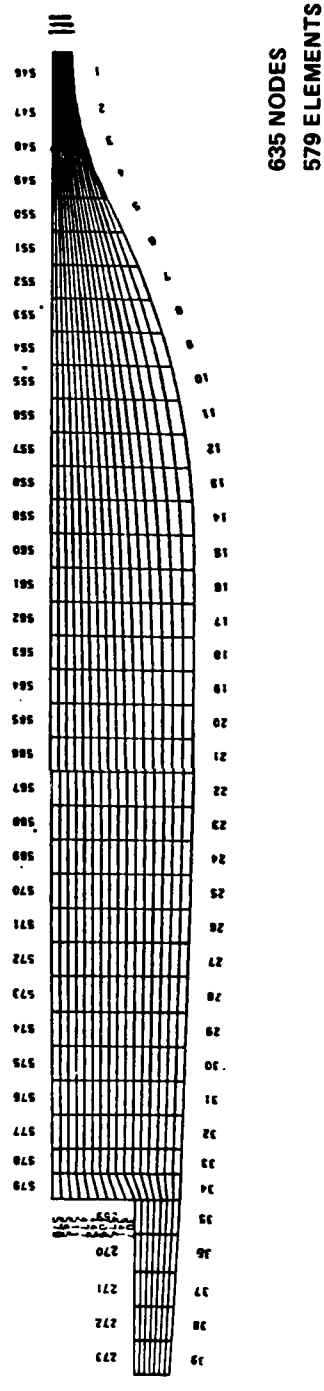


FIGURE D-1. FINITE ELEMENT MODEL OF M-10 NOZZLE THROAT INSERT WITH BOUNDARY ELEMENTS NUMBERED

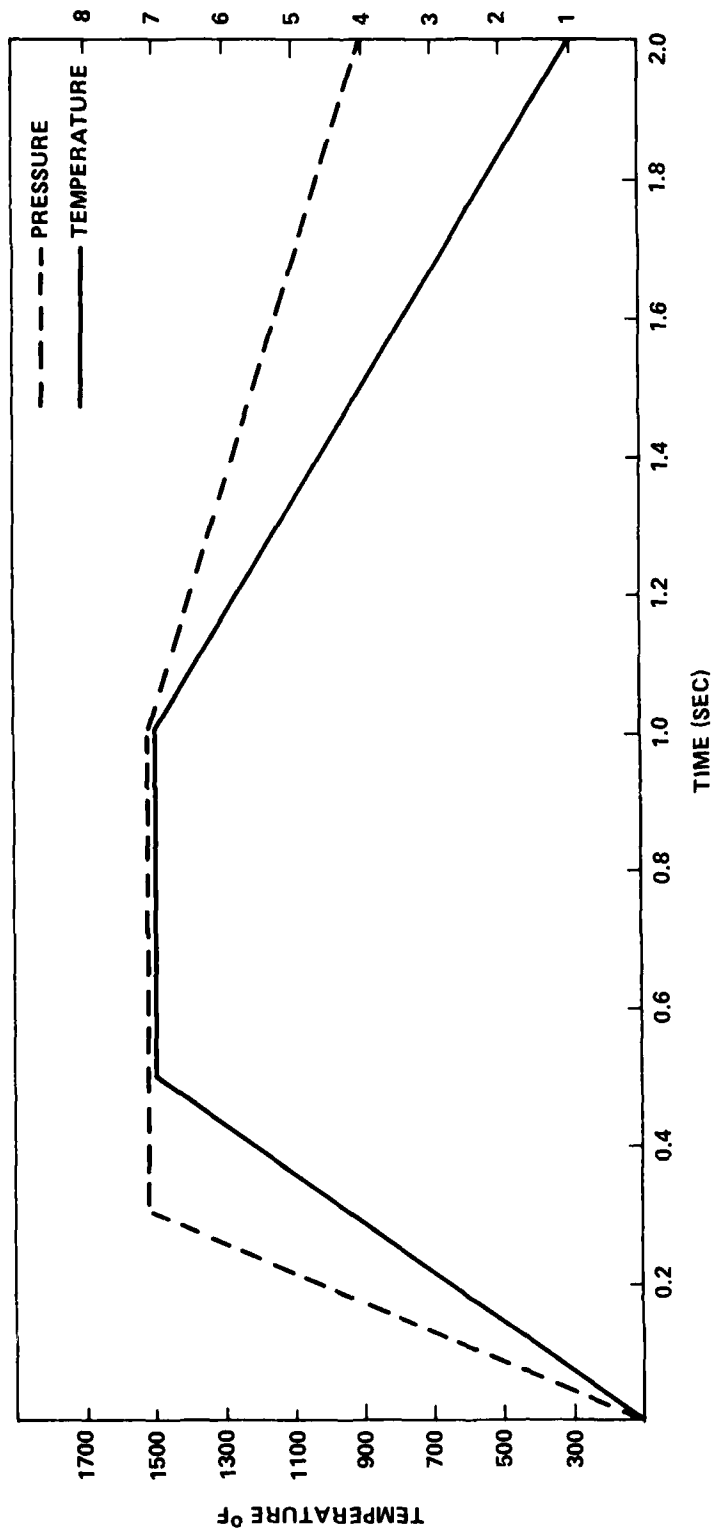


FIGURE D-2. TEMPERATURE, PRESSURE VS TIME FOR M-10 RUN

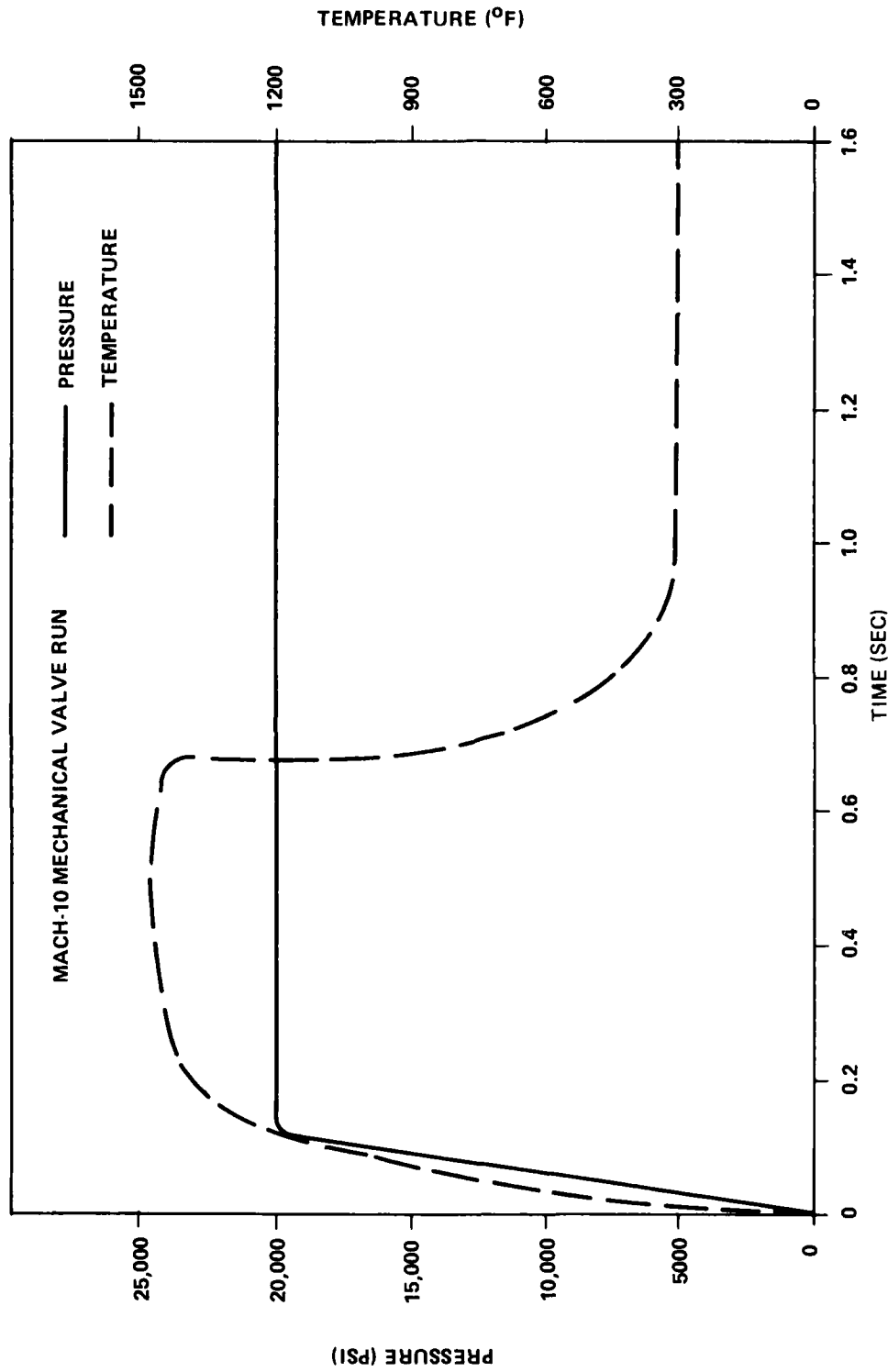


FIGURE D-3. ASSUMED TEMPERATURE, PRESSURE VS TIME FOR M-10 HIRE RUN

TABLE D-1. COMPARISON OF NOZZLE THROAT INSERT RESULTS FOR DESIGN (7000 PSI, 1500°F) AND M-10 HIRE CONDITIONS (20,000 PSI, 1500°F)

TIME (SEC)	DESIGN $h_T$ (BTU/IN <sup>2</sup> -SEC-°F)	M-10 HIRE $h_T$ (BTU/IN <sup>2</sup> -SEC-°F)	$h_T$ DESIGN / $h_T$ HIRE
0	0.0134	0.0684	0.20
0.1	0.0134	0.0684	0.20
0.2	0.0230	0.0828	0.28
0.3	0.0319	0.0778	0.41
0.4	0.0297	0.0759	0.39
0.5	0.0282	0.0759	0.37
0.6	0.0282	0.0844	0.33
0.7	0.0282	0.0763	0.37
0.8	0.0282	0.1037	0.27
0.9	0.0282	0.1074	0.26
1.0	0.0282	0.1046	0.27
1.1	0.0283	0.1046	0.27
1.2	0.0273	0.1046	0.26
1.3	0.0268	0.1046	0.26
1.4	0.0261	0.1046	0.25
1.5	0.0258	0.1046	0.25
1.6	0.0267	0.1046	0.25
1.7	0.0244	0.1046	0.23
1.8	0.0242	0.1046	0.23
2.0	0.0233	0.1046	0.22

$$\frac{h_T \text{ DESIGN}}{h_T \text{ HIRE}} (\text{AVERAGE}) \approx 28\%$$

TABLE D-2. TEMPERATURES PREDICTED AT THE THROAT SURFACE

TIME (SEC)	ASSUMED (°F) GAS TEMPERATURE		TEMP. PREDICTED AT THROAT SURFACE OATS HEAT TRANSFER CODE (°F)	
	DESIGN	HIRE	DESIGN	HIRE
0	70	70	70	70
0.1	380	1080	170	782
0.2	660	1375	393	1179
0.3	940	1440	691	1357
0.4	1220	1500	973	1423
0.5	1500	1500	1227	1454
0.6	1500	1400	1359	1378
0.7	1500	1260	1392	1264
0.8	1500	450	1402	596
0.9	1500	340	1406	391
1.0	1500	300	1410	316
1.1	1380	300	1361	302
1.2	1260	300	1268	301
1.3	1140	300	1164	301
1.4	1020	300	1058	301
1.5	900	300	952	300
1.6	780	300	841	300
1.7	660	300	733	300
1.8	540	300	626	300
1.9	420	300	518	300
2.0	300	300	408	300



TABLE D-3. SUMMARY AND COMPARISON OF ELASTIC/PLASTIC STRESS ANALYSIS RESULTS

LOADING CONDITIONS	COMPUTER PREDICTED STRESSES AT DESIGN CONDITIONS (7000 PSI, 1500°F)	COMPUTER PREDICTED STRESSES AT M-10 HIRE CONDITIONS (20,000 PSI, 1500°F)
PRESSURE ONLY	NO YIELDING; $\bar{\sigma}_{MAX} = 11,152$ PSI AT ELEMENT # 30; $\sigma_y = 185,000$ PSI AT # 30	NO YIELDING; $\bar{\sigma}_{MAX} = 31,897$ PSI AT ELEMENT # 30; $\sigma_y = 185,000$ PSI AT # 30
TEMP. ONLY	LOCAL YIELDING AT SURFACE ELEMENTS # 3 THRU # 38; $\bar{\sigma}_{MAX} = 121,150$ PSI AT ELEMENT # 35; $\sigma_y = 109,437$ PSI AT # 35; TIME = 1.0 SEC	LOCAL YIELDING AT SURFACE ELEMENTS # 1 THRU # 38, # 41, # 42; $\bar{\sigma}_{MAX} = 113,129$ PSI AT ELEMENT # 5; $\sigma_y = 98,437$ PSI AT ELEMENT # 5; TIME = 0.5 SEC
MAX. STATIC PRESSURE LOAD + TEMP. LOAD (TEMP. LOAD = F(T))	<p><math>t = 0.3</math> SEC — NO YIELDING; <math>\bar{\sigma}_{MAX} = 92,916</math> PSI AT ELEMENT # 1; <math>\sigma_y = 158,228</math> PSI AT # 1</p> <p><math>t = 0.4</math> SEC — NO YIELDING; <math>\bar{\sigma}_{MAX} = 110,073</math> PSI AT ELEMENT # 2; <math>\sigma_y = 149,307</math> PSI AT # 2</p> <p><math>t = 0.5</math> SEC — LOCAL YIELDING AT SURFACE ELEMENTS # 5, # 27, # 35; <math>\bar{\sigma}_{MAX} = 133,384</math> PSI AT ELEMENT # 5; <math>\sigma_y = 132,792</math> PSI AT # 5</p> <p><math>t = 0.6</math> SEC — LOCAL YIELDING AT SURFACE ELEMENTS # 2 THRU # 38; <math>\bar{\sigma}_{MAX} = 128,141</math> PSI AT ELEMENT # 5; <math>\sigma_y = 122,510</math> PSI AT # 5</p> <p><math>t = 0.8</math> SEC — LOCAL YIELDING AT SURFACE ELEMENTS # 2 THRU # 39; <math>\bar{\sigma}_{MAX} = 126,645</math> PSI AT ELEMENT # 35; <math>\sigma_y = 115,850</math> PSI AT # 35</p> <p><math>t = 1.0</math> SEC — LOCAL YIELDING AT SURFACE ELEMENTS # 2 THRU # 39; <math>\bar{\sigma}_{MAX} = 123,046</math> PSI AT ELEMENT # 35; <math>\sigma_y = 109,437</math> PSI AT # 35</p>	<p><math>t = 0.25</math> SEC — LOCAL YIELDING AT SURFACE ELEMENTS # 1 THRU # 6 AND # 15 THRU # 41; <math>\bar{\sigma}_{MAX} = 126,545</math> PSI AT ELEMENT # 2; <math>\sigma_y = 119,450</math> PSI AT ELEMENT # 2</p> <p><math>t = 0.35</math> SEC — LOCAL YIELDING AT SURFACE ELEMENTS # 1 THRU # 39 AND # 41; <math>\bar{\sigma}_{MAX} = 124,738</math> PSI AT # 4; <math>\sigma_y = 112,137</math></p> <p><math>t = 0.50</math> SEC — LOCAL YIELDING AT SURFACE ELEMENTS # 1 THRU # 39 AND # 41 THRU # 41; <math>\bar{\sigma}_{MAX} = 115,350</math> PSI AT # 4; <math>\sigma_y = 98,593</math></p> <p><math>t = 0.65</math> SEC — LOCAL YIELDING AT SURFACE ELEMENTS # 1 THRU # 39 AND # 41 THRU # 41; <math>\bar{\sigma}_{MAX} = 114,406</math> PSI AT ELEMENT # 4; <math>\sigma_y = 99,500</math> PSI AT # 4</p> <p><math>t = 0.75</math> SEC — LOCAL YIELDING AT SURFACE ELEMENTS # 2 THRU # 8, # 17 THRU # 37, # 41 THRU # 43; <math>\bar{\sigma}_{MAX} = 122,555</math> PSI AT ELEMENT # 4; <math>\sigma_y = 116,322</math> PSI AT ELEMENT # 4</p>

TABLE D-3. (CONTINUED) SUMMARY AND COMPARISON OF ELASTIC/PLASTIC STRESS ANALYSIS RESULTS

LOADING CONDITIONS	COMPUTER PREDICTED STRESSES AT DESIGN CONDITIONS (7000 PSI, 1500°F)	COMPUTER PREDICTED STRESSES AT M-10 HIRE CONDITIONS (20,000 PSI, 1500°F)
MAX. STATIC PRESSURE LOAD + TEMP. LOAD (CONTINUED)	<p><u>t = 1.1 SEC</u> — LOCAL YIELDING AT SURFACE ELEMENTS # 2 THRU # 39; <math>\bar{\sigma}_{MAX} = 122,628</math> PSI AT ELEMENT # 35; <math>\sigma_Y = 109,312</math> PSI AT # 35</p>	<p><u>t = 1.0 SEC</u> — NO YIELDING; <math>\bar{\sigma}_{MAX} = 89,898</math> PSI AT ELEMENT # 30; <math>\sigma_Y = 158,832</math> PSI AT ELEMENT # 30</p>
	<p><u>t = 1.2 SEC</u> — LOCAL YIELDING AT SURFACE ELEMENTS # 2 THRU # 38; <math>\bar{\sigma}_{MAX} = 123,403</math> PSI AT ELEMENT # 35; <math>\sigma_Y = 111,980</math> PSI AT # 35</p>	
	<p><u>t = 1.4 SEC</u> — LOCAL YIELDING AT SURFACE ELEMENTS # 3 THRU # 37; <math>\bar{\sigma}_{MAX} = 126,279</math> PSI AT ELEMENT # 35; <math>\sigma_Y = 119,990</math> PSI AT # 35</p>	
	<p><u>t = 1.6 SEC</u> — LOCAL YIELDING AT SURFACE ELEMENTS # 23 THRU # 31; <math>\bar{\sigma}_{MAX} = 135,230</math> PSI AT ELEMENT # 28; <math>\sigma_Y = 134,435</math> PSI AT # 28</p>	
	<p><u>t = 1.8 SEC</u> — NO YIELDING; <math>\bar{\sigma}_{MAX} = 115,863</math> PSI AT ELEMENT # 29; <math>\sigma_Y = 144,762</math> PSI AT # 29</p>	

## APPENDIX E

## PARTICLE SEPARATOR DESIGN AND ANALYSIS

In order to maintain gas flow characteristics consistent with the baseline separator and to improve the ( $P_o$ ) nozzle pressure capabilities desired at HIRE applications, the basic particle separator geometry was modified as shown in Figure E-1. Figure E-1A depicts the existing separator design. The new particle separator design incorporates (Figure E-1B) a conical nose tip fairing and also a constant hole size at each individual (row).

There are five major differences between Figure E-1A and E-1B:

1. The new separator design is 3.9 inches longer than the existing model.
2. The new separator design incorporates a conical nose tip design to help reduce the initial (contraction) pressure drop.
3. The new design allows for the threaded end of the particle separator to carry the loads (dynamic head pressure plus bearing loads) at that point. The particle separator shoulder supported the load in the existing model.
4. The separator row-diameters and the tip-to-tip envelope have all changed to accommodate the separator housing, and also to maintain annular areas, velocity ratios, etc., as in the baseline model.
5. Finally, it will be shown that a reduction in separator wall thickness was possible without significantly removing buckling strength safety margins.

Once the basic separator housing and the particle separator were defined, the geometrical envelopes for each were input into computer model PSAI. Typical input data for the new design is shown in Table E-1.

The processing of this input data by PSA-1 would produce the following data:

1. Ligament efficiencies (Axial-Z1, Circumferential -Z(x))
2. Hole/row data
3. Flow characteristics/row
4. Pressure drops
5. Losses tables

Tables E-2, E-3, E-4 and E-5 respectively, contain all of the preceding information. Table E-6 lists the abbreviated breakdown for Table E-4. It is worthwhile at this point to note a few key points about the new particle separator design:

1. The hole row data indicates that for a constant hole diameter of 0.25 inches, and an additional 1.9 inches in axial length, the separator requires 23 rows with a total of 825 holes (Table E-3).
2. The blowby required is 6%; the new particle separator design has a 6.03% blowby (Table E-4).
3. The pressure inside the separator is 18,417.3 psi, with a 1,582 psi total drop across the separator. Contraction losses account for 1,093.78 psi of the 1,582 psi drop across the separator; the remaining drop being a combination of turning losses and frictional losses through the separation region.

Comparing this data to the existing separator, improvements in pressure drops, losses and available separator pressure are readily noticeable. A 435 psi increase in available separator pressure, a 400 psi reduction in contraction losses, and a 500 psi reduction in the initial pressure drop are just a few of these improvements (Table E-7).

Table E-7 lists the particle deflection data. It should be noted that according to the data generated in PSAI, the new separator design will stop 20-micro diameter steel particles. The average hole velocity is approximately 205 FPS. Figure E-2 represents a summary of the particle deflection analysis from PSAI. The figure gives an indication of particle deflection versus particle size, with the hatched region representing the separation zone. It can be seen that there is no problem in separating 20 micron or above steel particles.

PSAI Option 1 was run as a check for PSAI Option 2. PSAI Option 1 can only be processed when the actual hole and row data are known. The output from PSAI Option was identical to PSAI Option 2; because of this no elaboration will be made on Option 1.

The vital dimensions of the new particle separator design were generated from the results from PSAI and a series of hand calculations. Table E-8 lists these dimensions.

#### STRUCTURAL ANALYSIS OF NEW PARTICLE SEPARATOR

The following flow characteristics are established upon diaphragm rupture upstream of the particle separator.

Flow Through Diagram

For a square duct of side  $a$ , the hydraulic diameter is given by:

Diaphragm Area

$$D = \frac{4A}{P} = \frac{4(a)^2}{4a} = a, \quad P = \text{wetted perimeter}$$

$A = \text{area}$

$$A_{\text{DIAP}} = \pi \cdot \frac{3.375^2}{4}$$

$$= 8.946 \text{ in}^2$$

$$A_{\text{DIAP}} = \frac{\pi(3.375)^2}{4} = 8.964 \text{ in}^2$$

Velocity through Diaphragm

$$\dot{m} = \rho A_{\text{DIAP}} V_{\text{DIAP}} \quad (\text{E-1})$$

where

$$\dot{m} = 1050 \text{ lb/sec}$$

$$V_{\text{DIAP}} = \frac{\dot{m}}{\rho A_{\text{DIAP}}} = \frac{1050 \text{ lb/sec}}{(18 \text{ lb/ft}^3)(8.946 \text{ in}^2) \frac{\text{ft}^2}{144 \text{ in}^2}}$$

$$V_{\text{DIAP}} = 938.97 \text{ ft/sec}$$

Dynamic Head Pressure on Separator Nose

$$q_{\text{MAX}} = 1/2 \rho V_{\text{DIAP}}^2 = \frac{(18 \text{ lb/ft}^3)(938.97 \text{ ft/sec})^2(0.5)}{(144 \text{ in}^2/\text{ft}^2)(32.2 \text{ ft/sec}^2)} \quad (\text{E-2})$$

$$q_{\text{MAX}} = 1711.31 \text{ lb/in}^2$$

The area of first concern will be the shear stress across the nose of the separator (section A-A, Figure E-3). Assuming the head pressure acts on the projected area shown in Figure E-3 (worst case) and across the thickness ( $t$ ), the maximum shear stress can be written as:

$$\tau_{MAX} = \frac{q_{MAX} \cdot A_{LOAD}}{A_{SHEAR}} = \frac{q_{MAX} \cdot \frac{\pi D^2}{4}}{\pi D t}$$

$$= \frac{(1711.23 \text{ lb/in}^2)(\pi(3.1336 \text{ in}^2)/4)}{\pi(3.1336)(0.5 \text{ in})} = \underline{2681.280 \text{ lb/in}^2} \quad (E-3)$$

Inconel X-750 at 1500°F has a yield strength ( $S_{yp}$ ) equivalent to 70,000 psi. For structural purposes 90% of  $S_{yp}$  (63,000) psi, will be used for a safety margin. The  $\tau_{allow} = 0.57 (S_{yp}) = 39,000$  psi. Therefore, result 3 poses no potential problem.

The force due to the dynamic head pressure acting on the nose can be written as:

$$F = q_{MAX} \cdot A_{LOAD}, \quad (E-4)$$

where

$$A_{LOAD} = \frac{\pi(3.1336)^2}{4} = 7.712 \text{ in}^2 = (1711.31 \text{ lb/in}^2)(7.712 \text{ in}^2)$$

$$\underline{F = 13,197.62 \text{ lbs}}$$

The bearing load at the nose can be written as:

$$F_{\Delta P} = (\Delta P - \text{LOAD AREA})(\Delta P), \quad P = 1,582.75 \text{ PSI (PSAI)}$$

$$= (7.712 \text{ in}^2)(1,582.75 \text{ lb/in}^2)$$

$$= 12,206.17 \text{ lbs}$$

The total bearing load is:

$$F_{BRG} = F_{\Delta P} + F = 12,206.17 \text{ lbs} + 13,197.0 \text{ lbs} \quad (E-5)$$

$$\underline{= 25,403.17 \text{ lbs}}$$

Bending at the Nose

Using the theory for a circular plate of thickness (t) simply supported around its periphery, and also assuming the maximum deflection of the plate  $< (0.5t)$ , the bending stress can be approximated by the following equation from Reference E-1:

$$f = (3/8)(3 + \nu)w(R/t)^2 \quad (E-6)$$

where

$\nu$  = Poissons Ratio

w = load

R = plate radius

t = plate thickness

The load acting on the nose of the separator is equivalent to:

$$w = q_{MAX} = 1,711.23 \text{ lb/in}^2, \quad t = 0.5, \quad R = 1.5668 \text{ in}, \quad \nu = 0.3.$$

Subbing back into E-6:

$$f = (3/8)(3 + 0.3)1,711.23 \text{ lb/in}^2(1.5668/0.5)^2$$

$$f_1 = 20,794.12 \text{ lb/in}^2$$

The maximum bending stress can be approximated by the following relation from Reference E-2:

$$\sigma_{MAX} = \frac{3F}{2\pi mt^2} \left[ m + (m + 1)\log A/R - (m - 1) \frac{R^2}{4a^2} \right] \quad (E-7)$$

where

$$F = 13,197.00 \text{ lbs}$$

$$m = 1/\nu = 1/0.3 = 3.33$$

$$t = 0.5$$

$$q = \text{plate radius} = R = \text{load radius} = 3.1336/2 = 1.5668$$

Subbing back into E-7:

$$\begin{aligned}\sigma_{MAX} &= \frac{3(13,197.00)}{2(\pi)(3.33)(0.5)^2} \left[ 3.3 + (4.3) \log \frac{1.5668}{1.5668} - (2.3) \frac{(1.5668)^2}{4(1.5668)^2} \right] \\ &= 7,568.89 \text{ lb/in}^2 (3.3 - 0.575) \\ \sigma_{MAX} &= 20,625.23 \text{ lb/in}^2\end{aligned}$$

The difference between  $f_1$  and  $\sigma_{MAX}$  (168.8 psi) is minimal.

#### Deflection at the Nose

The maximum deflection at the nose is governed by the following relation from Reference E-2:

$$Y = (1 - \nu)(s + \nu)fR_2/2(3 + \nu)Et \quad (E-8)$$

Subbing back into E-8 for:

$$f = f_1 \text{ and } f = s_{MAX}$$

$$Y_{f_1} = 0.00239 \text{ in} < 0.5t = 0.5(0.5) = 0.25 \text{ in}$$

$$Y_{\sigma_{MAX}} = 0.00237 \text{ in} < 0.5t = 0.25 \text{ in}$$

$$Y_{f_1} = Y_{\sigma_{MAX}}$$

Therefore, the initial assumption that the maximum deflection at the nose by  $0.5t$  is correct, with essentially no bending at the nose.

Cross sectioning through row A-A would appear as shown in Figure E-4. The total bearing stress can be calculated as follows:

$$\sigma_B = (F_{\Delta p} + F)/\text{Net Ligament Area} \quad (E-9)$$



The net ligament area corresponds to the crosshatched areas in Figure E-4. This area can be conservatively approximated by the following relation:

$$A_{LIG} = \frac{\pi}{4} (S_{DIA}^2 - MIN. DIA^2) - (Cross\ section\ hole\ area) \quad (E-10)$$

Values for the minimum diameter and cross sectional hole area are tabulated in Table E-9. Subbing back into Equation (E-9) the total bearing stress can be calculated.

$$= (25,403.17\ lb) / [\pi/4(2.75^2 - 2.25^2) - 1.50\ in^2]$$

$$\sigma_B = 54,807.81\ lb/in^2$$

This bearing stress level will present no structural problems.

The maximum allowable  $\Delta P$  for Section A-A can be written as:

$$\begin{aligned} \Delta P_{MAX} &= [(63,000\ lb/in^2)(NET\ LIG.\ AREA) - F] / \Delta P_{LOAD\ AREA} \\ &= [(63,000\ lb/in^2)(0.463495\ in^2) - 13,197.0\ lbs] / 7.712\ in^2 \quad (E-11) \end{aligned}$$

$$\Delta P_{MAX} = 2,075.102\ lb/in^2$$

Using the analysis for a cylindrical ring of thickness (t) under external pressure, buckling load capabilities can be obtained, using a method outlined in Reference E-3, at Section A-A.

$$\begin{aligned} P_{cr/A-A} &= \frac{E}{4(1 - \nu^2)} \left( \frac{t}{r} \right)^3 \\ &= \frac{24 \times 10^6}{4(1 - (0.3)^2)} \left( \frac{0.25}{1.375} \right)^3 \quad (E-12) \end{aligned}$$

$$P_{cr/A-A} = 39,629.75\ lb/in^2$$

where

$$E = 24 \times 10^6 \text{ psi}$$

$$R = S_{DIA}/2 \text{ (Table 1)}$$

$$t = 0.25 \text{ in (Table 1)}$$

$$\nu = 0.3$$

The calculated ligament efficiency for section A-A is given by the relation:

$$\eta = \frac{e-D}{e} \quad (E-13)$$

where

$$e = \frac{2\pi R}{\# \text{ holes}} = \frac{2(\pi)(1.375)}{24} = 0.3599$$

Thus

$$\eta = \frac{.3599 - .25}{.3599} = .305$$

An alternative method of calculating  $P_{cr}$  and  $\eta$  based on perforated plate theory shall be presented.

$$P_{cr}^* = \frac{E^*}{4(1 - \nu^{*2})} \left( \frac{t}{r} \right)^3 \quad (E-14)$$

$$\eta^* = \frac{P - D}{P} \quad (E-15)$$

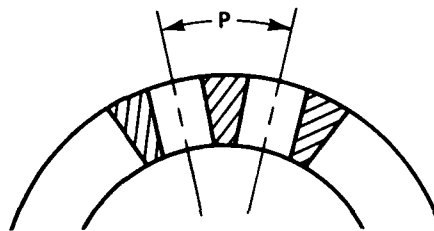
where

$P$  = circular pitch (15)

$D$  = hole diameter

The following steps can be used in calculating  $P_{cr}^*$  and  $\eta^*$ :

1. calculate  $\eta^*$



2. once  $\eta^*$  is known  $E^*/E$  and  $\nu^*$  can be obtained from the appropriate graph
3. calculated  $P^*_{cr}$

FOR SECTION A-A

$$\eta^*_{A-A} = \frac{0.390504 - 0.25}{0.39054} = \underline{0.359}$$

From Graphs

$$E^*/E = 0.25 \text{ thus } E^* = 0.25E, \nu^* = 0.455$$

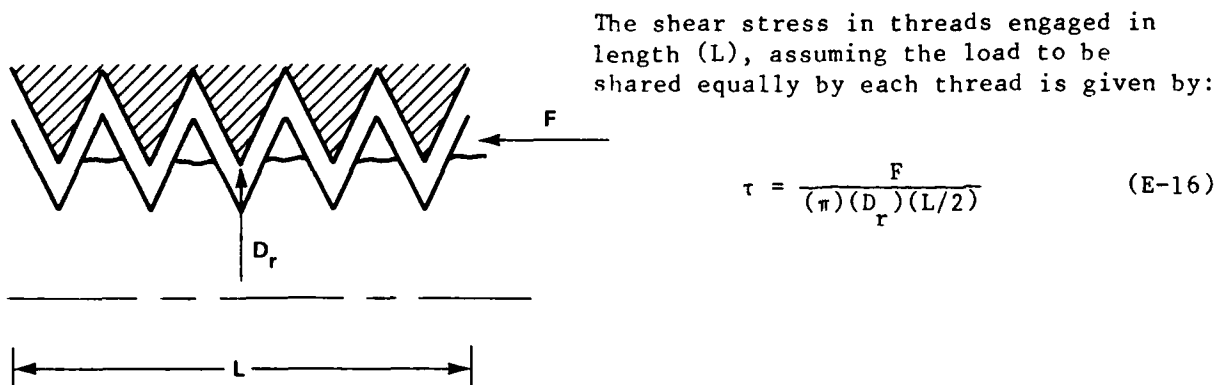
$$P^*_{cr} = \frac{0.25(24 \times 10^6)}{4(1 - (0.455)^2)} \frac{0.25^3}{1.375} = \underline{11,370 \text{ lb/in}^2}$$

Taking a cross section at the last row of holes (W-W), the same structural analysis is performed. Table E-9 contains the results of the analysis for both rows A-A and W-W.

#### STRESS ANALYSIS OF THREADED END OF SEPARATOR

Due to the geometry changes in the new separator design, it was necessary to analyze the threaded end for stress considerations. Assuming now that the threaded end takes all the load applied at W-W; and further that the load is equally shared by the threads, shear stresses and bearing stresses at the threads can be calculated.

#### Shear Stress in Threads



where

$$D_r = 6.0876 \text{ (for 6.25 - 8UN - 2A THD.)} = \text{Pitch Diameter}$$

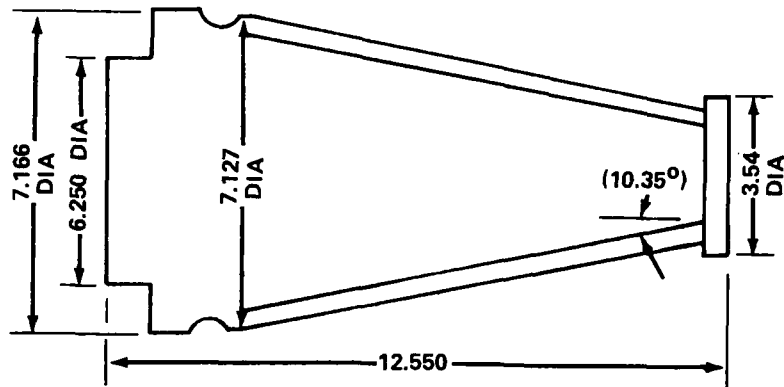
$$L = 1.0 \text{ in}$$

$$F = 53,930 \text{ lbs}$$

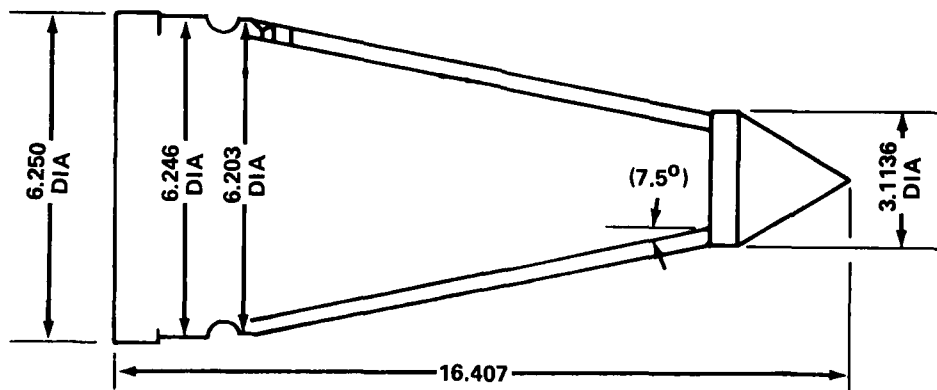
$$\tau = \frac{53,930 \text{ lbs}}{\pi(6.0875) \frac{1.00 \text{ in}^2}{2}}$$

$$\tau = 5,639.90 \text{ lb/in}^2$$

\*Yield strength for Inconel X-750 at 1500°F,  $S_{yp} = 70,000$  psi. Von Mises stress criteria require 57% ( $S_{yp}$ ) for structural comparison, or 39,900 psi. The result of Equation (E-16), therefore, represents no problem.



(A)



(B)

FIGURE E-1. PARTICLE SEPARATOR (A) OLD SEPARATOR, (B) NEW SEPARATOR

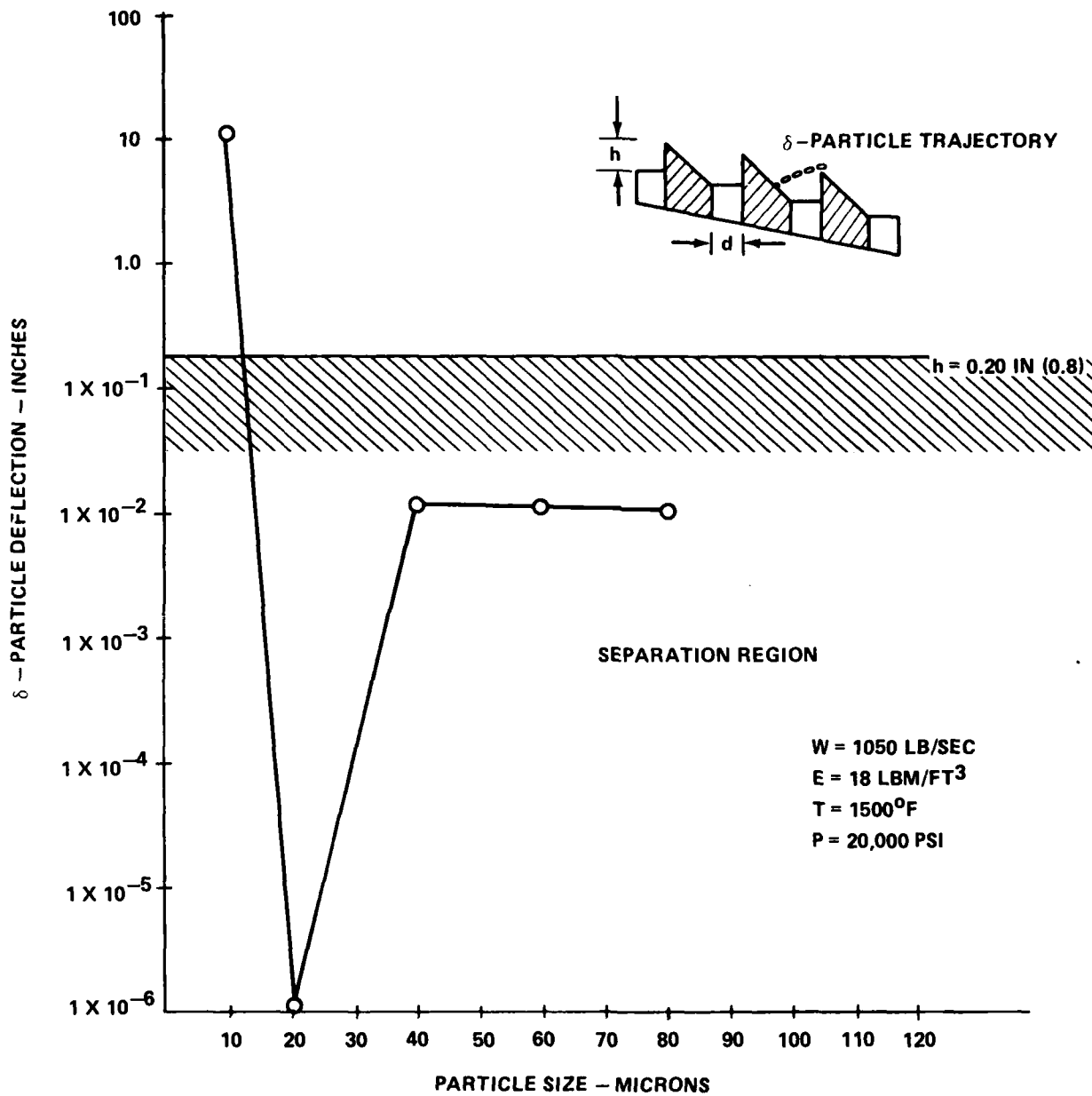


FIGURE E-2. PARTICLE DEFLECTION VS PARTICLE SIZE --STEEL ANALYSIS

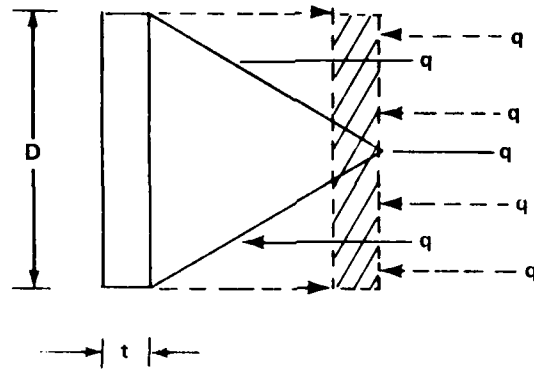
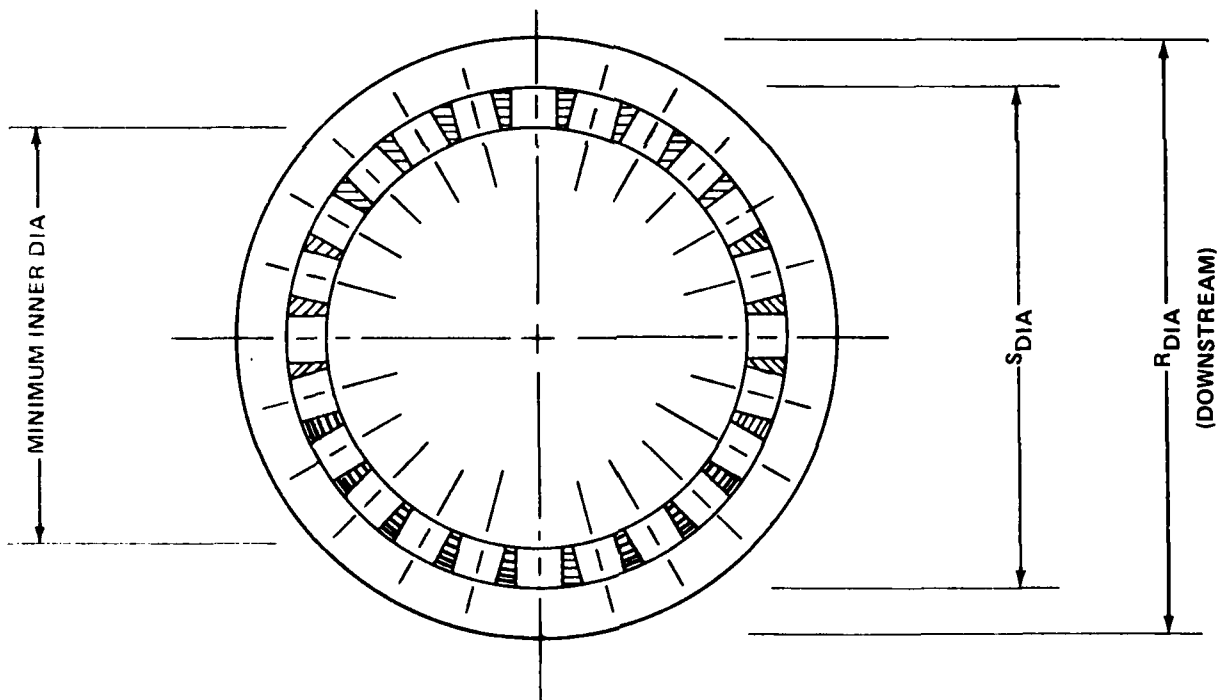


FIGURE E-3. ROW A-A (Worst Case Shear)



SECTION A-A (FULL SCALE)

FIGURE E-4. CROSS-SECTION A-A. LIGAMENT AREA

TABLE E-2. LIGAMENT EFFICIENCIES

Z(1) = .506726
Z(2) = .390504
Z(3) = .391041
Z(4) = .391536
Z(5) = .391994
Z(6) = .370719
Z(7) = .371875
Z(8) = .372953
Z(9) = .37396
Z(10) = .374903
Z(11) = .375788
Z(12) = .37662
Z(13) = .377404
Z(14) = .378144
Z(15) = .378843
Z(16) = .379505
Z(17) = .380133
Z(18) = .380729
Z(19) = .381295
Z(20) = .381834
Z(21) = .382347
Z(22) = .382837
Z(23) = .383305
Z(24) = .376641

TABLE E-3. HOLE/ROW DATA

NUMBER OF ROWS CALCULATED = 23  
 NUMBER OF HOLES CALCULATED = 825  
 CALCULATED HOLE SIZE CONSTANT

TABLE E-1. INPUT INFORMATION - PSAI

PARTICLE SEPARATOR ANALYSIS (P.S.A.)

TUNNEL HEATER DENSITY (LB/FT<sup>3</sup>) ? 18

TUNNEL UPSTREAM PRESSURE (LB/IN<sup>2</sup>) ? 20000

TUNNEL MASS FLOW RATE (LB/SEC) ? 1050

IS HOLE AND ROW DATA AT END USED (Y/N) ? N

AXIAL LENGTH FIRST TO LAST ROW (IN) ? 11.15

PARTICLE SEPARATOR RADIUS FIRST ROW (IN) ? 1.5668

PARTICLE SEPARATOR RADIUS LAST ROW (IN) ? 3.0347

AXIAL LENGTH FROM FRONT OF P.S. TO FIRST ROW (IN) ? 2.1

CHAMBER RADIUS AT FIRST ROW (IN) ? 2.446

CHAMBER RADIUS AT LAST ROW (IN) ? 3.096

ORIFICE COEF. ? .761

TOO MUCH DATA, RETYPE INPUT AT 870 ? .61

PARTICLE MATERIAL

1=STEEL, 2=GRAPHITE, 3=DELFIN ? 1

HOLE SIZE CONSTANT OR VARIABLE (C/U) ? C

HOLE DIAMETER (IN) (SAME ALL ROWS) ? .25

INPUT X1, TO K9, K7 ? 5, 1960, -2, -3

HOLE TO CHANNEL VELOCITY RATIO ? .25

LIGAMENT EFFICIENCY (CIR) ? .37

LIGAMENT EFFICIENCY (AXIAL) ? .49



TABLE E-4. FLOW DATA/ROW MODEL

I	P4(I) V(I)	W(I) U(I)	Q(I) U3(I)	F9(I) V9(I)	G(I) P2(I)
1	30633.	1050	29.7379	0	0
	757.891	201.944	.266455	0	2.68272E+6
2	31162.4	1020.26	31.2435	1820.32	2349.76
	750.927	203.682	.271241	743.606	2.68325E+6
3	31573.7	989.019	32.7069	1863.47	2274.76
	744.122	205.022	.275521	735.938	2.68366E+6
4	31863.5	956.312	34.1204	1911.73	2201.49
	737.477	205.96	.279277	728.385	2.68395E+6
5	32024.9	922.191	36.7405	1965.83	2127.19
	730.998	206.481	.282464	720.945	2.68411E+6
6	32387.5	885.451	38.222	2020.91	2383.53
	723.671	207.647	.286935	712.606	2.68447E+6
7	32671.6	847.229	39.6689	2082.1	2366.23
	716.322	208.556	.291148	704.174	2.68478E+6
8	32878.4	807.56	41.078	2150.23	2357.07
	708.926	209.215	.295115	695.608	2.68496E+6
9	33008.4	766.482	42.4453	2226.33	2356.25
	701.454	209.628	.298847	686.862	2.68509E+6
10	33060.8	724.037	43.7663	2311.64	2364.12
	693.877	209.794	.302351	677.883	2.68515E+6
11	33034.3	680.27	45.0354	2407.77	2381.19
	686.16	209.71	.305628	668.609	2.68512E+6
12	32925.7	635.235	46.246	2516.69	2408.14
	678.267	209.365	.308676	658.967	2.68501E+6
13	32730.6	588.989	47.3895	2640.99	2445.85
	670.155	208.744	.311486	648.866	2.68482E+6
14	32442.	541.599	48.4553	2783.98	2495.39
	661.276	207.821	.314036	638.194	2.68453E+6
15	32049.7	493.144	49.4288	2950.13	2557.88
	653.076	206.561	.31629	626.807	2.68413E+6
16	31538.5	443.715	50.2903	3145.5	2634.27
	643.993	204.907	.318182	614.515	2.68362E+6
17	30884.4	393.425	51.0102	3378.58	2724.45
	634.463	202.771	.319595	601.063	2.68297E+6
18	30047.5	342.415	51.5415	3661.79	2824.89
	624.427	200.005	.320301	586.097	2.68213E+6
19	28954.5	290.873	51.8001	4014.17	2921.23
	613.877	196.334	.319826	569.114	2.68104E+6
20	27450.8	239.073	51.61	4467.37	2963.62
	602.985	191.167	.317035	549.396	2.67954E+6
21	25137.7	187.463	50.5102	5081.72	2768.66
	592.629	182.936	.308686	525.986	2.67722E+6
22	20643.5	136.953	46.79	6009.25	1515.06
	586.884	165.779	.282472	498.3	2.67273E+6
23	6248.66	90.1631	26.862	7947.02	-6447.85
	610.958	91.2074	.149286	473.38	2.65833E+6
24		63.3011	BLOWBY $\approx$ 6.03%		

TABLE E-5. PRESSURE DROP/LOSSES

TURNING LOSS H9 AT NOSE OF PARTICLE CATCHER = 222.981 PSI  
 FRICTION LOSS H8 IN FIRST INCREMENT = 53.2598 PSI  
 CONTRACTION LOSS H7 = 1093.78 PSI  
 PRESSURE P3 AT INSIDE OF CATCHER = 18417.3 PSI  
 PRESSURE P2(1) AT INLET TO FIRST ROW OF HOLES = 18630. PSI  
 PRESSURE DROP (P1-P3) AT INLET = 1582.75 PSI  
 PRESSURE P2(F1) AT INLET TO LAST ROW OF HOLES = 18460.6 PSI  
 ORIFICE AREA A4 OF BLOWDOWN = .286429 SQ.IN.  
 FRICTION FACTOR F= .04

TABLE E-6. ABBREVIATED BREAKDOWN

I	- Row Number	
$P_4(I)$	- Pressure drop across holes in row "I"	psf
$W(I)$	- Flow rate through annulus upstream of row "I"	lbs/sec
$Q(I)$	- Flow rate through holes in row "I"	psf
$F_9(I)$	- Pressure drop in annulus (See equation (A-10))	pst
$G(I)$	- Pressure recovery in annulus (See equation (A-10))	psf
$V(I)$	- Flow velocity in annulus just upstream of row "I" (Same as $V_x$ )	fps
$U(I)$	- Flow velocity through holes (Same as $V_y$ )	fps
$U_3(I)$	- Ratio of velocity through holes to velocity in annulus (Same as $V_y/V_x$ )	fps
$V_9(I)$	- Average velocity in annulus over the length between holes	fps
$P_2(I)$	- Static pressure at upstream side of orifice holes	psf

TABLE E-7. STEEL PARTICLE ANALYSIS

PARTICLE SIZE	BALISTIC COEF (LB/FT <sup>2</sup> )	Y DEFL (IN)	HOLE VEL (FT/SEC)	HOLE DYN PRES (LB/FT <sup>2</sup> )
FOR ROW 1 WITH 24 HOLES				
10 MICRON	2.57509E-2	13.0781	201.944	11398.5
20 MICRON	1225.93	1.35753E-6	201.944	11398.5
40 MICRON	.102972	7.03808E-2	201.944	11398.5
60 MICRON	.154537	2.91439E-2	201.944	11398.5
80 MICRON	.206023	1.71044E-2	201.944	11398.5
FOR ROW 2 WITH 25 HOLES				
10 MICRON	2.57509E-2	13.316	203.682	11595.5
20 MICRON	1225.93	1.40673E-6	203.682	11595.5
40 MICRON	.102972	7.23602E-2	203.682	11595.5
60 MICRON	.154537	.03005	203.682	11595.5
80 MICRON	.206023	1.76611E-2	203.682	11595.5
FOR ROW 3 WITH 26 HOLES				
10 MICRON	2.57509E-2	13.5288	205.022	11748.6
20 MICRON	1225.93	1.45149E-6	205.022	11748.6
40 MICRON	.102972	7.41433E-2	205.022	11748.6
60 MICRON	.154537	3.08689E-2	205.022	11748.6
80 MICRON	.206023	.018165	205.022	11748.6
FOR ROW 4 WITH 27 HOLES				
10 MICRON	2.57509E-2	13.7156	205.96	11856.4
20 MICRON	1225.93	1.49131E-6	205.96	11856.4
40 MICRON	.102972	.075717	205.96	11856.4
60 MICRON	.154537	3.15937E-2	205.96	11856.4
80 MICRON	.206023	1.86118E-2	205.96	11856.4
FOR ROW 5 WITH 29 HOLES				
10 MICRON	2.57509E-2	13.8741	206.481	11916.5
20 MICRON	1225.93	1.52556E-6	206.481	11916.5
40 MICRON	.102972	7.70596E-2	206.481	11916.5
60 MICRON	.154537	3.22135E-2	206.481	11916.5
80 MICRON	.206023	1.89943E-2	206.481	11916.5
FOR ROW 6 WITH 30 HOLES				
10 MICRON	2.57509E-2	14.0964	207.647	12051.4
20 MICRON	1225.93	1.57423E-6	207.647	12051.4
40 MICRON	.102972	.078953	207.647	12051.4
60 MICRON	.154537	3.30899E-2	207.647	12051.4
80 MICRON	.206023	1.95359E-2	207.647	12051.4
FOR ROW 7 WITH 31 HOLES				
10 MICRON	2.57509E-2	14.3059	208.556	12157.1
20 MICRON	1225.93	1.62079E-6	208.556	12157.1
40 MICRON	.102972	8.07479E-2	208.556	12157.1
60 MICRON	.154537	3.39232E-2	208.556	12157.1
80 MICRON	.206023	2.00517E-2	208.556	12157.1

TABLE E-8. PARTICLE SEPARATOR VITAL DIMENSIONS

Section	Holes	R <sub>DIA</sub>	S <sub>DIA</sub>	L2	T°
A-A	24	3.267	2.750	2.1000	15°-0'
B-B	25	3.400	2.883	2.6068	14°-24'
C-C	26	3.534	3.017	3.1136	13°-50'
D-D	27	3.667	3.150	3.6204	13°-33'
E-E	29	3.801	3.284	4.1273	12°-24'
F-F	30	3.934	3.417	4.6341	12°-0'
G-G	31	4.067	3.551	5.1409	11°-36'
H-H	32	4.201	3.684	5.6477	11°-15'
I-I	33	4.335	3.817	6.1545	10°-54'
J-J	34	4.468	3.951	6.66136	10°-35'
K-K	35	4.601	4.084	7.1682	10°-17'
L-L	36	4.735	4.218	7.6749	10°-0'
M-M	37	4.868	4.351	8.1818	9°-43'
N-N	38	5.002	4.485	8.6886	9°-28'
O-O	39	5.152	4.618	9.1954	9°-13'
P-P	40	5.269	4.752	9.7023	9°-0'
Q-Q	41	5.402	4.885	10.2091	8°-46'
R-R	42	5.535	5.018	10.7159	8°-34'
S-S	43	5.669	5.152	11.2227	8°-22'
T-T	44	5.802	5.285	11.7295	8°-10'
U-U	45	5.936	5.419	12.2364	8°-0'
V-V	46	6.069	5.552	12.7432	7°-49'
W-W	48	6.203	5.686	13.2500	7°-30'

TABLE E-9. STRESS ANALYSIS SUMMARY

SECTION	R-DIA. (IN.)	SDIA. (IN.)	MIN. INNER DIA. (IN.)	# HOLES	HOLE DIA. (IN.)	CROSS-SECT. HOLE AREA (IN <sup>2</sup> )	NET LIG. AREA (IN <sup>2</sup> )	$\Delta P$ LOAD AREA (IN <sup>2</sup> )	BEARING LOAD $\Delta P$ (lbf)	T + 1 BRG. LOAD (lbf)	BEARING STRESS (lb/IN <sup>2</sup> )	MAX. $\Delta P$ - ALLOW. (lb/IN <sup>2</sup> )
NOSE	3.1136	-	-	-	-	-	-	7.712	12,206.17	25,403.17	54807	-
A-A	3.1136	2.750	2.250	24	.25	1.500	.4635	7.712	12,206.17	25,403.17	54807	2075
W-W	6.0694	5.686	4.396	48	.25	7.740	2.475	28.93	45,792.24	58,989.24	23834	18507

SECTION	(e) THICKNESS (IN.)	$P_c$ R (IN.)	$P_{cr}$ (lb/IN <sup>2</sup> )	$P_{cr}^*$ (lb/IN <sup>2</sup> )	$\eta$	$\eta^*$	$e$	$E^*$ (lb/IN <sup>2</sup> )	$\nu^*$	SHEAR STRESS (lb/IN <sup>2</sup> )	BENDING STRESS (lb/IN <sup>2</sup> )
NOSE	.50	-	-	-	-	-	-	-	-	2681.15	20,625
A-A	.25	1.375	39629	11370	.334	.359	.3756	.25E	.455	-	-
W-W	.645	2.843	76994	20358	.328	.325	.372	.225E	.475	-	-

## NOTES:

- CROSS SECTIONAL HOLE AREA =  $\left( \frac{SDIA \cdot MIN. DIA.}{2} \right) \cdot (HOLE DIA.) \cdot (\# HOLES)$
- NET LIGAMENT AREA =  $\pi/4 (SDIA^2 \cdot MIN. DIA^2) - (CROSS SECT. HOLE AREA)$
- $\Delta P \cdot LOAD AREA = \pi/4 (RDIA)^2$
- $F_{\Delta P}$  (BEARING LOAD) =  $(\Delta P \cdot LOAD AREA) \cdot (\Delta P)$
- TOTAL BEARING LOAD =  $F + F_{\Delta P}$
- BEARING STRESS =  $(F + F_{\Delta P}) / NET LIGAMENT AREA$
- $\Delta P_{MAX} = (16300)/(NET LIGAMENT AREA) \cdot F / \Delta P \cdot LOAD AREA$
- $P_{cr} = \frac{E}{4(1-\nu^2)} \left( \frac{1}{R} \right)^3$
- $\eta = \frac{e \cdot D}{\phi}$
- MATERIAL - INCONEL X-750 AT 1500°F SYP = 70,000 PSI
- SAFETY LEVEL FOR STRUCTURAL ANALYSIS 90% OF SYP  $\approx$  63,000 PSI
- ALLOWABLE SHEAR 57% OF SYP  $\approx$  39,900 PSI

REFERENCES

- E-1. Hicks, Standard Handbook of Engineering Calculations, (New York: McGraw-Hill, 1972).
- E-2. Roark, R. J., Formulas for Stress and Strain, Fourth Edition, (New York: McGraw-Hill, 1965).
- E-3. Horvay, "The Plain Stress Problem of Perforated Plates," Journal of Applied Mechanics, Volume 19, 1962.

## APPENDIX F

## DIAPHRAGM AREA COMPONENTS' ANALYSIS

## PRESSURE CONTAINMENT COMPONENTS

The pressure containment components in the diaphragm area consist of the horizontal elbow flange, thermocouple ring, flow restrictor housing, upstream and downstream diaphragm separator bodies, and particle separator housing, as shown in Figure 8 of the main report. Before diaphragm rupture these components are subjected to the lockup load applied to the diaphragms which squeeze the components together. After diaphragm rupture the components are subjected to high internal pressures resulting from the gas flow into the diaphragm area, as well as the lockup load.

For the pressure containment components, the critical stress region is at the bore. The principle stresses,  $\sigma_\theta$ ,  $\sigma_r$ , and  $\sigma_z$  that arise due to the internal pressure loading condition may be calculated from the following equations (Reference F-1):

$$\sigma_\theta = k \cdot p \frac{w^2 + 1}{w^2 - 1} \quad - \text{Hoop Stress} \quad (F-1)$$

$$\sigma_r = -p \quad - \text{Radial Stress}$$

$$\sigma_z = 0 \quad - \text{Axial Stress}$$

where

$k$  = stress concentration factor due to a discontinuity

$p$  = operating pressure (psi)

$w$  = wall ratio (O.D./I.D.)

Table F-1 contains values of component O.D., I.D., and  $k$ . Also shown are the resultant principal stresses resulting from the 22,000 psi maximum internal pressure. (Two sets of calculations were made for the thermocouple ring, one at the downstream bore of 9.125 in., the other at the 7.5 in bore, where a stress concentration exists due the presence of a side port.)

Also given in Table F-1 are values of  $\sigma_z$  (axial stress) for each component due to the lockup load of  $1.86 \times 10^6$  lbs. The bearing given is based on the cross section of the component which is under the lockup load. The value of  $\sigma_a$  listed is obtained by dividing the lockup load by the bearing area.

The values in the  $\sigma_z$  column which are in parentheses were obtained by combining the two values of  $\sigma_z$  obtained for the two loading conditions. With the values of principal stresses obtained above, calculations can now be performed to determine component fatigue life, and component acceptability per ASME code criteria (Reference F-2).

The ASME code requires that:

1. The average primary membrane stress intensity ( $\bar{s}$ ) be less than or equal to the smaller of  $2/3$  of the material yield strength, or  $1/2$  of the material ultimate strength.  $\bar{s}$  is obtained from:

$$\bar{s} = \frac{2 \cdot p \cdot w}{w^2 - 1} \quad (F-4)$$

Table F-2 contains values of  $\sigma_y$  and  $\sigma_{ult}$  for the components of interest. Note that in each case  $1/2 \sigma_{ult}$  is the smaller of the two values noted above. Also given in Table F-2 are values of  $\bar{s}$  for each component. In each case, the value of  $\bar{s}$  meets the ASME code criteria.

The ASME code also requires:

2. The maximum stress intensity  $S_{ij_{max}}$ , be less than the yield strength of the material. Stress intensity is based on Tresca failure criteria, as is defined as the maximum difference between the three principal stresses  $\sigma_\theta$ ,  $\sigma_r$ , and  $\sigma_z$ . Hence,

$$\left. \begin{aligned} S_{\theta r} &= \sigma_\theta - \sigma_r \\ S_{rz} &= \sigma_r - \sigma_z \\ S_{z\theta} &= \sigma_z - \sigma_\theta \end{aligned} \right\} S_{ij} = S_i - S_j \quad (F-5)$$

Values of  $S_{ij_{max}}$  are listed in Table F-2 for the various components. Note that the value obtained for the thermocouple ring does not meet the ASME code criteria on  $S_{ij_{max}}$ . However, there is a degree of conservatism in the stress concentration factor used that, if slightly reduced, would bring this component into compliance with the code. Also, there is a rigorous inspection sequence required by the Hypervelocity Facility's standard operating procedure which would detect a very small crack at the bore, if one were to be present. Thus, this value was deemed acceptable.



Fatigue life is evaluated using design curves (Figure F-2) from Reference F-2, which give allowable number of pressure cycles as a function of alternating stress intensity.

Alternating and mean stress intensities are obtained from:

$$S_A = \frac{(S_{ij})_{\max} - (S_{ij})_{\min}}{2} \quad (F-6)$$

$$S_M = \frac{(S_{ij})_{\max} + (S_{ij})_{\min}}{2} \quad (F-7)$$

Values of  $S_A$  and  $S_M$  are listed in Table F-2. The values of  $(S_{ij})_{\max}$  were obtained from the values of  $\sigma_z$  calculated earlier for the lockup load condition.

The effective mean stress  $S'_{\text{mean}}$  is obtained from the following:

$$\text{If } S_A + S_M \leq \sigma_y, \text{ then } S'_{\text{mean}} = S_M \quad (F-8)$$

$$\text{If } S_A + S_M \geq \sigma_y \text{ and } S_A < \sigma_y, \text{ then } S'_{\text{mean}} = \sigma_y - S_A \quad (F-9)$$

$$\text{If } S_A > \sigma_y, \text{ then } S'_{\text{mean}} = 0 \quad (F-10)$$

The equivalent alternating stress intensity used to account for mean stress effects is obtained using Peterson's cubic equation:

$$S_{\text{eq}} = \frac{7S_A}{8 - \left(1 + \frac{S'_{\text{mean}}}{\sigma_{\text{ult}}}\right)^3} \quad (F-11)$$

Table F-2 also contains values of  $S_A$ ,  $S_M$ , and  $S'_{\text{mean}}$  for the pressure containment components. Using the values of  $S_{\text{eq}}$  obtained, Figure A-1 of Appendix A was then used to obtain the allowable number of cycles for a given component. These fatigue life values are given in Table F-2.

Present design philosophy with regards to pressure containment components used in the facility requires that the components be protected from the flow of hot gas through the diaphragm section, to preclude the possibility of developing cracks at the bore of such components. This objective is accomplished by using thermal liners (Figure 8) throughout the diaphragm area.

Based on prior heat transfer and stress calculations made for both the nozzle throat insert (Appendix D), and the Mach-14 flow restrictor (Reference F-3), it has been determined that severe thermal gradients in the radial direction are present, which result in a stress distribution shown in Figure F-1. Note there is a thin band of material along the bore which experiences very high compressive stresses (usually greater than the yield strength of the material). Due to the self-equilibrating nature of thermal stresses, there is a volume of material outside this compressive band which is subjected to a lower level of tensile stressing. When the compressive stresses do in fact exceed yield, residual tensile stresses may be present upon cooldown of the material. After a number of such cycles, cracking may occur at the bore of the component. When the cracking becomes severe the thermal liner is summarily replaced. The bottom line is that the thermal liners are not designed to survive this thermal cycling condition indefinitely. Enclosure (1) of this Appendix is a thermal analysis of the particle separator housing liner. Note in the analysis that the observations cited above are applicable to this component.

The thermal liners are also subjected to mechanical loads due to the gas pressure on the liners, and the depressurization of the volume of gas between the liner and I.D. of the component in which it is situated. Enclosure (2) of this Appendix analyzes this loading condition.

## THERMAL LINER HEAT TRANSFER CALCULATIONS

## INTRODUCTION

Heat transfer and pressure analysis were performed on the preliminary design of an inner sleeve for the particle separator housing, a component used in the Mach-10 leg of Wind Tunnel Number Nine. Three computer codes, or programs, were used to calculate temperature gradients, deflections, and stresses in the particle separator housing liner. Some experimental data were used in the analyses to determine the temperature of the Wind Tunnel gas flow.

## BACKGROUND

The particle separator assembly portion of Wind Tunnel Number Nine removes solid particles from gas used in wind tunnel tests. During prior tests the inside surface of the particle separator housing became cracked and permanently deformed. The causes were thermal stresses and pressure differentials. They resulted from the flow of high pressure and high temperature gases during a relatively short period of time.

Tunnel Number Nine is in the process of being upgraded to have a capability for handling gas flows necessary for increased Reynold's Numbers at Mach-10. Such gas flows could cause greater thermal stresses on the inner surface of the particle separator housing. To avoid progressive and permanent failure, plans were made to bore out the housing and insert a replaceable inner sleeve. The inner sleeve's design was analyzed to assure that the sleeve would satisfactorily withstand transient conditions of high pressure, temperature, and heat transfer. This involved calculations and evaluations of the following five items:

- a. Thermal stresses,
- b. Gas pressure stresses,
- c. Thermal growth of the liner and stresses due to interference fit,
- d. Plastic yielding and permanent deformation,
- e. Thermal cracking.

## USE OF COMPUTER CODES

Calculations for those five items were performed using the following three computer codes:

- a. The MESHGEN code was used to generate finite elements (an imaginary grid overlay) for the axial cross section of the sleeve,
- b. The OATS code used those finite elements to calculate temperatures and temperature gradients which occur in an axial cross section of the sleeve during a test,
- c. The DOASIS code used the values of temperatures and pressures which occur during a hypervelocity wind tunnel test to determine values of the five items listed above.

The following paragraphs provide additional details concerning this process.

MESHGEN

The particle separator inner liner is shown in Figure 8 of the main report. A grid was drawn on the sleeve's cross section. Each node, or intersection of two lines, on the periphery of the cross section was assigned a set of coordinate numbers together with a nodal point number. These were used as inputs to the MESHGEN code. MESHGEN was then used to generate Figure F-2 and record its coordinates and nodal points for later use in the OATS code.

OATS

The inputs to OATS were outputs from MESHGEN and two different heat transfer coefficients for the insert liner. One heat transfer coefficient was used for the inner surface of the sleeve and the other for its ends. The inner surface coefficients vary with time because the temperature of the gas with which it comes into contact varies with time. The inner surface coefficients were calculated from the following equation after Reference F-4:

$$h = 0.23 \left( \frac{k}{d} \right) \left( \frac{vd\rho}{u} \right)^{0.8} (P_r)^{0.4} \quad (1)$$

where

- h = heat transfer coefficient of the inner surface of the insert liner,
- k = thermal conductivity of the wind tunnel gas (nitrogen),
- d = hydraulic diameter (the inside diameter of the inner sleeve minus the diameter of the particle separator) of the tunnel section,
- v = velocity of the wind tunnel gas,

$\rho$  = density of the gas,

$u$  = viscosity of the gas,

$P_r$  = Prandtl's number,

Values of the heat transfer coefficients calculated are listed in the last column of Table F-3.

The convection heat transfer coefficient is assumed to be a constant for the ends of the insert liner. This is based on the assumption that there is relatively little change in the temperature and density of the gas which is trapped between the ends of the inner sleeve and the particle-separator housing during the tunnel run. Calculation of a heat transfer coefficient for the ends of the sleeve required that Grashof and Nusselt numbers be calculated first as follows:

$$G_{rf} = 2.g \frac{(T_{\infty} - T_w) X^3}{(T_w + T_{\infty}) \nu^2} = \text{Grashof number} \quad (2)$$

where

$g$  = 9.8 m/s = acceleration of gravity,

$T_w$  = temperature of the inner surface of the insert liner,

$T_{\infty}$  = temperature of the gas free of wall effects,

$\nu$  = viscosity of the gas,

$X$  = length of the insert liner's heat transfer surface.

$$N_{uf} = c (G_{rf} P_{rf})^m = \text{Nusselt number} \quad (3)$$

where

$G_{rf}$  = Grashof's number from Equation (2) above,

$c$  and  $m$  = constants tabulated in Reference F-5 as a function of temperature,

$P_{rf}$  = tabulated in Reference F-5 as a function of temperature.

$$h = \frac{N_{uf} K}{X} \quad (4)$$

where  $N_{uf}$  comes from equation (3) above,

$K$  = heat constant conduction coefficient constant tabulated in Reference 16 as a function of temperature,

$X$  = length of the insert liner's heat transfer surface.

The calculated convection-heat-transfer coefficients, and finite elements from MESHGEN were entered into OATS code. Also, data was entered for the assumption that the outside surface of the inner sleeve remained at a temperature of 70 degrees Fahrenheit for two seconds. Then OATS was used to calculate inner sleeve nodal-point temperatures and to plot resulting temperature gradients that were caused by the flow of gas through the wind tunnel. Temperature gradients were plotted for 0.5 and 0.95 second after firing of the wind tunnel. The plots are shown in Figures F-3 and F-4. Data for the plots were also stored for use in DOASIS.

#### DOASIS

Entered into DOASIS were insert liner temperatures calculated by OATS and specifications for the sleeve's material properties. DOASIS then computed the sleeve's stress and deflections for each of the nodal points generated by MESHGEN. These calculations were made for 0.2, 0.5, 0.75, and 0.95 seconds after firing of the wind tunnel.

DOASIS was also used to calculate whether the wind tunnel's gas pressure or gas temperature contributed most to the sleeve's stress and deflection. This resulted in two listings of stress and deflection. One listing showed the effects of gas pressure and the second showed the effects of gas temperature.

#### DISCUSSION OF RESULTS

When the Hypervelocity Wind Tunnel is fired, the inner surface of the particle-separator-housing inner sleeve will be subjected to a one second heating and cooling cycle. From previous empirical data it was determined that the tunnel gas temperature is 300 degrees Fahrenheit when the diaphragm bursts and the gas initially flows. It reaches and maintains a maximum temperature of 1,500 degrees Fahrenheit during run time, which is approximately 0.3 through 0.55 second after firing. The temperature drops to 1,260 degrees at 0.75 second and 300 degrees after one second.

Figures F-3 and F-4 show isotherms plotted in the axial cross section of the inner sleeve at small time intervals after diaphragm burst. The isotherms depict the temperature distribution as a function of time. Evidence of the high heat transfer coefficient is that the temperature of the inner surface was approximately the same as the free-stream temperature of the tunnel gas. Physically the rate of heat convection to the sleeve's inner surface is approximately the same as the heat conduction through the sleeve wall.

The highest inner surface temperature occurs at approximately 0.5 seconds after tunnel firing. At that instant the maximum temperature gradient of 6000 degrees per inch occurs in the sleeve. Also, all heating is within approximately 0.2 inch of the sleeve's inner surface.

After 0.95 seconds, the tunnel gases and the sleeve's inner surface cool to 300 degrees Fahrenheit causing a more evenly heated sleeve and a lower maximum temperature, as shown in Figure F-4.

Heating of the inner sleeve's outer surface occurs after approximately one second.

Reference to Figure F-4 confirms the validity of assuming that the sleeve's outer surface remains at a constant temperature during a tunnel run. Based on that assumption, 70 degrees Fahrenheit was used as the sleeve's outer-surface temperature for the OATS code computations.

Calculations show that ten percent of the material along the inner surface of the sleeve yields due to compressive stresses. Deflections causing the stresses were due mostly to tunnel-gas temperature effects rather than tunnel-gas pressure. This is shown by two separate sets of calculations which were performed to determine effects of temperature and pressure.

The set of calculations for only temperature effects shows that heating by tunnel gas will cause high compressive stresses and yielding in ten percent of the material along the inner surface of the sleeve. The inner volume of material is at a higher temperature and expanding. As the temperature increases from 70 to 1500 degrees Fahrenheit, the yield point of the inner material (4340 steel) decreases from 135,000 psi to 9,390 psi, and yielding occurs. In contrast, the outer sleeve material is at a temperature of 70 degrees and under a maximum tensile stress of 45,000 psi, which is well within the yield strength at that temperature. The cooler outer material partially restrains expansion of the inner material.

The set of pressure calculations show that pressure by itself causes low compressive stresses through the sleeve. From Appendix E it was found that during run time the average gas pressure on the inside of the insert sleeve was 18,600 psi. On the outside of the sleeve, next to the particle separator housing, the pressure averaged 18,750 psi. Accordingly, tunnel gas pressure causes an average of 150 psi differential between the inner and outer surfaces of the sleeve. This will cause the sleeve to contract.

Temperature causes the sleeve to expand a maximum of 0.0025 inch of the outward direction. Pressure causes a maximum inward deflection of 0.0005. The net deflection is 0.002 inch outward. Accordingly a cold clearance of 0.005 inch between the inner sleeve and the particle separator housing should be adequate.

## SAMPLE CALCULATIONS FOR HEAT TRANSFER COEFFICIENTS

Inner Surface Heat Transfer Coefficient

Assume that nitrogen flow in the inner sleeve is similar to gas flow in a pipe. Then using Equation (1) (which is for pipe flow) the convection heat transfer coefficient along the inside of the inner sleeve is calculated as follows using Equation (1) from Reference (a).

$$h = \frac{k}{d} (.023) \left( \frac{vd\rho}{N} \right)^{0.8} (P_r)^{0.4}$$

where

$d$  = hydraulic diameter,

$d$  = [inner diameter of the inner sleeve] - [outside diameter of the particle separator],

$d$  = 5.7" - 4.6" = 1.1" = .0917 ft.

$P_r$  = .68, which is a function of gas temperature.

The remaining values for Equation (1) are listed in Table F-3 as a function of time after diaphragm burst.

Choosing values from Table A-1 at time = 1.0 second:

$N = 3.36 \times 10^{-5}$  lb/sec · ft,

$K = 1.2 \times 10^{-6}$  Btu/in·sec·°F,

$V = 684$  ft/sec,

$\rho = 34$  lb/ft<sup>3</sup>.

Substituting the above values into Equation (1) gives:

$$h = \frac{(1.2 \times 10^{-6})(.023)}{(1.1 \text{ in})} \left( \frac{(684)(.0917)(34)}{3.36 \times 10^{-5}} \right)^{0.8} (.68)^{0.4}$$

$$h = 0.0368 \frac{\text{Btu}}{\text{in}^2\text{-sec-}^\circ\text{F}}$$

The remaining values of  $h$  listed in column #8 of Table F-3 were calculated in a similar manner.



Calculation of the Inner Sleeve End Surface Heat Transfer Coefficient

Calculation of the free convection heat transfer coefficient for the ends of the inner sleeve was accomplished using Equation (2), (3), and (4) (from Reference F-5). That is, the value of Equation (2) or the Grashof number is used in Equation (3). In turn, the value of Equation (3) or the Nusselt number is used to calculate Equation (4) or the heat transfer coefficient for the ends of the inner sleeve.

$$G_{rf} = \frac{2g(T_{\infty} - T_w) X^3}{(T_w + T_{\infty}) \nu^2}$$

where

$\nu$  depends on the film temperature,

$T_f$ , which is the average of  $T_w$  and  $T_{\infty}$ ,

$T_w$  = wall temperature average = 700°F,

$X$  = length of heat transfer surface.

$$T_f = \frac{T_{\infty} + T_w}{2} = \frac{700^{\circ}\text{F} + 295^{\circ}}{2} = 497^{\circ}\text{K}$$

This film temperature was used to find the value of  $\nu$  in Reference F-5 tabulated as a function of temperature.

$$\nu = 37.9 \times 10^{-6} \frac{\text{m}^2}{\text{sec}}$$

then

$$G_{rf} = \frac{2(9.8)(700 - 295)(.0254)^3}{[295 + 700] 37.9 \times 10^{-6}} = 91014$$

Now the Nusselt number can be obtained:

$$N_{uf} = C[G_{rf} P_{rf}]^m$$

where  $c$  and  $m$  are tabulated in Reference F-5 as a function of  $G_{rf}$  which was calculated above.  $P_{rf}$  is the same as above.

$$N_{uf} = (.59)[(91014)(.86)]^{.25} = 9.86$$

Finally, the film coefficient is found from:

$$h = \frac{N_{uf} K}{X}$$

where

$$K = .04038 \text{ w/}^\circ\text{cm for N}_2 \text{ at } 497^\circ\text{K,}$$

$$X = .0254\text{m.}$$

Substitution yields:

$$h = \frac{(9.86)(.04038 \frac{\text{w}}{^\circ\text{cm}})}{.0254\text{m}} = 15.68 \frac{\text{w}}{\text{m}^2 \text{ } ^\circ\text{C}}$$

$$h = 5.33 \times 10^{-6} \frac{\text{Btu}}{\text{in}^2 \text{ sec } ^\circ\text{F}}$$

## THERMAL LINER STRUCTURAL ANALYSIS

The thermal sleeves, as noted earlier, are not designed for indefinite usage. However, a number of calculations were made to ensure that the sleeves would not undergo gross mechanical failure, which would adversely affect operations or result in damage to other equipment.

All of the thermal liners were designed to preclude interference stresses from occurring between the O.D. of the liner and the I.D. of the pressure containment component.

Due to the venting holes located 45° off center axis of the upstream sleeve, it is necessary to look at sleeve depressurization to ensure the structural integrity of the piece. The depressurization rate is given by the following relation:

$$\frac{1}{P_H} \frac{dp}{dt} = \frac{\gamma K_N A}{H} \quad (1)$$

where

$P_H$  = heater pressure = 22 kpsi,

$\gamma$  = 2.94,

$K_N$  = 0.5 (nozzle coefficient),

$A$  = throat area = 4.524 in<sup>2</sup>,

$a_H$  = sound speed = 3200 ft/sec,

$V_H$  = 54K in<sup>3</sup> (heater volume).

Subbing into (1), and solving for  $dp/dt$ ,

$$\frac{dp}{dt} = \frac{(22000 \text{ lb/in}^2)(2.94)(0.5)(4.524 \text{ in}^2)(3200 \text{ ft/sec})(12 \text{ in/ft})}{54,000 \text{ in}^3}$$

$$\frac{dp}{dt} = 104,039.9 \text{ lb/in}^2 \text{ sec}.$$

The time it will take the gas being vented to reach a vent hole is obtained from:

$$t = \frac{D}{V}$$

where

$$D = \text{distance travelled} = \pi(5.870)/8 = 2.3 \text{ in} = .19 \text{ ft}$$

$$V = \text{gas velocity} = 3200 \text{ ft/sec}$$

Substitution yields:

$$t = \frac{.19}{3200} = .00006 \text{ sec}$$

The pressure drop across the liner is then simply:

$$dp = dp/dt \cdot dt = 104,040 (.00006) = 6.2 \text{ psi}$$

which is negligible.

Just prior to rupture, the upstream separator body liner will see a 16,500 psi  $\Delta p$  load. This load is taken in bearing on the shoulder. In addition, shear across the shoulder must be calculated.  $\sigma_B$  is calculated from:

$$\sigma_B = \frac{\Delta p A_L}{A_B}$$

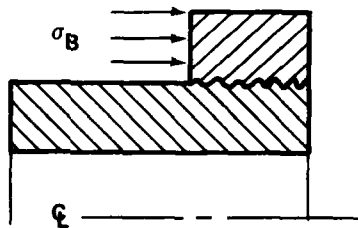
where

$$\Delta p = 16,500 \text{ psi}$$

$$A_L = \pi/4(5.870)^2 = 27 \text{ in}^2$$

$$A_B = \pi/4(5.745^2 - 5.230^2) = 4.44 \text{ in}^2$$

Note these diameters account for chamfers and radii on corners



Thus

$$\sigma_B = \frac{16,500(27)}{4.44} = 100,400 \text{ psi}$$

The room temperature yield is 130,000 psi, thus  $\sigma_B = 100,400$  psi is no problem. The shear stress is obtained from:

$$\tau = \frac{\Delta p A_L'}{A_S}$$

where

$$\Delta p = 16,500 \text{ psi}$$

$$A_L' = \pi/4(5.112)^2 = 20.6$$

$$A_S = \pi(5.112)(26.50) = 10 \text{ in}^2$$

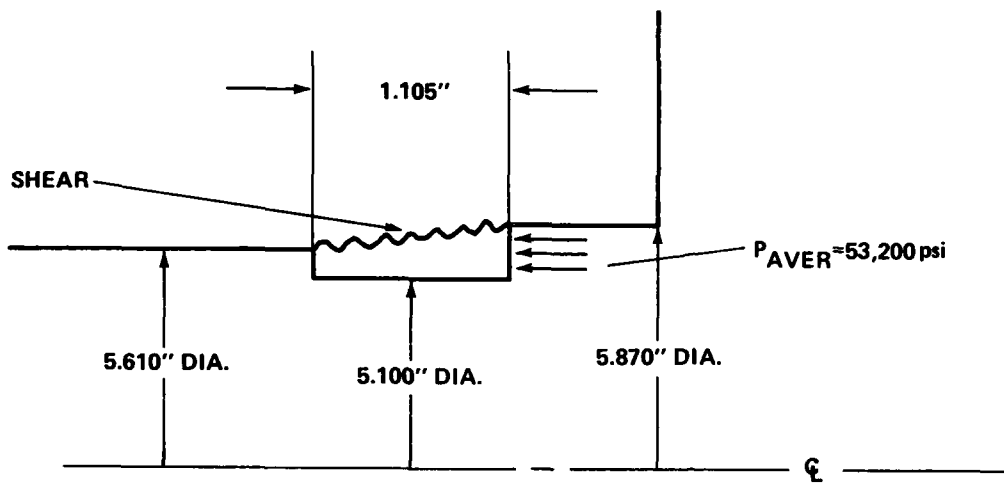
Thus

$$\tau = \frac{16,500(20.6)}{10} = 34,000 \text{ psi}$$

Based on a shear yield of .57 (130,000 psi) = 74,100 psi,  $\tau = 34,000$  psi is no problem.

The downstream diaphragm separator body has its bore lined with two pieces. The upstream liner, or piece "A" is almost identical to the upstream separator body liner previously analyzed. Due to the fact that the loading condition of this piece "A" is so identical, and that the thickness of the shear section is slightly larger than the aforementioned liner, piece "A" will not be analyzed. However, the flange that piece "A" bears against will be investigated for possible bending stress and shear stress problems.

CONSIDER THE FLANGE AS A SIMPLE FIXED END PLATE

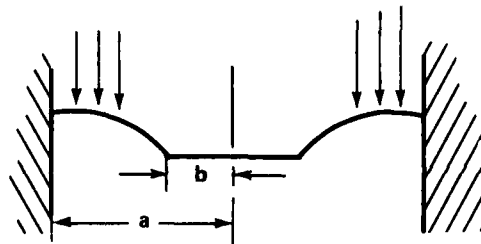


Case 2e from Reference F-6

$$a = \frac{5.87}{2} = 2.935''$$

$$b = \frac{5.1}{2} = 2.55''$$

$$\frac{b}{a} = \frac{2.55}{2.935} = .87$$



The radial stress at the fixed edge is obtained from:

$$\sigma_R = \frac{+6M_R}{t^2}$$

where

$$M_R = K_{mra} q a^2 = \text{radial moment/inch}$$

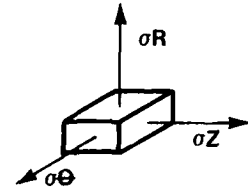
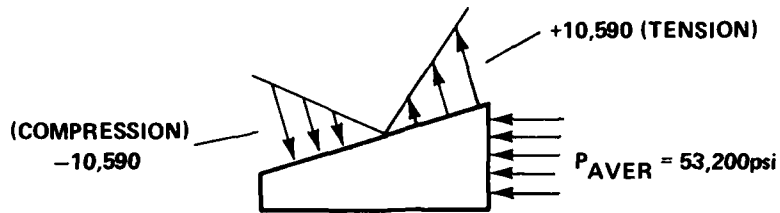
$$K_{mra} = .0047 \text{ (based on } b/a = .87)$$

$$q = 53,200 \text{ psi}$$

$$t = 1.105''$$

Substitution yields:

$$\sigma_R = \frac{\pm 6[(.0047)(53,200)(2.935)^2]}{(1.105)^2} = \pm 10590 \text{ psi}$$



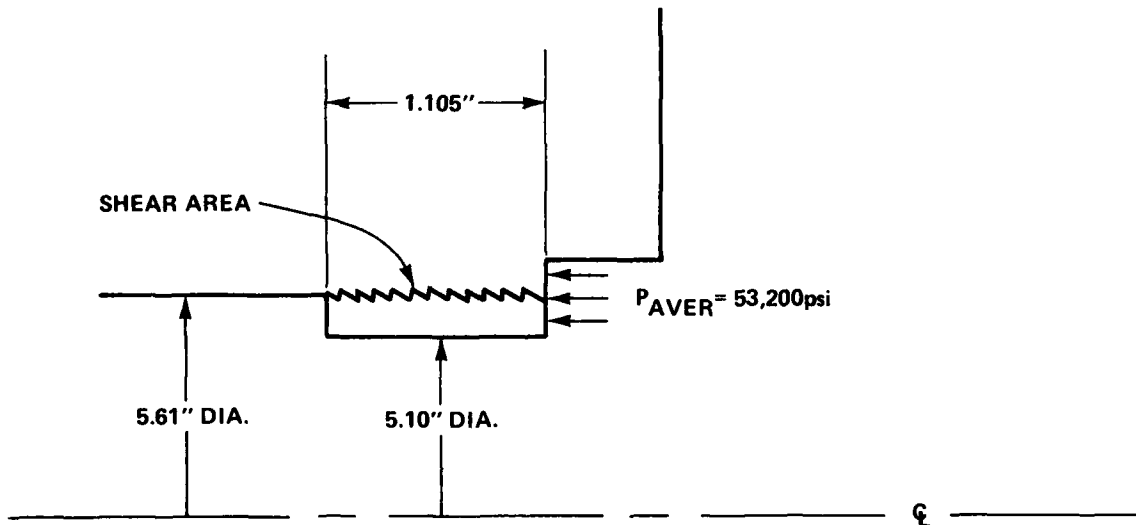
From Tresca, max stress intensity is:

$$\bar{S} = \sigma_R - \sigma_z = +10,590 - (-53,200)$$

$$\bar{S} = 63,790 \text{ psi}$$

Thus,  $\bar{S}$  is much less than 90% of yield ( $.9 \times 130,000 = 117,000$ ) therefore no problem.

#### SHEAR STRESS



The shear stress through the section shown above is determined from:

$$\tau = \frac{P_{\text{aver}} A_L}{A_S}$$

where

$$P_{\text{aver}} = 53,200 \text{ psi}$$

$$A_L = \pi/4[(5.61)^2 - (5.1)^2] = 4.3 \text{ in}^2$$

$$A_S = \pi(5.61)(1.105) = 19.5 \text{ in}^2$$

Substitution yields:

$$\tau = \frac{53,200(4.3)}{19.5} = 11,740 \text{ psi}$$

This shear value is much less than the shear allowable (.57 x 130,000 = 74,100 psi) therefore no problem.



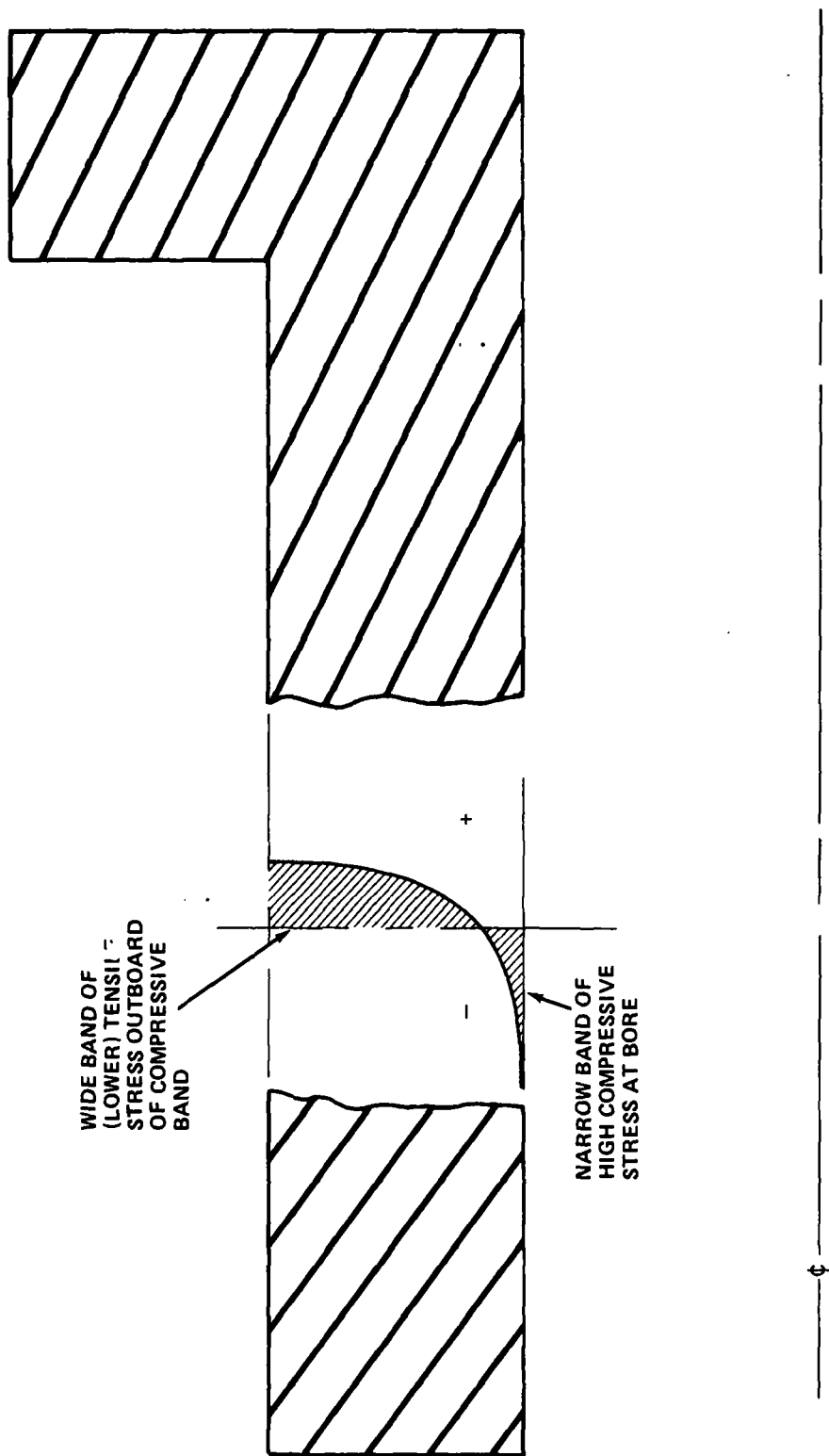


FIGURE F-1. STRESS DISTRIBUTION THROUGH THERMAL LINER

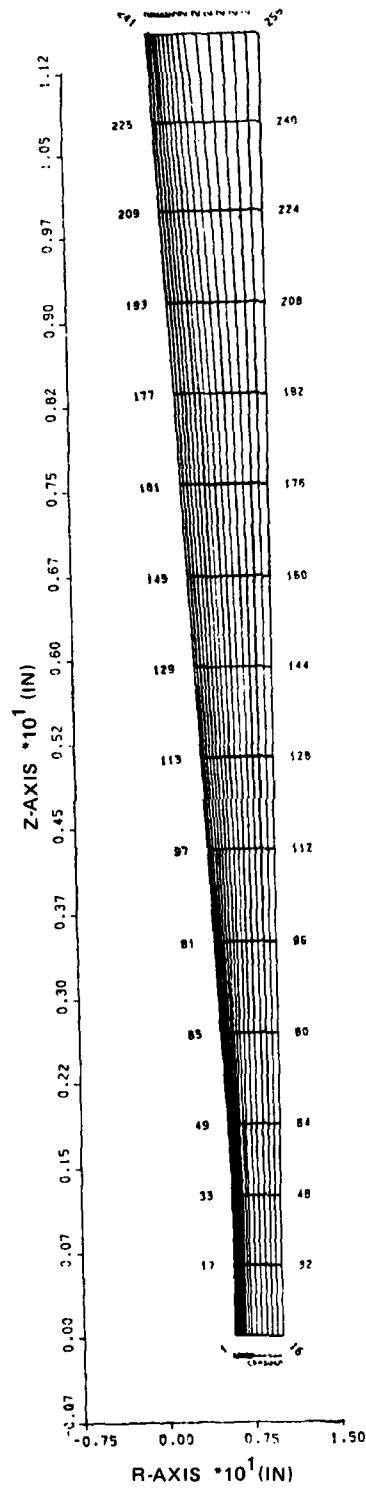


FIGURE F-2. FINITE ELEMENT MESH

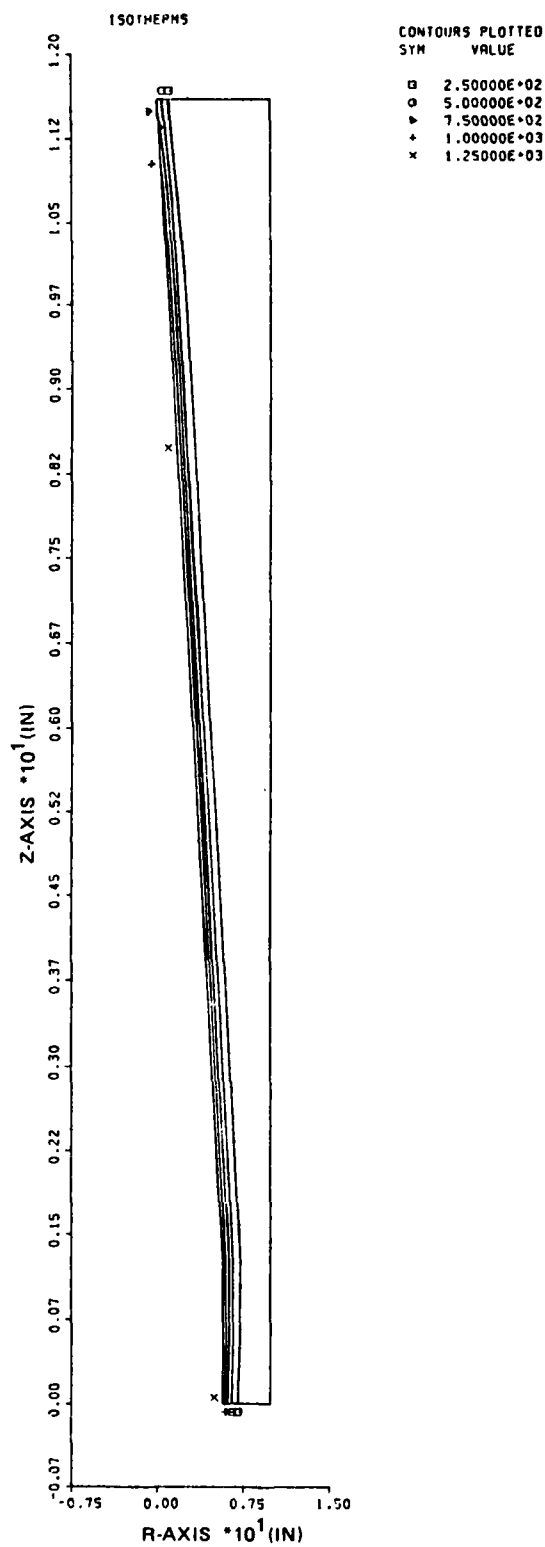


FIGURE F-3. ISOTHERMS IN A MACH 10 INNER SLEEVE 0.5 SECOND AFTER DIAPHRAGM RUPTURE

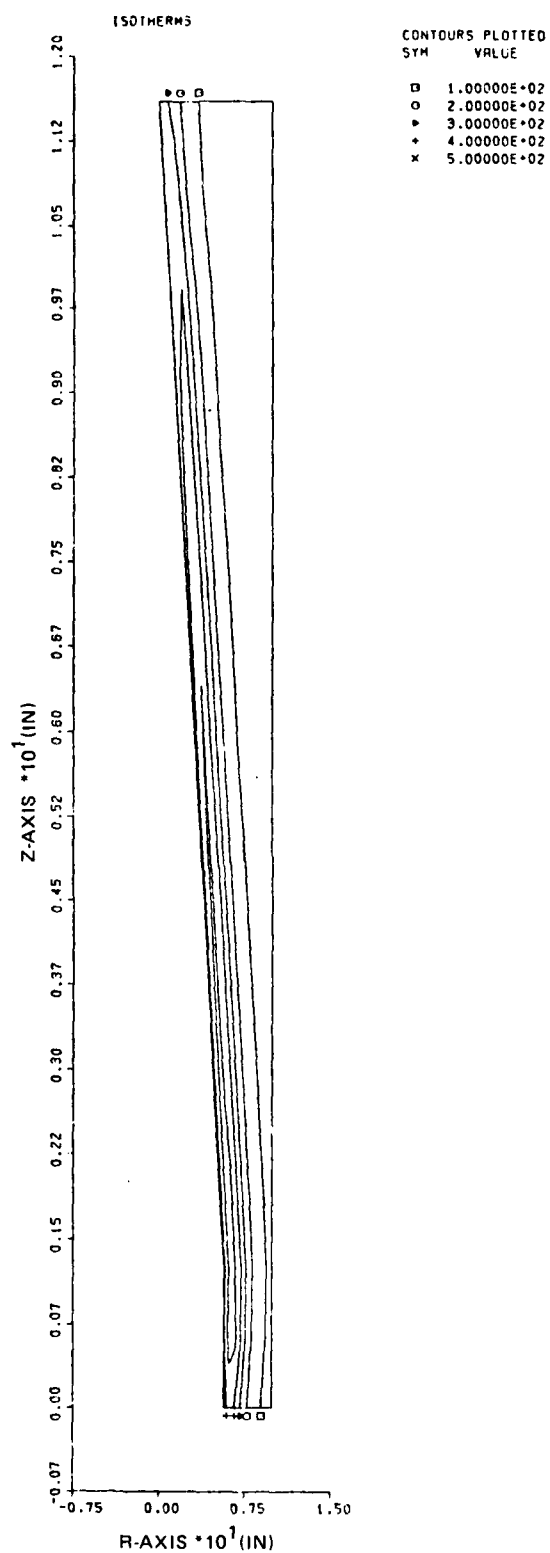


FIGURE F-4. ISOTHERMS IN A MACH 10 INNER SLEEVE 0.95 SECOND AFTER DIAPHRAGM RUPTURE

TABLE F-1. PRESSURE CONTAINMENT COMPONENT STRESSES

COMPONENT	O.D. (IN)	I.D. (IN)	K	INTERNAL PRESSURE			LOCKUP LOAD	
				$\sigma_\theta$ (PSI)	$\sigma_R$ (PSI)	$\sigma_z$ (PSI)	BEARING AREA (IN <sup>2</sup> )	$\sigma_z$ (PSI)
HORIZONTAL ELBOW FLANGE	13.875	5.0	—	28,567	-22,000	<sup>0</sup> (-18,307)	101.6	-18,307
THERMOCOUPLE RING	13.875	7.5	2.5	100,408	-22,000	<sup>0</sup> (-18,307)	101.6	-18,307
		9.125" DIA	—	55,500	-22,000	<sup>0</sup> (-23,134)	80.4	-23,134
FLOW RESTRICTOR HOUSING	13.875	9.0	—	53,936	-22,000	<sup>0</sup> (-22,628)	82.2	-22,628
UPSTREAM SEPARATOR BODY	13.875	5.875	2.5	79,000	-22,000	<sup>0</sup> (-26,600)	70.0	-26,600
DOWNSTREAM SEPARATOR BODY	13.875	5.875	2.5	79,000	-22,000	<sup>0</sup> (-26,600)	70.0	-26,600
PARTICLE SEPARATOR HOUSING	14.5	8.5	2.5	112,600	-22,000	<sup>0</sup> (-20,700)	$\frac{\pi}{4} [13^2 - 7.406^2]$ = 90	-20,700

NOTE: VALVES IN PARENTHESES ARE THE COMBINED  
VALUES OF  $\sigma_z$  FOR THE TWO LOADING CONDITIONS

TABLE F-2. ASME CODE CRITERIA AND FATIGUE LIFE PARAMETERS

COMPONENT	MATERIAL PROPERTIES		ASME CODE CRITERIA				FATIGUE LIFE PARAMETERS					
	$\sigma_y$ (PSI)	$\sigma_{ULT}$ (PSI)	LESSER OF $2/3 \sigma_y$ OR $1/2 \sigma_{ULT}$	$\bar{S}$ (PSI)	$S_{ijMAX}$ (PSI)	$S_{ijMIN}$ (PSI)	$S_A$ (PSI)	$S_M$ (PSI)	$S'$ (MEAN) (PSI)	SEQ (PSI)	N (CYCLES)	
HORIZONTAL ELBOW FLANGE	120,000	140,000	70,000	18,221	50,567	-18,307	34,437	16,130	16,130	36,452	140,000	
THERMOCOUPLE RING	120,000	140,000	70,000	33,602	122,408	-23,134	72,771	49,637	47,229	90,832	1,700	
FLOW RESTRICTOR HOUSING	120,000	140,000	70,000	49,245	76,564	-22,628	49,596	26,968	26,968	55,075	17,000	
UPSTREAM SEPARATOR BODY	120,000	140,000	70,000	22,700	105,600	-26,600	66,100	39,500	39,500	78,526	3,600	
DOWNSTREAM SEPARATOR BODY	120,000	140,000	70,000	22,700	105,600	-26,600	66,100	39,500	39,500	78,526	3,600	
PARTICLE SEPARATOR HOUSING	120,000	140,000	70,000	39,297	* 134,600	-20,700	77,650	56,950	42,350	93,873	1,600	

TABLE F-3. TABULATED TUNNEL GAS PROPERTIES AND HEAT TRANSFER COEFFICIENTS AT THE INSIDE SURFACE OF THE INNER SLEEVE

TIME AFTER DIAPHRAGM BURST (SEC)	TEMPERATURE OF N <sub>2</sub> (°F)	VELOCITY OF N <sub>2</sub> (FT/S)	K FOR N <sub>2</sub> $\left(\frac{\text{BTU}}{\text{IN}^2\text{-SEC-}^\circ\text{F}}\right)$	$\rho$ FOR N <sub>2</sub> (LB/FT <sup>3</sup> )	PRESSURE OF N <sub>2</sub> (P.S.I.)	$\mu$ FOR N <sub>2</sub> (LB/SEC-FT)	h $\left(\frac{\text{BTU}}{\text{IN}^2\text{-SEC-}^\circ\text{F}}\right)$
0.1	1080	684	$1.27 \times 10^{-6}$	20.9	17,500	$3.50 \times 10^{-5}$	0.0255
0.2	1375	684	$1.62 \times 10^{-6}$	20.9	20,000	$4.20 \times 10^{-5}$	0.0282
0.3	1440	684	$1.67 \times 10^{-6}$	18.1	20,000	$4.30 \times 10^{-5}$	0.0252
0.4	1500	684	$1.70 \times 10^{-6}$	18.1	20,000	$4.38 \times 10^{-5}$	0.0255
0.5	1500	684	$1.70 \times 10^{-6}$	20.9	20,000	$4.38 \times 10^{-5}$	0.0255
0.6	1400	684	$1.67 \times 10^{-6}$	20.5	20,000	$4.26 \times 10^{-5}$	0.0287
0.7	1260	684	$1.50 \times 10^{-6}$	31.0	20,000	$4.08 \times 10^{-5}$	0.0263
0.8	450	684	$1.30 \times 10^{-6}$	34.0	20,000	$3.48 \times 10^{-5}$	0.0361
0.9	340	684	$1.25 \times 10^{-6}$	34.0	20,000	$3.42 \times 10^{-5}$	0.0378
1.0	300	684	$1.20 \times 10^{-6}$	34.0	20,000	$3.36 \times 10^{-5}$	0.0368
1.1	300	684	$1.20 \times 10^{-6}$	34.0	20,000	$3.36 \times 10^{-5}$	0.0368
1.2	300	684	$1.20 \times 10^{-6}$	34.0	20,000	$3.36 \times 10^{-5}$	0.0368
1.3	300	684	$1.20 \times 10^{-6}$	34.0	20,000	$3.36 \times 10^{-5}$	0.0368
1.4	300	684	$1.20 \times 10^{-6}$	34.0	20,000	$3.36 \times 10^{-5}$	0.0368
1.5	300	684	$1.20 \times 10^{-6}$	34.0	20,000	$3.36 \times 10^{-5}$	0.0368
1.6	300	684	$1.20 \times 10^{-6}$	34.0	20,000	$3.36 \times 10^{-5}$	0.0368
1.7	300	684	$1.20 \times 10^{-6}$	34.0	20,000	$3.36 \times 10^{-5}$	0.0368
1.8	300	684	$1.20 \times 10^{-6}$	34.0	20,000	$3.36 \times 10^{-5}$	0.0368
1.9	300	684	$1.20 \times 10^{-6}$	34.0	20,000	$3.36 \times 10^{-5}$	0.0368
2.0	300	684	$1.20 \times 10^{-6}$	34.0	20,000	$3.36 \times 10^{-5}$	0.0368

REFERENCES

- F-1. O'Donnell and Associates, Inc., Hypervelocity Wind Tunnel Components Structural Evaluation-Final Report, May 1979.
- F-2. ASME Boiler and Pressure Vessel Code, Section VIII, Division 2, 1968.
- F-3. Kavetsky, R. A., Mach 10/14 Operations in the NSWC Hypervelocity Wind Tunnel No. 9 (Vertical Heater Vessel Leg), NSWC TR 80-487, Jul 1982.
- F-4. Streeter, V. L., Fluid Mechanics, Fifth Edition, (New York: McGraw-Hill, 1971).
- F-5. Holman, J. D., Heat Transfer, (New York: McGraw-Hill, 1976).
- F-6. Roark, R. J., Formulas for Stress and Strain, Fourth Edition, (New York: McGraw-Hill, 1965).



## APPENDIX G

## THROAT BLOCK INSERT CARRIER ANALYSIS

## INTRODUCTION

This appendix presents the results of a preliminary Finite Element static stress analysis of a Nozzle Throat Insert Carrier (NSWC Dwg. #77-E-1130). This component is located in the diaphragm assembly of the high Reynolds No. (HIRE) Mach 10 leg of the Hypervelocity Wind Tunnel (Tunnel 9). The mechanical loadings assumed to act on the piece in this analysis cover the case of a COLD SHAKEDOWN run only which does not involve consideration of elevated temperature performance of the component.

## BACKGROUND

A view of the Mach 10 diaphragm assembly, in Figure G-1, shows how the Nozzle Throat Insert Carrier is installed and its relation to adjacent pieces. As shown, the Carrier "carries" the Nozzle Throat Insert. The Carrier in turn is held in place inside the Nozzle Block by means of both an interference shrink fit (at the cylindrical interface between Carrier and Nozzle Block) and a flange on the upstream end of the Carrier (Nozzle Block Flange) which bears against the Nozzle Block. Note that the Particle Separator Housing bears against the Nozzle Block Flange of the Carrier and the exit nozzle is attached to the downstream end of the Carrier by means of a bolted flange connection. The Insert Carrier itself is shown in Figure G-2 which indicates the various parts of the component.

## PRESENTATION OF PROBLEM

The Insert Carrier is subjected to a variety of mechanical loads. These can be broken down as follows:

1. Pressure loading resulting from nozzle flow pressure.
2. Bearing load on Throat Insert Flange resulting from Throat Insert bearing against this flange.
3. Tensile bolt loading at Exit Nozzle Flange connection resulting from a 'Vacuum Loading' on the Exit Nozzle.

4. Compressive bearing between Nozzle Block and Nozzle Block Flange or Carrier (the Flange at upstream end of Carrier). This loading arises as a result of the loads acting on the Carrier which tend to force Carrier in downstream direction but which are reacted at this flange.

5. Direct compression of the Nozzle Block Flange resulting from the diaphragm lock-up load which compresses the Particle Separator Housing and Nozzle Block together thus "sandwiching" the Nozzle Block Flange.

6. Compressive external pressure over cylindrical surface of Carrier resulting from the shrink fit at the Carrier/Nozzle Block interface.

This analysis was concerned with investigating the loading on the Throat Insert Flange of the Carrier resulting from items (1) and (2) above and was carried out based on a recommendation by J. Goeller. Preliminary calculations show that the nozzle supply pressure of 20,000 psi, required for the cold shakedown of the Mach-10 HIRE modifications, could result in a maximum Tresca stress intensity in the flange root which would exceed the yield stress of the carrier material, which is Annealed Type 304 stainless.

#### OBJECTIVES/SCOPE OF ANALYSIS

The primary objectives of this analysis were as follows:

1. Obtain a more accurate assessment of the stresses in the Insert Flange than can be obtained using hand calculations by carrying out an elastic, and if necessary, an elastic/plastic, static, finite element analysis of the carrier.
2. Obtain the maximum Tresca stress intensity occurring in the Throat Insert flange root for both the elastic and elastic/plastic analysis. From the elastic results, perform a ratioing calculation, (described later) to obtain the maximum allowable supply operating pressure which would limit Tresca stress to a value below material yield stress.
3. Run a Finite Element case using 4340 stainless steel properties for the Carrier and show that stresses are acceptable for the case of a 20,000 psi supply pressure.

The structural finite element code NOASIS was utilized for this analysis.

#### FINITE ELEMENT MODEL

##### Idealizations of Actual Structure

Several idealizations were made in the development of the finite element model in order to facilitate computer solution within a reasonable time. A computer plot of the model, showing boundary element numbers is given in Figure G-3. The plot in Figure G-4 indicates boundary node numbers. The nodes and elements are numbered in succession along the r-axis, hence, I.D. numbers of

interior nodes and elements can be easily determined from the plots. The major structural idealizations which apply to the Finite Element model in Figure G-3 are as follows:

1. Radiused corners and chamfered edges have been squared off.
2. O-ring groove in downstream face of the Insert Flange as well as tapped holes have been omitted. Buttress threads in Nozzle Block have been replaced by a straight edge.
3. The lock-up load is neglected since the Throat Insert Flange, which was the main concern of this analysis, is, for all practical purposes, not affected by it.
4. A 0.0005 inch radial interference boundary condition is applied to the cylindrical Carrier/Nozzle Block interface defined by the line segment between nodes #30 and 460.
5. The Nozzle Block Flange does not bear against the Nozzle Block. Instead, the four nodes which define bearing face of the flange (#478-481) are simply restrained against motion in the z-direction and thus react out the net axial load applied to the structure. Elements #431-434 (shaded in Figure G-3) are actually "void" elements which create a clearance gap between the flange and Nozzle Block. This type of boundary condition, with the flange bearing against the Nozzle Block and the axial loads reacted by the buttress threads, can be obtained with the current model after some minor changes to the input data. It was felt that the selected restraint, although simplistic, would not seriously affect the results obtained at the Insert Flange region which is located on the opposite end of the Carrier body, far away from the restraint. The Nozzle Block, then, does not react the axial loads, but is required in the model in order to impose the shrink fit boundary condition.

#### Loading

The loading on the Finite Element model is described in Figure G-5. The following should be noted:

1. All loadings consist of boundary normal pressure loads.
2. O-ring seals limit the area over which certain pressure loads act on the model.
3. The bearing pressure due to the Nozzle Throat Insert bearing against the Insert Flange is calculated in the Enclosure.
4. The loading due to the Exit Nozzle Flange connection is idealized as a uniform pressure acting over an annular surface with a width equal to the Flange bolt diameter of .875 inches.

Material Properties

Due to the lack of time it was not possible to obtain stress-strain curves for Type 304 Annealed stainless from which the existing Carrier is fabricated. A stress/strain curve is needed to construct a bilinear stress strain curve which is required by the DOASIS code for an elastic/plastic analysis. Instead, a survey for Type 301 Annealed stainless, which has properties close to 304, was used to generate a bilinear curve for 304. Figure G-6 shows the curve and the bilinear construction. The line segments for E and  $E_T$  have been made to intersect at a value of stress equal to 30,000 psi which is the yield strength of 304. In summary the following mechanical properties were used for Type 304 Annealed stainless:

<u>TYPE 304 S.S.</u>	<u>PROPERTIES USED</u>
Young's Mod. E	$28.7 \times 10^6$ psi
Tangent Mod. $E_T$	$2.53 \times 10^6$ psi
Pois. Ratio $\nu$	0.264
Yield Str. $\sigma$	30,000 psi

The Nozzle Block is fabricated out of "Alloy Steel" having a yield strength of 90,000 psi. The following properties were used for this place.

<u>TYPE 304 S.S.</u>	<u>PROPERTIES USED</u>
Young's Mod. E	$28.7 \times 10^6$ psi
Tan. Mod. $E_T$	$2.53 \times 10^6$ psi
Pois. Ratio $\nu$	0.264
Yield Str. $\sigma$	90,000 psi

As mentioned earlier, an elastic run was made using 4340 material for the carrier. The material properties data which were used for this run are given in the table:

4340 STAINLESS STEEL PROPERTIES

Young's Mod. E	$28.0 \times 10^6$ psi
Poisson's $\nu$	.3
Yield Str. $\sigma$	120,000 psi

## RESULTS AND DISCUSSION

General

The elastic analysis using Type 304 stainless for the Carrier material showed that stresses in the carrier exceeded the 30,000 psi yield strength. Hence, an elastic/plastic analysis was performed and results of this run are summarized in the plot in Figure G-7. The numbered regions indicate where an equivalent stress (similar to the Tresca stress,  $\bar{\sigma}$  describes a multiaxial stress state with one number which can be compared to the material yield stress) exceeds the yield stress.

304 El./Pl.

$$\sigma_t = \sigma_r - \sigma_z = (20,000) - (-31,182)$$

$$\sigma_t = 51,182 \text{ psi}$$

The 20,000 psi supply pressure results in a maximum Tresca stress of 72,182 psi (based on principal stresses), or 62,682 psi (based on normal stresses at surface) for the elastic case. The maximum supply pressure  $P_s$  which would limit  $\sigma_t$  to below the yield stress can be obtained by using the ratioing formula:

$$P_{s \text{ allow}} = \frac{\sigma_y}{\sigma_{t \text{ elastic}}} \cdot P_{s \text{ elastic}}$$

Using this formula, the following estimates of  $P_s$  allow are made:

From Normal Stresses at Surface

$$P_{s \text{ allow}} = \frac{30,000}{62,682} \times 20,000 = 9572 \text{ psi}$$

From Principal Stresses

$$P_{s \text{ allow}} = \frac{30,000}{72,182} \times 20,000 = 8312 \text{ psi}$$

Based on these preliminary results, to preclude yielding in the flange the nozzle supply pressure should probably be limited to 10,000 psi.

SUMMARY

A Finite Element static stress analysis was carried out on a TUN-9 Nozzle Throat Insert Carrier, intended for use in the Mach-10 HIRE Facility. A room temperature loading condition, corresponding to a cold shakedown tunnel run, with a nozzle supply pressure equal to 20,000 psi, was assumed to apply in all cases examined. The results of this analysis are as follows:

1. For a 20,000 psi supply pressure the maximum Tresca stress intensity in the Throat Insert flange region of the existing Carrier would probably exceed the material yield strength.

2. Based on results of an all-elastic stress analysis of the existing carrier under the 20,000 psi supply pressure loading, the maximum allowable nozzle supply pressure would have to be limited to 10,000 psi in order to preclude yielding in the Throat Insert Flange root. Thus approval for 10,000 psi max operation appears reasonable.

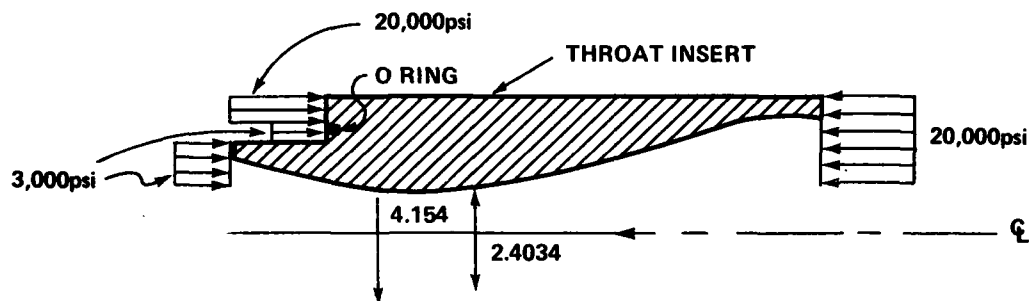
3. For the case of a 20,000 psi supply pressure, maximum Tresca stress intensities, in a Carrier fabricated from 4340 stainless steel, would probably remain below material yield stress.

Thermal and fatigue affects were not considered in this analysis.

# CALCULATION OF THROAT INSERT BEARING LOAD AND EXIT NOZZLE FLANGE BOLT LOAD

## THROAT BEARING LOAD

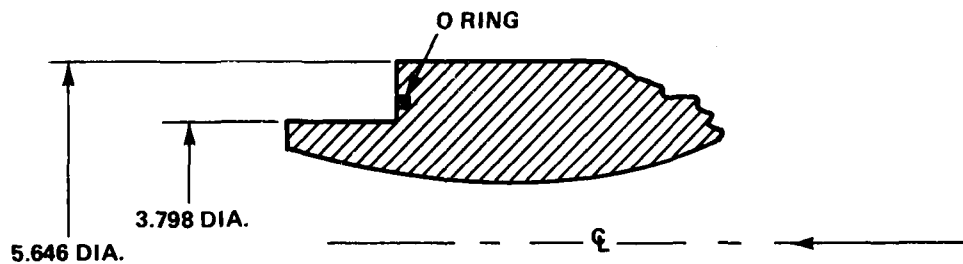
O-ring diameter (nozzle throat): 4.154"  
 Nozzle throat diameter: 2.4034"  
 Supply pressure: 20,000 psi  
 Down steam pressure: 3,000 psi



$$F_{th} = \pi/4((4.154)^2 - (2.4034)^2) (20,000 - 3000)$$

$$F_{th} = 153,270 \text{ lbs}$$

## BEARING PRESSURE (Due To Throat Load Only)



$$P_{th} = F_{th}/A$$

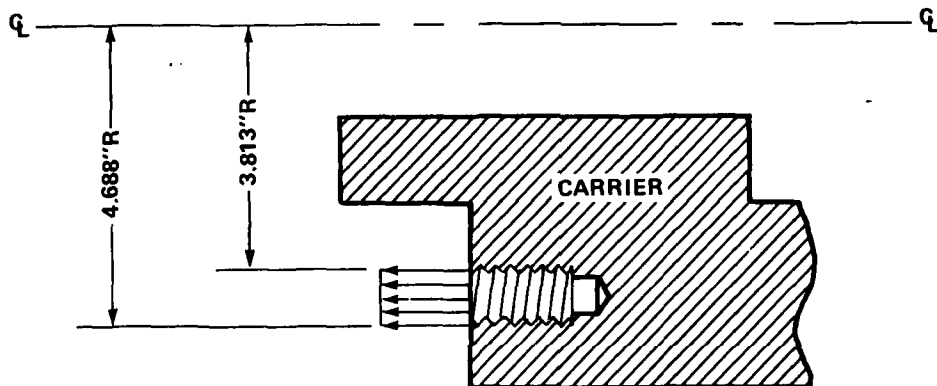
$$P_{th} = \frac{153,270}{\frac{\pi}{4} (5.646^2 - 3.798)^2}$$

$$P_{th} = 11,182 \text{ psi}$$

EXIT NOZZLE FLANGE LOAD

Vac. Load = 42,000 lbs

Determine equivalent pressure acting over axis symmetric annulus area:



$$P = F_{vacuum}/A_{annulus}$$

$$P = 42,000/\frac{\pi}{4}(4.688^2 - 3.813^2)$$

$$P = 7198 \text{ psi}$$



For the run using 4340 stainless for the carrier material, the maximum value of the equivalent stress  $\bar{\sigma}$  occurred in element #447 (in the Nozzle Block Flange region) and was equal to 74,558 psi. Although this is below yield it is felt that this value of  $\bar{\sigma}$  is misleading since the boundary nodes for the Nozzle Block Flange are made to react the next axial loads instead of being allowed to bear against the Nozzle Block. The maximum value of  $\bar{\sigma}$ , which occurred in the Insert Flange region, was equal to 51,237 psi and occurred in element #113.

Note that the element stresses quoted above occur at the element centroids.

#### Throat Insert Flange

The curves in Figures G-8 through G-12 show stress distributions through the Insert Flange section defined by elements #3, 9, 15, 35, 55, 75 and 95. Element centroid stresses were plotted and curves fitted and extrapolated to obtain the stress values at the surface of the butt shoulder near the Insert Flange root. Note that Figure G-8 plots element normal stresses in the r, z, and  $\theta$  directions for the Type 304 elastic case. In Figure G-9 the principal stresses are plotted. Since the shear stress at the surface is zero the normal stresses ( $\sigma_r$ ,  $\sigma_z$  and  $\sigma_\theta$ ) they are principal stresses and so should correspond to the principal stress values in Figure G-9 at this point. As the figures show, exact correlation was not obtained for the  $\sigma_r$  stress and this is probably due to a too coarse mesh and inaccuracies in the extrapolations.

Tresca stresses are computed for the Type 304 elastic case from the principal stresses, in Figure G-9, and from the normal stresses at the surface in Figure G-8, and also for the Type 304 elastic/plastic case, in Figure G-10, as follows:

#### 304 El. (Normal Stress at Surface)

$$\sigma_t = \sigma_r - \sigma_z = (31,500) - (-31,182)$$

$$\sigma_t = 62,682 \text{ psi}$$

#### 304 El. (Principal Stresses at Surface)

$$\sigma_t = \sigma_{\max} - \sigma_{\min} = (41,000) - (-31,182)$$

$$\sigma_t = 72,182 \text{ psi}$$

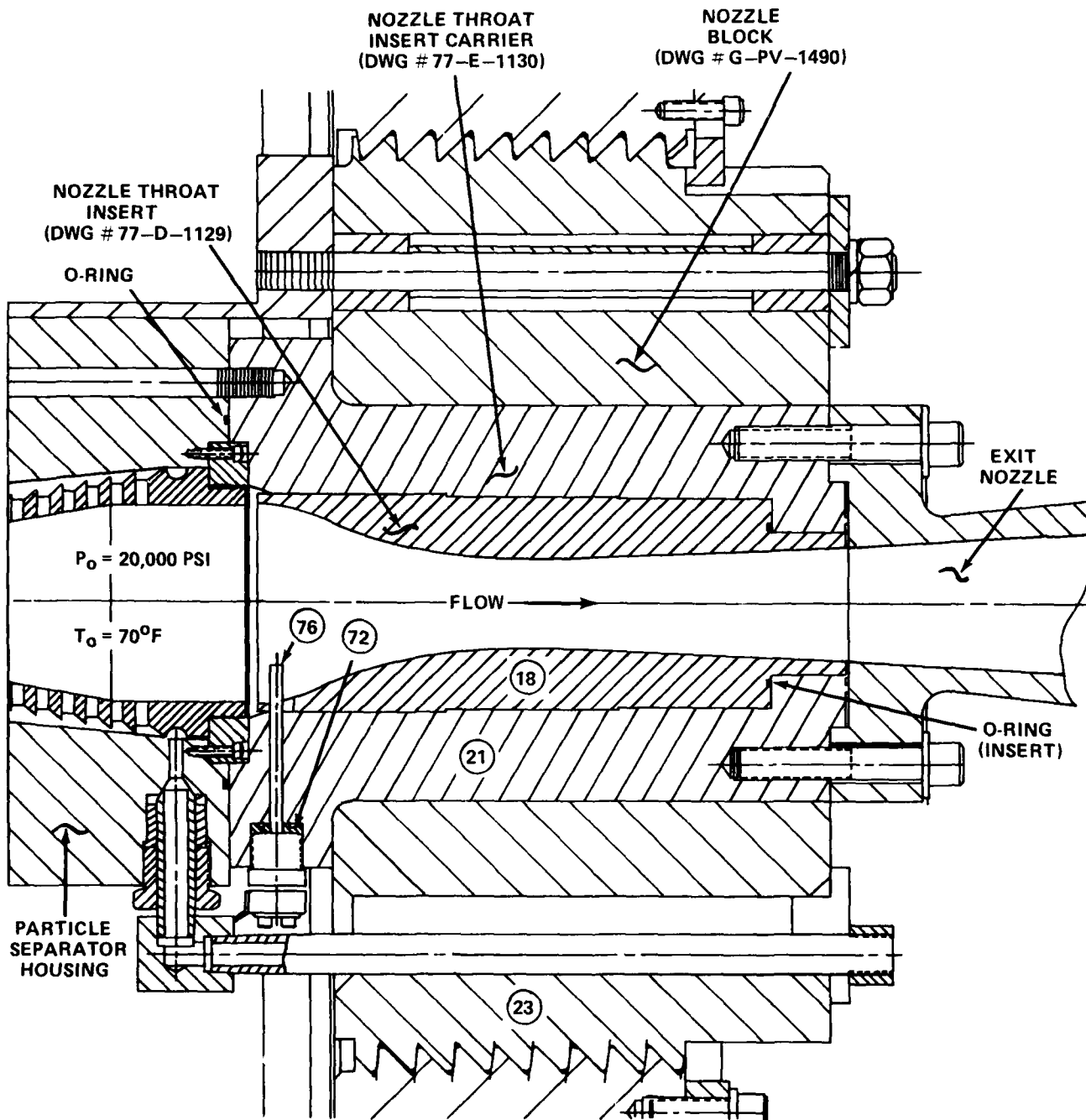
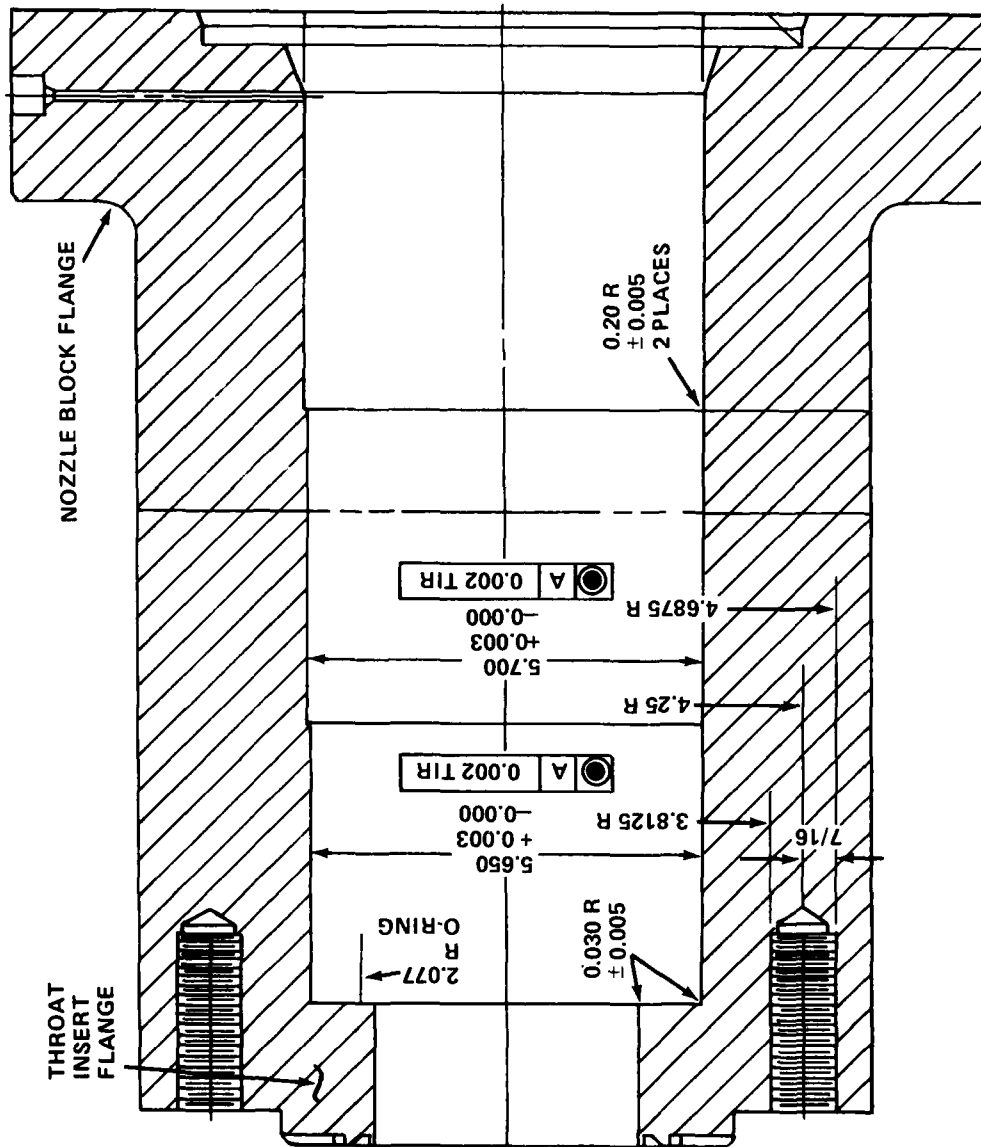


FIGURE G-1. SECTION OF ASSY DWG # 77-F-1131 SHOWING PLACEMENT OF CARRIER



**FIGURE G-2. DETAIL OF NOZZLE THROAT CARRIER FROM DWG # 77-E-1130**

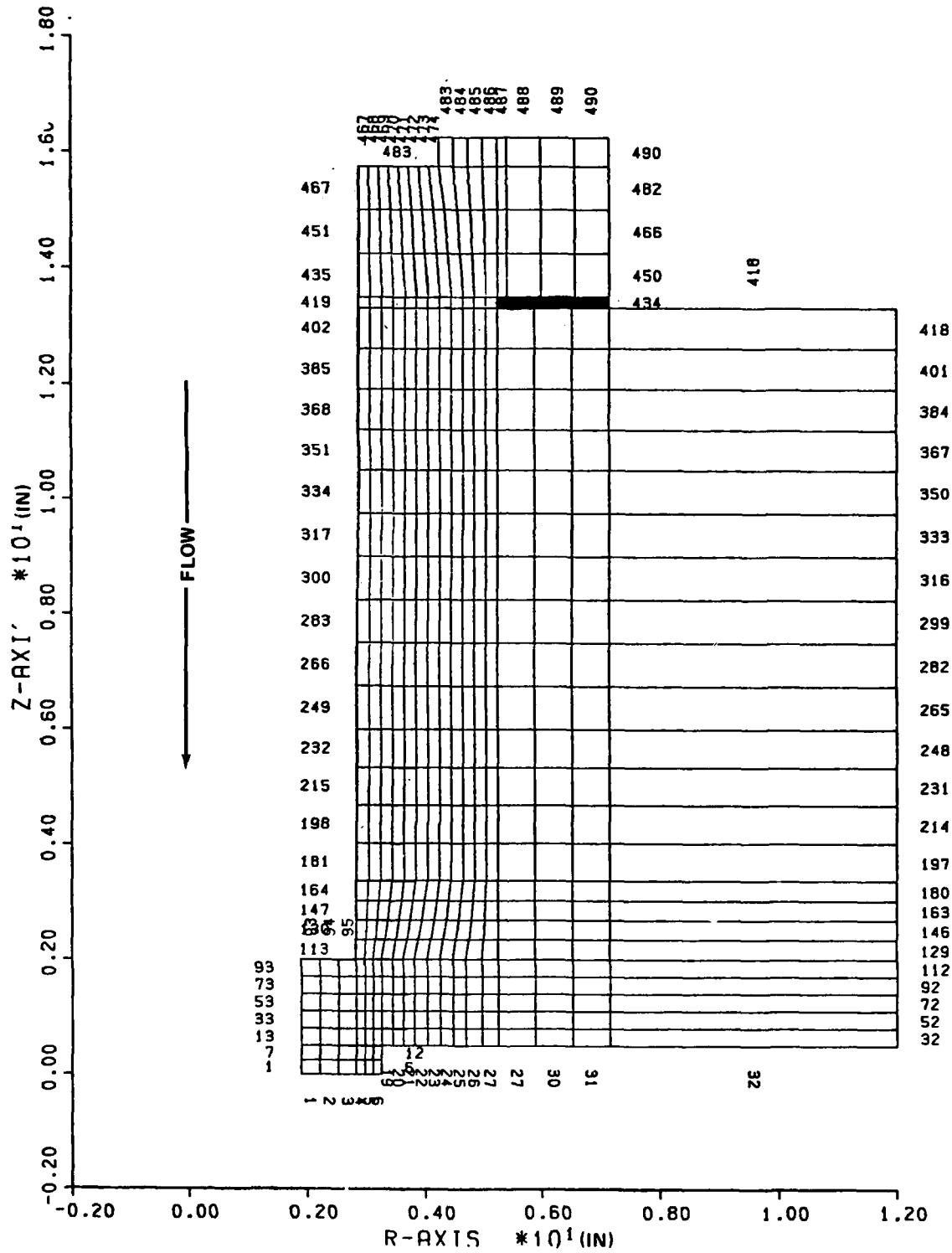


FIGURE G-3. MACH 10 NOZZLE - THROAT INSERT CARRIER - ELEMENT NUMBERS

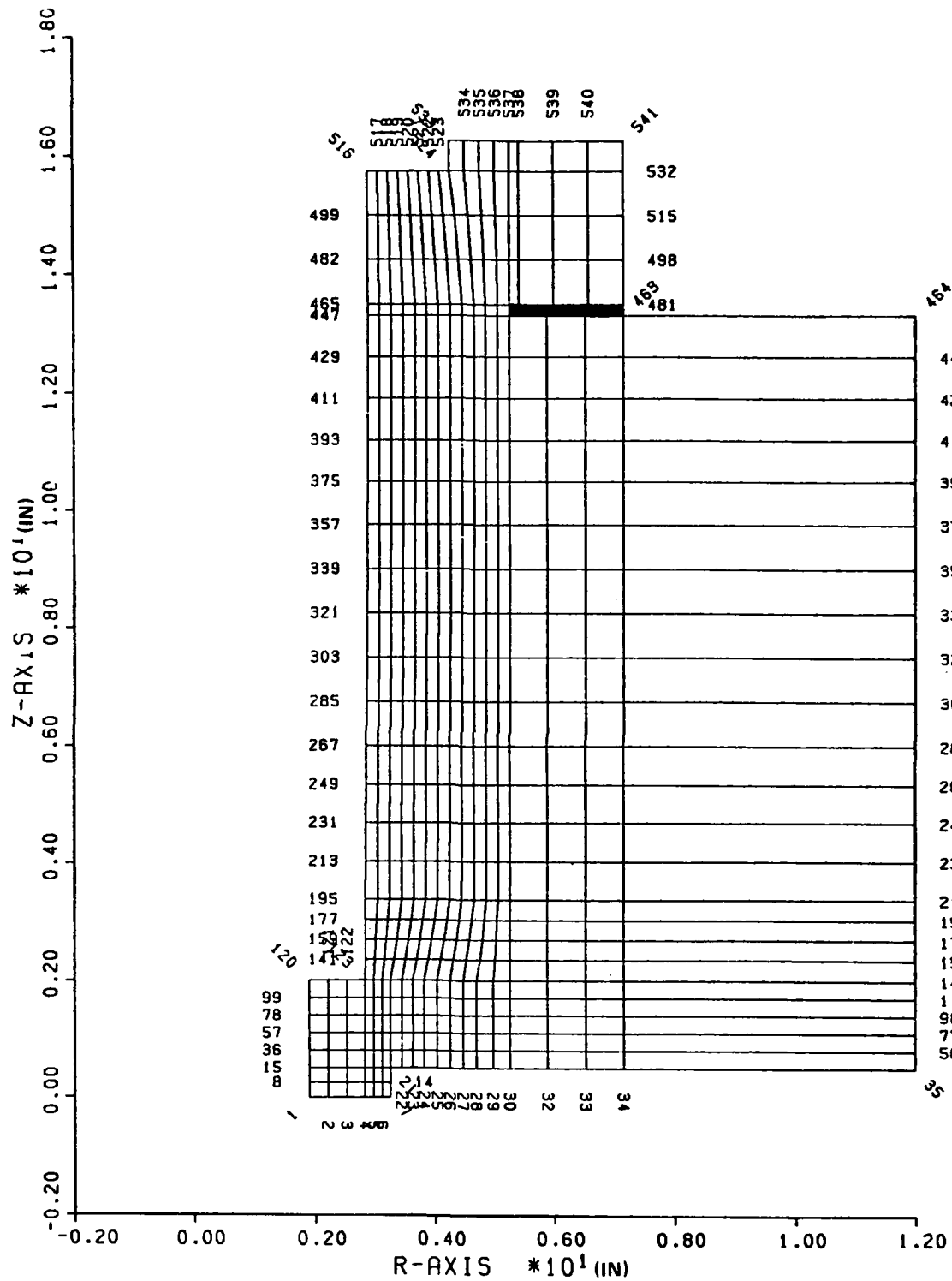


FIGURE G-4. MACH 10 NOZZLE - THROAT INSERT CARRIER - NODE NUMBERS

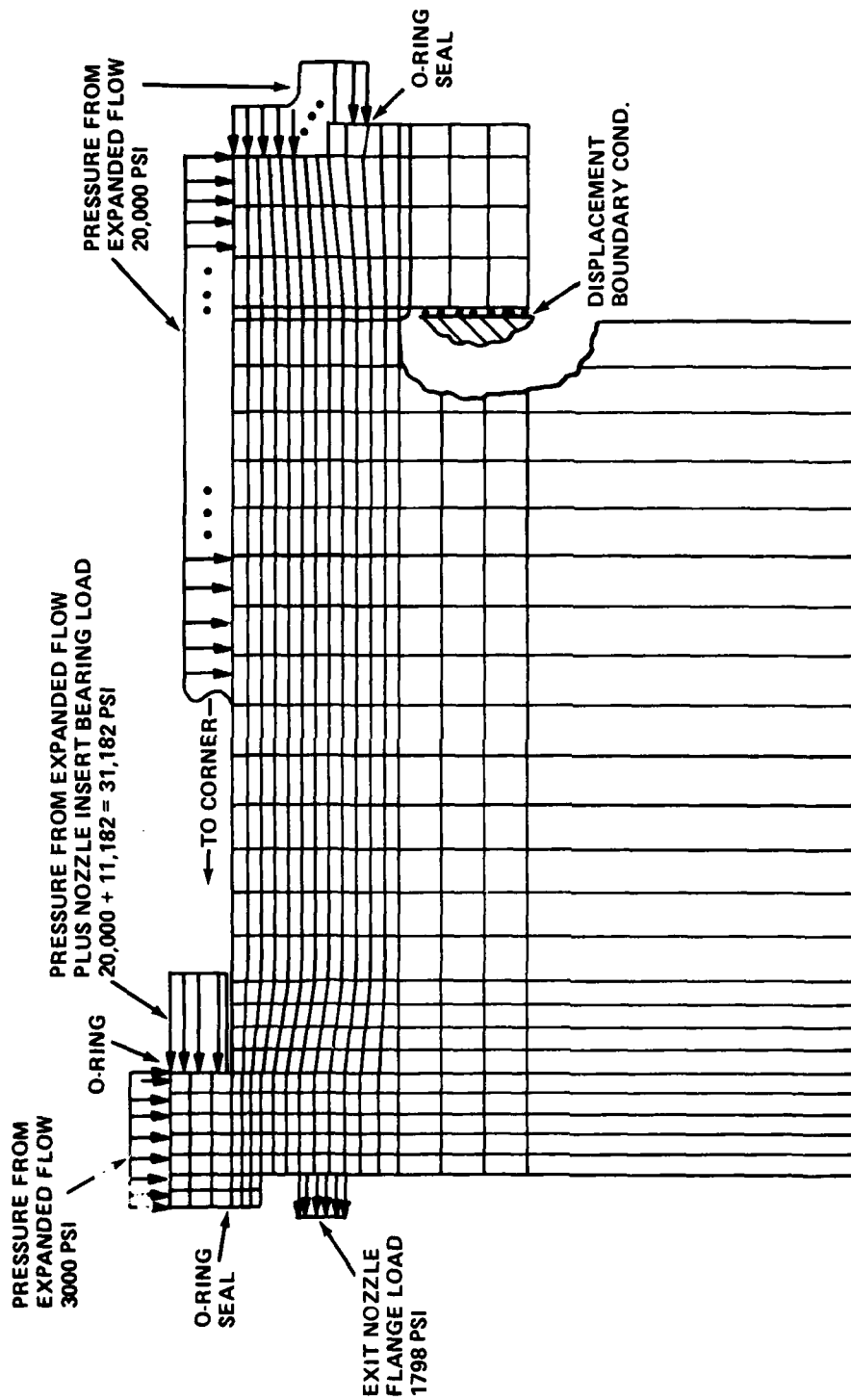


FIGURE G-5. PRESSURE & DISPLACEMENT BOUNDARY CONDITIONS FOR FINITE ELEMENT MODEL

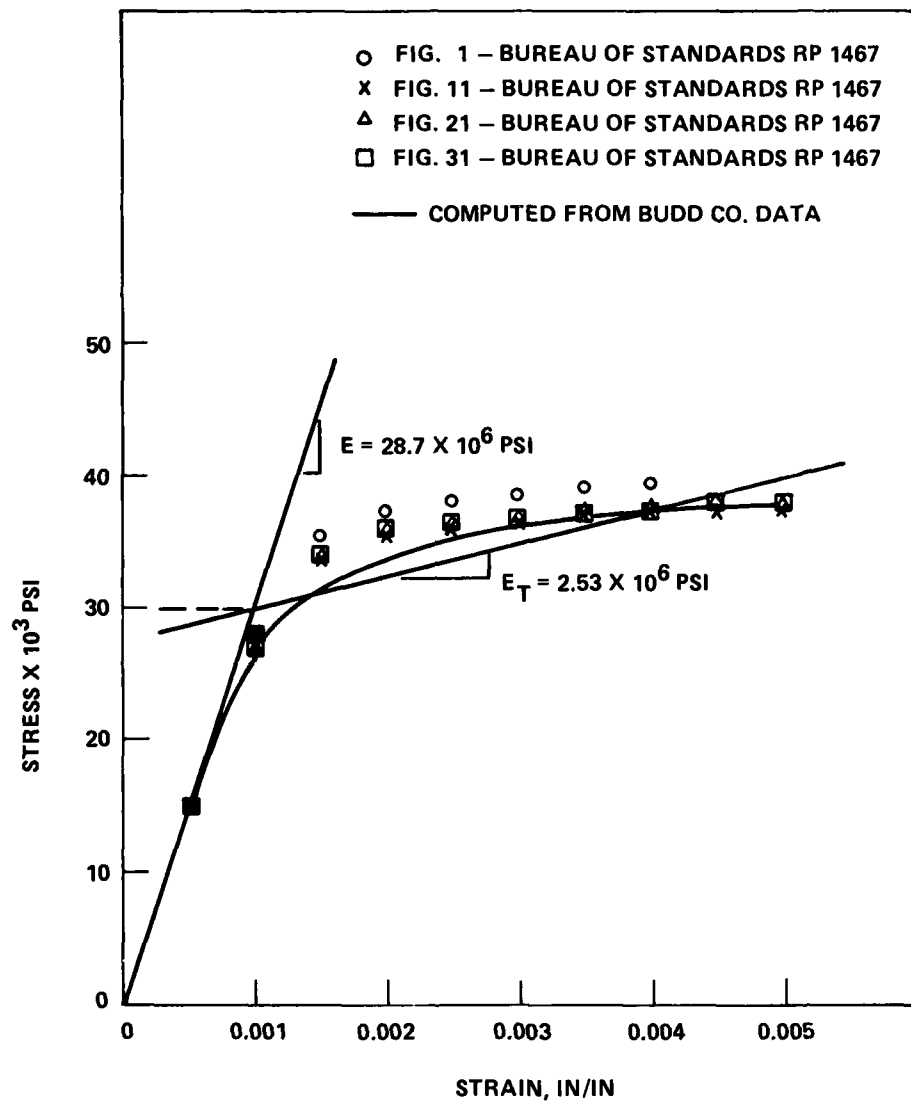
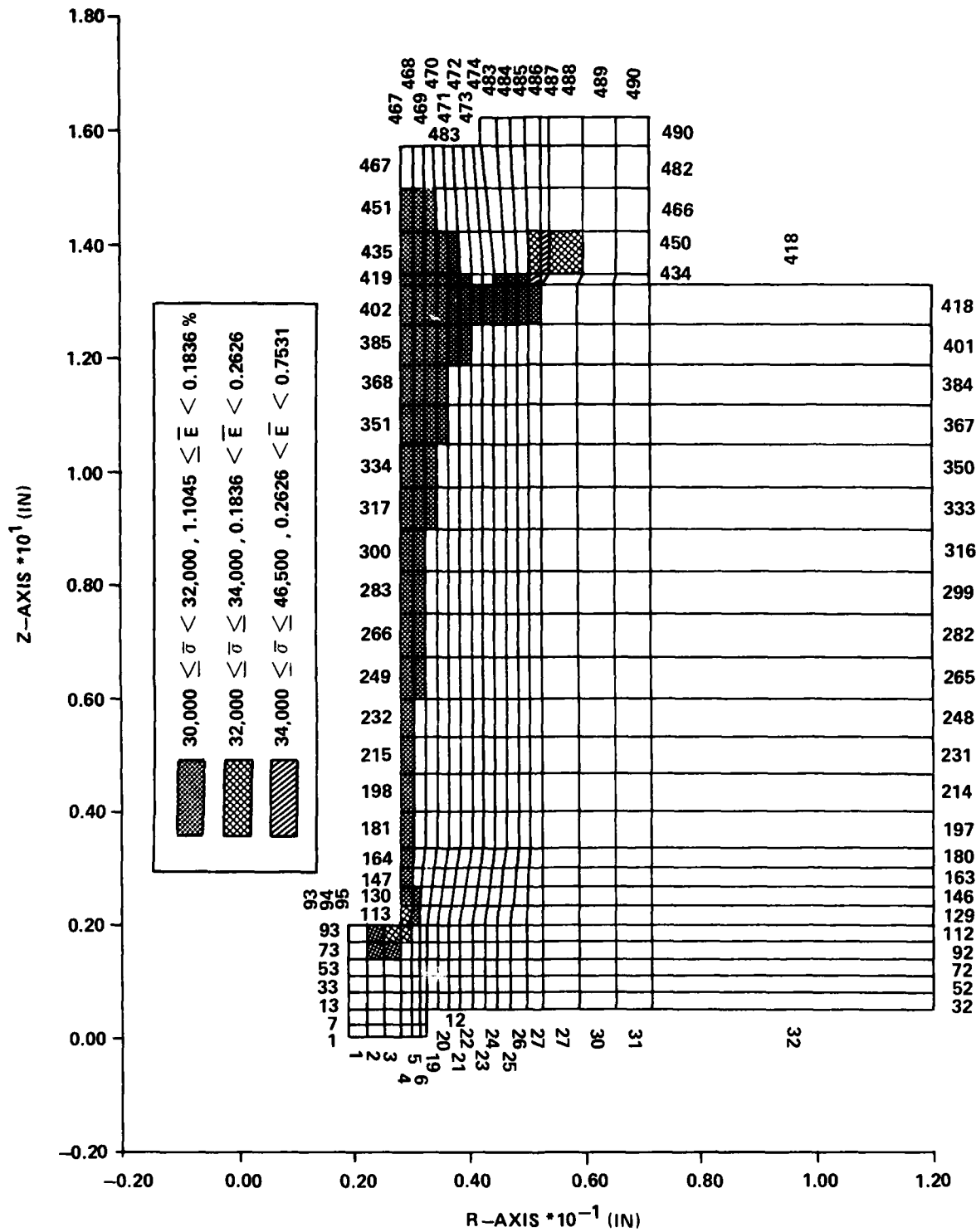


FIGURE G-6. CONSTRUCTION OF BILINEAR STRESS - STRAIN CURVE FOR 304 ANNEALED STAINLESS





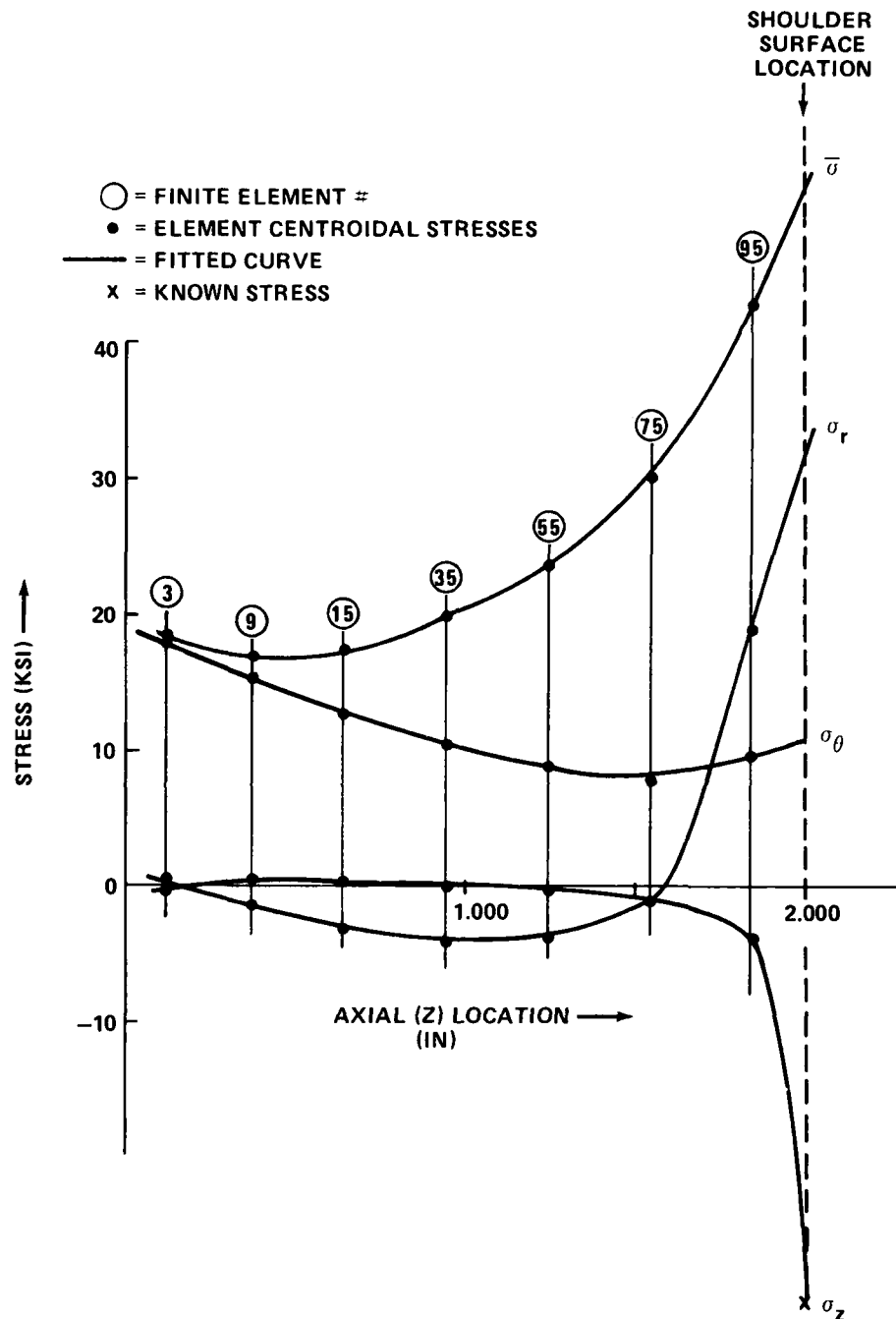


FIGURE G-8. STRESS DISTRIBUTIONS THRU NOZZLE CARRIER FLANGE THICKNESS —  
 TYPE 304 STAINLESS STEEL, ELASTIC CASE

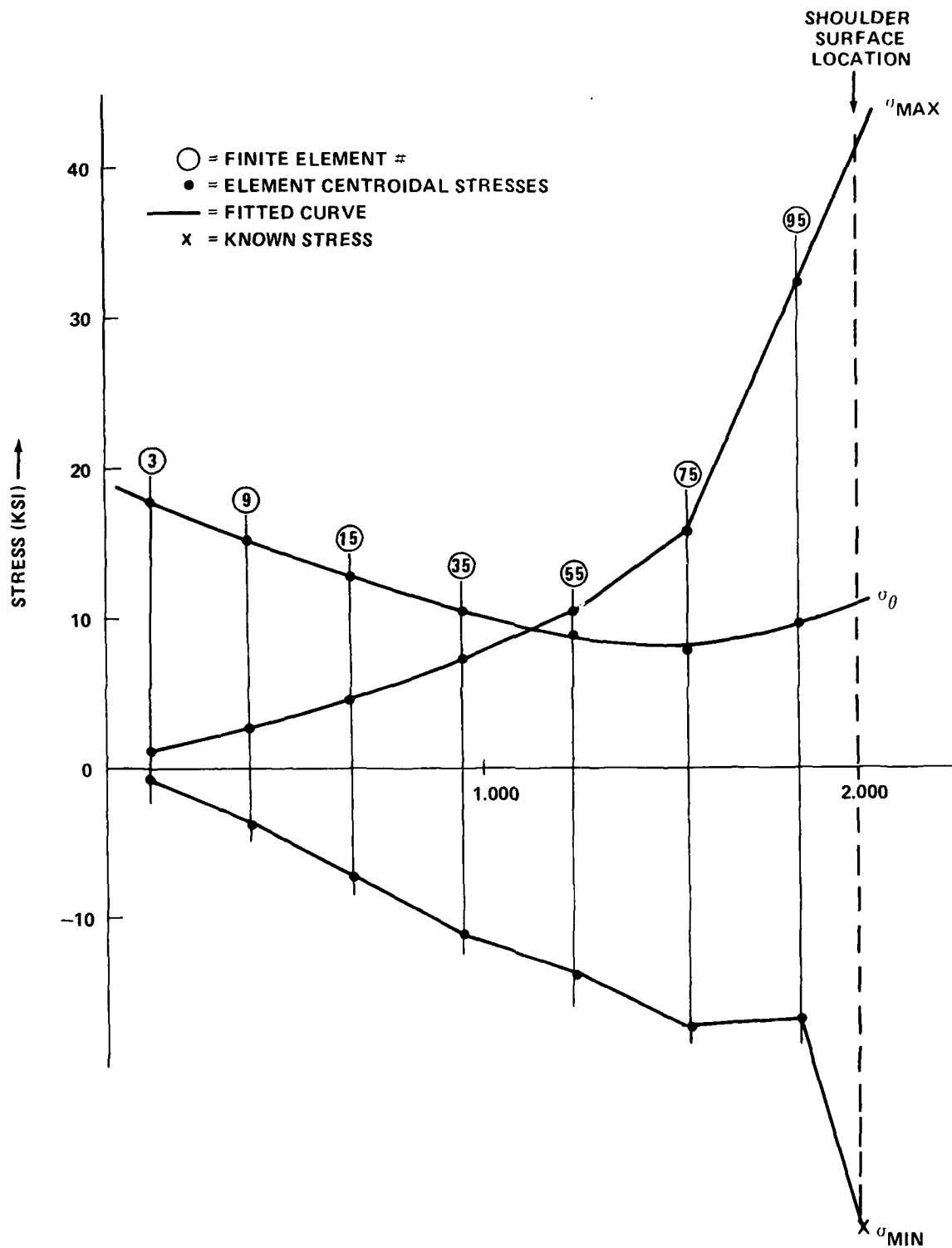


FIGURE G-9. PRINCIPAL STRESS DISTRIBUTIONS THRU NOZZLE CARRIER FLANGE THICKNESS — TYPE 304 STAINLESS STEEL, ELASTIC CASE

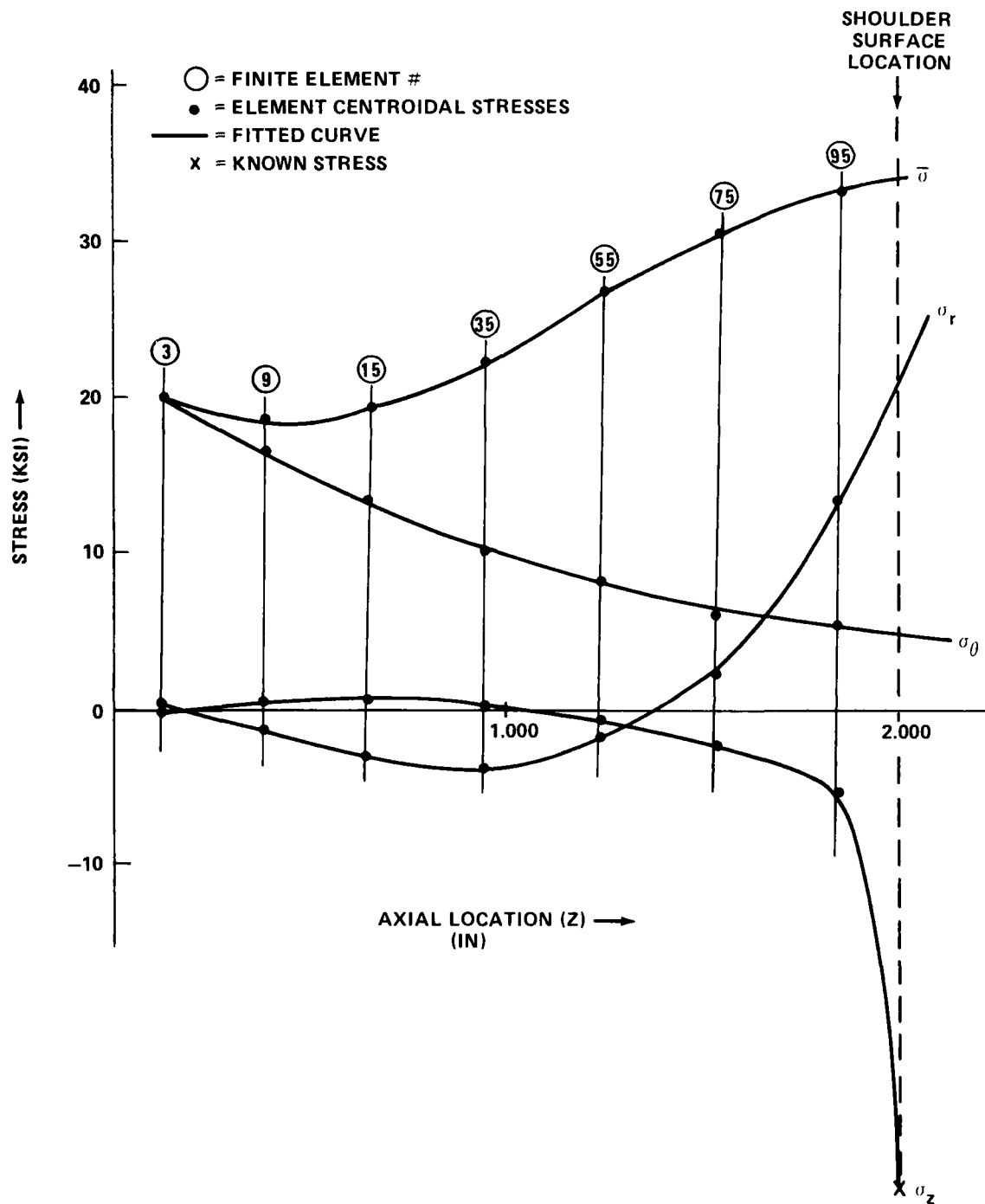


FIGURE G-10. STRESS DISTRIBUTIONS THRU NOZZLE CARRIER FLANGE THICKNESS — TYPE 304 STAINLESS STEEL, PLASTIC CASE

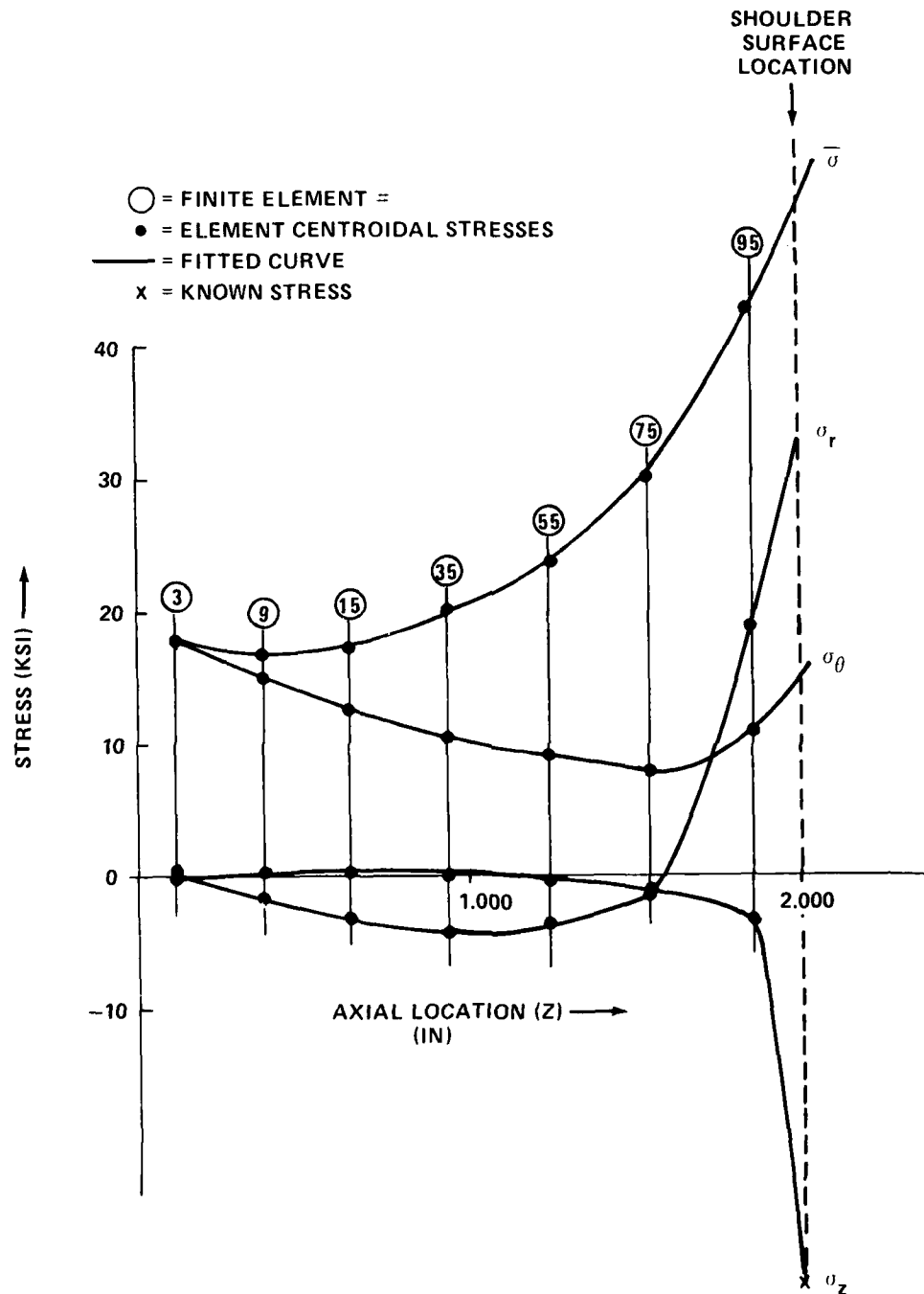


FIGURE G-11. STRESS DISTRIBUTION THRU NOZZLE CARRIER FLANGE THICKNESS — TYPE 4340 STAINLESS STEEL, ELASTIC CASE

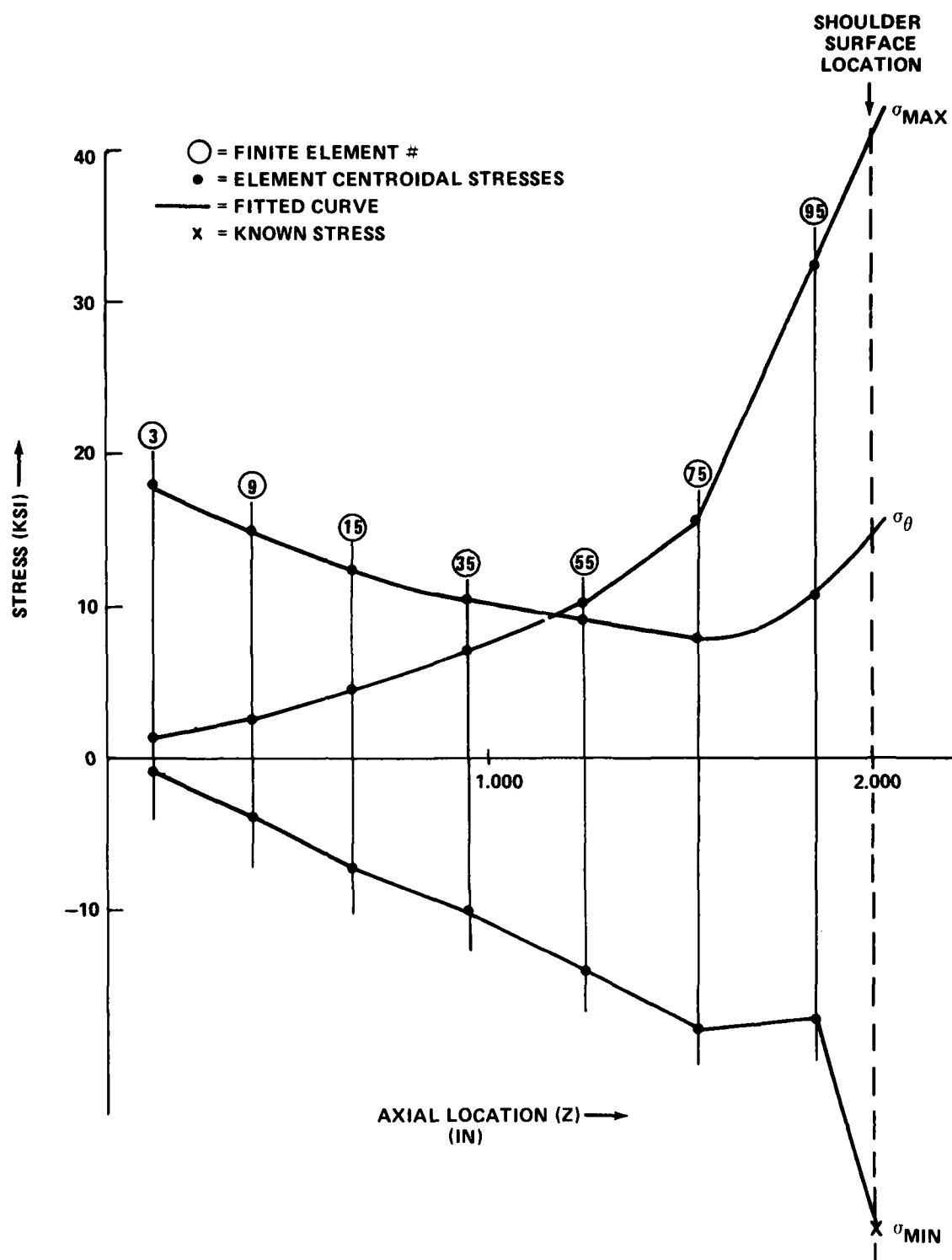


FIGURE G-12. PRINCIPAL STRESS DISTRIBUTIONS THRU NOZZLE CARRIER FLANGE THICKNESS - TYPE 4340 STAINLESS STEEL, ELASTIC CASE

## APPENDIX H

## VERIFICATION OF SMALL DISTURBANCE FORMULA

The M10 HIRE cold shakedown tests were run in February (WTR 1354). For those tests, the heater was assembled without liners and the control valves were not opened. Heater pressure transients caused by diaphragm rupture were measured with the flow restrictor valve blocked full open during Run 615. Operation was with 10,000 psi nitrogen in the heater at ambient temperature. Figure H-1 shows the heater geometry and location of the pressure transducers. Expected pressure values can be calculated from Equation (8) of Reference H-1:

$$\Delta P = P_H \gamma K_N \frac{A_R}{A} \quad (H-1)$$

where

$\Delta P$  = 1/2 peak to peak pressure transient

$P_H$  = heater pressure

$\gamma$  = isentropic exponent

$K_N$  = nozzle flow coefficient

$A_R$  = flow restrictor area

$A$  = heater passage area

Values of the constants for use in the equation, for 10,000 psi nitrogen at 300°K (81°F), are, from Reference H-2:

$P_H$  = 10,000 psi

$\gamma$  = 3.42

$K_N$  = 0.46

and for the seven 1.073" diameter flow restrictor holes,

$A_R$  = 6.33 in<sup>2</sup>

Table H-1 gives the calculated values of  $\Delta P$  along with measured pressures,  $P_{\text{meas}}$ , from Figures H-2 through H-4. The  $P_{\text{meas}}$  values are taken as the difference between a mean and the maximum pressure transient. In Table H-1, the measured value of pressure at the bottom of the heater is taken from Figure H-4 rather than Figure H-5 because of electrical noise in the latter.

TABLE H-1. PRESSURE DROPS

Heater Location	Heater Dia. (in)	Area (in <sup>2</sup> )	Calculated $\Delta P$ , psi	Measurement $P_{\text{meas}}$ , psi	Ratio $P_{\text{meas}}/\Delta P$
Exit	5.5	23.8	4,184	3,924	.94
Top	10	78.5	1,268	1,347	1.06
Bottom	24	452.4	220	550	2.50

Table H-1 also includes the values of the ratio  $P_{\text{meas}}/\Delta P$  to indicate the accuracy of the calculated predictions. The ratio should be 1.0 for the exit and top, and 2.0 for the bottom where the pressure wave reflects and doubles. The first two values are within 6% of the theoretical value of 1.0, which is very good correlation; but the value of 2.50 at the bottom is high compared to the value of 2.0 based on wave reflection. A similar result was obtained by Hill in earlier tests in the same heater as shown in Figures 16 and 17 of Reference H-1. It is probably reasonable to assume that with the obstruction of the heater element and heater base in the final assembly, the pressure wave will be broken up and mitigated, resulting in a ratio closer to 2.0. The new heater liners were designed based on calculated values of  $\Delta P$ , which this test indicate to be rather accurate. The main liner is correctly designed for one  $\Delta P$  rather than the 2 $\Delta P$  bottom reflected value because although the wave is reflected at the bottom, a one  $\Delta P$  magnitude wave is transmitted up the annular area outside the liner so the difference in pressure across the liner is still one  $\Delta P$ .

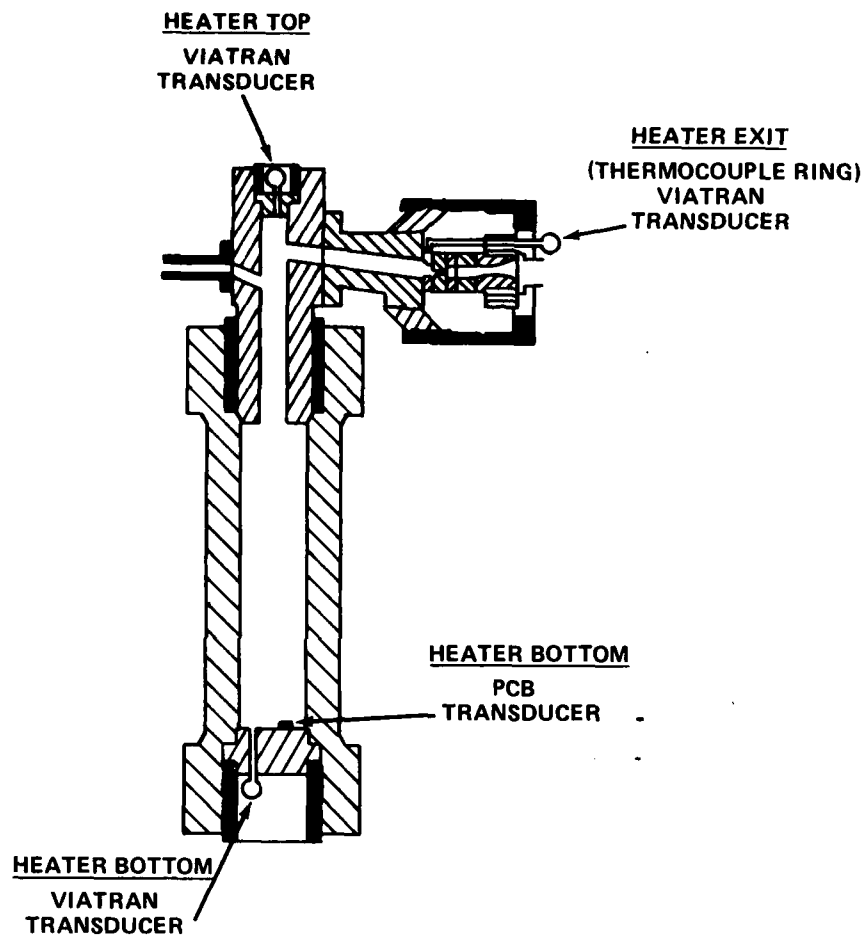


FIGURE H-1. PRESSURE TRANSDUCER LOCATIONS



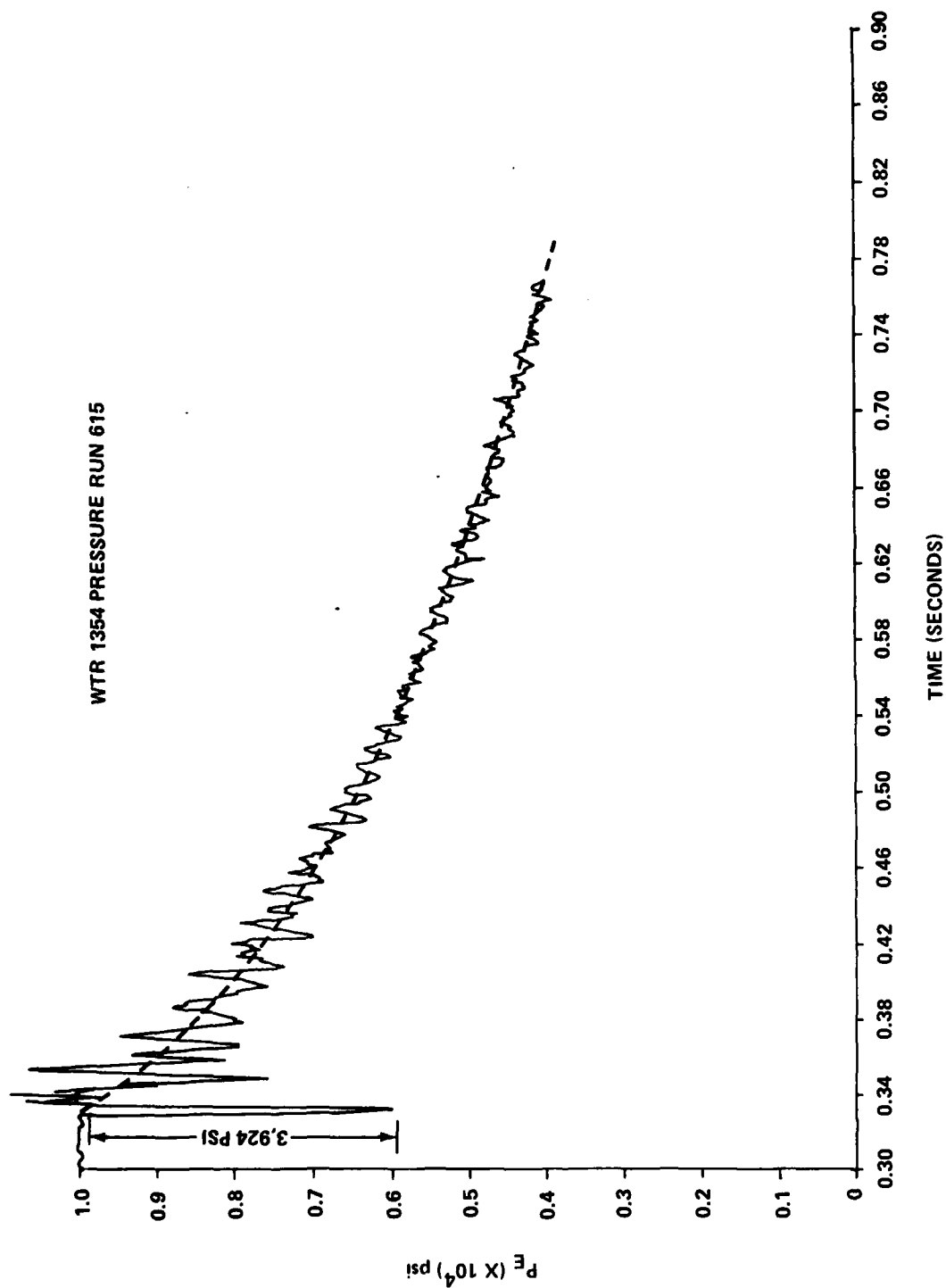


FIGURE H-2. THERMOCOUPLE RING PRESSURE

WTR 1354 PRESSURE RUN 615

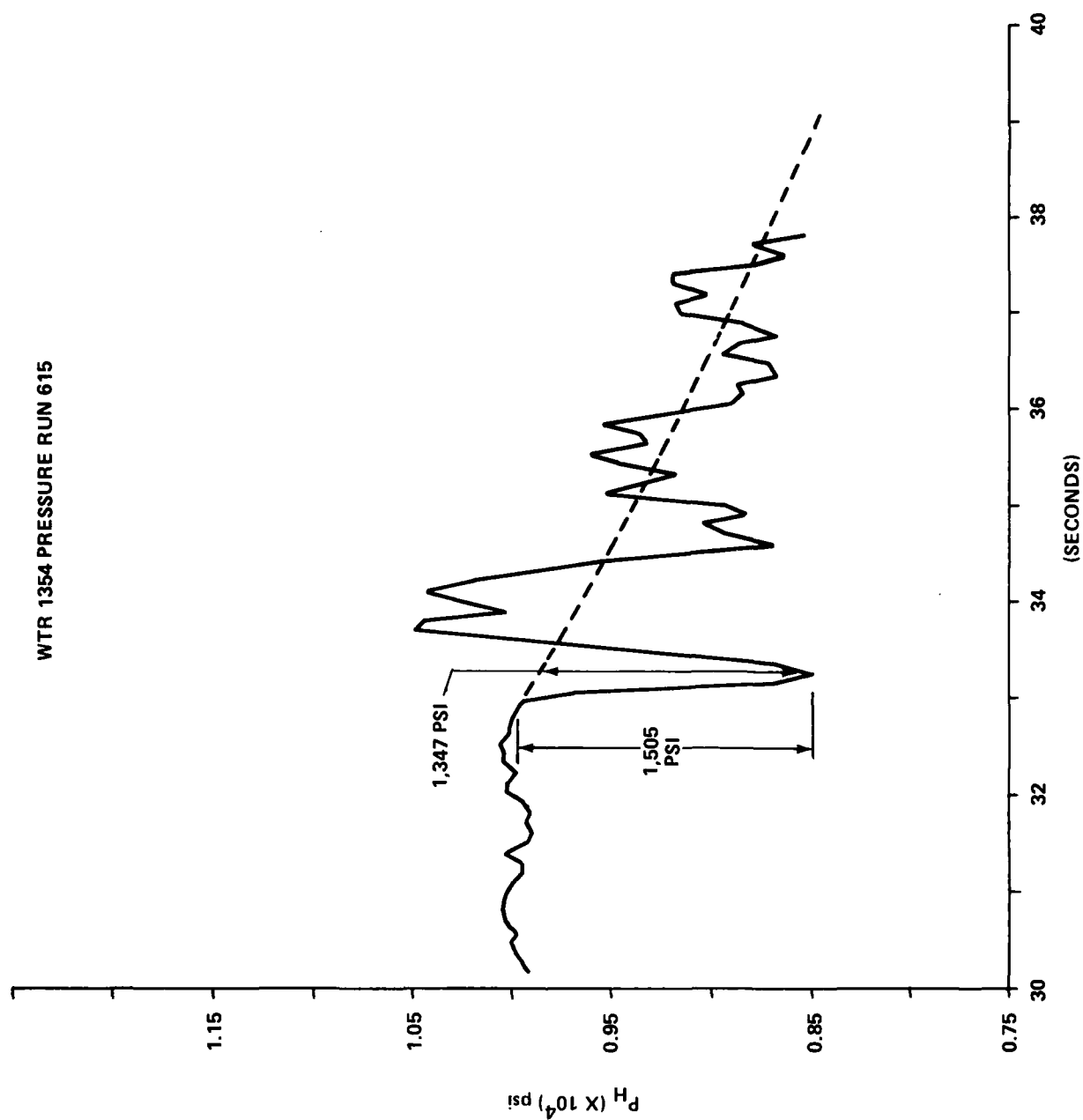


FIGURE H-3. HEATER TOP PRESSURE

WTR 1354 PRESSURE RUN 615

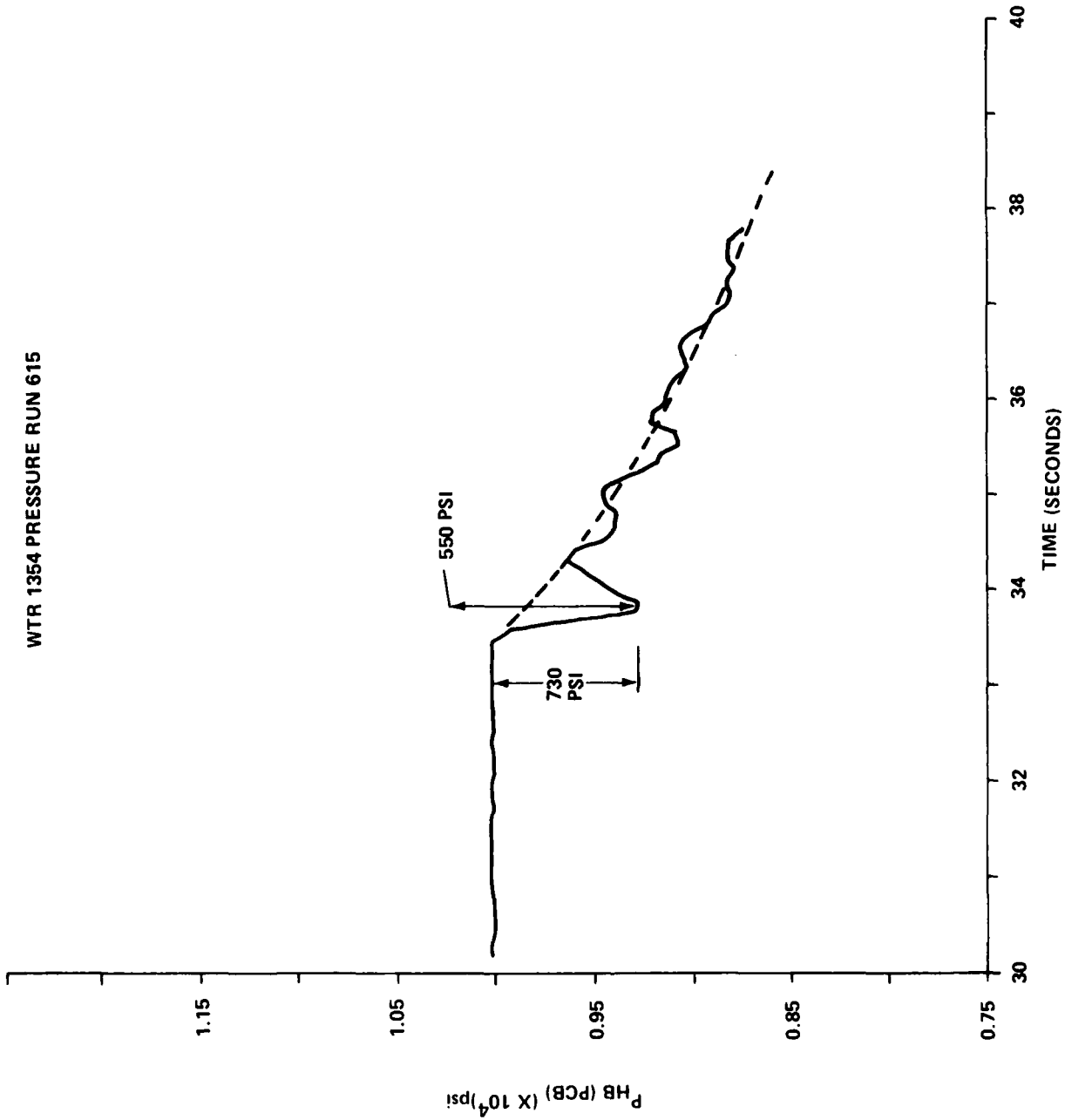


FIGURE H-4. HEATER BOTTOM PRESSURE PCB TRANSDUCER

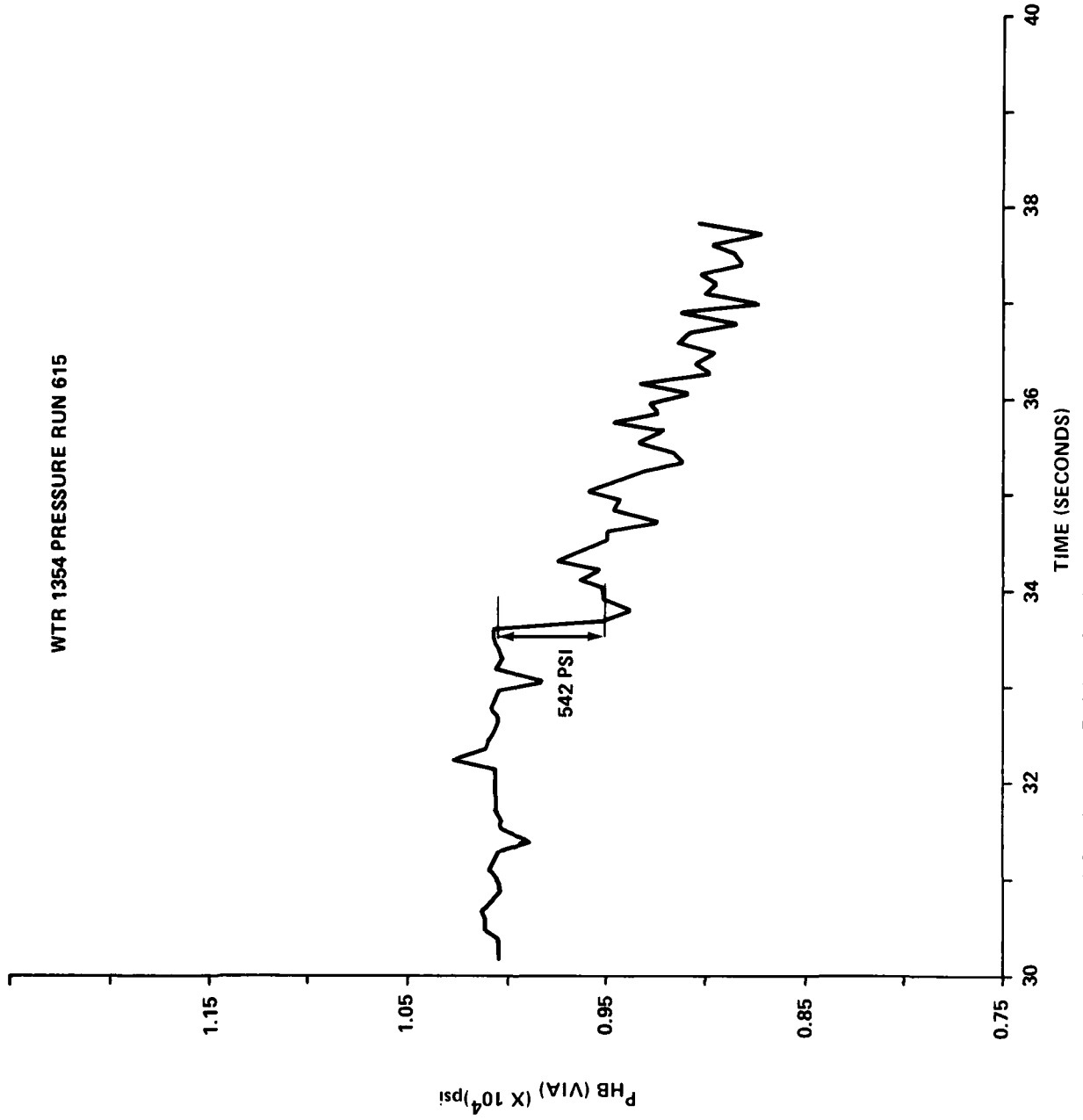


FIGURE H-5. HEATER BOTTOM PRESSURE VIATRAN TRANSDUCER

REFERENCES

- H-1. Hill, J. A. F., Initial Operation of the NOL Hypervelocity Tunnel, AIAA Paper No. 74-608, Jul 1974.
- H-2. Brahinsky, H. S., and Neel, C. A., Tables of Equilibrium Thermodynamic Properties of Nitrogen, Volume IV, Aug 1969.

## APPENDIX I

## ABLATOR FUNCTION MODEL

The objective of the M10-HIRE program is to run Tunnel 9 at Reynolds numbers up to about  $20 \times 10^6$ /foot, using the vertical heater pressurized to 22,000 psi. Since the heater volume is fixed, this increase in Reynolds number above the currently available  $5.4 \times 10^6$ /foot will result in a shorter run time. If we continue to use a flow restrictor with ablative inserts, we cannot afford to use much of the hot gas in the heater for the ablation process. In this appendix a simple model of the ablation in the flow restrictor is developed and used to predict whether ablators could be used at the upper limit of the planned Reynolds number range for M10. In this model only the ablation process itself is considered; a study of the equally important mechanical problems will be reported separately.

## PROBLEM STATEMENT

The problem is to predict the amount of hot gas used in opening up the ablative inserts of the flow restrictor. It will be assumed that the heater is pressurized to 22,000 psi at the temperature for M10 operation. The final open area in the flow restrictor should range as large as  $1.4 A^*$ , where  $A^*$  is the M10 throat area of  $4.52 \text{ in}^2$ . The ablator material is DELRIN, currently used for all Tunnel 9 operations.

## APPROACH

Using the data from current M10 operations, a simple model of the ablation process will be formulated. This model will then be verified by comparing its predictions with measurements of the initial pressure and temperature rise in Tunnel 9 at M10. Finally, the results of a parametric study of the performance of various flow restrictor designs will be presented.

## DATA BASE

For convenience, because the data are so readily available, only the last three M10 runs, conducted for the boundary layer survey, will be considered. The test conditions, including the initial and final hole sizes in the flow restrictor, are given in Table I-1. Figures I-1 through I-3 show the starting process in terms of time histories of  $T_{oc}$  (upstream of the flow restrictor) and  $p_o$ , with the latter drawn to an arbitrary scale to be roughly as large as  $T_{oc}$ . For the low pressure run (678) the pressure controller was set incorrectly

and the pressure control performance was very poor. There was some difference in the heater temperatures between these runs but they are close enough that we will assume them equal.

The most striking feature in these figures is the change in the relative rise time of the pressure and temperature traces. At the lowest pressure, where the ablator does not open very far, the entire ablation process is over before the gas temperature gets above 500°F. At the intermediate pressure ablation is also completed before the gas reaches maximum temperature. At the highest pressure the rise times are approximately equal.

## ANALYSIS

The data show two processes going on during the tunnel start, both of which must be analyzed in order to obtain a complete understanding. One is the ablation of the DELRIN inserts, which occurs under conditions of changing gas temperature and hence heat input. The other is the warming up of the efflux from the heater as the cold gas in the horizontal leg of the elbow is replaced by hotter gas from the vertical leg of the elbow and eventually from the heater core.

### Ablation

The simplest equation for the recession rate of an ablator may be written:

$$s = q/Q_{eff} \quad (I-1)$$

where  $q$  is the heat transfer rate and  $Q_{eff}$  is the effective heat of ablation, expressed in volumetric terms such as Btu/ft<sup>3</sup> and here assumed to be constant.

In a flow such as that in the hole of an ablative insert, the heat transfer rate may be written:

$$q = St \rho u c_p (T - T_w) \quad (I-2)$$

where

$St$  is the Stanton number

$\rho$  is the density of the flowing gas

$u$  is the velocity of the flowing gas

$c_p$  is the specific heat of the flowing gas

$T$  is the temperature of the flowing gas

$T_w$  is the surface temperature of the ablator

Now in turbulent pipe flow, applicable here, the Stanton number varies as  $(Re)^{-0.2}$ , which is not very much for a fixed supply pressure of 22,000 psi. We shall neglect this variation.

For most of the ablative process (all of it except at the upper end of the  $p_0$  range) the flow in the ablaters is sonic and we may write:

$$\rho_u = k p_H / \sqrt{T_{oc}} \quad (I-3)$$

If

$$\rho_u \text{ in lb/sec in}^2, p_H \text{ in psi, } T_{oc} \text{ in } ^\circ R$$

Then the value of  $k$  for nitrogen behaving as a perfect gas is 0.523. In the M10 nozzle operating at the design condition the real-gas effects change this value to:

$$k = 0.51$$

which will be used here.

Neglecting variations in  $c_p$ , and recalling that  $p_H$  is fixed, these equations show that ablation should proceed according to the expression:

$$s = c(T_{oc} - T_w) / \sqrt{T_{oc}} \quad (I-4)$$

To derive a value of  $c$  from the data, mean values of  $s$  have been computed from the initial and final hole diameters and the elapsed time. For  $T$  the value at the mid point of the time interval has been used, and these quantities for the three runs are given in Table I-2.

Figure I-4 is a plot of  $s\sqrt{T_{oc}}$  versus  $T_{oc}$ . A straight line fits the three points quite well and yields the ablation formula:

$$s = 0.039(T_{oc} - 720) / \rho \sqrt{T_{oc}} \quad (I-5)$$

The melting temperature of DELRIN, at atmospheric pressure, is given in the handbook as  $835^\circ R$ , somewhat higher than the temperature at which our data suggests that ablation begins.



Temperature Rise in the Heater Efflux

With the pressure and temperature in the heater fixed, one would expect a fixed mass of gas to be associated with each level of temperature in the temperature profile along the elbow duct. Thus the rise in  $T_H$  as the gas begins to flow should be associated with total mass which has flowed out of the heater.

From the tunnel data it is easy to compute the mass flow rate out of the heater since the nozzle throat is an excellent metering orifice:

$$\dot{m} = 0.51 A^* p_o / \rho T_o \quad (I-6)$$

(This neglects a small correction due to the accumulation of gas in the volume between the flow restrictor and the nozzle throat, where the pressure is rising.)

Data from the three runs has been plotted in Figure I-5, in terms of  $T_{oc}$  versus  $M$  where

$$M = \int \dot{m} dt \quad (I-7)$$

is the mass of gas which has left the heater. The correlation is surprisingly good and we have a pretty definite indication that at 22,000 psi 45 pounds of gas must flow out of the heater before the efflux temperature reaches its nominal value.

The straight-line fit shown in the figure was used to obtain the following equation for  $T_{oc}$  as a function of  $M$ :

$$T_{oc} = 580 + 26.2M \text{ for } 0 \leq M < 45$$

$$T_{oc} = 1760 \quad \text{for } M \geq 45 \quad (I-8)$$

with  $T_{oc}$  here in  $^{\circ}R$ , though in the figure it is shown in  $^{\circ}F$ .

## MATHEMATICAL MODEL

At any stage of the ablation process, if  $M$  is known, Equation (I-8) gives  $T_{oc}$  and Equation (I-5) the ablation rate. To obtain  $M$  we simply integrate the flow rate through the flow restrictor, which is:

$$\frac{dM}{dt} = \dot{m} = \frac{0.51 \times 22,000}{\sqrt{T_{oc}}} \times N \pi r^2 \times C_d \quad (I-9)$$

where

$N$  is the number of orifices in the flow restrictor

$r$  is the instantaneous radius of the hole in the ablator

$C_d$  is the discharge coefficient, here taken as 0.8

The radius of the hole in the flow restrictor is initially  $r_1$ , which is given. The current limit on the strength of the expansion wave allowed into the heater sets  $r_1 = 0.085$  inch for  $N = 7$ . The growth of  $r$  given by Equation (I-5) is:

$$\begin{aligned} \frac{dr}{dt} &= 0.039(T_{oc} - 720)/\sqrt{T_{oc}} \quad \text{for } 0 \leq r < r_2 \\ \frac{dr}{dt} &= 0 \quad \text{for } r \geq r_2 \end{aligned} \quad (I-10)$$

where  $r_2$  is the radius of the metal insert into which the ablator is placed.

Equations (I-8), (I-9), and (I-10) are sufficient to describe the process for given values of  $N$ ,  $r_1$ , and  $r_2$ . They require the integration of two coupled first-order differential equations with variable coefficients. This has been carried out with the very simple (if not naive) BASIC program attached.

#### MODEL VERIFICATION

Figures I-6, I-7, and I-8 show the initial pressure and temperature histories from runs 677-679. The data points are compared with the predictions of our model.

The predictions of our model lag the data by a considerable amount. The problem appears to be associated with the value of  $T_w$  derived from Figure I-4. The low pressure run 678 shows that  $p_o$  is increasing (i.e., ablation is taking place) for  $T_{oc}$  as low as  $600^\circ R$ . To account for this we rewrite Equation (I-5):

$$s = 0.036(T_{oc} - 600)/\sqrt{T_{oc}} \quad (I-11)$$

where the change from 0.039 to 0.036 compensates for the change in the temperature differential. With this change the agreement between the model and the data becomes very good.

The principal deficiency in this simple model is in the treatment of the ablation of DELRIN, which here has been based on an effective heat of ablation derived from the data. It would probably be worthwhile to check this against

basic thermochemical data for DELRIN and to incorporate a blocking effect on the heat input due to mass injection.

If this could be and were done, the effect of Reynolds number on the heat transfer rate should also be accounted for.

#### PARAMETRIC STUDY

The previous hesitation to use an ablative flow restrictor for M10 HIRE is not unjustified. Suppose we tried to increase  $p_o$  above the current limit of about 4000 psi using a flow restrictor with 7 holes. The final hole diameter, for  $A_R = 1.4 A^*$  would be 1.073 inches, so that  $r_2 = 0.5365$  inches, with  $C_d = 0.8$ .

Figure I-9 shows the pressure and temperature histories predicted by our model for these conditions.  $T_{oc}$  is up to its nominal value of 1300°F long before ablation is finished. The total efflux from the heater at the end of ablation is 265 pounds, of which 220 pounds constitute hot gas which might have been used for testing. The estimated useful volume of the new heater is 12.8 ft<sup>3</sup> which at 22,000 psi and 1400°F holds 250 pounds of nitrogen. The loss in useful run time while waiting for the pressure to rise is about 88%.

Better results may be obtained by using a larger number of holes in the flow restrictor, while keeping the initial and final hole areas constant. Calculations have been made for the following values of  $N$ , which correspond to optimum packing in a circular duct:

$$N = 19, 37, 61, 97, 139, 187, 241$$

Figure I-10 shows the mass of hot gas wasted in ablation versus  $N$ , and also expresses this as a percentage of the hot gas available. This waste is acceptable only for  $N > 100$ .

These estimates are conservative because towards the end of ablation, as  $p_o$  rises above half of  $p_H$ , the ablators become unchoked and the mass flux is less than given by Equation (I-9).

#### CONCLUSIONS

1. A model has been developed for the ablation of DELRIN flow restrictor inserts which accounts quite well for their observed performance.
2. This model shows that an ablative flow restrictor with a large number of orifices (say 100) would be suitable for M10-HIRE operation at maximum pressure.
3. About 45 pounds of gas must be expelled from the heater before the efflux warms up to the core temperature.

4. The implications for the mechanical flow restrictor is that its opening time need not be shorter than 0.2 seconds.

#### RECOMMENDATIONS

1. Analyze, or determine experimentally, whether DELRIN ablators would be strong enough for M10-HIRE operation at maximum pressure.

2. Consider relaxing the limitation on the strength of the expansion wave and thus increasing the initial diameter of the abalators. This would help both in terms of wasted hot gas and in the strength of the ablators.

3. If the strength analysis is favorable, plan to test an ablating flow restrictor at maximum pressure in June 1982.

```
100 PRINT "N=";  
110 INPUT N  
120 PRINT "RMIN=";  
130 INPUT R1  
140 PRINT "RMAX=";  
150 INPUT R2  
153 PRINT "CD=";  
155 INPUT C  
160 PRINT "DELTA T =";  
170 INPUT "TMAX =";  
180 PRINT "TMAX =";  
190 INPUT H2  
193 PRINT "PRINT INTERVAL=";  
195 INPUT I  
196 PRINT @71:"N=";N,"RMIN=";R1,"RMAX=";R2,"CD=";C  
197 PRINT @71:  
199 J=0  
200 H=0  
210 M=0  
215 R=R1  
220 P=PI  
230 IF H= H2 THEN 320  
235 IF M= 45 THEN 245  
240 T=580+26.2*M  
241 GO TO 250  
245 T-1760  
250 M=M+22000*0.51*P*R*R*N*C*Z/SQR(T)  
255 IF T 600 THEN 290  
260 R=R+0.036*(T-600)*Z/SQR(T)  
270 IF R R2 THEN 285  
280 GO TO 290  
285 R=R2  
290 H=H+Z  
294 J=J+1  
295 IF J I/Z THEN 310  
300 PRINT @71:H,M,T-460,R*R/R2/R2  
301 PRINT @71:  
305 J=0  
310 GO TO 230  
320 END
```

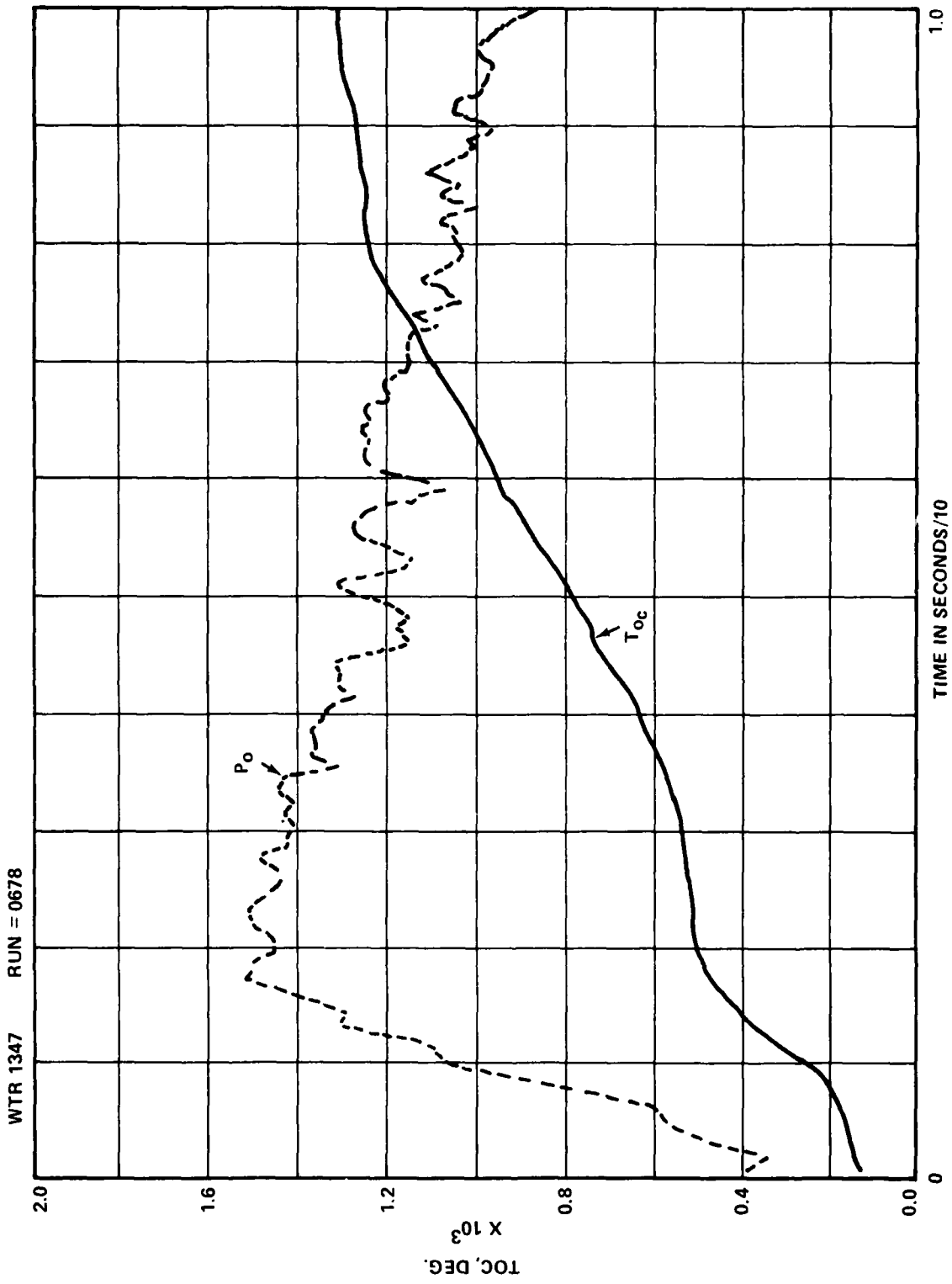


FIGURE I-1. SUPPLY TEMPERATURE, TOC, DEG. F

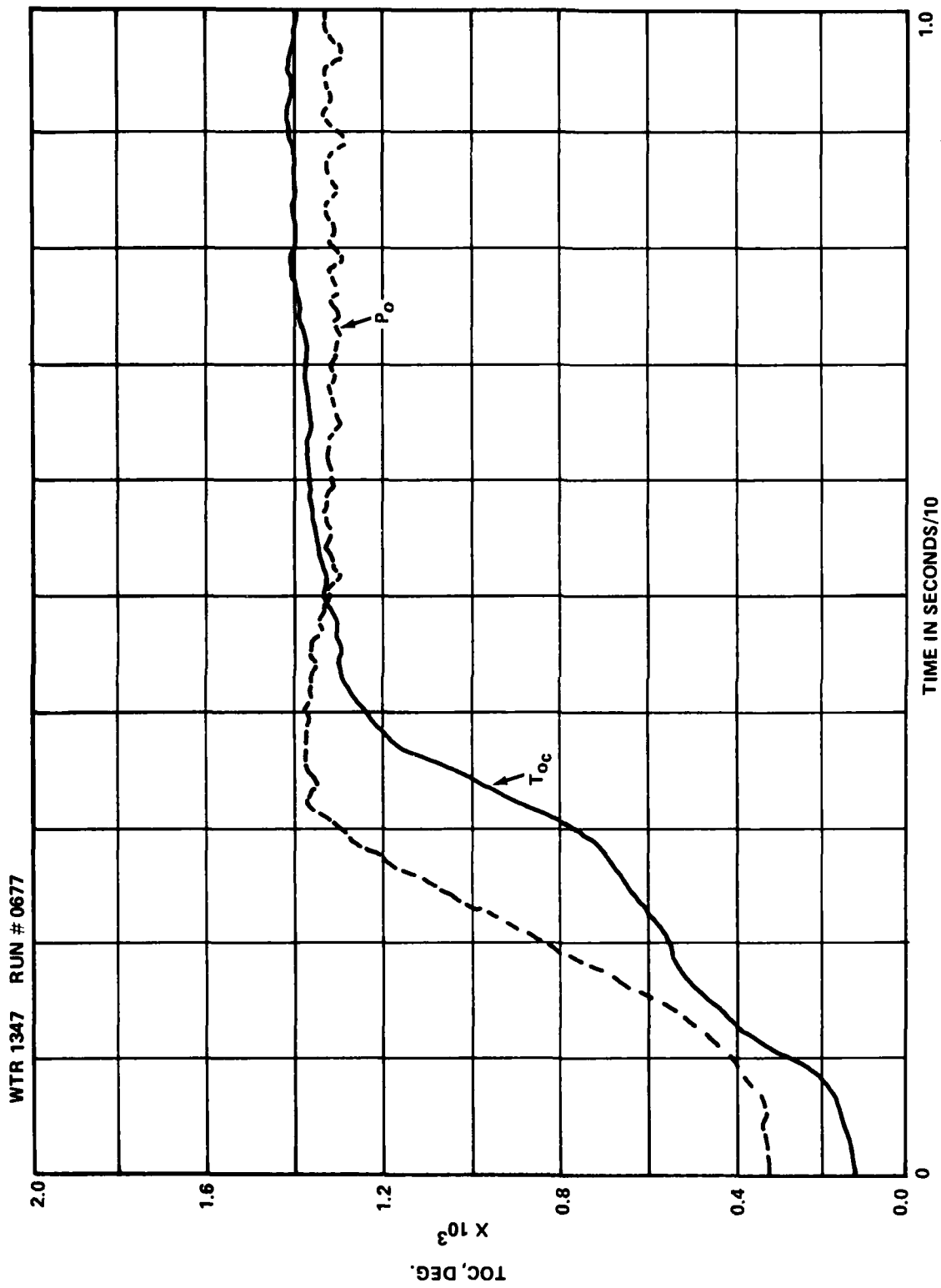


FIGURE I-2. SUPPLY TEMPERATURE, TOC, DEG. F

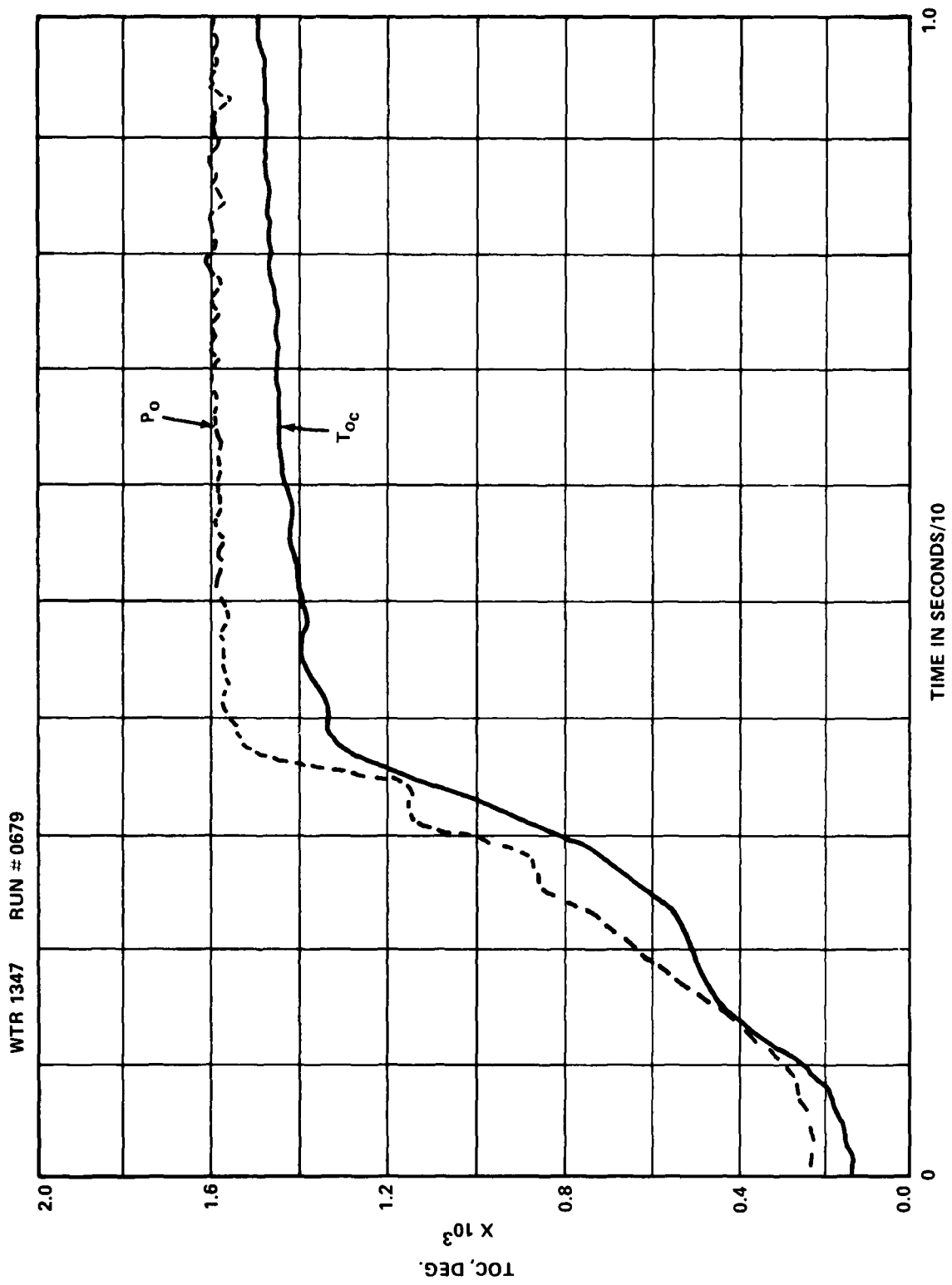


FIGURE I-3. SUPPLY TEMPERATURE, TOC, DEG. F



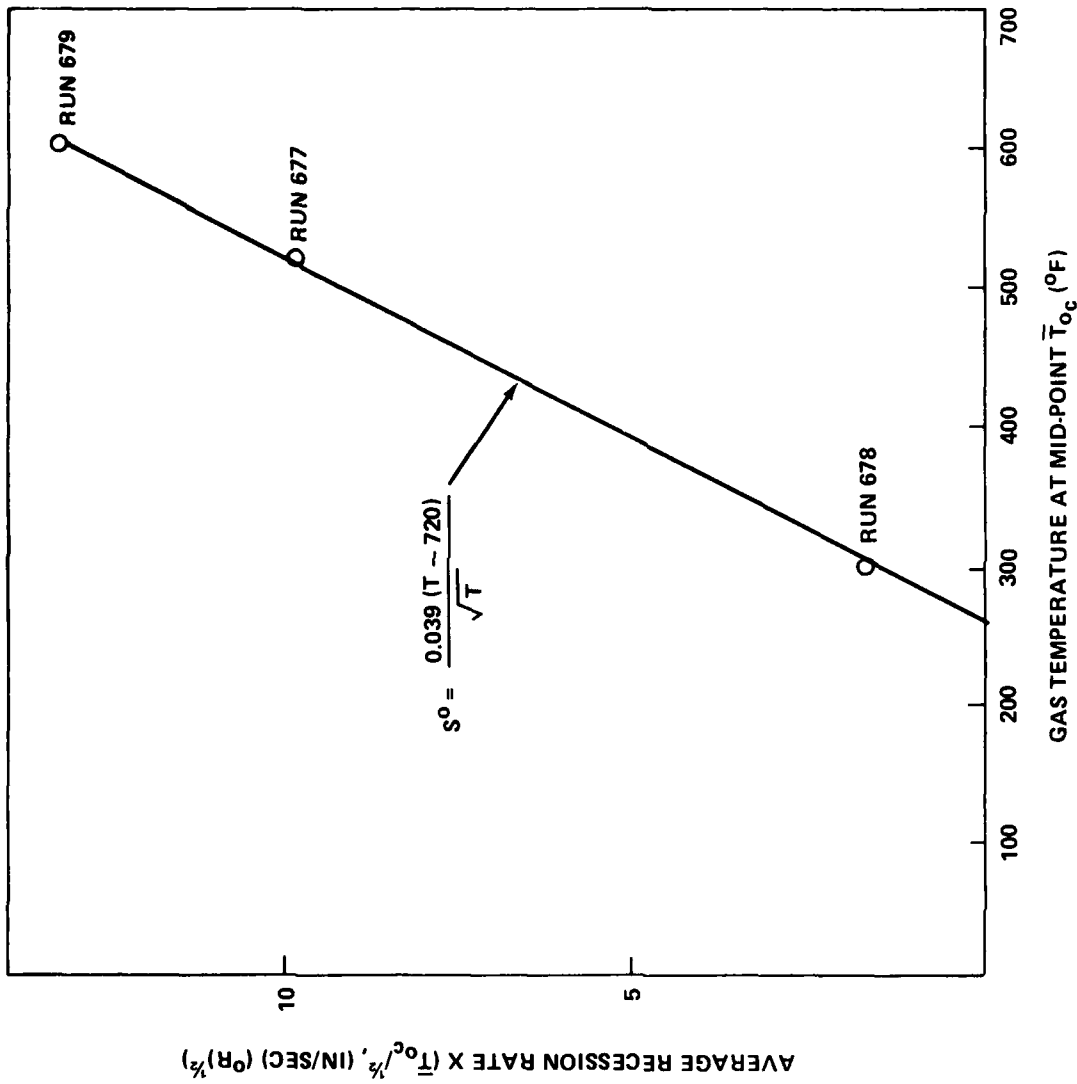


FIGURE I-4. AVERAGE RECESSION RATE VS GAS TEMPERATURE

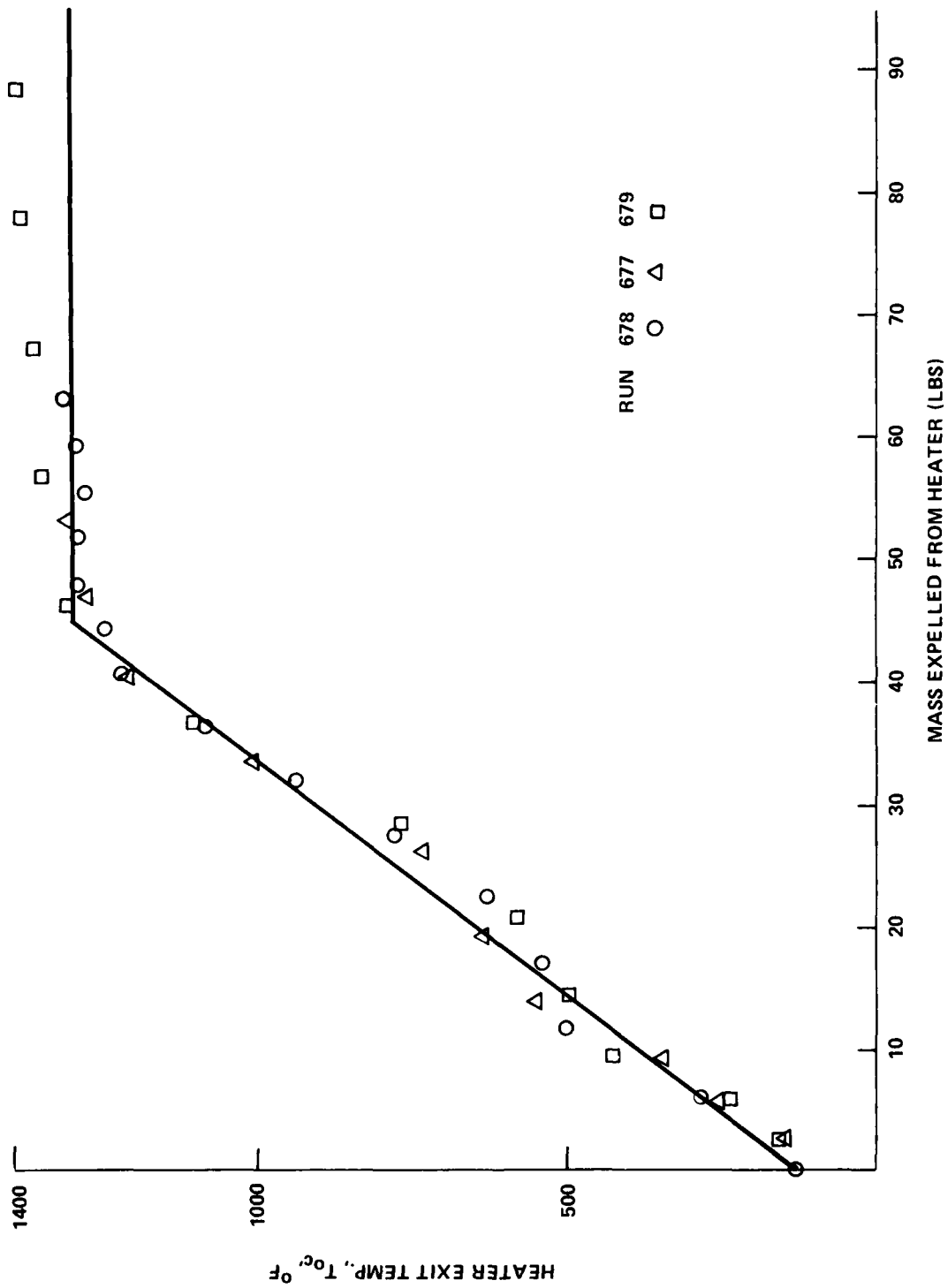


FIGURE I-5. TEMPERATURE RISE IN HEATER EFFLUX

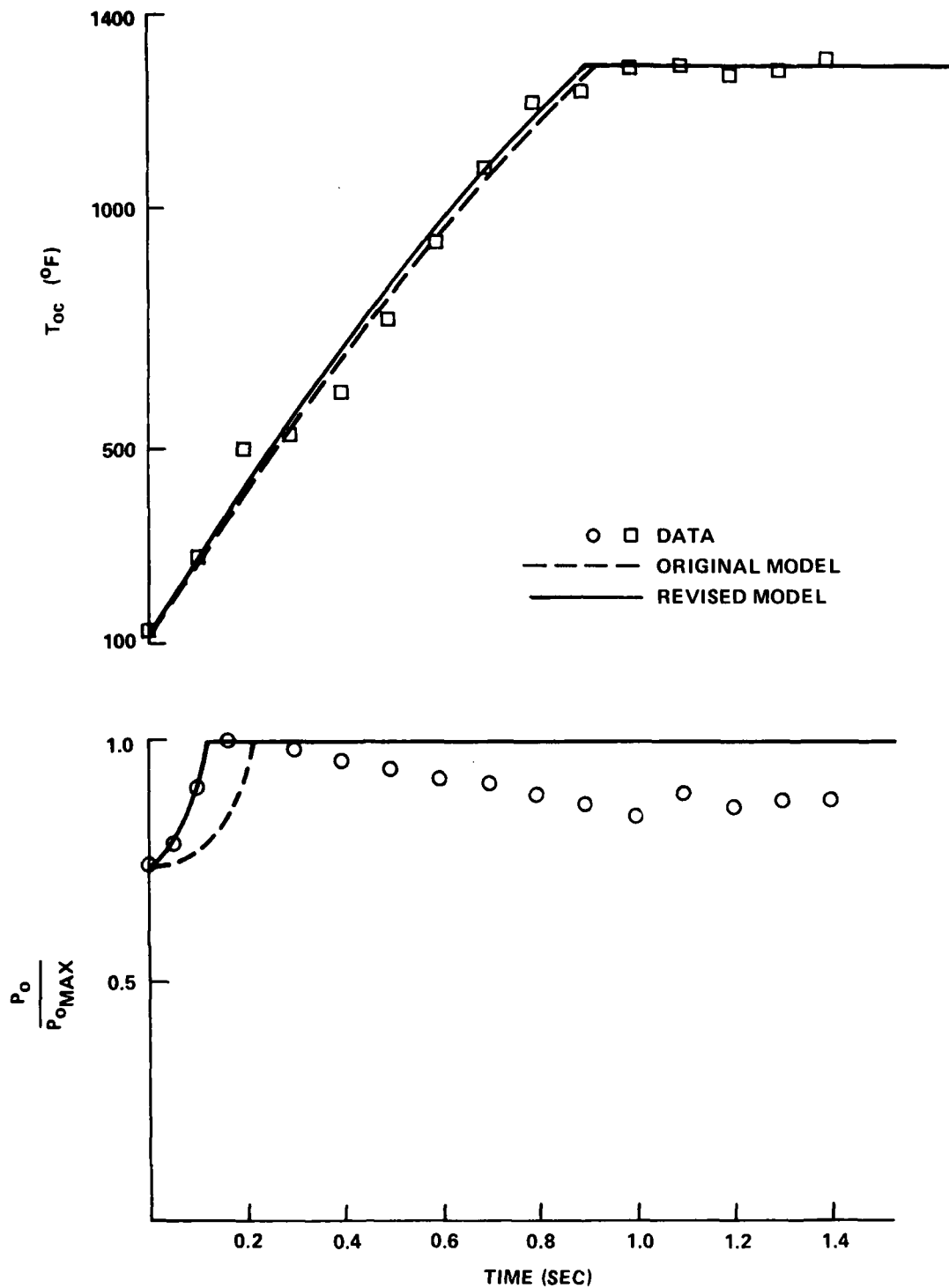


FIGURE I-6. FLOW START-UP RUN 678

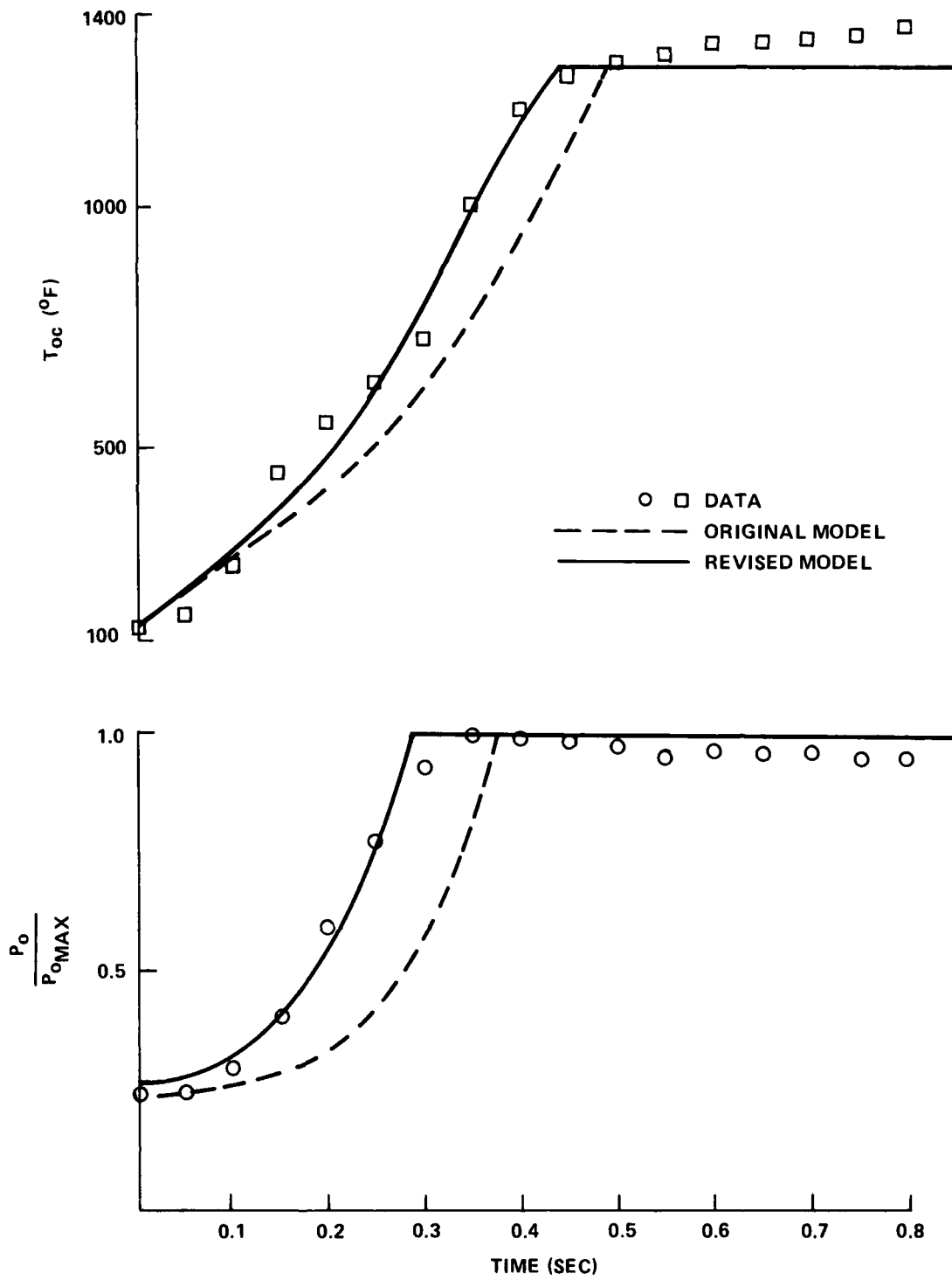


FIGURE I-7. FLOW START-UP RUN 677

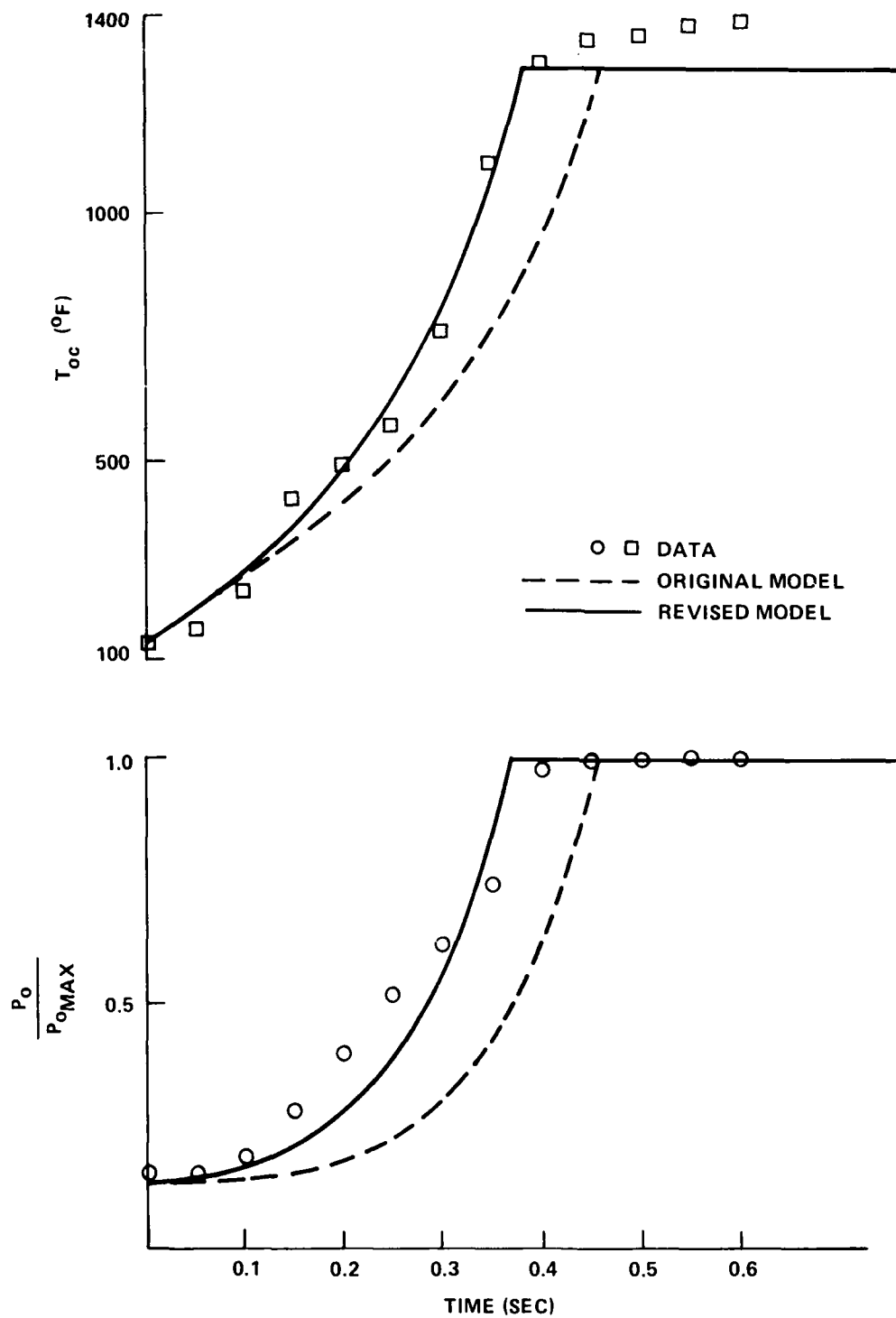


FIGURE I-8. FLOW START-UP RUN 679

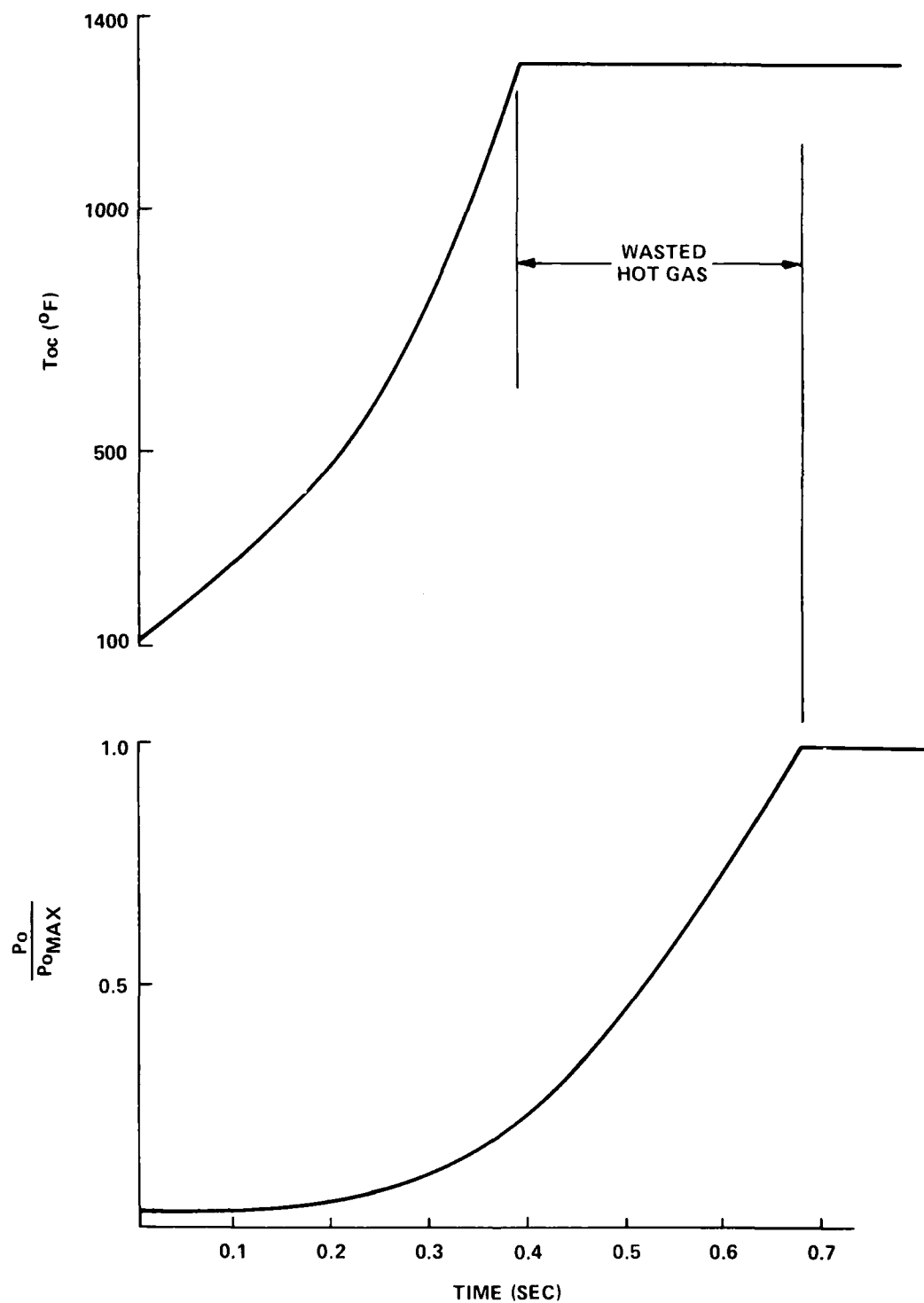


FIGURE I-9. 7-HOLE FLOW RESTRICTOR OPENING UP TO 1.4A\*

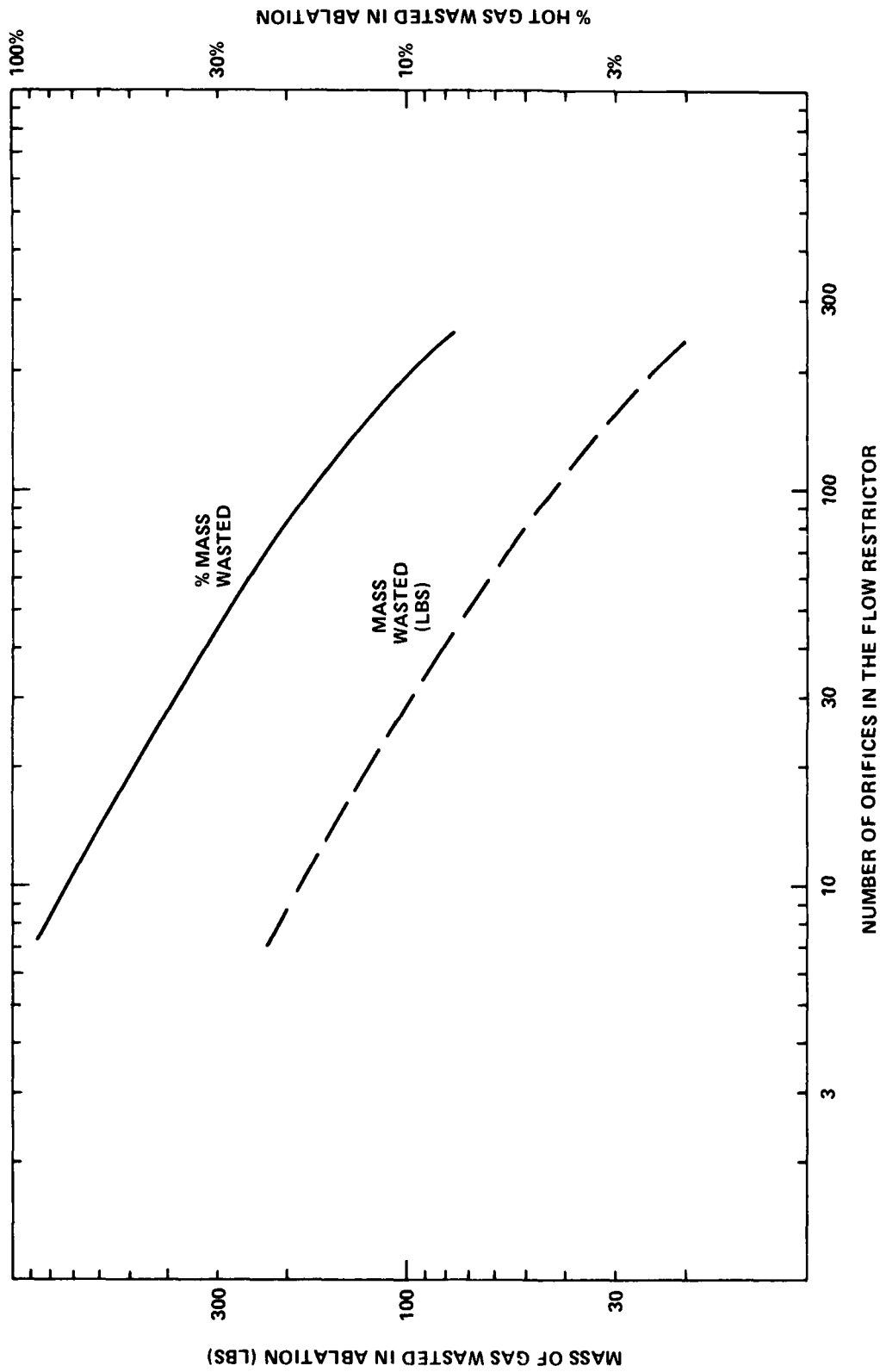


FIGURE I-10. HOT GAS USED FOR ABLATION

TABLE I-1. TEST CONDITIONS

<u>RUN</u>	<u>DATA</u> <u>R<sub>i</sub> (in)</u>	<u>BASE</u> <u>R<sub>f</sub> (in)</u>	<u>P<sub>o</sub> (psi)</u>
678	0.085	0.0935	780
677	0.085	0.166	2400
679	0.085	0.230	3950

TABLE I-2. ABLATION TABLE

<u>RUN</u>	<u>TIME</u> <u>RECESSION (in)</u>	<u>MID-POINT</u> <u>INTERVAL (sec)</u>	<u>TEMPERATURE (°R)</u>
678	.009	.148	760
677	.081	.258	980
679	.145	.355	1060



## APPENDIX J

## FLOW RESTRICTOR ANALYSIS

Prior to diaphragm rupture, the flow restrictor plate is subjected to a 22,000 psi hydrostatic pressure loading condition as shown in Figure J-1. The yield strength of Inconel X-750, heated treated to ASM 5670, is 140,000 psi at room temperature. Thus, this loading condition presents no problem.

Immediately following diaphragm rupture, a large pressure drop exists (albeit for a short period of time) across the flow restrictor plate. The magnitude of the pressure drop decreases as the ablators "open up" to the full open area defined by 241-.187" diameter holes (6.62 in<sup>2</sup>). During the period that the high pressure drop exists, the gas flowing through the flow restrictor is relatively cool ( $\leq 600^{\circ}\text{F}$ ) thus keeping the flow restrictor plate's mechanical strength high. Once the ablators have been removed completely, hot gas (1500°F) begins flowing through the holes in the flow restrictor plate, subjecting the material between adjacent holes to high heating rates and resulting high temperature gradients, as shown in Figure J-1.

From a structural viewpoint the flow restrictor plate must be able to survive two loading conditions:

Condition 1-- $\Delta p = 22,000$  psi,  $T_{\text{plate}} \leq 600^{\circ}\text{F}$

Condition 2-- $\Delta p = 2,000$  psi, "High"  $\Delta T$

## ANALYSIS OF CONDITION 1

For the large  $\Delta p$  loading condition, the primary concern is with bending stresses resulting from flexure of the flow restrictor plate. Reference J-1 contains a method for obtaining bending stresses in a perforated plate. A brief description of the method is in order.

Basically, one first obtains bending stresses, using textbook solutions, for a homogeneous plate of constant thickness. Then, using a "ligament efficient parameter,"  $\eta$ , a stress concentration factor  $k$  is obtained from Reference J-1. The ligament efficiency parameter  $\eta$  is obtained from:

$$\eta = \frac{p - D}{p}$$

where

$p$  = center to center distance between holes = .4 in

$D$  = hole diameter = .187 in

For the flow restrictor:

$$\eta = \frac{.4 - .187}{.4} = .5325$$

From Figure 3b of Reference J-1, for  $\eta = .5325$  a stress concentration factor of 2.3 was obtained.

To obtain bending stresses and deflections, Reference J-2 was used. For a fixed edge plate, the maximum bending stress is:

$$\sigma_{\max} = \frac{.75 p a^2}{t^2}$$

where

$p$  = 22,000 psi

$a$  = 3.8 in = outer plate radius (supported)

$t$  = 2 in = plate thickness

This stress occurs at the fixed edge of the plate.

Substitution yields:

$$\sigma_{\max} = \frac{.75(22,000)(3.8)^2}{(2)^2} = 59,565 \text{ psi}$$

Now using the  $k = 2.3$  to account for the reduced stiffness of the plate due to the holes:

$$\sigma = 2.3(59,565) = 137,000 \text{ psi}$$

which is below the yield strength of Inconel X-750 at room temperature (140,000 psi). The reason the room temperature yield strength is used, instead of the yield strength at 600°F, is that calculations have shown that during the very short run time the fixed outer edge of the plate does not heat up. Thus, the room temperature yield strength is used for comparison purposes.

The equation used above to calculate bending stress is normally employed when dealing with a thin plate. To determine the accuracy of the hand calculation, a 3-D finite element model was constructed, as shown in Figure J-2. The model was simply a 30° wedge of a solid plate, 2" thick. The model was exercised having both a fixed edge and supported edge condition. The loading placed on the model was a uniform pressure over the entire upstream face, as shown in Figure J-2.

The results of the finite element analysis were in very close agreement with the hand calculation. The supported edge condition gave a maximum stress result 8% lower (126,000 psi) than the hand calculation, and the fixed edge condition yielded a result (161,000 psi) 18% higher than the hand calculation. Intuitively, the supported edge condition shown in Figure J-2 appears more realistic, thus, the hand calculation result was accepted as accurate, and surprisingly good for such a simple method. In addition, Reference J-2 contained a method for calculating deflections. This was done, and compared to the finite element analysis results. The comparison indicated agreement with 5% between the two analytical methods.

#### ANALYSIS OF CONDITION 2

To analyze the transient thermal condition, and simultaneous pressure loading, a second finite element model was created, as shown in Figure J-3. This model was a 1/2 in thick perforated plate, simulating a 30° wedge of the flow restrictor. (The main reason a 1/2" thick plate was analyzed was that there was a limit on the number of 3-D finite elements which could be run on our CDC mainframe, due to storage limitations. It was felt that if thermal results could be obtained, the pressure results could be ratioed by the square of the thicknesses,  $(.5/2)^2$ , based on our confidence in the accuracy of the hand calculations noted earlier.) The results obtained in the finite element analysis indicated there could be some compressive yielding of material at the inner surface of the holes. However, the magnitude of the compressive stress obtained (181,000 psi) was only 5,000 psi greater than the compressive yield strength of the material (176,000 psi) at 1500°F. The conclusion drawn was that the flow restrictor plate would be acceptable, with the condition that it be periodically inspected for cracks.

#### ADDENDUM

Following the QUICKPROOF test series, it was decided the flow restrictors should be able to take a pressure drop equal to the full heater pressure, in the hot condition. The reason was to allow for very low  $p_0$  (300 psi) testing, requested by wind tunnel users. The final flow restrictor design, cited in the main report, was 2.8" thick, and was fabricated from Rene 41, a high strength superalloy.

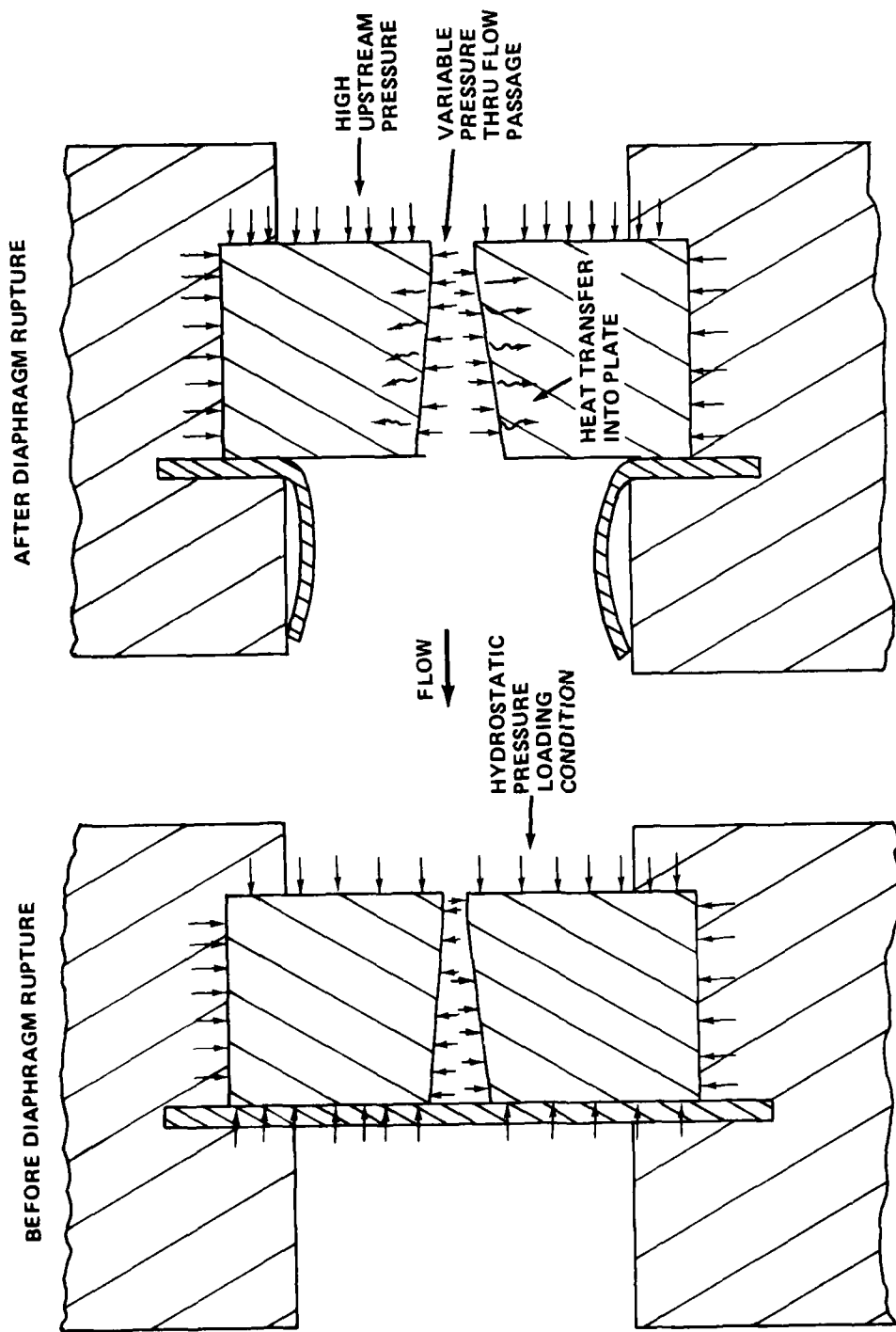


FIGURE J-1. LOADING CONDITIONS

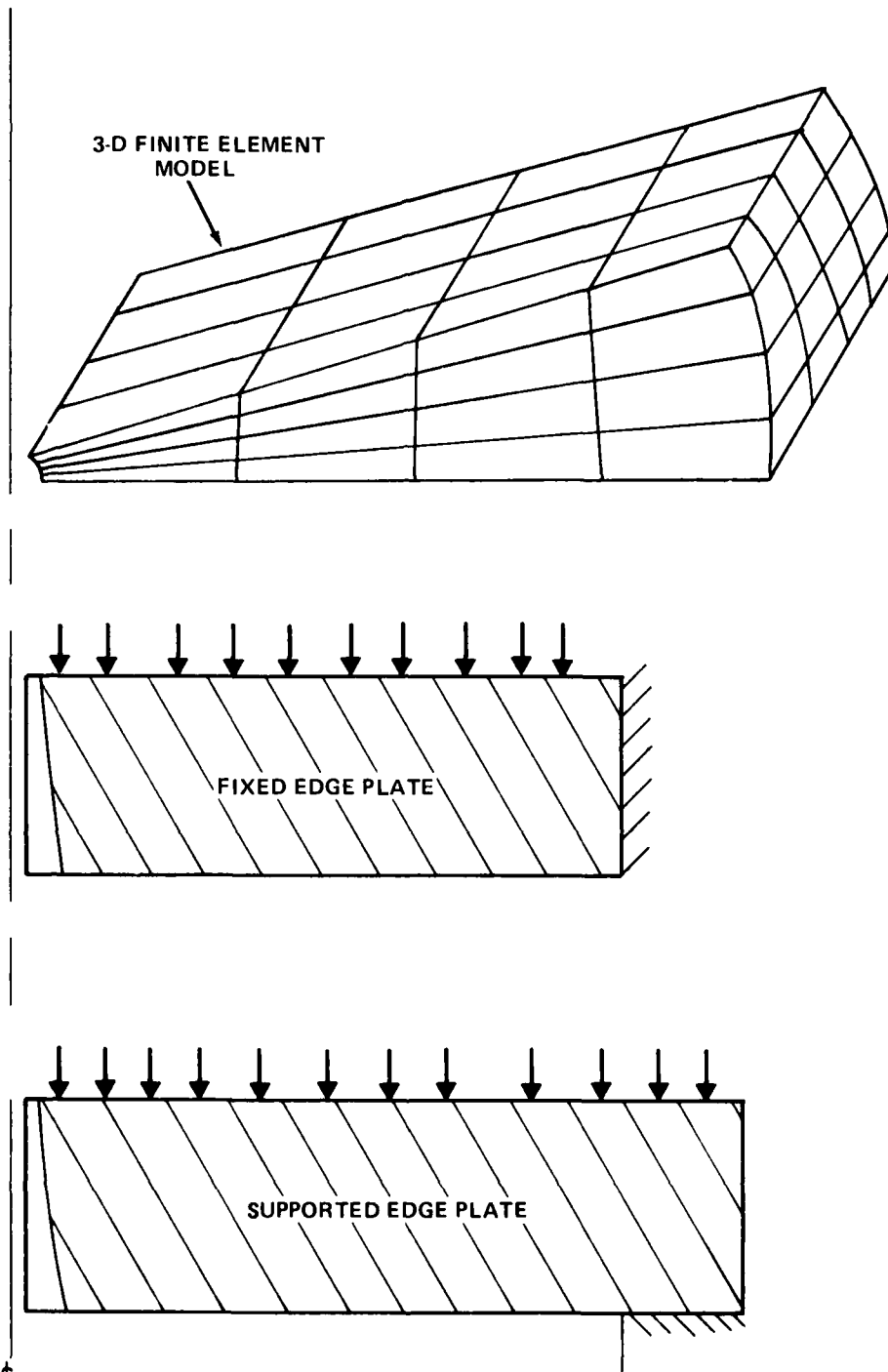


FIGURE J-2. 2" THICK SOLID PLATE

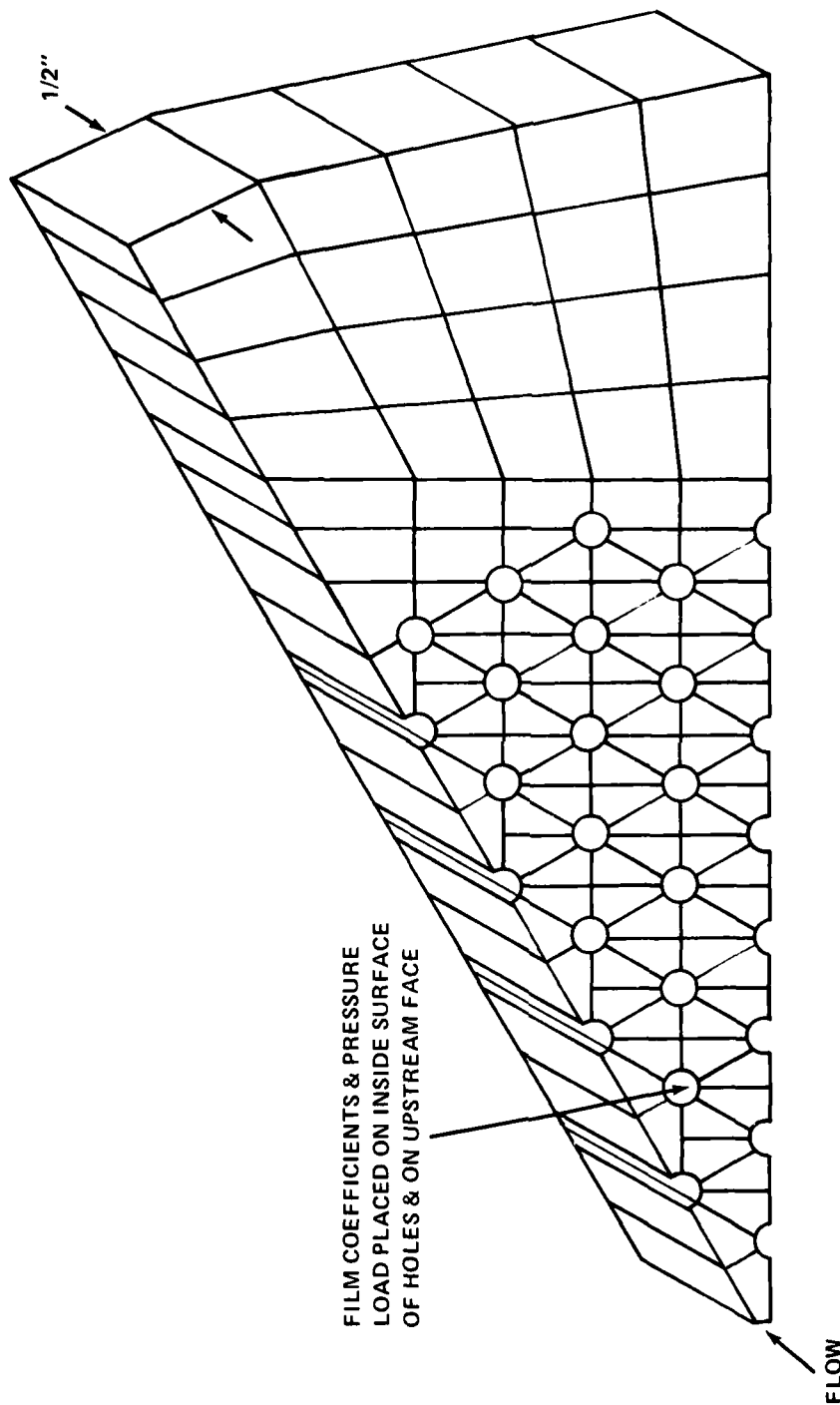


FIGURE J-3. 1/2" THICK PERFORATED 3-D MODEL

REFERENCES

- J-1. Horvay, "The Plain Stress Problem of Perforated Plates," Journal of Applied Mechanics, Volume 19, 1962.
- J-2. Timoshenko, Y., Theory of Plates and Shells, Second Edition, (New York: McGraw-Hill, 1968).

APPENDIX K  
ABLATOR STRUCTURAL ANALYSIS

INTRODUCTION

The objective of the M10-HIRE program is to run Tunnel 9 at Reynold's numbers up to about  $20 \times 10^6$  per foot using the vertical heater pressurized to 22,000 psi. This requires a final open area of 6.62 square inches in the wind tunnel's restrictor. Because the heater volume is fixed, the increase in the Reynold's number above the currently available  $5 \times 10^6$  per foot will result in a shorter run time. If we continue to use a flow restrictor with ablative inserts, we have the problem of not being able to afford to use too much of the hot heater gas for the ablation process.

The solution to the ablation problems lies in using a larger number of smaller ablative inserts. Calculations in Appendix I showed that the ablation time is dependent on the number of ablative inserts according to the following proportionality:

$$T \propto \frac{1}{N}$$

where

T = ablation time

N = number of ablative inserts used in the restrictor

The results of the analysis contained in Appendix J indicated N is limited to a maximum of 241 ablative inserts for Wind Tunnel 9. This limitation is due to the need for maintaining structural integrity of the flow restrictor while maintaining a final flow restrictor open area of 6.62 square inches.

The initial open area of each ablative insert is determined by the following equation:

$$A_i = \frac{A_o}{N}$$



where

$A_i$  = initial open area in each ablative insert

$A_o$  = initial open area of flow restrictor

$N$  = number of ablative inserts

$A_o$  must not be greater than 0.17 square inches as to avoid damage to wind tunnel heater internal components. Thus, with  $N$  limited to 241, the above relation yields:

$$A_i = \frac{0.17}{241} = 0.00070 \text{ square inches.}$$

This corresponds to the initial diameter of 0.030 inches.

Figure K-1 shows the proposed ablative insert design needed to achieve an initial open area of 0.17 square inches and a final open area of 6.62 square inches.

The purpose of this memorandum is to provide structural analysis of the proposed ablative insert and predict the likelihood of it passing 30,000 psi cold pressure testing.

#### BACKGROUND

The existing ablative insert, made of DELRIN, was designed using rudimentary shear analysis. Other stresses and hydrodynamic loading were not considered. The ablative inserts were successfully subjected to laboratory cold pressure tests up to 30,000 psi. They have been used successfully in over 500 wind tunnel runs.

Prediction of ablator performance is difficult because:

- a. Exact criteria for ablator rupture is not known,
- b. The ablative insert is operated near its failure point, albeit for a brief time,
- c. Uncertainties in the modelling loads can lead to incorrect predictions of failure.

#### ANALYTICAL APPROACH

The approach taken was to create a finite element mesh of an ablative insert cross section, and to utilize finite element structural analysis. The following steps were taken in the stress analysis:

a. MESHGEN, DOASIS, and CONTOUR computer codes were selected for performing the analysis.

1. MESHGEN generated finite element meshes for the ablative inserts. DOASIS generated axial, radial, hoop, and shear stress values. The DOASIS code also combined the four stresses into an effective stress at each element. The effective stress is a means of relating each element's three dimensional state of stress to the uniaxial properties of the insert material.

2. DOASIS provided radial strains, axial strains, and deflection values for each nodal point. This nodal point deflection data was used in CONTOUR to generate axial cross section views of the deformed ablative insert.

3. The plots generated by MESHGEN were coded to show which elements exceeded their yield point and the direction (axial, radial, hoop) of stress which contributed most heavily to yielding.

b. Assumptions were made regarding gas pressure loadings and material properties. The general types of gas pressures and their time durations are shown in Figure K-2 and described below.

1. The three microsecond transient gas pressure load is assumed not to exist on the ablative insert. This dynamic condition is ill-defined and DOASIS cannot handle dynamic loading conditions. The transient occurs immediately after wind tunnel diaphragms rupture. It was felt that the steady-state conditions (described below) were much harsher than the transient condition noted above.

2. After the transient time, steady-state loading on the inserts is caused by gas pressures of 22,000 psi on the outside diameter of the ablative insert and 11,000 psi in its throat. Three seconds after diaphragms rupture the expansion wave has passed through the throat of the insert. At that time the gas pressure is 11,000 psi because of sonic gas flow. It is still 22,000 psi between the outside diameter of the insert and the restrictor wall because gas is trapped and not in motion. These pressures are shown in Figure K-3.

3. The analysis used material properties of DELRIN at 122° Fahrenheit, which is the known temperature of the insert prior to ablation.

c. The load assumptions in the DOASIS finite element computer code were partially tested and confirmed by analyzing the existing ablative insert and assuring that results agreed with actual insert usage (no failures).

d. A parametric study and analysis were performed. Ablative insert length, outside diameter, and support area dimensions were varied. Stresses were computed for the present ablative insert after it was scaled by a factor of 0.406 to achieve a Reynold's number of  $20 \times 10^6$  per foot. The resulting maximum effective stresses were graphed.

e. Stresses in the existing and new insert design were compared.

## ANALYSIS OF RESULTS

The maximum effective stress, composed of axial, radial, hoop, and shear stresses, was computed to be 12,070 psi in the present ablative insert. This value does not exceed the ultimate compressive strength of 14,800 psi for DELRIN at a temperature of 122° Fahrenheit. This lends credibility to the computer model used and the loading conditions assumed.

When the size of the ablative insert support area is varied by increasing the inside diameter of the support surface, its maximum effective stress changes as shown in Figure K-4. Figure K-4 also shows that the maximum effective stress remains essentially constant for ablative insert support areas which are equal to or greater than the existing one.

When the 0.5 inch length of the current ablative insert is shortened by removing material from its upstream side, the resulting maximum effective stress changes as shown in Figure K-5. The stress increases rapidly as the length of the present insert is made shorter than 0.4 inches. When the insert length is approximately 0.2 inches the maximum effective stress is 15,000 psi, which exceeds DELRIN's ultimate compressive strength of 14,800 psi.

Axial stress contributed most to the maximum effective stress in the present ablative insert. The crosshatching in Figure K-6 indicates where the largest component of the combined stress is axial stress. This stress distribution is due to the gas pressure differential across the flow restrictor. This gas pressure forces the ablative insert against the limited support area provided by the flow restrictor. The maximum axial stress was calculated to be 18,000 psi.

The hoop stress component of effective stress is caused by the pressure differential between the outside and inside walls of the existing ablative insert. The volume of the insert material which yields due to hoop stress is indicated by the solid shading in Figure K-6. The maximum hoop stress was calculated to be 16,300 psi.

Radial stress, with a maximum value of 13,520 psi, made small contributions to the effective stress in the present ablative insert.

Shear stress contributes least to effective stress in the existing insert. The analysis shows that a maximum of 4,200 psi shear stress is generated in the insert. This maximum is located at the downstream end. The minimum is located at the upstream end of the insert.

Deformations due to effective stress were calculated for the present insert and are plotted in Figure K-7. The following two types of deformation are superimposed on the graph's curve:

- a. Hydrostatic compression. This causes low effective stress and no yielding.
- b. Extrusion. This caused a 0.009-inch deformation in the downstream portion of the ablative insert.

The stresses, strains, deflections, and deformations are identical for the present ablative insert and a 0.406 scale version of it. This can be seen by comparing the yield and deformation plots (Figures K-6 and K-7) for the present ablative insert with those (Figures K-8 and K-9) for the 0.406 scale version. These similarities occur because they are both subjected to the static loading conditions, and are geometrically similar.

Computations for the proposed new ablative insert show that the maximum effective stress and the percentage of deformed material is reduced from that encountered in the present insert. The proposed design has a maximum effective stress of 12,000 psi which also does not exceed DELRIN's ultimate compressive strength of 14,800 psi. The components of effective stress are addressed below for the proposed new ablative insert.

Axial stress was the largest component of effective stress. This is due to the limited ablative-insert support area which causes the observed stress distribution. The amount of material which yielded due to compressive stress is shown in Figure K-10. Maximum axial stress was 17,800 psi.

The hoop stress part of effective stress caused less yielding than it did in the present ablative insert. This was due to thicker insert walls which distributed the load over a greater area. The solid shading in Figure K-10 shows where yielding was due primarily to hoop stress in the proposed design. Maximum hoop stress was 16,000 psi.

Radial stress in the proposed ablative insert increased about eight percent compared to the present design. This was due to more bending caused by additional overhanging material. The dotted element in Figure K-10 shows where radial stress was the principal contributor to the maximum effective stress. Maximum radial stress was computed to be 15,200 psi.

Shear stress increased about ten percent compared to the present insert design. This increase was due to a larger unsupported mass, or overhang. Shear stress was not the primary contributor to yielding in elements of the proposed ablative insert. Maximum shear stress was 14,600 psi.

Deformations due to yielding in the proposed ablative insert are shown in Figure K-11. A maximum deflection of 0.004 of an inch was calculated: its location is indicated in the figure. Note the slight reduction in the length of the insert due to hydrostatic compression.

#### SUMMARY AND CONCLUSIONS

A finite element analysis of both the existing ablator geometry and a proposed new configuration was performed. It was concluded that:

- a. Use of static loads provides the worst case, or conservative analysis.
- b. The proposed design of the new ablative insert appears to have greater structural integrity than the present insert. It should pass the laboratory cold pressure tests.

It is recommended that:

- a. Proposed new ablative insert be subjected to cold pressure tests at 30,000 psi to verify the results of the computer analysis.
- b. Tests be conducted on the proposed new ablative inserts, which have been shortened. Successively shorter lengths should be tested until a failure occurs.
- c. Future analysis be performed on an ablative insert which has a quarter-circle cross section. The objective of this analysis would be to reduce the overall length of the insert to improve the aerodynamics of the flow restrictor, and reduce the amount of material that was to be ablated.

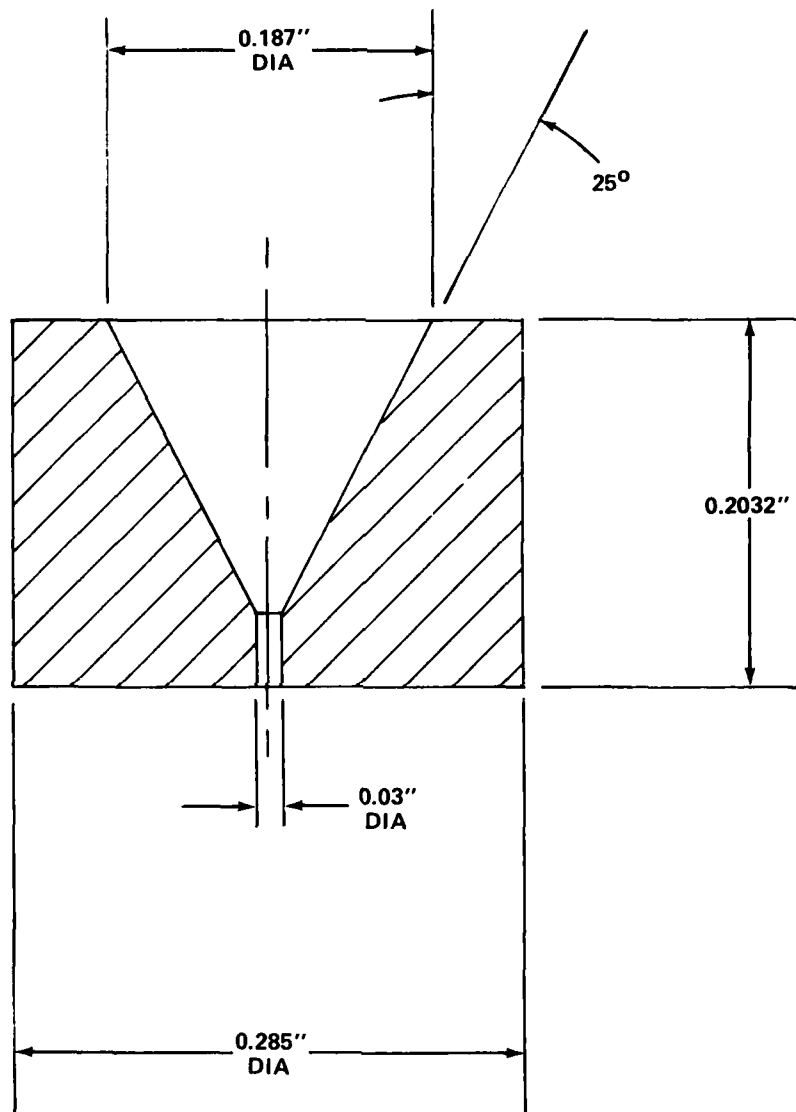


FIGURE K-1. PROPOSED NEW ABLATIVE INSERT

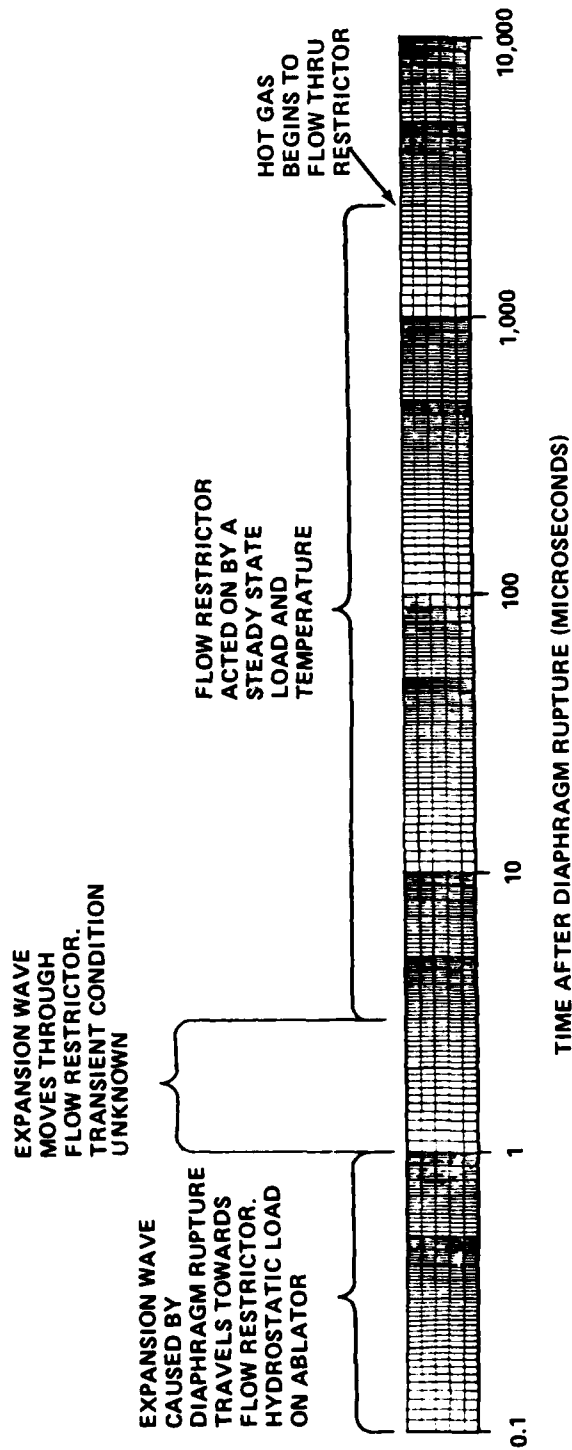


FIGURE K-2. TIME HISTORY OF GAS PRESSURE ON TUNNEL 9 ABLATOR

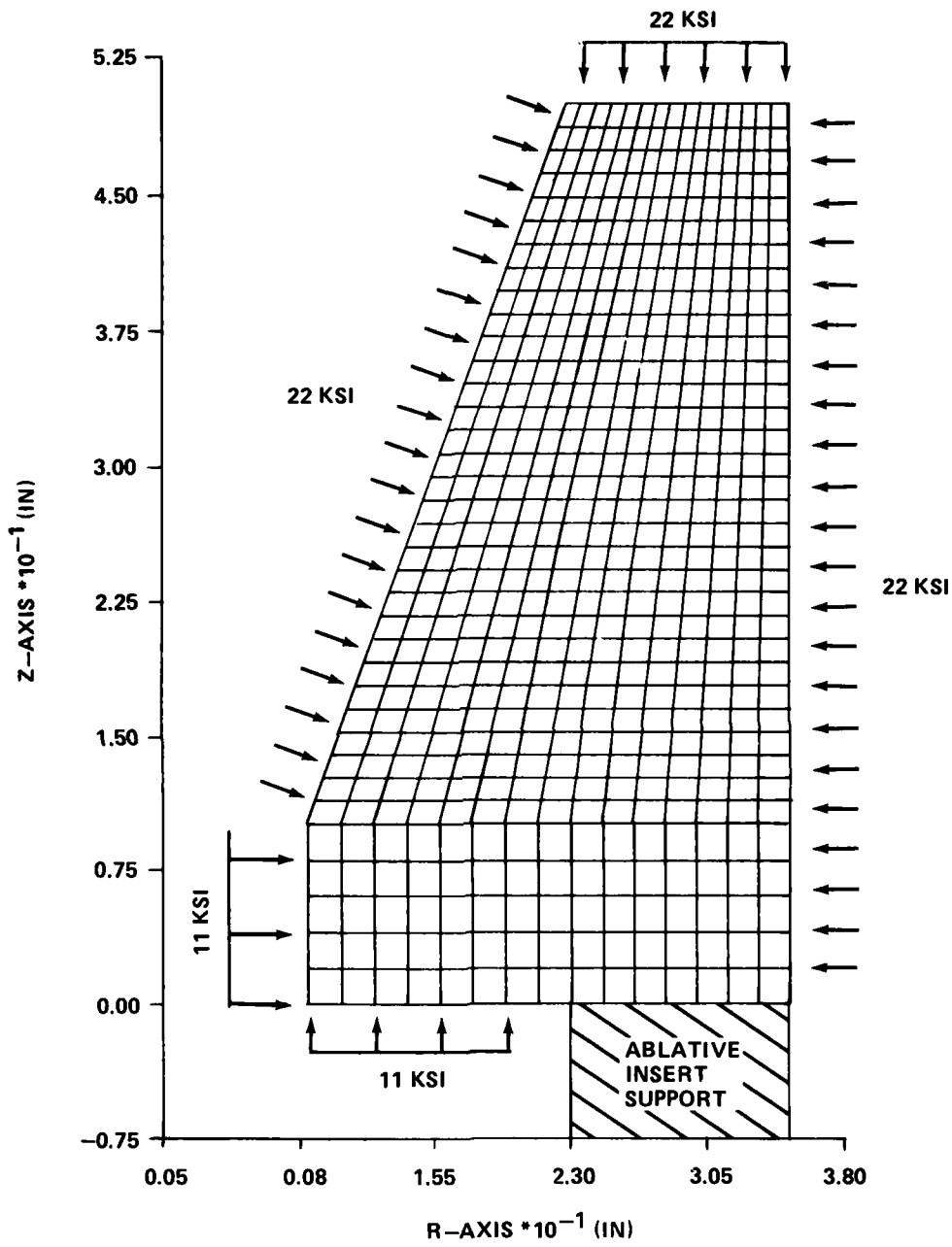


FIGURE K-3. GAS PRESSURES ON ABLATIVE INSERT



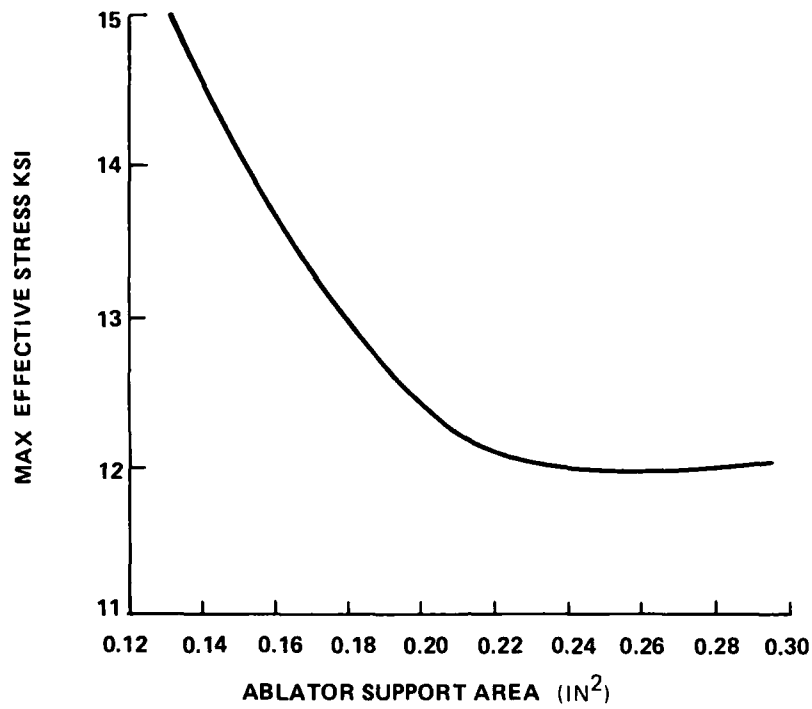


FIGURE K-4. ABLATIVE INSERT STRESS AS A FUNCTION OF INSERT SUPPORT AREA

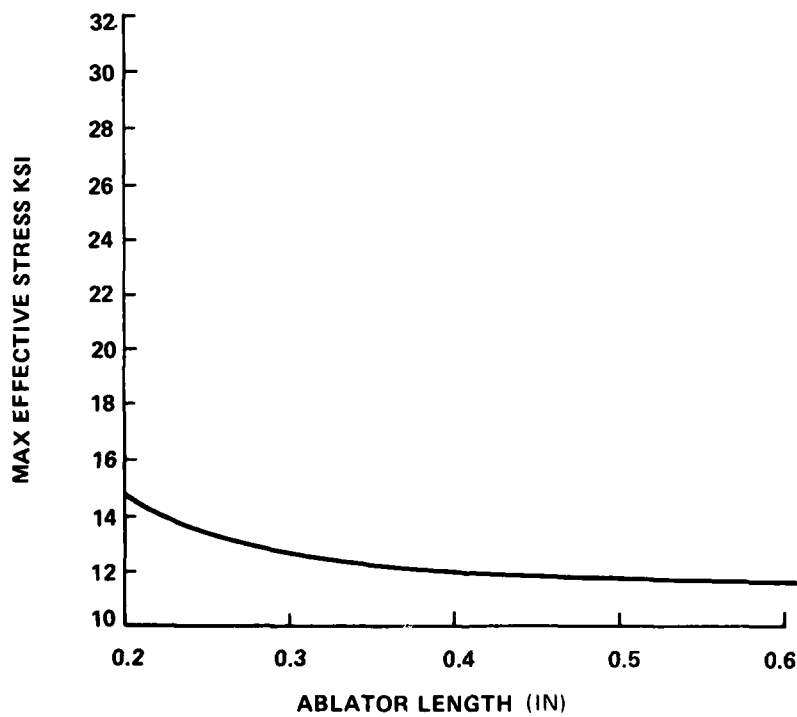


FIGURE K-5. ABLATIVE INSERT STRESS AS A FUNCTION OF INSERT LENGTH

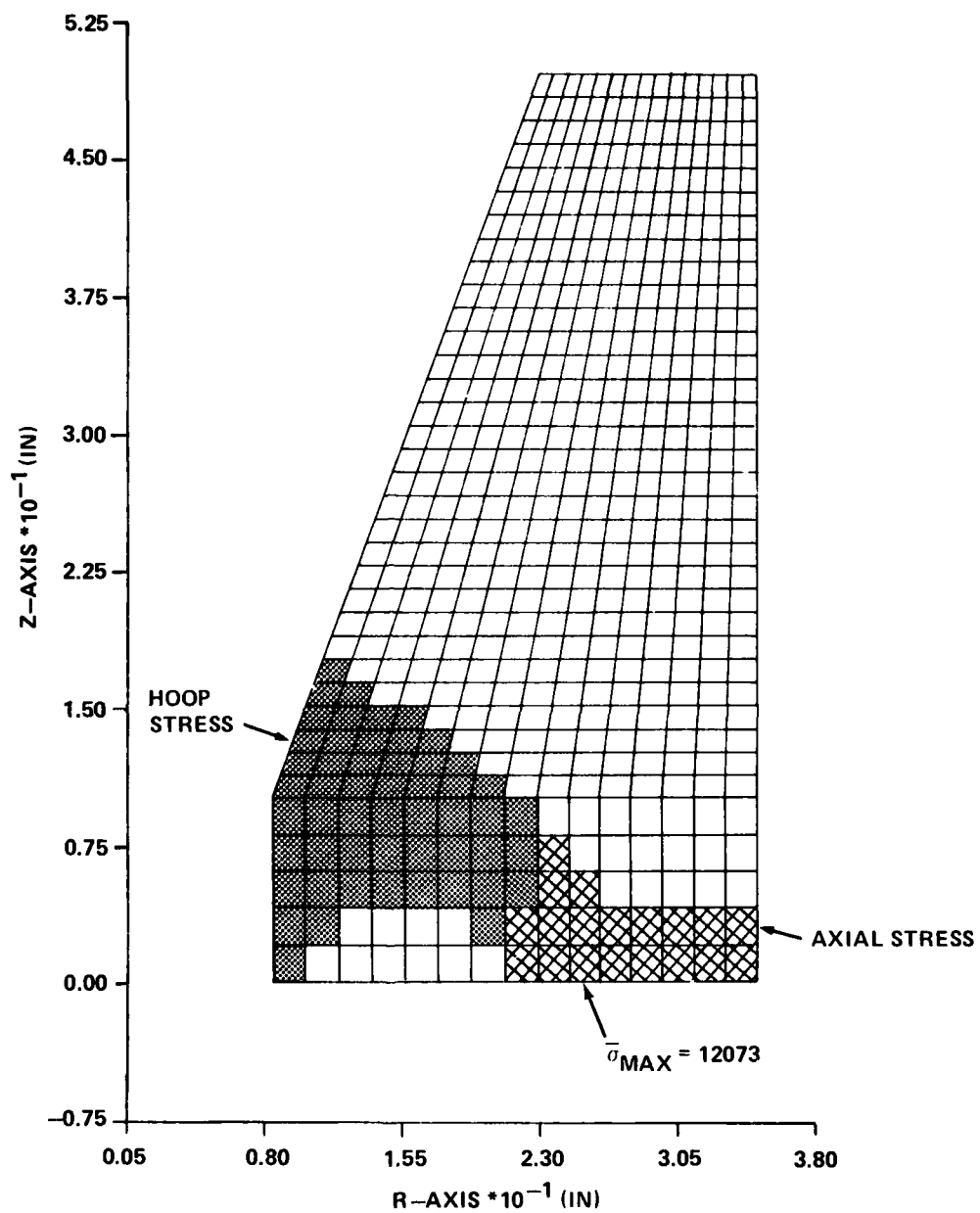


FIGURE K-6. HOOP AND AXIAL STRESS YIELDING IN EXISTING ABLATIVE INSERT

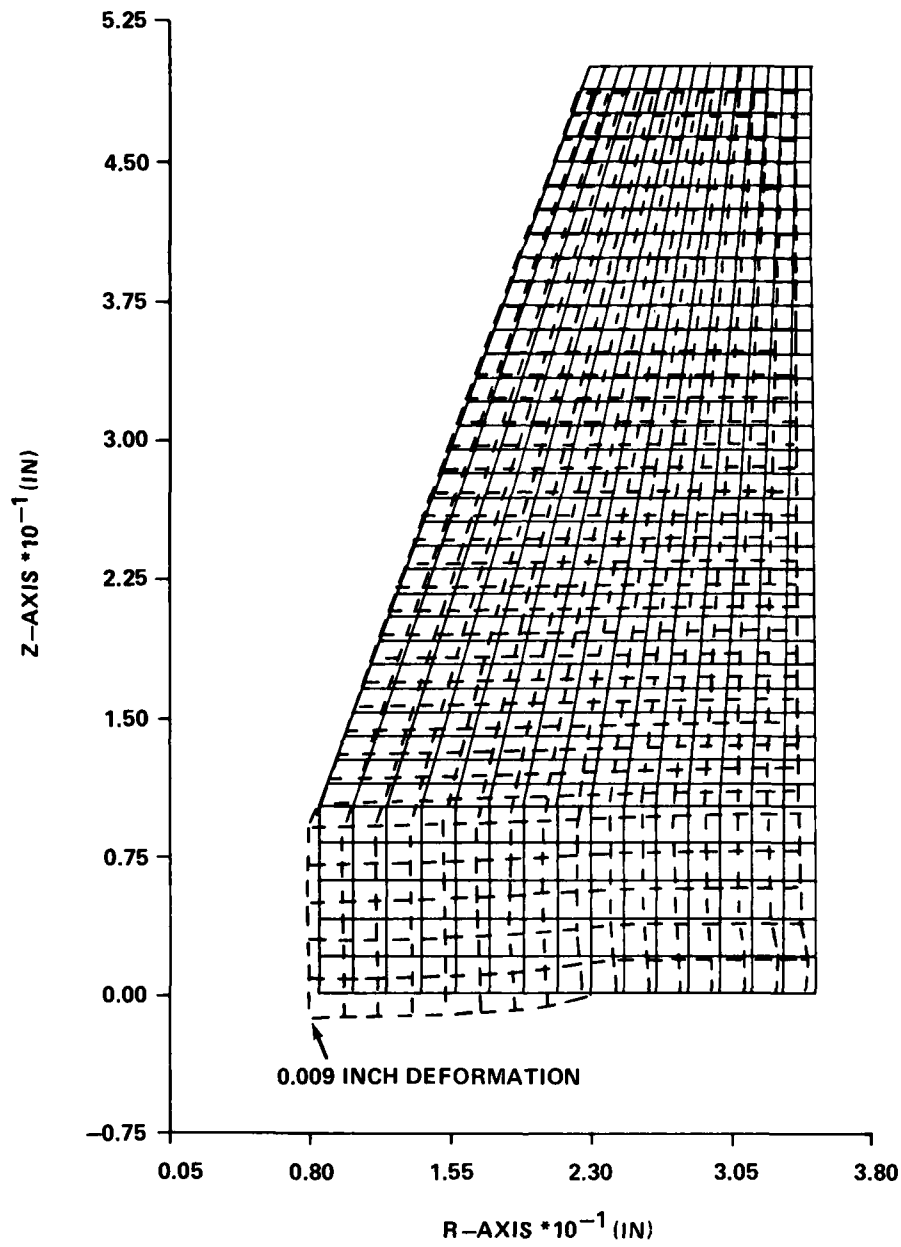


FIGURE K-7. DEFORMATION OF EXISTING ABLATIVE INSERT DUE TO EFFECTIVE STRESS

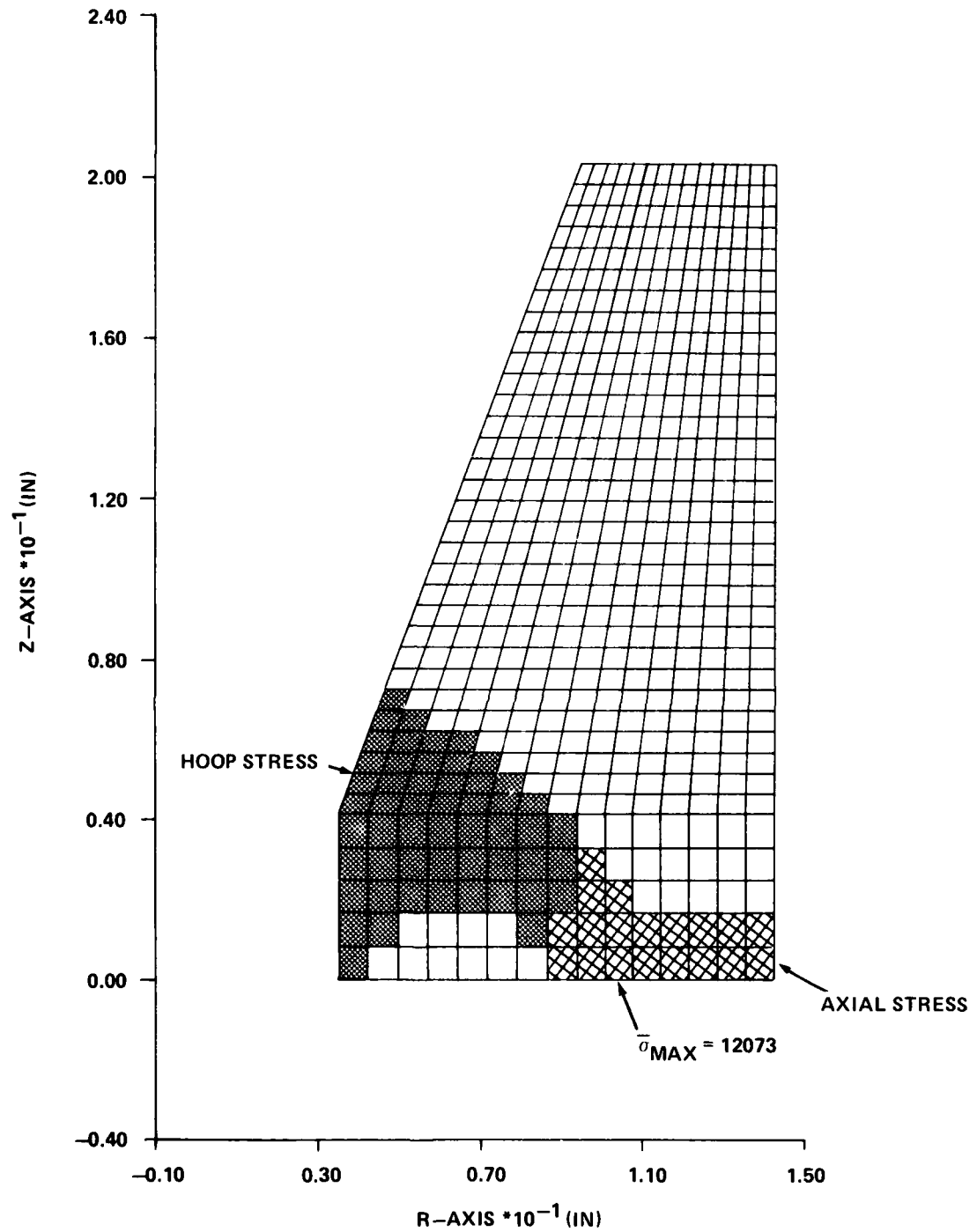


FIGURE K-8. HOOP AND AXIAL STRESS YIELDING IN 0.406 SCALE ABLATIVE INSERT

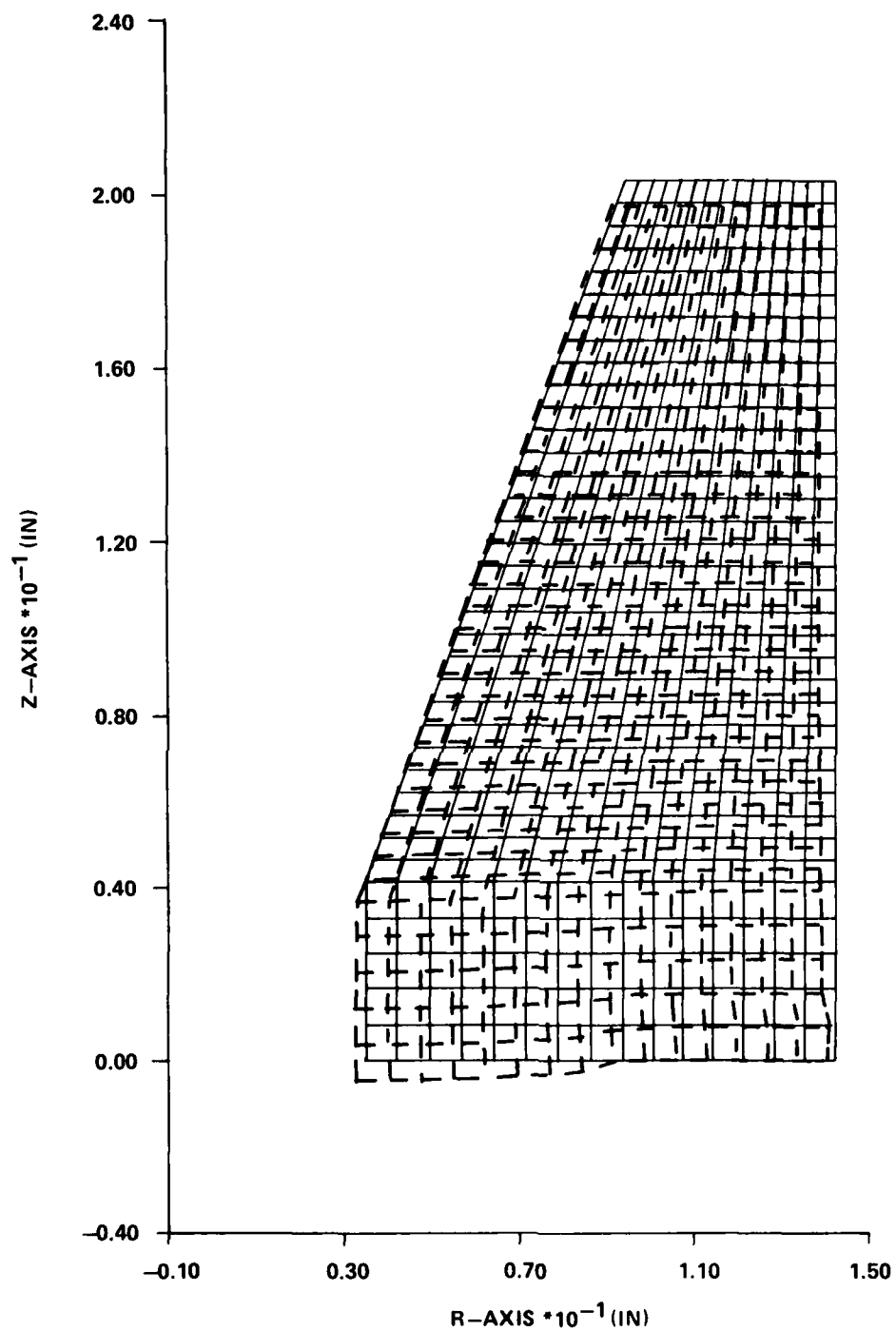


FIGURE K-9. DEFORMATIONS IN 0.406 SCALE ABLATIVE INSERT

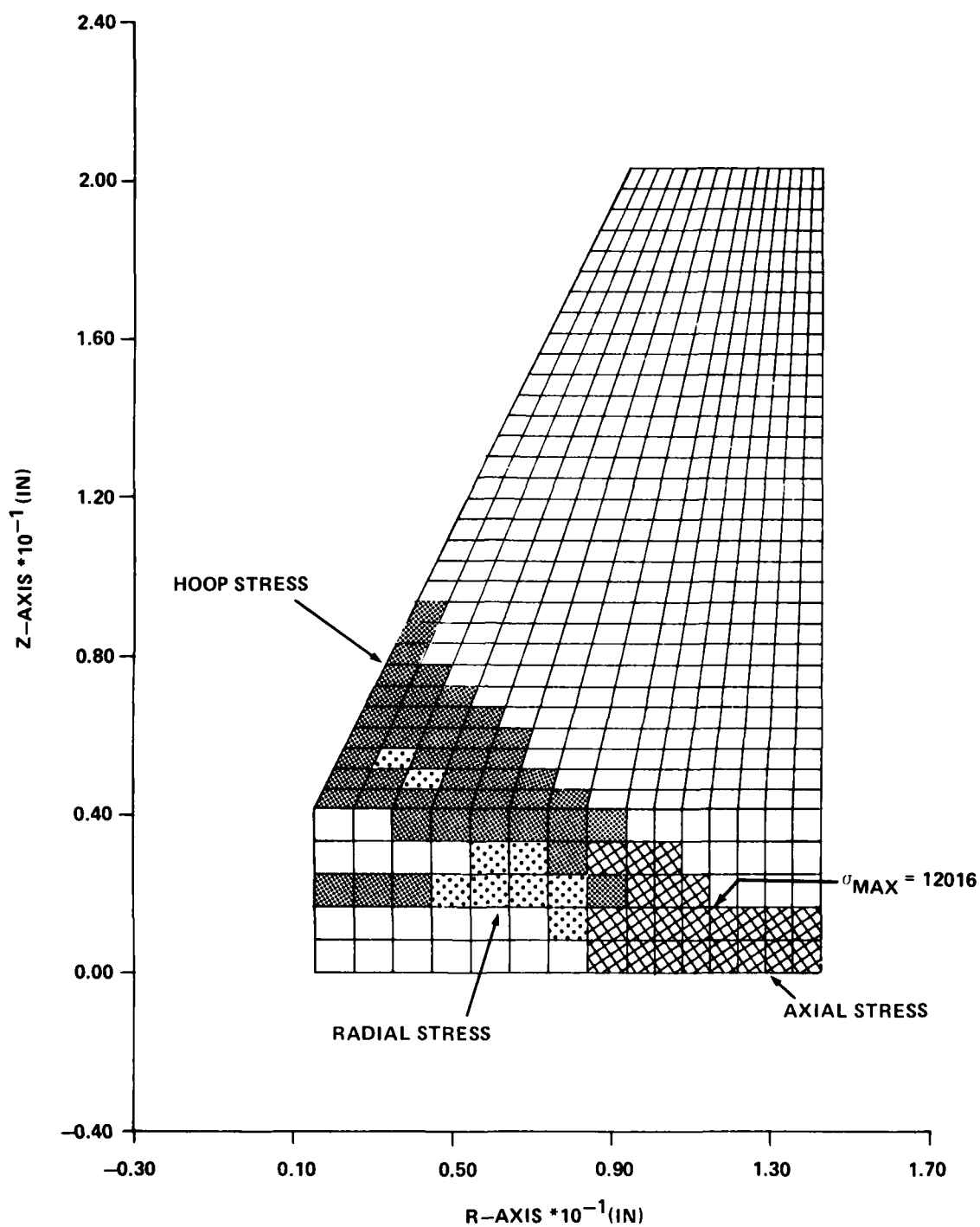


FIGURE K-10. YIELDING DUE TO AXIAL, HOOP, AND RADIAL STRESSES IN THE PROPOSED ABLATOR

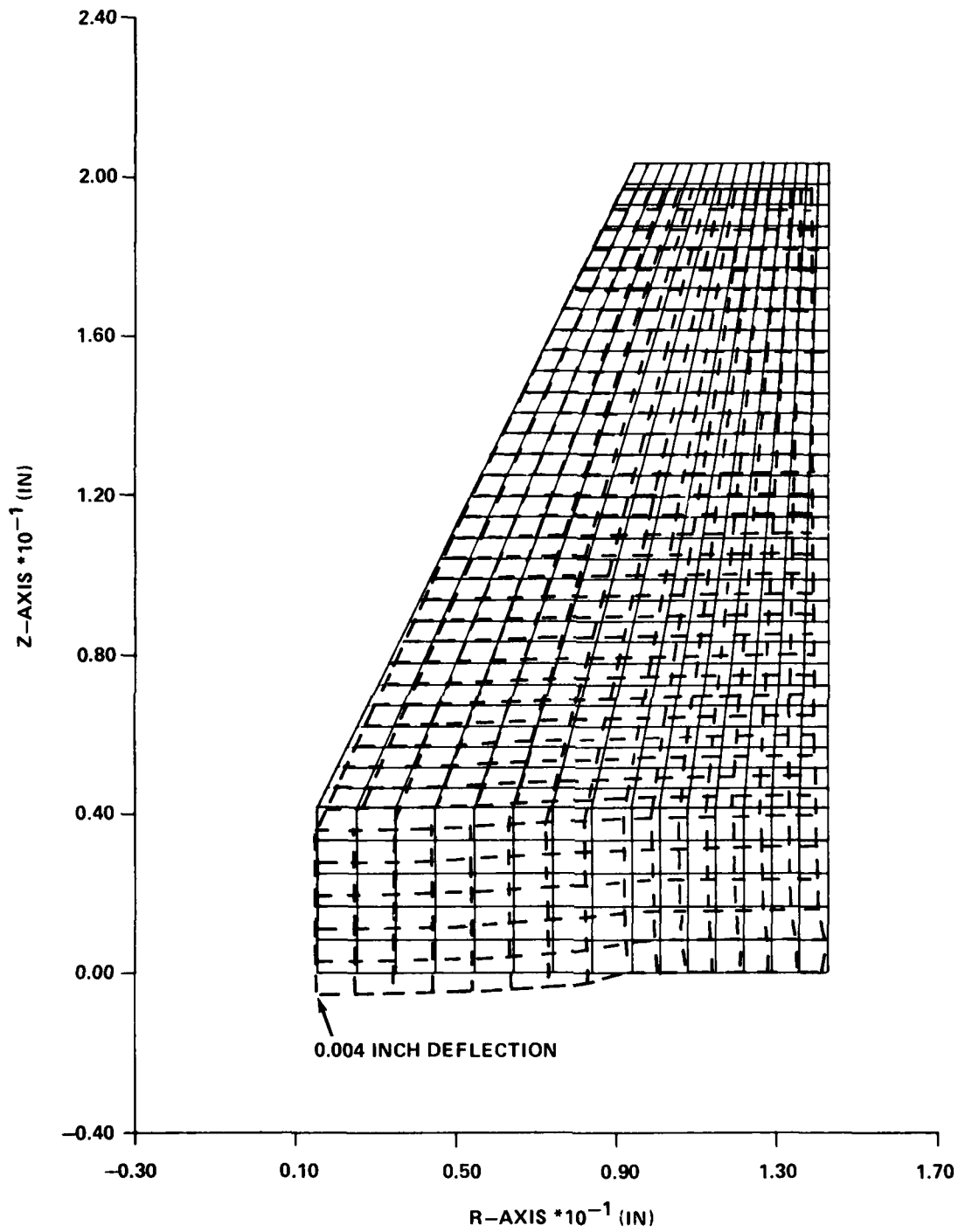


FIGURE K-11. DEFORMATIONS DUE TO LOADING IN THE PROPOSED ABLATIVE INSERT

## APPENDIX L

## BLOWDOWN COMPUTER MODEL

## INTRODUCTION

The Mach-10 HIRE program requires a much higher  $P_0$  as compared to the original design  $P_0$  specification at Mach-10. In order to obtain the higher  $P_0$ , the gas supply control valves must pass a greater mass flow (lbs/sec). To pass this additional mass flow through the control valves, without increasing the number of valves, the storage vessel pressure and temperature must be increased. Calculations must be done to determine what the higher storage pressures and temperatures must be in order to obtain the higher mass flows, the higher  $P_0$ , and the desired run time. In the past these tedious calculations were done by hand using a tabular format and were known as "Storage Vessel Blowdown Performance" calculations. This appendix outlines a computer program that was written to perform the "Storage Vessel Blowdown" calculations. In addition, the computer program models the control valves and calculates the valve area needed to obtain the necessary mass flow and  $P_0$ . The volumetric flow rate out of the heater was needed as input to the computer program so a small computer program was generated to calculate this parameter taking the imperfect behavior of gas at high pressure into account. This appendix also presents the results obtained from the computer programs as applicable to the Mach-10 HIRE program and to the upcoming "Quick-Proof" hot and cold tests.

## COMPUTER MODEL

The computer programs utilize real-nitrogen thermodynamic subroutines which have been derived from Reference L-1. Using a pressure and a temperature as input parameters, subroutines have been constructed which return nitrogen density, entropy, enthalpy, and speed of sound. In addition, two subroutines have been written which model constant entropy and constant enthalpy processes. These subroutines require a pressure and an entropy or enthalpy as input and return a temperature while holding the given entropy or enthalpy constant.

Volumetric Flow Rate

The volumetric flow rate program models the flow from the heater to the nozzle as an isentropic expansion from the gas conditions in the heater to the sonic gas conditions at the nozzle throat. The program drops the pressure in preselected decrements and calculates a new temperature at constant entropy. Knowing the pressure and temperature, the density, enthalpy, gas velocity, and sound speed can be calculated. The program continues until the gas velocity is



equal to the sound speed. When this condition is achieved the sonic conditions have been reached. The mass flow rate through the nozzle can now be calculated using the density and nozzle area. Since the mass flow rate can be assumed constant from the nozzle to the heater, the volumetric flow rate out of the heater can be calculated using the original heater gas density. Figure L-1 shows a schematic diagram of the flow rate process which is being modelled.

#### Storage Vessel Blowdown

The storage vessel blowdown program models the flow of the driver gas from the storage vessels, through the control valves, and into the heater. It is assumed that the heater pressure remains constant and that an ideal cold gas/hot gas interface exists in the heater so that the more dense driver gas expels the heater gas without mixing. The program allows the storage vessel pressure to drop in preselected decrements. As the pressure drops the temperature and density on both sides of the valves are determined. In addition, the mass flow and time to reach each lower value of storage pressure is calculated. The program assumes a constant entropy process in the storage vessel and a constant enthalpy expansion across the control valves. Figure L-2 shows a schematic diagram of the blowdown process being modelled. A pressure drop of 3,200 psi, from the downstream side of the control valves to the bottom of the heater, has been calculated in Enclosure 1 of this appendix and is assumed to be constant throughout the blowdown program. Using the relationship:

$$A = \frac{m}{5.28 \text{ S.G. } (\Delta P)}$$

where

A = valve area,

m = mass flow rate,

S.G. = average specific gravity of inlet and exit nitrogen,

$\Delta P$  = pressure drop across the valves,

which was derived by the control valve manufacturer, the required valve area versus time was calculated by the program. The program is terminated when a preselected storage pressure is reached.

The input variables to the blowdown program are the following: (1) initial storage pressure, (2) initial storage temperature, (3) storage pressure decrement, (4) storage volume, (5) heater pressure, (6) volumetric flow rate out of heater, (7) final storage pressure, (8) pressure at downstream side of control valves.

The output from the program is printed out in tabular form for each pressure decrement and consists of the following: (1) storage pressure, (2) storage temperature, (3) storage density, (4) weight of nitrogen gas in storage vessels, (5) heater pressure (constant), (6) temperature of driver gas

in heater, (7) density of driver gas in heater, (8) mass flow rate of driver gas into heater, (9) weight of nitrogen gas exiting driver vessels, (10) elapsed time during pressure decrement, (11) run time elapsed, (12) volume of heater gas that has left heater, (13) pressure drop across the control valves, (14) average specific gravity of nitrogen gas entering and exiting control valves, (15) total control valve area needed, (16) area needed per control valve (9 valves), (17) driver gas temperature at exit of control valves.

## RESULTS

The results obtained from the flow rate program are shown in graphical form in Figures L-3 and L-4. Figure L-3 shows volumetric flow rate versus pressure at 80°F and 1500°F. Figure L-4 shows mass flow rate versus pressure for the same temperature conditions. The results shown in both figures were obtained using a Mach-10 nozzle throat area of 4.52 in<sup>2</sup>.

As can be seen from Figures L-3 and L-4 the flow rates for the hot condition are fairly linear over a wide range of supply pressures. At the higher pressures the hot condition curves make a slight rise upward. This slight rise is due to a corresponding rise in the sound speed at these conditions. Several of the points plotted in Figures L-3 and L-4 have been checked against hand calculations. At the lower pressures the correlation is extremely good, while at the higher pressures; and in particular at the high temperature; the differences are greater. For example, at 10,000 psi and 80°F hand calculations show a volumetric flow rate of 32.5 ft<sup>3</sup>/sec while the computer program predicts a flow rate of 34.0 ft<sup>3</sup>/sec. At 20,000 psi and 1500°F the hand calculation yields a flow rate of 58.6 ft<sup>3</sup>/sec and the computer program predicts a value of 51.8 ft<sup>3</sup>/sec. The values predicted by the computer program, and shown in Figures L-3 and L-4, have been used as input in the "blowdown" computer program.

The preliminary results from the "blowdown" program showed that the initial storage conditions could be as low as 38,000 psi and 700°R with satisfactory tunnel run time still being achieved before the "cut-off" pressure is reached. The "cut-off" pressure is the storage pressure below which sufficient flow through the control valves cannot be maintained for a given heater pressure. For the Mach-10 HIRE conditions the cut-off pressure has been defined as the heater pressure plus 5,000 psi, or 27,000 psi. The preliminary blowdown results are shown in Figure L-5 for initial storage pressures of 38,000 and 40,000 psi and initial storage temperatures of 700 and 800°R.

The capability to compute the control valve area required to obtain the blowdown performance shown in Figure L-5 was next incorporated into the computer program. The results of this computer calculation for initial storage pressures of 38,000, 40,000, and 42,000 psi at 800°R are shown in Figure L-5. The results show that the "baseline" M-10 HIRE initial driver conditions of 40,000 psi, 800°R will achieve the desired run time before the maximum available control valve area is reached. Figure L-6 shows that with an initial storage temperature of 800°R, the storage pressure can be as low as 39,000 psi to achieve the desired run time before the maximum valve area is reached.

Concern was expressed that an initial storage temperature of 800°R (340°F) may be too high for some of the internal storage vessel components. Due to this concern additional computer calculations were done using an initial storage temperature of 700°R (240°F). The results of these calculations are shown in Figure L-7. From the figure one can see that at 40,000 psi the maximum valve area is reached before the maximum run time is attained. Thus, if the maximum run time is to be achieved with an initial storage temperature of 700°R, an initial storage pressure greater than 40,000 psi must be used.

For the upcoming M-10 HIRE "Quick-Proof" program the "baseline" driver conditions of 40,000 psi and 800°R have been proposed to obtain a run time of approximately .25 seconds. However, only 6 control valves will be operational for this test. This translates to a maximum valve area of 4.5 in<sup>2</sup>. It was desired to find how low the heater pressure must be to obtain the desired run time given these control valve and storage conditions. Calculations were performed using the blowdown program and the appropriate value of volumetric flow rate from Figure L-3. The results of these computer calculations are shown in Figure L-8. The results indicate that the heater pressure must be reduced to at least 18,000 psi in order to obtain the desired run time using only 6 control valves.

As an additional requirement for the M-10 "Quick-Proof" program it was desired to find what storage pressure was needed (at 800°R) to achieve the desired run time using a heater pressure of 10,000 psi and 6 control valves. Based on computer calculations done using the blowdown program it was determined that an initial storage pressure of at least 23,000 psi was needed to achieve the run time at these conditions.

#### CONCLUSIONS

The results of the computer calculations presented in this memo indicate that 9 control valves, each capable of a maximum open area of .75 in<sup>2</sup>, will be sufficient to pass the needed mass flow rate from the storage vessels at nominal initial M-10 HIRE conditions of 40,000 psi and 800°R to the heater vessel. The heater vessel has been assumed to be at a constant pressure of 22,000 psi throughout the storage vessel blowdown.

For the M-10 HIRE "Quick-Proof" testing a heater pressure of 18,000 psi, with initial storage conditions of 40,000 psi and 800°R, will be sufficient to obtain a 1/4 second run time with 6 control valves. For the "Quick-Proof" testing to be done at a heater pressure of 10,000 psi a storage pressure of at least 23,000 psi should be used.

# CALCULATION OF PRESSURE DROP FROM CONTROL VALVES TO BOTTOM OF HEATER

In order to introduce an element of conservatism into the pressure drop calculation a valve of  $Q = 58.6 \text{ ft}^3/\text{sec}$  is used instead of the computer predicted value of  $Q = 51.8 \text{ ft}^3/\text{sec}$  at  $P_H = 22,000 \text{ psi}$  and  $T_H = 1500^\circ\text{F}$ . In addition, the pressure drop calculated has been held constant in the blowdown computer program used to calculate required valve area. This gives a conservatively high prediction for the required valve area. In the calculations below, dimensions were taken from Figure L-9.

## HORIZONTAL PIPE FROM VALVES TO HEATER ENTRANCE

$$D = 3 \frac{11}{16}'' = .307 \text{ ft.}$$

$$L = 241'' = 20.1 \text{ ft.}$$

$$\Delta P(\text{psi}) = h_f \frac{\rho}{144}$$

where

$$h_f = f \frac{L}{D} \frac{V^2}{2g} \text{ for pipe flow}$$

$$V = \frac{Q}{A} = \frac{58.6 \text{ ft}^3/\text{sec}}{\frac{\pi}{4} (.307)^2 \text{ ft}^2} = 792 \text{ ft/sec}$$

$$f = \text{friction factor} = f(\text{Re})$$

$$\text{Re} = \frac{VD\rho}{\mu} = \frac{(792)(.307)(36.5)}{3.88 \times 10^{-5}} = 2.28 \times 10^8$$

From Moody Diagram for Smooth Pipes

$$f = .005$$

$$h_f = .005 \frac{20.1}{.307} \frac{(792^2)}{(2)(32.2)} = 3188 \text{ ft}$$

$$\Delta P = \frac{(3188)(36.5)}{144} = 808 \text{ psi}$$

PIPE CONTRACTION FROM HORIZONTAL PIPE TO 30° ELBOW

$$\frac{A_2}{A_1} = \frac{(3.0)^2}{(3.68)^2} = .66$$

$$C_c = \text{contraction coefficient} = .73$$

(For water from Ref. L-2, p. 296.)

$$h_c = \left( \frac{1}{C_c} - 1 \right)^2 \frac{\rho v_2^2}{2g}$$

$$v_2 = \frac{Q}{A} = \frac{58.6 \text{ ft}^3/\text{sec}}{\frac{\pi}{4} (.25)^2 \text{ ft}^2} = 1193 \text{ ft/sec}$$

$$\Delta P = \left( \frac{1}{.73} - 1 \right)^2 \frac{(1193)^2}{(2)(32.2)} \frac{36.5}{144} = 766 \text{ psi}$$

60° TURN AT MOUTH OF ELBOW

For Standard 90° Elbow  $K = .9$

For Our 60° Elbow Take  $K = .6$

$$h_f = K \frac{v^2}{2g}$$

$$v = \frac{Q}{A} = \frac{58.6 \text{ ft}^3/\text{sec}}{\pi \left[ \left( \frac{5}{12} \right)^2 - \frac{4.12}{12} \right]^2} = 334 \text{ ft/sec}$$

$$h_f = .6 \frac{(334)^2}{64.4} = 1039 \text{ ft}$$

$$\Delta P = h_f \frac{\rho}{144} = 1039 \frac{36.5}{144} = 263 \text{ psi}$$

FLOW THRU VERTICAL ELBOW LINER ANNULUS

$$\Delta P (\text{psi}) = .001294 \frac{L}{D} v^2$$

where

$$L = 50'' = 4.16 \text{ ft}$$

$$D = \text{equiv. dia.} = D_2 - D_1 = 1.75'' = .145 \text{ ft}$$

$$V = \text{velocity in annulus} = 334 \text{ ft/sec}$$

$$R_e = \frac{DV\rho}{\mu}$$

where

$$\rho = 36.5 \text{ lbs/ft}^3$$

$$\mu(23,200 \text{ psi}, 750^\circ\text{R}) = 3.88 \times 10^{-5} \text{ lbs/sec-ft}$$

$$R_e = \frac{(.145)(334)(36.5)}{3.88 \times 10^{-5}} = 4.55 \times 10^7 \quad f = .02 \text{ (Ref. L-2)}$$

$$\Delta P = \frac{(.001294)(.02)(4.16)(36.5)(334)^2}{1.75} = 250 \text{ psi}$$

#### SUDDEN EXPANSION AT EXIT FROM VERTICAL ELBOW ANNULUS

$$h_f = K \frac{V_1^2}{2g} \quad K = \left[ 1 - \left( \frac{D_1}{D_2} \right)^2 \right]^2 = \left[ 1 - \left( \frac{10}{24} \right)^2 \right]^2 = .68$$

$$V_1 = \text{velocity in annulus} = 334 \text{ ft/sec}$$

$$h_f = .68 \frac{(334)^2}{(2)(32.2)} = 1178 \text{ ft}$$

$$\Delta P = h_f \frac{\rho}{144} = (1178) \frac{36.5}{144} = 298 \text{ psi}$$

#### SUDDEN CONTRACTION AT ENTRANCE TO MAIN LINER ANNULUS

$$h_c = \left( \frac{1}{C_c} - 1 \right)^2 \frac{V_2^2}{2g} \quad \text{for} \quad \frac{A_2}{A_1} = \frac{[(12)^2 - (11.5)^2]}{[(12)^2 - (4.12)^2]} = \frac{36.9}{399} = .10$$

$$C_c = .62 \text{ (For water from Ref. L-2, p. 296).}$$

$$V_2 = \frac{Q}{A} = \frac{58.6 \text{ ft}^3/\text{sec}}{.256 \text{ ft}^2} = 228 \text{ ft/sec}$$

$$h_c = \left( \frac{1}{.62} - 1 \right)^2 \frac{(228)^2}{64.4} = 303 \text{ ft}$$

$$\Delta P = h_c \frac{\rho}{144} = (303) \frac{36.5}{144} = 77 \text{ psi}$$

## FLOW THROUGH MAIN LINER ANNULUS

$$\Delta P \text{ (psi)} = .001294 f \left( \frac{L}{D} \right) \rho V^2$$

where

$$L = 107'' = 8.92 \text{ ft}$$

$$D = \text{equiv. dia.} = D_1 - D_2 = 1.0'' = .083 \text{ ft}$$

$$V = \text{velocity in annulus} = 228 \text{ ft/sec}$$

$$R_e = \frac{DV\rho}{\mu} = \frac{(.083)(228)(36.5)}{3.88 \times 10^{-5}} = 1.78 \times 10^7 \quad f = .022 \text{ (Ref. L-2).}$$

$$\Delta P = (.001294)(.022) \frac{8.92}{1.0} (36.5)(228)^2 = 482 \text{ psi}$$

## 90° TURN AT EXIT FROM MAIN LINER ANNULUS

$$h_f = K \frac{V_1^2}{2g} \text{ For } 90^\circ \text{ Standard Elbow } K = .9$$

where

$$V = \text{velocity in liner annulus} = 228 \text{ ft/sec}$$

$$h_f = .9 \frac{(228)^2}{64.4} = 726 \text{ ft}$$

$$\Delta P = h_f \frac{\rho}{144} = 726 \frac{(36.5)}{144} = 184 \text{ psi}$$

## SUMMARY OF PRESSURE DROPS FROM CONTROL VALVES TO HEATER

1. Friction loss through horizontal pipe	808 psi	
2. Contraction loss from horizontal pipe--elbow	766 psi	
3. 60°F turning loss at elbow	263 psi	
4. Friction loss through elbow annulus	250 psi	
5. Expansion loss at elbow annulus exit	298 psi	
6. Contraction loss/main liner annulus	77 psi	
7. Friction loss through main liner annulus	482 psi	
8. 90° turning loss at main liner annulus exit	184 psi	
TOTAL	3128 psi	<u>use 3200 psi</u>



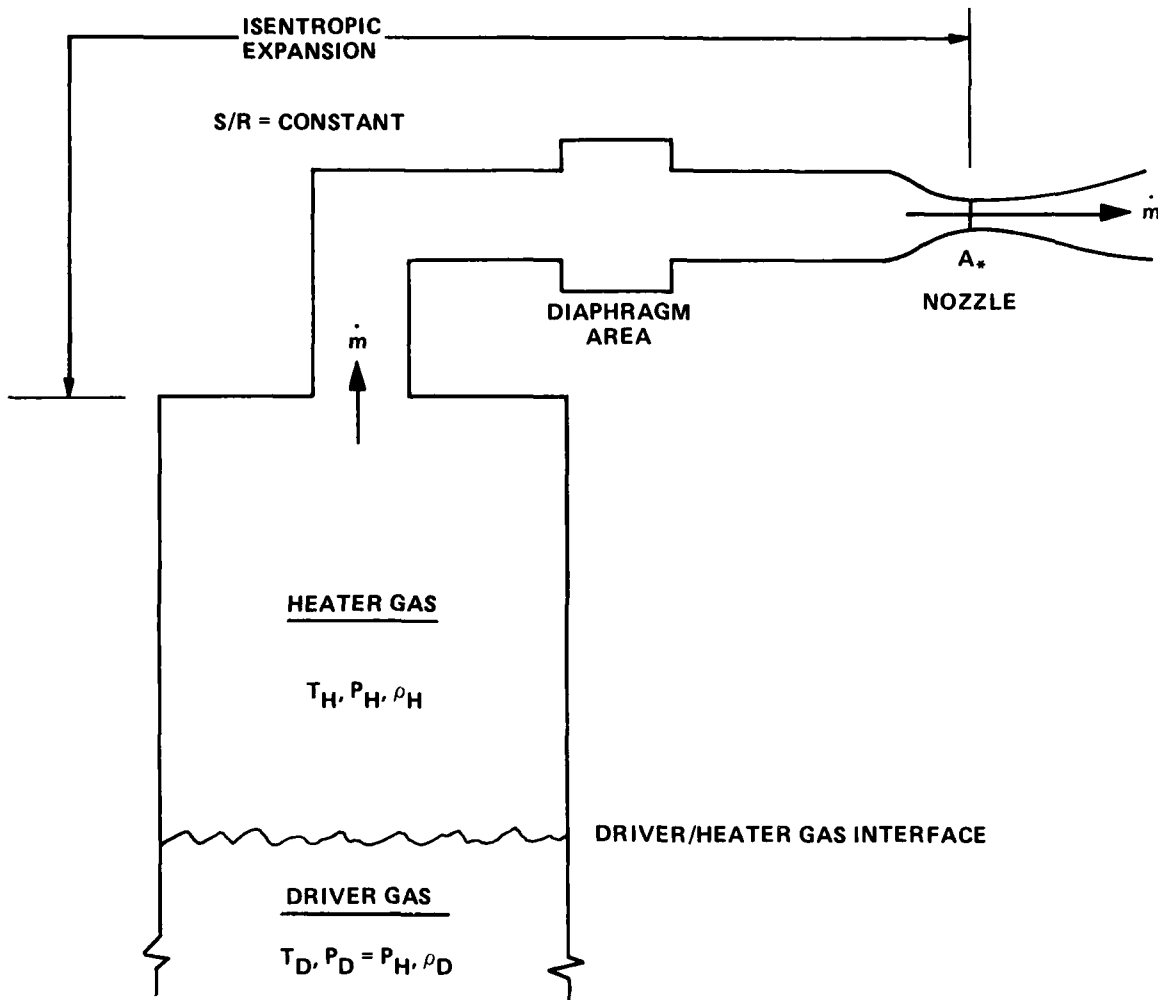


FIGURE L-1. SCHEMATIC DIAGRAM OF FLOW RATE MODEL

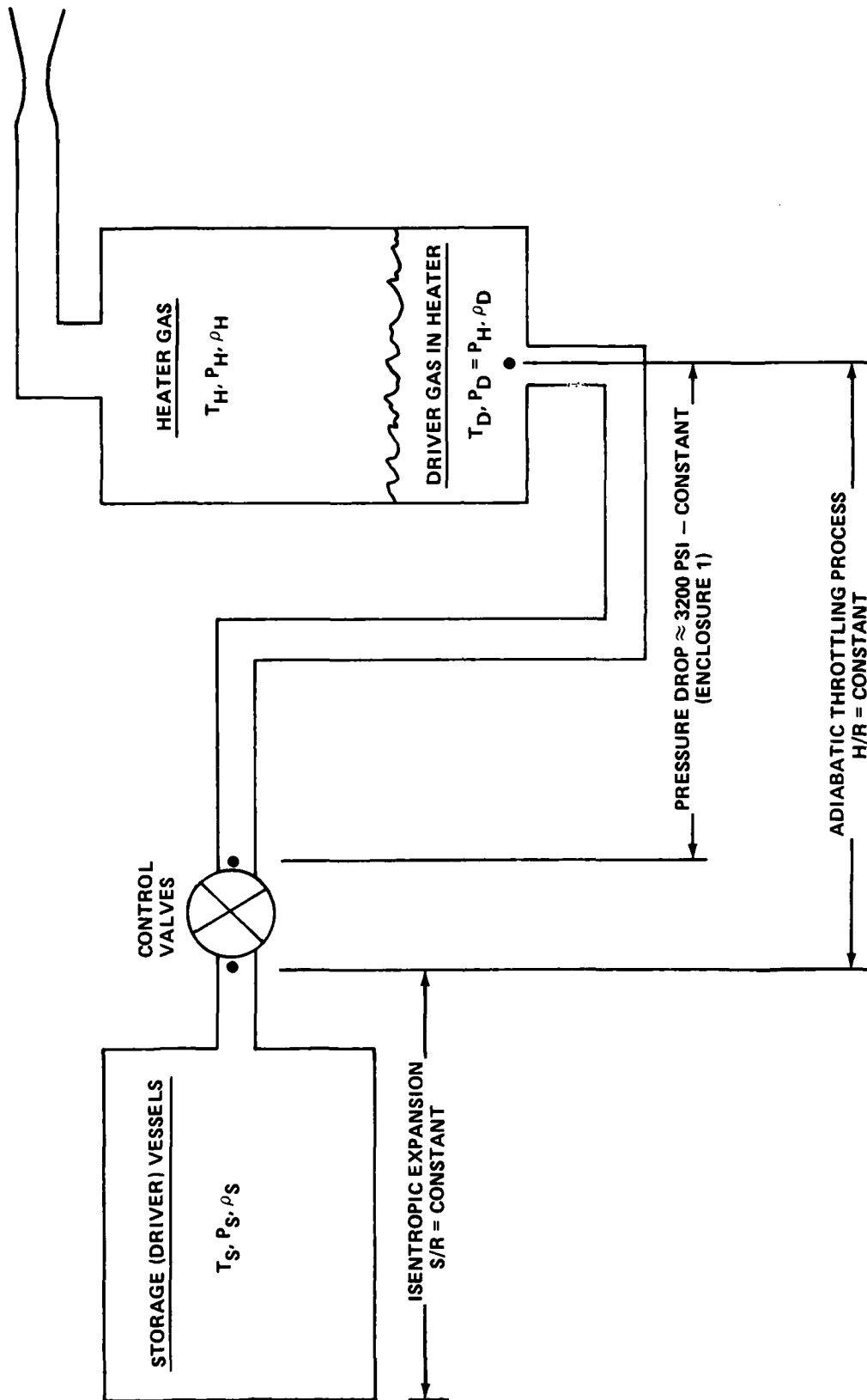


FIGURE L-2. SCHEMATIC DIAGRAM OF BLOWDOWN MODEL

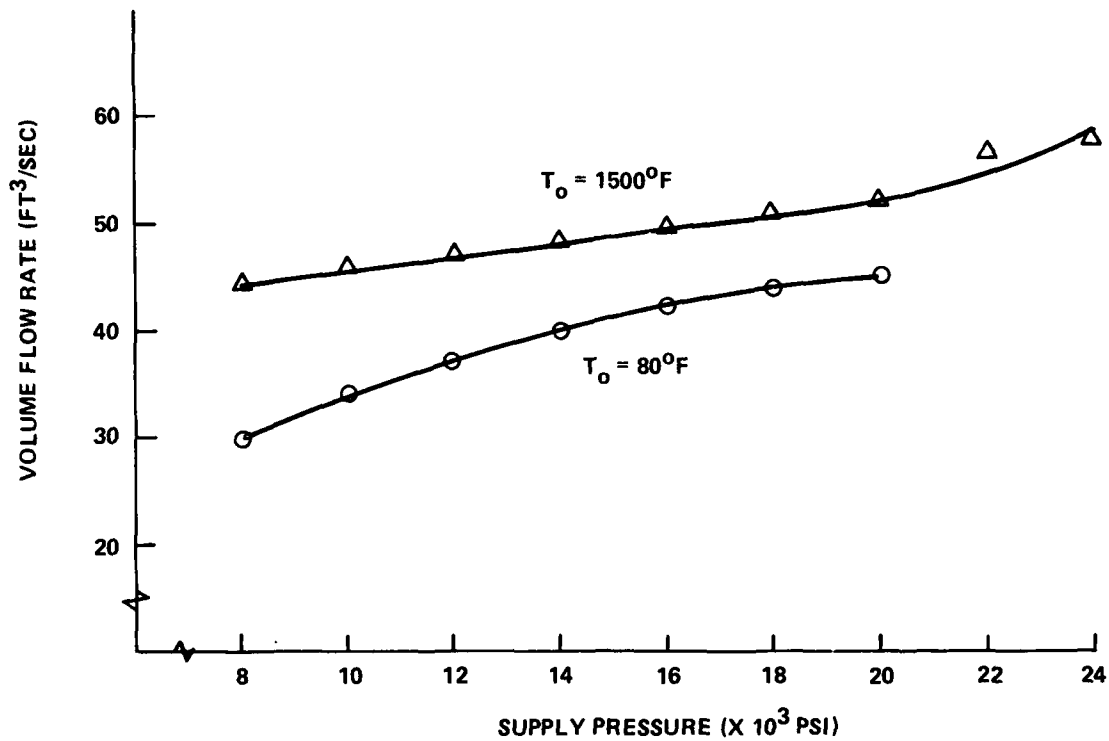


FIGURE L-3. MACH-10 HEATER VOLUMETRIC FLOW RATE VS SUPPLY PRESSURE @ CONSTANT TEMPERATURE

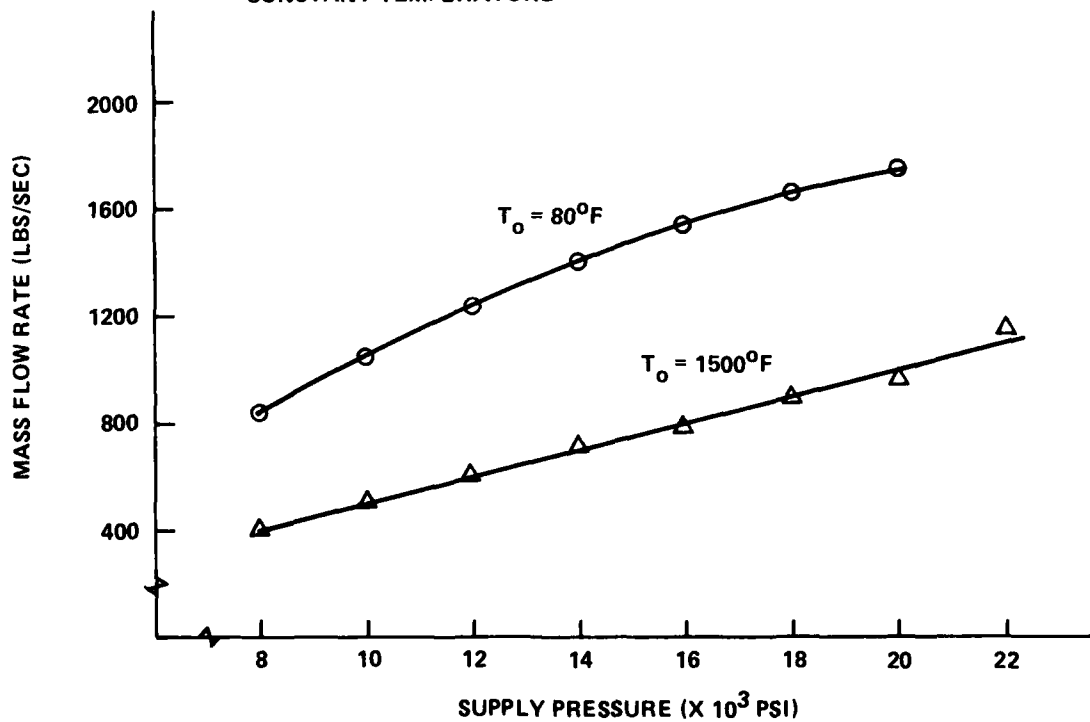


FIGURE L-4. MACH-10 HEATER MASS FLOW RATE VS SUPPLY PRESSURE @ CONSTANT TEMPERATURE

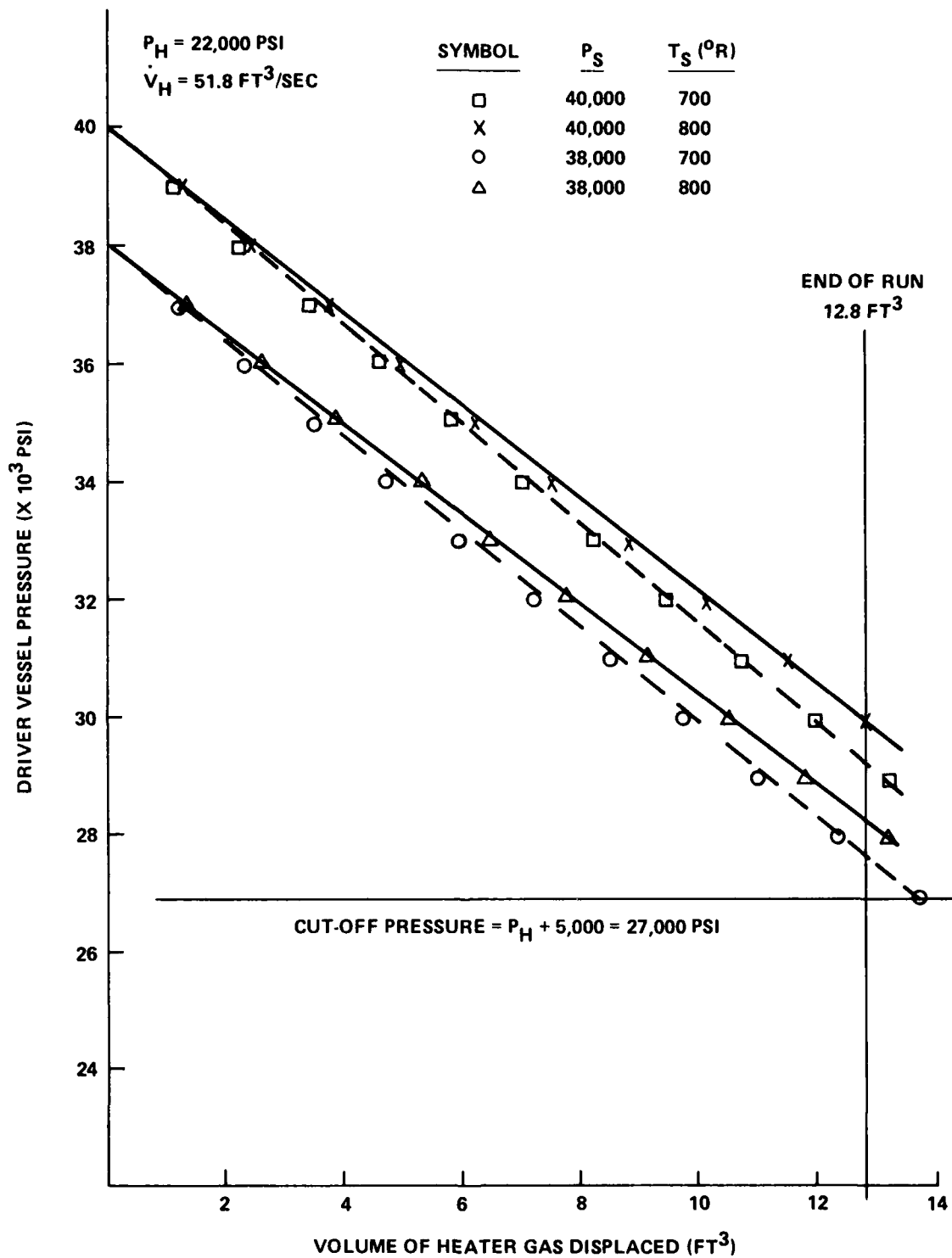
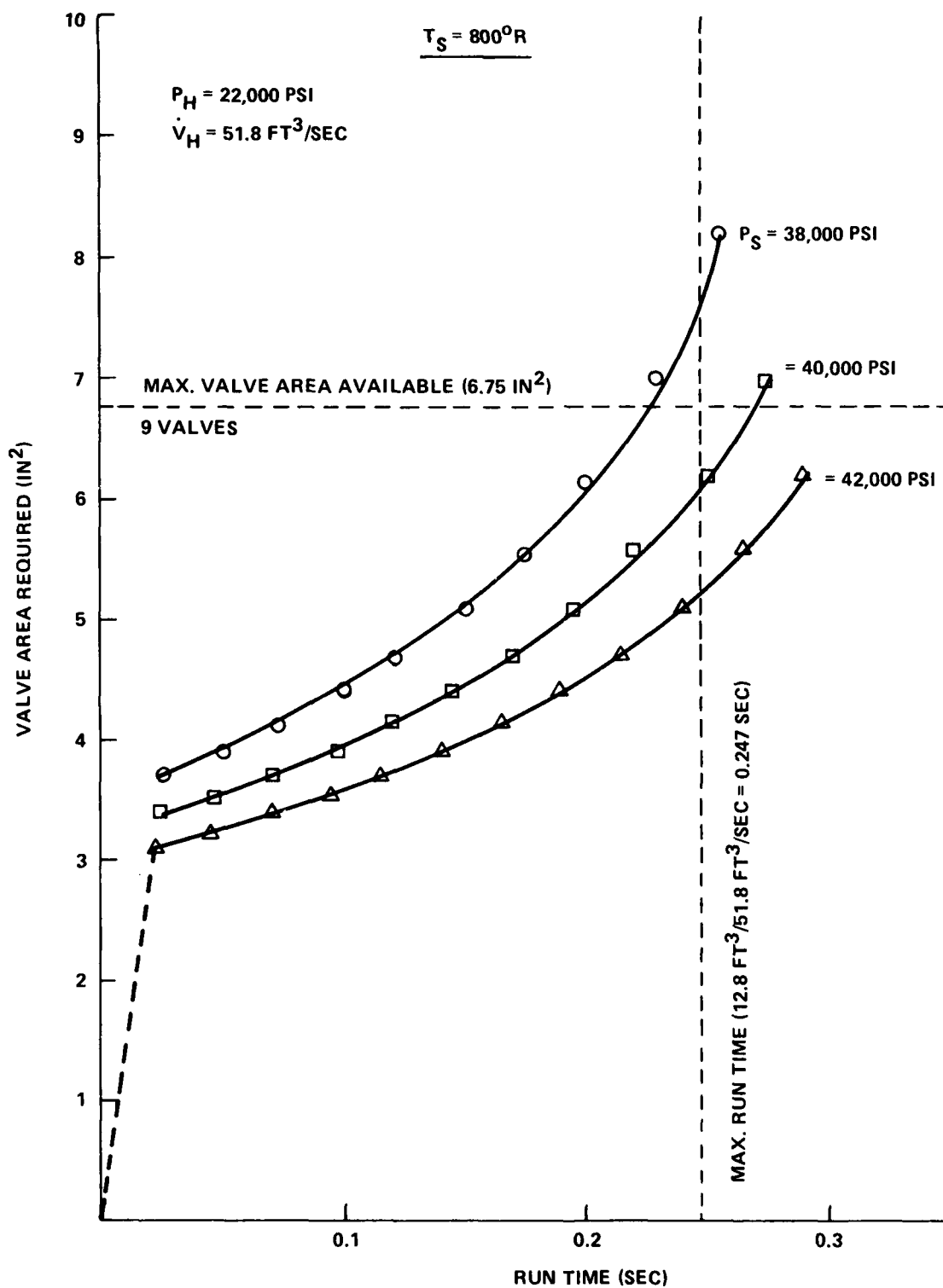
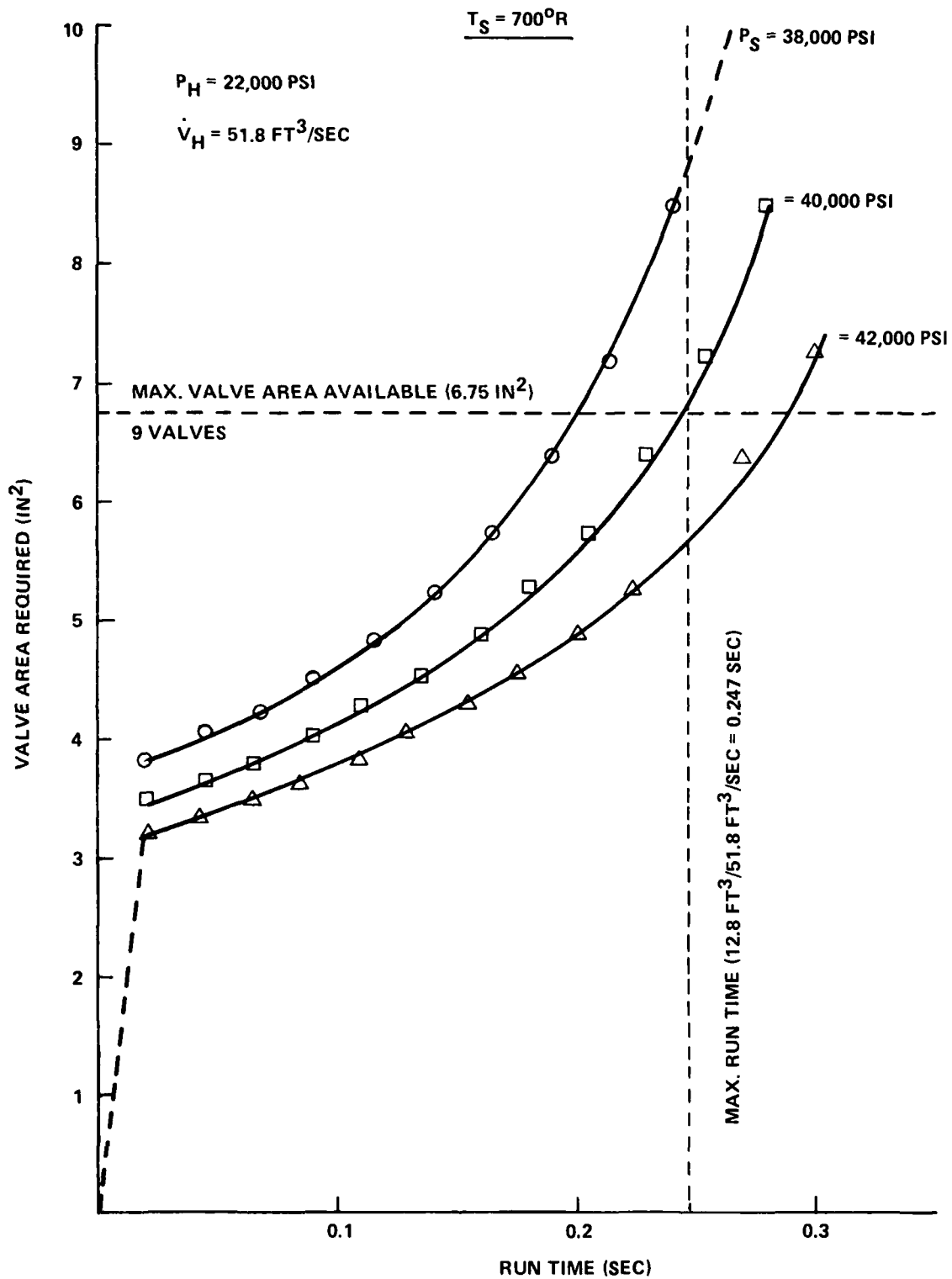


FIGURE L-5. PRELIMINARY BLOWDOWN PERFORMANCE - M-10 HIRE

FIGURE L-6. REQUIRED VALVE AREA VS RUN TIME FOR M-10 HIR BLOWDOWN AT  $800^\circ R$

FIGURE L-7. REQUIRED VALVE AREA VS RUN TIME FOR M-10 HIRE BLOWDOWN AT  $700^{\circ}\text{R}$

$$\begin{aligned} \dot{V}_H &= 51.8 \text{ FT}^3/\text{SEC AT } P_H = 22,000 \text{ PSI, } 1500^\circ\text{F} \\ &= 50.5 \text{ FT}^3/\text{SEC AT } P_H = 20,000 \text{ PSI, } 1500^\circ\text{F} \\ &= 49.6 \text{ FT}^3/\text{SEC AT } P_H = 18,000 \text{ PSI, } 1500^\circ\text{F} \end{aligned}$$

DRIVER CONDITIONS: 40,000 PSI  
800°R

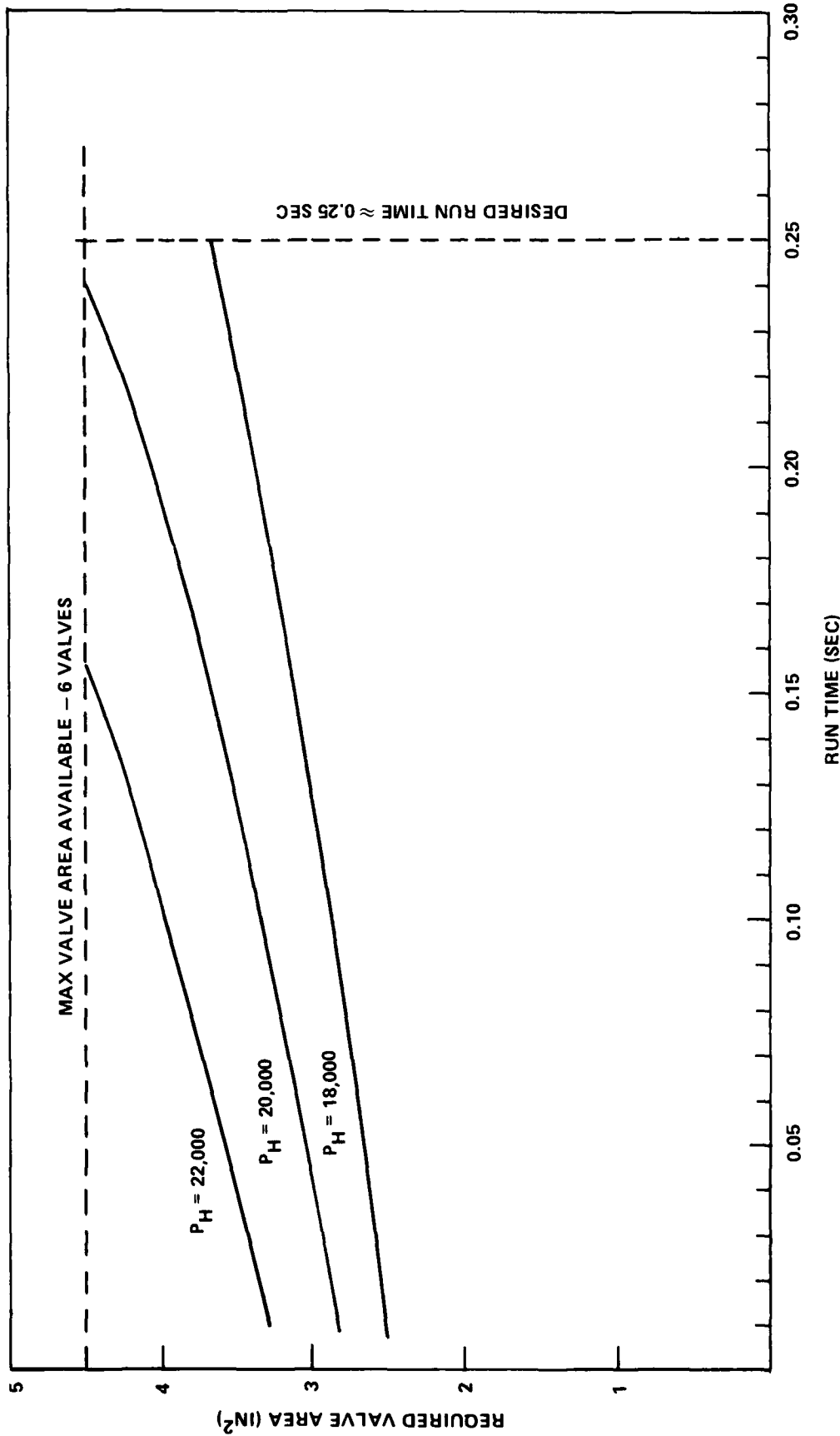


FIGURE L-8. VALVE AREA VS RUN TIME FOR SEVERAL HEATER PRESSURES - 6 CONTROL VALVES

L-17



REFERENCES

- L-1. Brahinsky, H. S., and Neel, C. A., Tables of Equilibrium Thermodynamic Properties of Nitrogen, Volume IV, Aug 1969.
- L-2. Streeter, V. L., Fluid Mechanics, Fifth Edition, (New York: McGraw-Hill, 1971).

## APPENDIX M

### PRESSURE PULSE ANALYSIS AND NEW CONTROL VALVE OPERATION

#### INTRODUCTION

This appendix contains three sections. In Section A, a working hypothesis for the observed pressure pulse is generated. In Section B, a new synthetic valve command is generated to be used to determine if the REXROTH servocontrollers could be used. Section C describes the test run with the new synthetic command driving the REXROTH.

#### SECTION A--GENERATION OF HYPOTHESIS

##### INTRODUCTION

As described in the main report, the QUICKPROOF test program of the M10-HIRE Project was interrupted when a 2,000 psi pressure pulse was observed in the annulus between the heater can and pressure vessel wall. The reason for this pulse was not understood at the time, and the pressures of the schedule denied us the opportunity to take some time for analysis.

We now have a working hypothesis to explain how this pulse is generated and how we may operate so as to avoid it. This section describes the hypothesis and recommends how we should proceed with testing when time again becomes available in the schedule.

##### HYPOTHESIS

The entire system from the downstream side of the control valves to the flow restrictor may be considered as one long duct with many changes in cross sectional area. During a run, driver gas flows down this duct and eventually through the flow restrictor into the nozzle.

The velocity and pressure histories at any point in this duct, produced by opening the control valves, could in principle be calculated by means of the equations for unsteady one-dimensional flow as given, for instance, in Reference M-1. Computer codes exist for making such calculations.

For our purposes, we will draw on only two general results which can be derived from such calculations:

a. The distinction between the rapid opening or closing of a valve, which will generate wave phenomena, and slow motion, producing quasi-steady flows, may be made on the basis of a characteristic time,

$$t = 2L/a \quad (M-1)$$

where  $L$  is the length of the duct and  $a$  is the sound speed. If  $t$  is the time in which the valves move,

Rapid opening corresponds to  $t < t$

Slow opening corresponds to  $t > t$ .

Of course the transition from one regime to the other is in reality somewhat gradual.

b. The strength of the pressure wave generated in establishing the flow at a velocity  $v$  is,

$$\Delta p = \rho a v \quad (M-2)$$

where  $\rho$  is the density.

Consider now a very simple picture of the wave system generated by the rapid opening of a valve at one end, A, of the duct shown in Figure M-1. The condition at the other end of the duct, B, is that another valve has been opening slowly (ablating flow resistor) and has produced an appreciable outflow velocity before valve A opens.

When valve A opens, a compression wave starts down the duct towards end B. Without analyzing the boundary condition at B rigorously, we postulate that because the gas there is already moving, the reflected wave is an expansion wave.

Any fixed point in the duct then sees the passing first of the compression wave, traveling A to B, and then the expansion wave, traveling B to A. This is observed as a pressure pulse, narrow at points near B and wider at points near A.

Of course this picture is a gross oversimplification, neglecting many features of the real flow, but it does constitute the first step in the acquisition of some insight into what is happening.

#### NUMERICAL MAGNITUDES

The second step in developing some understanding of what is happening is to check the actual observations against the formulas (M-1) and (M-2) of the previous section.

Consider first the characteristic time for a sound wave to travel from the control valves into the heater and back. If we consider the duct to extend all the way to the flow restrictor,

$$L = 55 \text{ ft.}$$

The sound speed is of course different in the hot and cold gas. At 10,000 psi we have

$$a(\text{hot}) = 2580 \text{ ft/sec}$$

$$b(\text{cold}) = 2030 \text{ ft/sec.}$$

Of the total 55 feet, about 22 feet is occupied by hot gas and 33 feet by cold gas. Combining these we get

$$t = 50 \text{ msec.}$$

The observed 60 msec opening time of the valves is thus close to the borderline between rapid and slow opening.

To compute the magnitude of the pressure pulse, we need the velocity in the annulus. At a heater pressure of 22,000 psi, Reference M-2 gives this as 228 ft/sec. Scaling this to 10,000 psi yields  $v = 252 \text{ ft/sec}$ . Equation (M-2) then predicts:

$$\Delta p = (30.9/32.17) \times 2030 \times 252 \text{ psf} = 3400 \text{ psi}$$

which is about the right magnitude.

The pulse length should be the time for a sound wave to travel from the measuring station to the flow restrictor and back. The one-way distance is about 26 feet. Using the sound speeds given above, we obtain

$$\Delta t = 21 \text{ msec}$$

which is about half the observed value.

The agreement of our hypothesis with the observations is not exact, but it is close enough to be phenomenologically correct. The hypothesis should be good enough to predict trends, if not numerical magnitudes. Note that we should expect a lower than calculated pressure for a valve opening time longer than 50 msec.

## CONCLUSIONS

- a. The observed pressure pulse apparently is produced by the unsteady flow generated by rapidly opened valves.
- b. If the valves were opened rapidly with 22,000 psi in the heater, the magnitude of the pressure pulse in the annulus could be about 4000 psi.
- c. This pressure pulse can be greatly reduced by opening the valves more slowly.

## SECTION B--NEW SYNTHETIC VALVE COMMAND

## NEW MODE OF VALVE OPERATION

The valve motion required during a run may be calculated from driver-vessel blowdown calculations such as given in Appendix L. It has been found that in M10 HIRE operations the valves need to be about half open at the beginning of the run.

Until now a step command has been used to achieve the initial opening, both in tunnel operations and in the no-flow test noted earlier. In Section A it was recommended that the initial opening be commanded by the servo as the flow restrictor inserts ablate. This process took about 0.2 seconds with the heater pressure at 10,000 psi, it will be somewhat quicker (probably) at 22,000 psi.

For a quick approximation to the valve motion required by this new scheme we will neglect the change in driver vessel pressure and open the valves in proportion to the mass flow rate or nozzle supply pressure:

$$A_v/A_v(i) = P_o/P_o(i)$$

where (i) denotes the initial values in the calculations of Appendix L, when the full supply pressure is first established.

Using the data from Run 720, Figure M-2 has been drawn to show the required valve motion. Also shown is the corresponding hydraulic flow into the actuator which does not exceed 30 GPM.

## NEW SYNTHETIC COMMAND

For the valve test, the synthetic command will be written on an analog tape at 0.938 ips as before and played back at 120 ips.

The run time, calculated in Appendix L, is about 0.25 seconds. As shown in Figure M-1, the duration of ablation in the flow restrictor may also be taken as 0.25 seconds. Thus the total duration of the synthetic command is 0.5 seconds or 64 seconds at the writing speed. Figure M-3 shows the proposed command with both time scales. Here the initial rise of Figure M-2 and the results of the blowdown calculation have been faired by eye at the mid point. The peak velocity at the end of the stroke corresponds to a hydraulic flow of about 50 GPM. Limiting this to 30 GPM might not compromise pressure regulation appreciably.

The chart for curve following on the X-Y recorder is shown in Figure M-4. The pen speed in the X-direction will correspond to the 10 sec/in. In playback, the 1.5 volt amplitude will be doubled, and biased so that the command voltage to the valve will be:

0.1 volt for 0% stroke

3.1 volts for 100% stroke.

It thus appears that use of the servo to generate the initial valve opening during flow restrictor ablation is compatible with a 30 GPM limit on servo-valve flow.

#### SECTION C--NO FLOW TEST OF THE NEW SYNTHETIC COMMAND

##### TEST DESCRIPTION

The synthetic command derived in Section B was written on a magnetic tape using the Honeywell 101 recorder. The recorder output was then fed through an amplifier to two flow control valves:

V7 equipped with a REXROTH servovalve

V4 equipped with a MOOG servovalve.

The MOOG servovalve was fitted with spool stops which limited the maximum flow rate to about 50 GPM.

The voltage swing required to move the valves from closed to open is about 3 volts. This is larger than the tape recorder output, which had a swing of 1.5 volts. With the amplifier gain set at 2, the valves could then be moved full stroke. Some tests were run with an amplifier gain of 1, producing about 50% stroke, so that the overshoot could be observed.

To check out the capabilities of the REXROTH servovalve a series of tests was run with different values of gain the servoamplifier driving the valve. The following data were recorded on the Honeywell 1858 Visicorder:

Valve Command

Valve Motion with REXROTH servovalve

Valve Motion with MOOG servovalve

Spool Motion of the MOOG servovalve.

## TEST RESULTS

Typical results obtained with the half-stroke command are shown in Figures M-5 and M-6, with low and high values of the gain in the REXROTH loop. The increase in the amplitude of the overshoot with the increased gain is clearly visible.

Results obtained with the full-stroke command (the real synthetic command) are shown in Figures M-7 and M-8. Here there is of course no overshoot because the valve is up against the limit of its travel. The response during the stroke can be seen to be slightly oscillatory at the higher gain.

The most rapid valve motions observed are during the initial motion (corresponding to the ablation time in the real flow) and at the end of the stroke. Reading the slopes of the curves, apparent hydraulic flow rates have been calculated and are shown on the curves. They exceed the nominal rating of the REXROTH servovalve and correspond approximately to those calculated for the synthetic command.

How well the valve motion follows the synthetic command is shown in the overlays of Figures M-9, M-10, and M-11. All valve motions reproduce the command quite well. In all three there is a delay before the valve starts to move after the command has been given; this delay is noticeably larger at the lowest gain. At the highest gain the onset of oscillatory motion is noticeable.

From these overlays we may conclude that the REXROTH servovalves will produce adequate valve responses for M10 HIRE operations.

## CHECKOUT OF EIGHT REXROTH VALVES

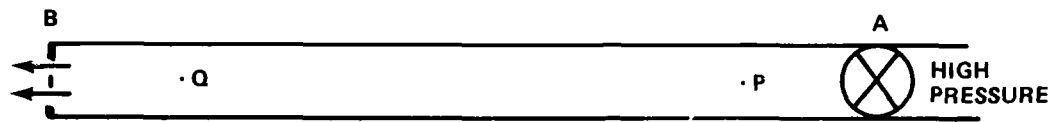
After eight flow control valves had been mounted and fitted with REXROTH servovalves, the synthetic command was fed to the servo and the motions of all the valves were recorded on the DARE V system. The QUICK-100K system was then used to produce plots of valve motion, one of which is shown in Figure M-12. As can be seen, all 8 valves were able to follow the synthetic command, with only a small amount of scatter.

## CONCLUSIONS AND RECOMMENDATIONS

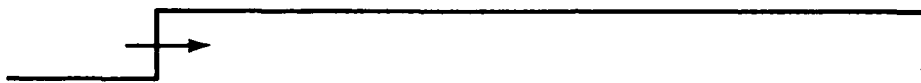
a. A flow control valve equipped with a REXROTH servovalve can follow the M10 HIRE synthetic command well enough.

- b. The optimum setting of the servoamplifier gain is about 20.
- c. There is some scatter in the valve responses of eight valves responding to the synthetic command, but it appears to be tolerable.
- d. It is recommended that M10 HIRE operations be carried out with REXROTH servovalves.
- e. The MOOG servovalve performance was not analyzed because the REXROTH is obviously preferable if acceptable.

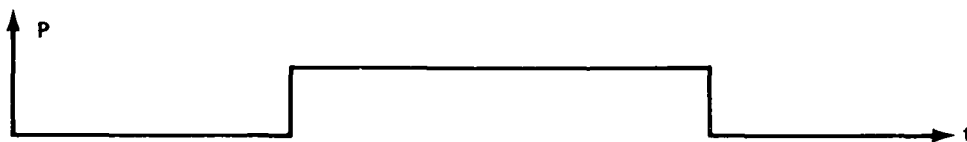




COMPRESSION WAVE FROM VALVE



REFLECTED EXPANSION WAVE



PRESSURE PULSE AT P



PRESSURE PULSE AT Q

FIGURE M-1. GENERATION OF PRESSURE PULSE

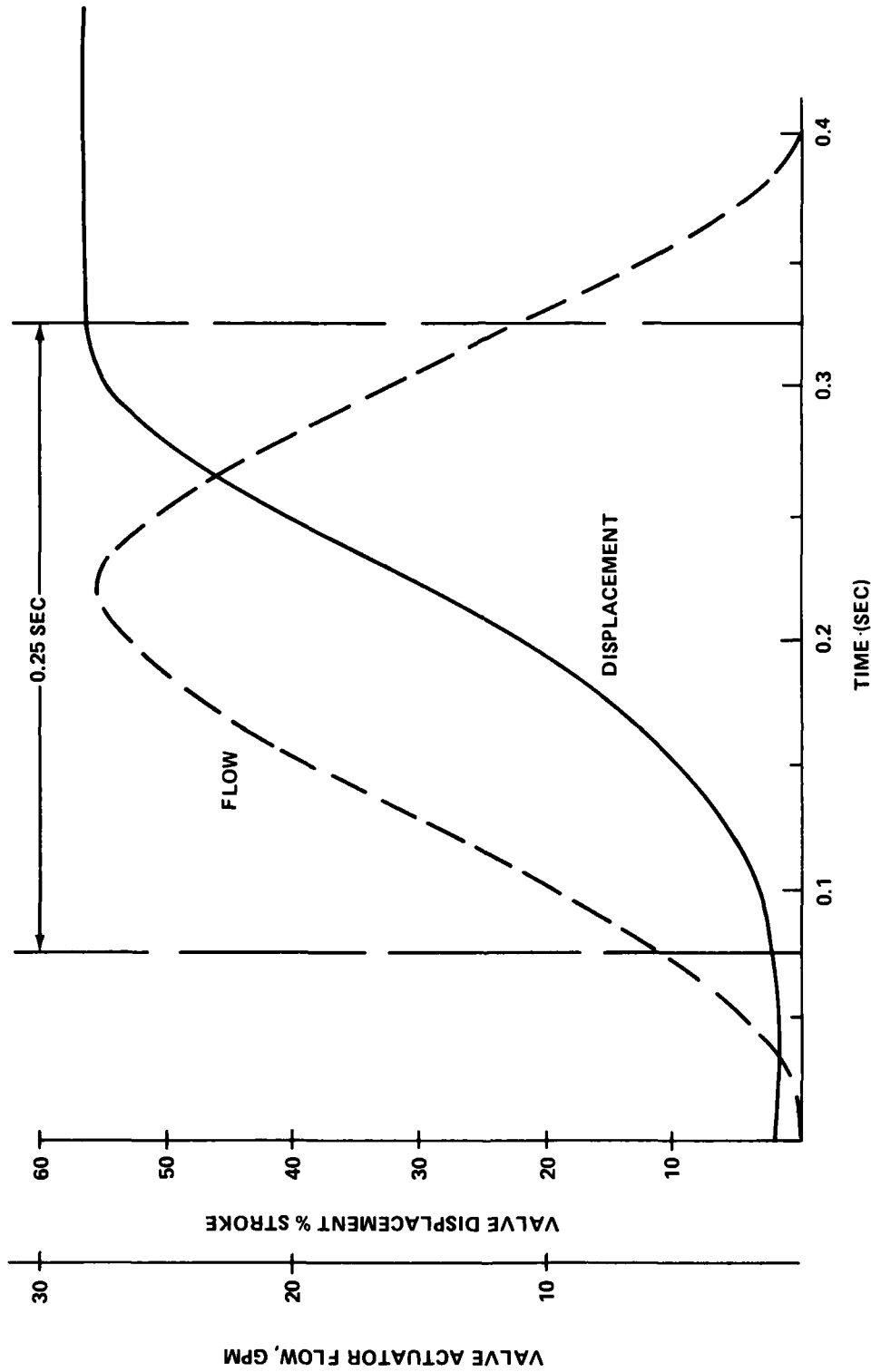


FIGURE M-2. SYNTHETIC VALVE COMMAND DERIVED FROM FLOW RESTRICTOR ABLATION, RUN 720

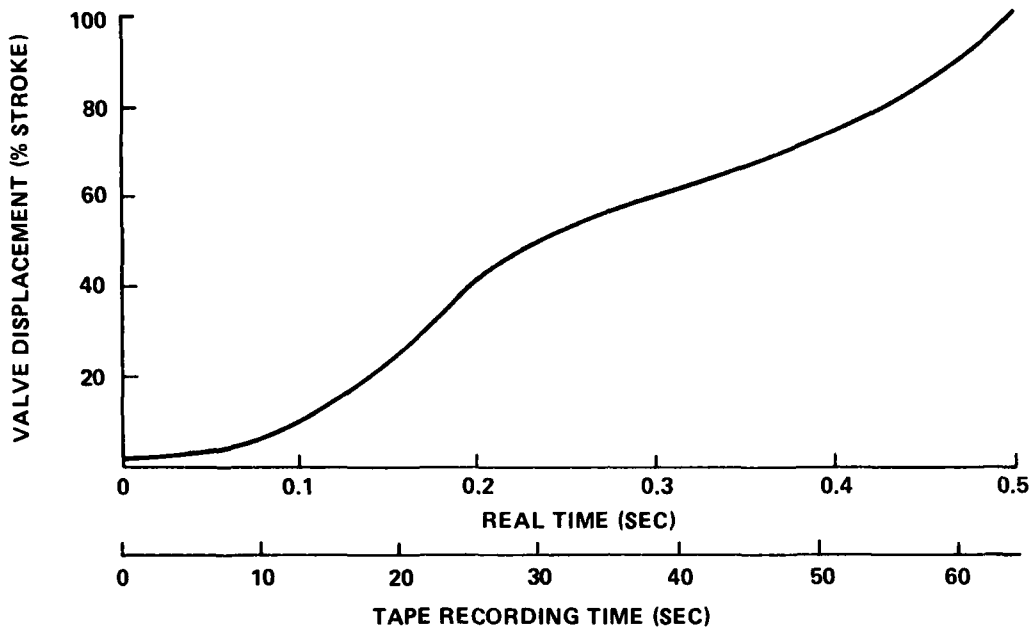


FIGURE M-3. SYNTHETIC VALVE COMMAND

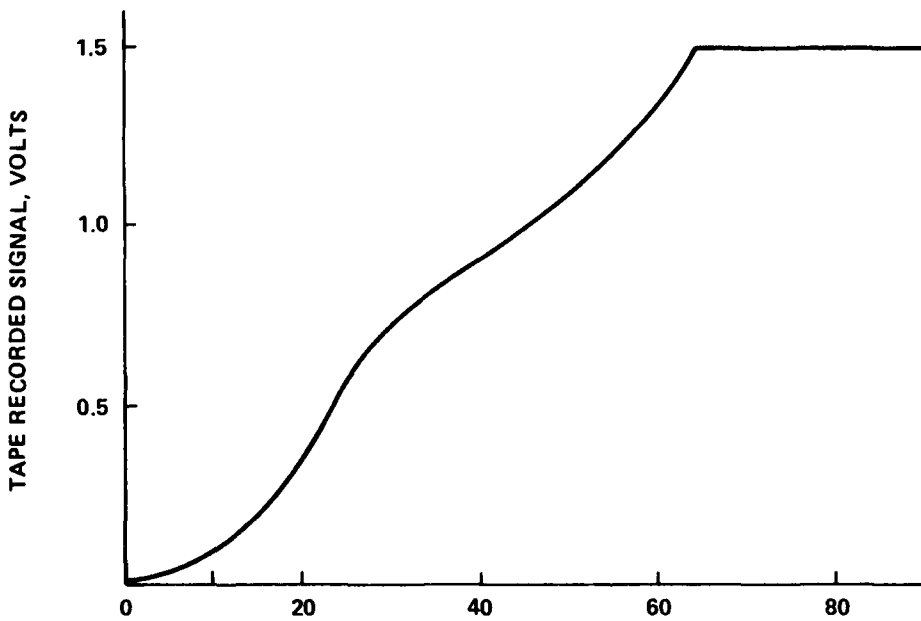


FIGURE M-4. CHART FOR GENERATING SYNTHETIC VALVE COMMAND

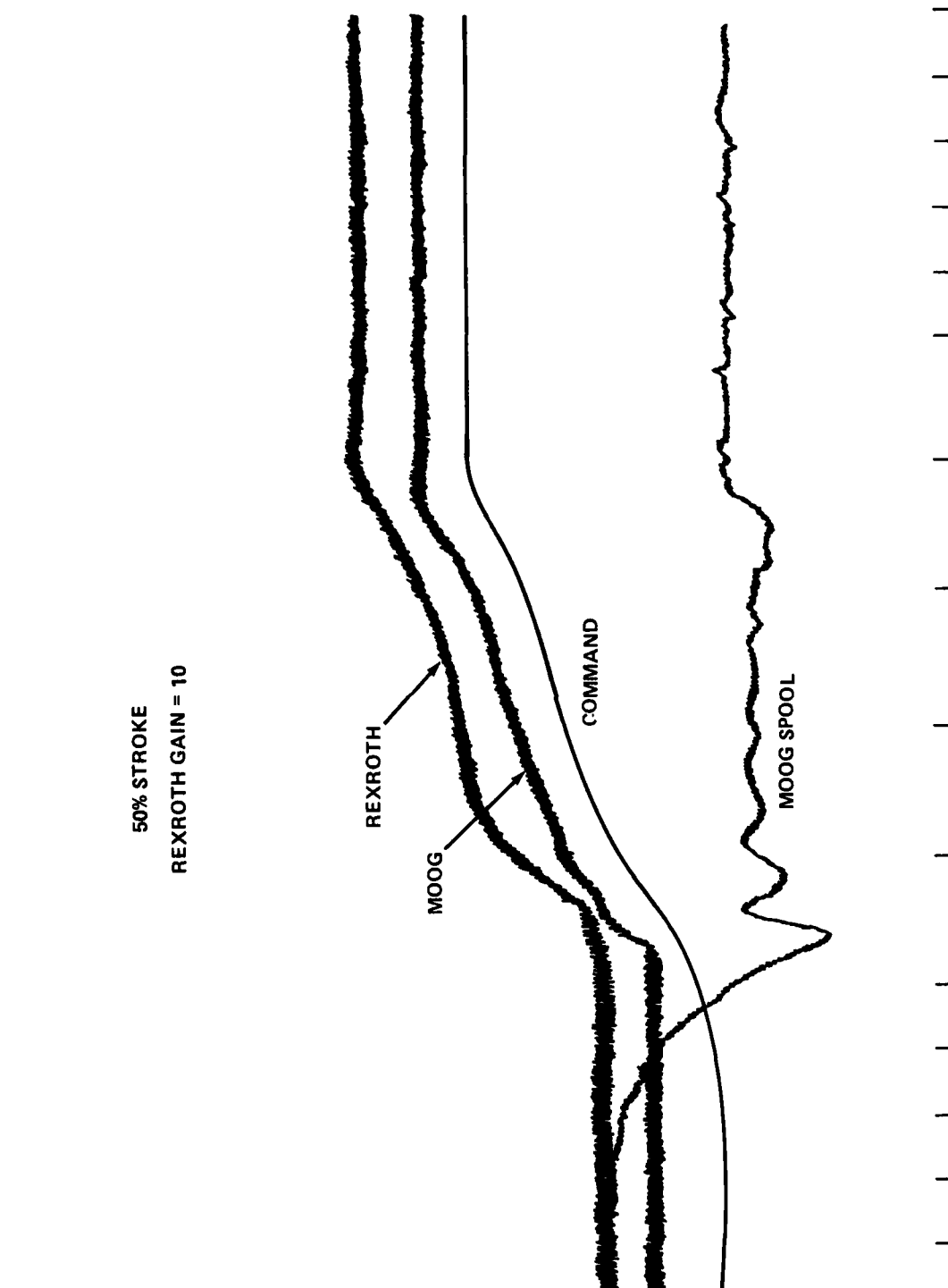


FIGURE M-5. VALVE RESPONSE WITH REXROTH SERVOVALVE AT LOW GAIN

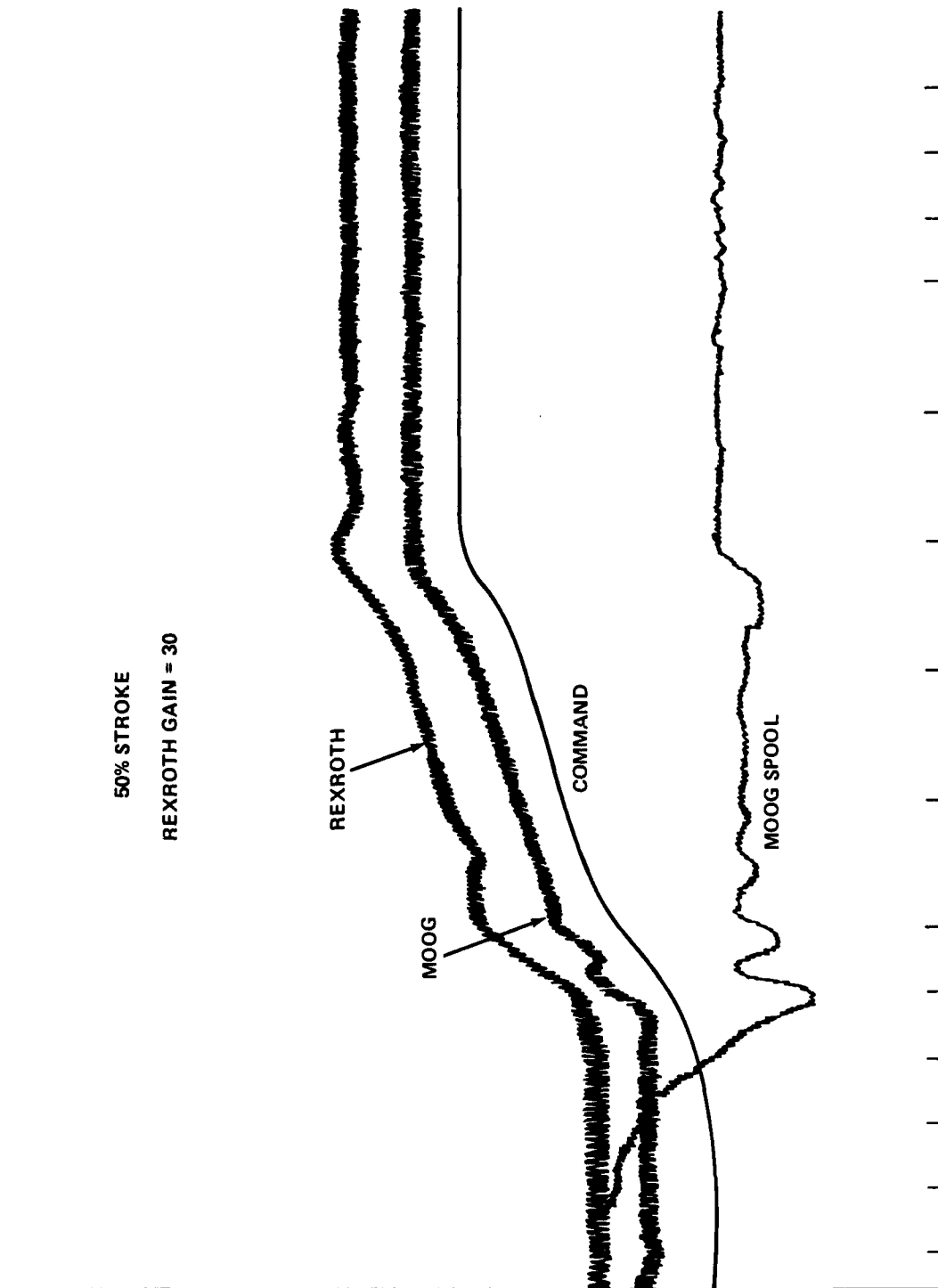


FIGURE M-6. VALVE RESPONSE WITH REXROTH SERVOVALVE AT HIGH GAIN

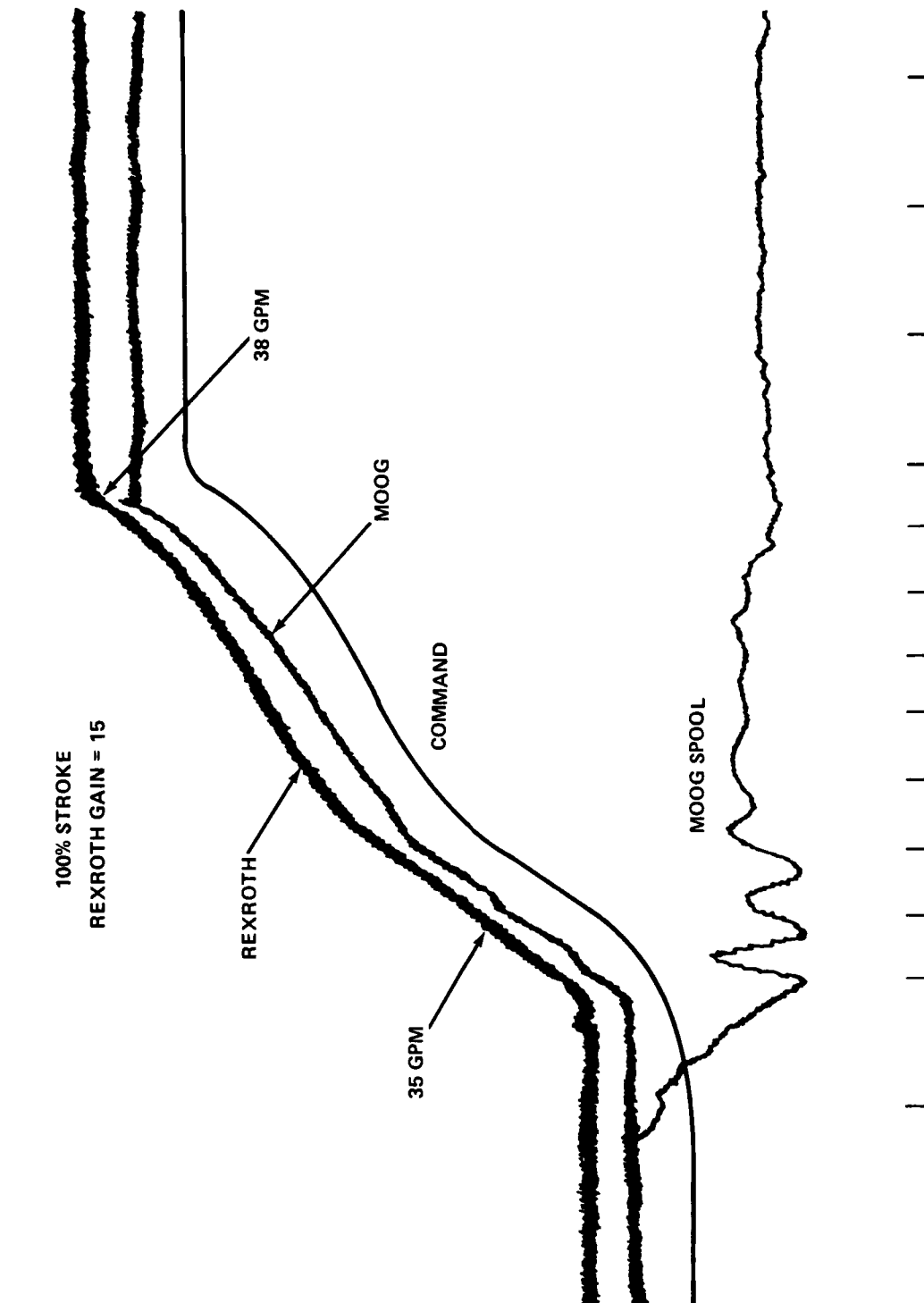


FIGURE M-7. VALVE RESPONSE WITH REXROTH SERVOVALVE AT LOW GAIN

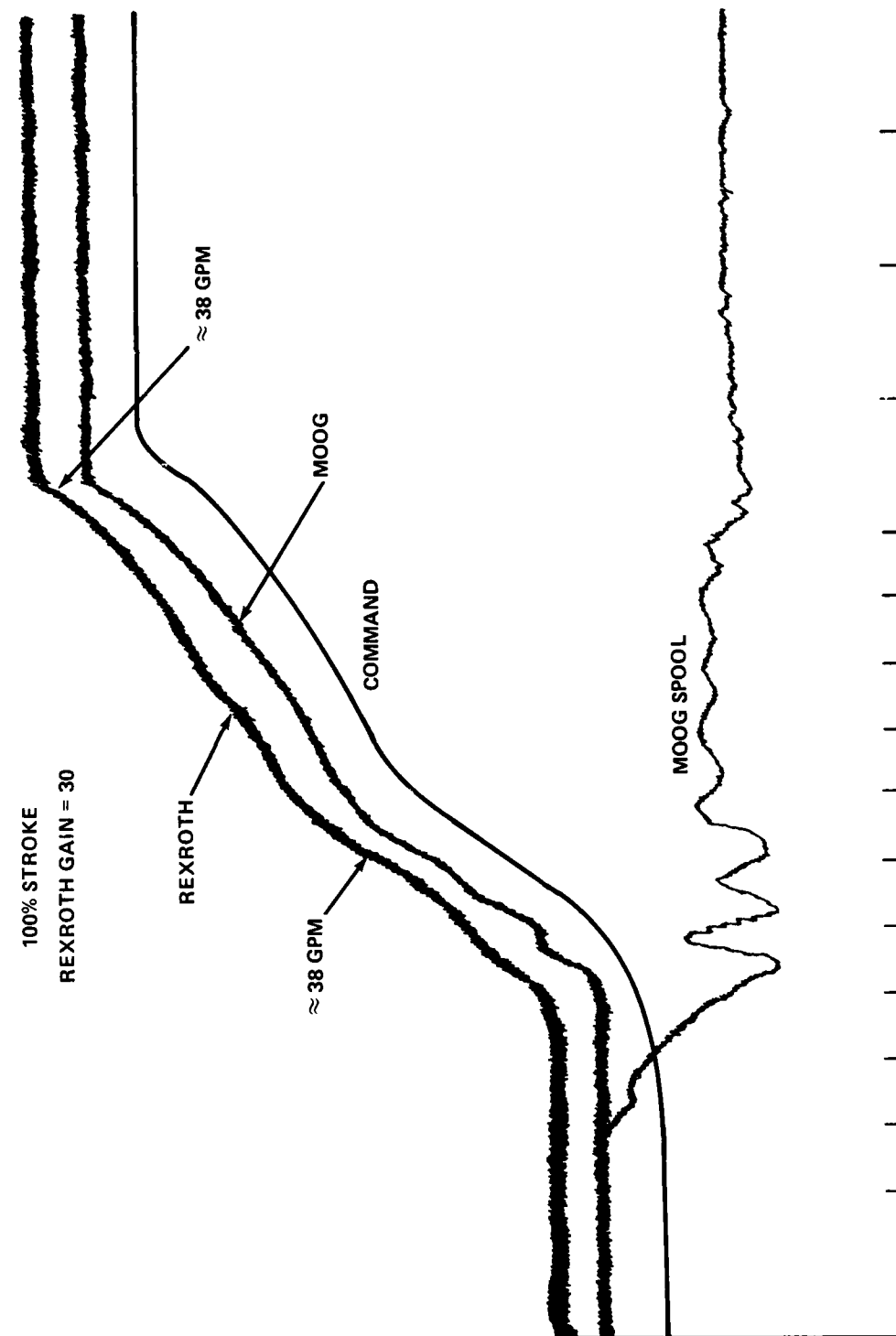


FIGURE M-8. VALVE RESPONSE WITH REXROTH SERVOVALVE AT HIGH GAIN

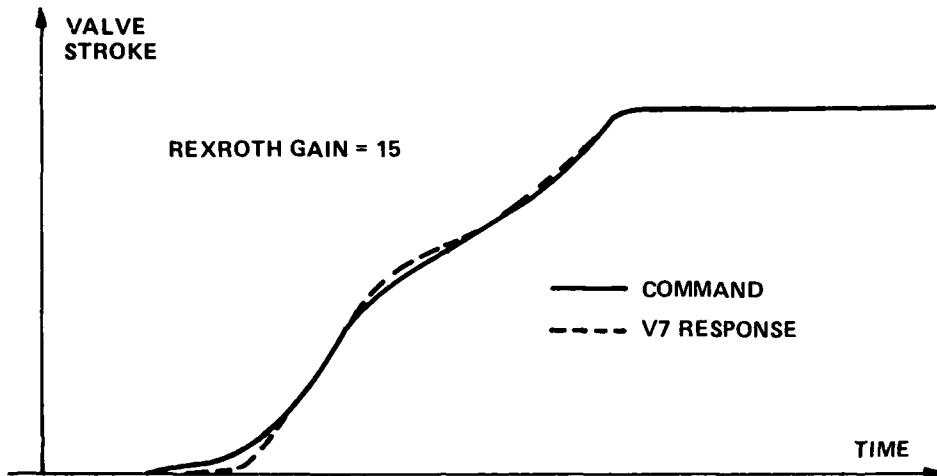


FIGURE M-9. OVERLAY OF COMMAND & V7 RESPONSE, LOW GAIN

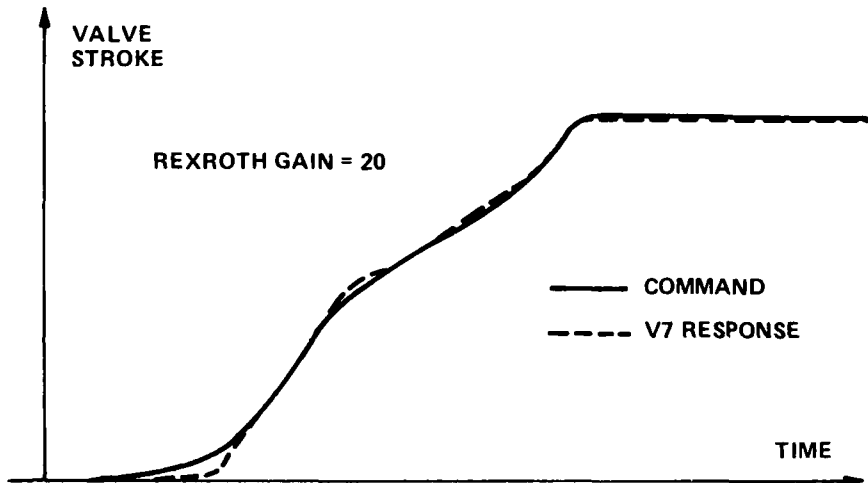


FIGURE M-10. OVERLAY OF COMMAND & V7 RESPONSE, MEDIUM GAIN

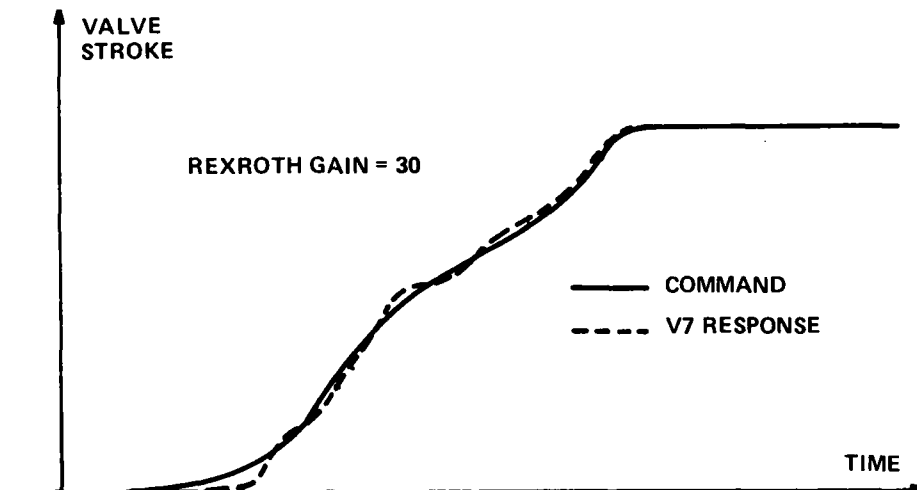


FIGURE M-11. OVERLAY OF COMMAND & V7 RESPONSE, HIGH GAIN



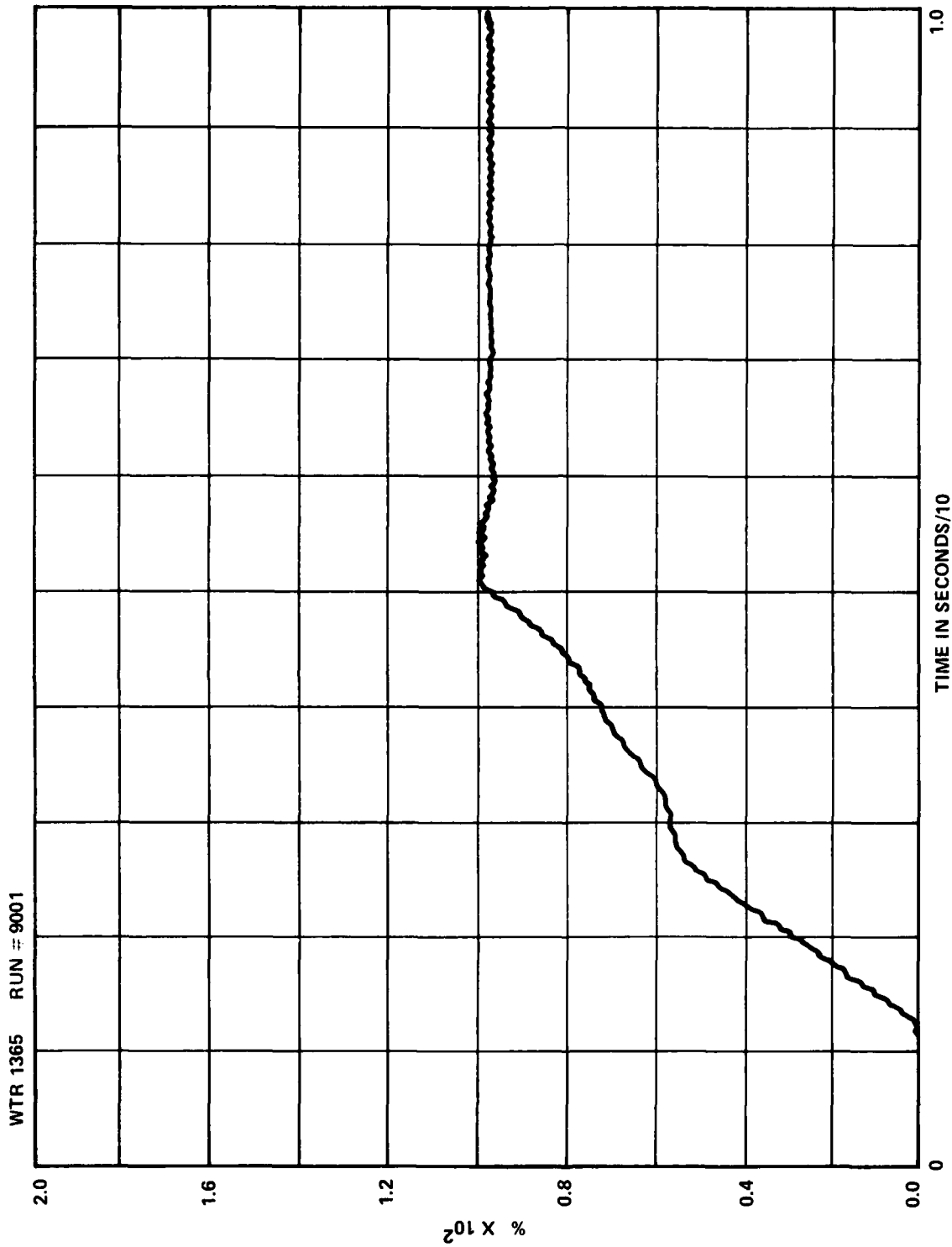


FIGURE M-12. VALVE RESPONSE TO SYNTHETIC COMMAND

REFERENCES

- M-1. Streeter, V. L., Fluid Mechanics, Fifth Edition, (New York: McGraw-Hill, 1971).
- M-2. Brahinsky, H. S., and Neel, C. A., Tables of Equilibrium Thermodynamic Properties of Nitrogen, Volume IV, Aug 1969.

## APPENDIX N

 $T_o$  PROBE DESIGN AND ANALYSIS

## INTRODUCTION

Thermocouple operational problems were experienced during QUICKPROOF testing at high Reynold's numbers. The problems were that the thermocouples  $T_{oa}$ ,  $T_{ob}$ , and  $T_{oc}$  bent, and gas temperature data were inconsistent. Subsequent analysis showed that most of the inconsistencies were probably the result of unsatisfactory thermocouple performance. There is a need to improve gas temperature measurement accuracy and insure thermocouple survivability during high Reynold's number conditions. The needed improvements are provided by an improved thermocouple design. The design calculations and specifications are contained in this appendix.

## DESIGN APPROACH

Equations predicting thermocouple conduction errors, radiation errors, response time, and survivability were developed. The predictions of these equations are referred to as thermocouple performance characteristics. Each of these equations is a function of tunnel gas conditions and two or more thermocouple design parameters (wire diameter, projection length, material, et cetera). Because of this functional dependence, improvement in one of the performance characteristics comes at the expense of another.

A sample set of thermocouple design calculations is shown in Enclosure (1) of this Appendix. Design calculations were made iteratively. One iteration consisted of changing a design parameter and recalculating all performance characteristics. The design parameters were varied based on the comparisons of the results of the two previous iterations. This process resulted in an optimized design. Sample calculations of the thermocouple performance characteristics in Enclosure (1) of this Appendix used these optimized values.

The calculations showed that two thermocouple configurations are necessary to minimize response time, minimize conduction errors, and insure survivability at all operating conditions. The first thermocouple configuration (shielded), shown in Figure N-1 must be used for high Reynold's number operations. The second configuration (unshielded) uses a slightly different thermocouple tube for low Reynold's number operations. These two configurations are necessary to obtain the desired thermocouple performance characteristics when the tunnel is operated at different Reynold's numbers.

3. The unshielded tube must be used during low Reynold's number operations. It differs from the shielded tube in that it does not have the backstop which shields the thermocouple wire junction. This unshielded tube reduces the thermocouple measurement inaccuracies at low Reynold's number operations.

4. Thermocouple response time for measuring changes in tunnel gas temperatures is improved by using thin (0.015 inch diameter) Chrome-Alumel wire. The faster response time is provided because the thinner wire results in less thermal inertia when measuring hot tunnel gases.

## DESIGN CALCULATIONS

## THERMOCOUPLE-WIRE-TO-BACKSTOP SPACING

Previous calculations and experience showed that the wire projection of the thermocouple would bend during high Reynold's number operations. Addition of a backstop will solve the problem. However, spacing between the junction and the backstop, as shown in Figure N-1, is calculated using the following equation from Reference N-1:

$$\cos \theta = \frac{V}{V_{\infty}} \quad (1)$$

Several calculations were performed using different values of  $V$ . For each value, thermocouple wire stress analysis and temperature measurement error analysis was performed. Examination of results showed that  $V/V_{\infty} = 0.5$  optimizes wire stress and temperature measurement error.

## CALCULATION OF THERMOCOUPLE WIRE PARAMETERS

Calculation of the thermocouple wire's length-over-diameter ratio ( $l/D$ ) was accomplished using a mathematical model based on Figure N-2. First calculate the maximum stress on the wire as follows:

$$\sigma = \frac{Mc^3}{I} \quad (2)$$

where

$$c = \frac{D}{2}$$

$$I = \frac{\pi D^4}{64}$$

$$M = \frac{W l^2}{2}$$

but

$$W_d = C q D$$

$$q = \frac{V^2 \rho}{M}$$

$$V = \frac{M}{2 A \rho}$$

Substituting back into Equation (2) gives the following.

$$\sigma = \frac{2 C_d M^2 l^2}{\rho A \pi D^2}$$

or

$$\frac{l}{D} = \frac{A}{M} \frac{\sigma \rho \pi}{2 C_d} \quad (3)$$

Equation (3) is used to calculate specific  $l/D$  ratios for the three thermocouples  $T_{Oa}$ ,  $T_{Ob}$ , and  $T_{Oc}$  which are used in tunnel nine. To calculate the maximum  $l/D$  for thermocouples  $T_{Oa}$  and  $T_{Ob}$  substitute the following values into Equation (3):

$M = 24.71 \text{ slug/sec}^4 = \text{maximum density tunnel mass flow rate,}$

$\rho = 0.4995 \text{ slug/ft}^3 = \text{density of nitrogen at } 1500^\circ\text{F and } 16,000 \text{ psi,}$

$A = 0.1503 \text{ ft}^2 = \text{nozzle inlet area,}$

$\sigma = 1,152,000 \text{ lb/ft}^2 = \text{yield strength of Alumel at } 1500^\circ\text{F,}$

$$\frac{l}{D} = \frac{0.1503}{24.71} \left[ \frac{(1152000)(0.4995)(\pi)}{2(1.2)} \right]^{1/2} = 5.28 .$$

But  $D = 0.015$  inch is the maximum diameter of the thermocouple wire to give the desired temperature measurement response time. Substitute this value and calculate the maximum length of the wire projections for thermocouples  $T_{Oa}$  and  $T_{Ob}$ :

$$l = 5.28D = 5.28(0.015) = 0.079 \text{ inch}$$

Substitute the following values into Equation (3) to calculate the maximum  $l/D$  for thermocouple  $T_{oc}$ .

$\dot{M} = 24.71 \text{ slugs/sec} = \text{maximum density tunnel mass flow rate,}$

$\rho = 0.545 \text{ slugs/ft}^3 \text{ at } 1500^\circ\text{F and } 18,000 \text{ psi,}$

$A = 0.1835 \text{ ft}^2 = \text{cross section area of gas flow at thermocouple } T_{oc},$

$\sigma = 1,152,000 \text{ lb/ft}^2 = \text{yield strength of Alume1 at } 1500^\circ\text{F,}$

$$\frac{l}{D} = \frac{0.1835}{24.71} \left[ \frac{1152000(0.545)(\pi)}{2(1.2)} \right]^{1/2} = 6.73,$$

or

$$l = 6.73D = 6.73(0.015) = 0.101 \text{ inch.}$$

#### CALCULATION OF THERMOCOUPLE TUBE STRESS

The maximum stress on thermocouple tubes  $T_{oa}$ ,  $T_{ob}$  and  $T_{oc}$  is calculated by combining normal and shear stress calculations. First calculate normal and shear stresses using Equation (2) as the starting point:

$$\sigma = \frac{Mc}{I} = \text{normal stress.}$$

but

$$c = \frac{d_o}{2}$$

and

$$I = \frac{(d_o^4 - d_i^4)}{64}. \text{ Figure N-3 shows } d_o \text{ and } d_i.$$

$$M = W_1 l_2 (l_1 + (0.5)l_2). \text{ Figure N-3 shows } l_1 \text{ and } l_2.$$

But,

$$W_1 = C_d q d_o$$

where

$$q = \frac{V^2 \rho}{2} \quad \text{and} \quad V = \frac{M}{\rho A}$$

Substituting the equations into each other gives the following general equation for normal stress in the thermocouple tube:

$$\sigma = \frac{16 C_d^2 M^2 d_o^2 l_2 (l_1 + 0.5(l_2))}{\rho A^2 \pi (d_o^4 - d_i^4)} \quad (4)$$

To calculate maximum normal stress for thermocouple tubes  $T_{0a}$  and  $T_{0b}$  substitute the following values into Equation (4):

$$l_1 = 0.020833 \text{ ft},$$

$$l_2 = 0.08333 \text{ ft},$$

$$M = 24.71 \text{ slug/sec} = \text{maximum tunnel mass flow rate},$$

$$\rho = 0.4995 \text{ slug/ft}^3 \text{ for } 1500^\circ\text{F and } 16,000 \text{ psi},$$

$$A = 0.150533 \text{ ft}^2 \text{ nozzle inlet area},$$

$$d_o = 0.04166 \text{ ft},$$

$$d_i = 0.011333 \text{ ft},$$

$$C_d = 1.2,$$

$$\sigma = \frac{16(1.2)(24.71^2)(0.04166^2)(0.08333)(0.0208333 + 0.04166)}{0.499(0.1503^2)(\pi)(0.0416^4 - 0.0113^4)} = 997,776 \text{ lb/ft}^2$$

or

$$\sigma = 6929 \text{ lb/in}^2.$$



To calculate maximum normal stress for thermocouple tube  $T_{oc}$  substitute the following values in Equation (4):

$\dot{M} = 24.71 \text{ slug/sec} = \text{maximum tunnel mass flow rate,}$

$\rho = 0.545 \text{ slug/ft}^3 \text{ at } 1500^\circ\text{F and } 18,000 \text{ psi,}$

$A = 0.1833 \text{ ft}^2 \text{ which is the flow restrictor inlet area,}$

$d_o = 0.0416 \text{ ft,}$

$d_i = 0.01133 \text{ ft,}$

$C_d = 1.2,$

$l_2 = 0.125 \text{ ft,}$

$l_1 = 0.05833 \text{ ft,}$

$$\sigma = \frac{16(1.2)(24.71^2)(0.0416^2)(0.125)(0.0583 + 0.0625)}{0.545(0.1833^2)(\pi)(0.0416^4 + 0.0113^4)}$$

$$\sigma = 1,769,760 \text{ lb/ft}^2 = 12,290 \text{ psi.}$$

The following equation was used to calculate the shear stresses for the thermocouple tubes. The results were that shear stress for  $T_{oa}$  and  $T_{ob}$  was 621 psi, which is negligible when combined with the normal stress. For  $T_{oc}$  the shear stress was 569 psi, which is also negligible.

$$\tau_1 = \frac{2C_d \dot{M} l_2}{A^2(d_o^2 - d_i^2)} \quad (5)$$

#### CHANGEOVER POINT CALCULATION

The unshielded thermocouple to be used for low Reynold's number tunnel operations gives more accuracy when measuring tunnel gas temperatures. Accordingly, it should be used over as wide a range of Reynold's numbers as possible. To determine maximum Reynold's number conditions the unshielded thermocouple can withstand, thermocouple wire stress calculations were made as follows, starting with Equation (2):

$$\sigma = \frac{Mc}{I}$$

where

$$c = \frac{D}{2} ,$$

$$I = \frac{\pi D^4}{64} ,$$

$$M = \frac{W l^2}{2} ,$$

but

$$W = C_d q D ,$$

$$q = \frac{V^2 \rho}{2} ,$$

$$V = \frac{\dot{M}}{A \rho} ,$$

Substituting into Equation (2) gives the following:

$$\sigma = \frac{8 C_d^2 \dot{M}^2 l^2}{\rho A^2 D^2 \pi} . \quad (6)$$

Insert the following values into Equation (6) to calculate normal stress values for  $T_{0a}$  and  $T_{0b}$ :

$$C_d = 1.2 ,$$

$$\dot{M} = 24.71 \text{ slug/sec} = \text{maximum tunnel mass flow rate} ,$$

$$l/D = 5.28 ,$$

$$\rho = 0.4995 \text{ slugs/ft}^3 \text{ at } 1500^\circ\text{F and } 16,000 \text{ psi} ,$$

$$A = 0.1503 \text{ ft}^2 = \text{cross section area of gas flow at } T_{0a} ,$$

$$\sigma = \frac{8(1.2)(24.71^2)(5.28^2)}{0.4995(0.1503^2)(\pi)} = 4,609,791 \text{ lb/ft}^2 = 32,000 \text{ psi} .$$

In the same manner, the following stresses were calculated for column 5 in Table N-1.

TABLE N-1. WIRE STRESS FOR VARIOUS TUNNEL CONDITIONS ( $T_{oa}$  AND  $T_{ob}$ )

$P_H$ psi	$P_S$ psi	$M$ Slug Sec	$\rho$ Slug ft <sup>3</sup>	$\sigma$ psi
20,000	16,000	24.71	0.4995	32,000
20,000	13,090	20.20	0.4390	24,789
20,000	10,180	15.54	0.3518	17,916
20,000	7,270	10.88	0.2657	11,662
22,000	6,000	9.3	0.2249	10,121
22,000	5,500	8.082	0.2083	8,200

The changeover point is found from the stress data above. The thermocouple wire has a yield point of 8000 psi at 1500°F. To find the changeover point, find the nearest value to 8000 in the fifth column of the table above. That value is 8200, found in the last row, last column. Go across the last row to the second column and read the  $P_S$  (nozzle supply pressure) of 5500 psi. This is the pressure at which the change in thermocouple tubes should be made. That is, below 5500 psi nozzle supply pressure use the unshielded thermocouple tube for operations. Above 5500 psi nozzle supply pressure, use the shielded thermocouple tube for operations.

To calculate the changeover point for the  $T_{oc}$  thermocouple, insert the following variables into Equation (6):

$$C_d = 1.2,$$

$$M = 24.71 \text{ slug/sec} = \text{maximum tunnel mass flow rate},$$

$$l/D = 6.73,$$

$$\rho = 0.545 \text{ slug/ft}^3 \text{ at } 1500^\circ\text{F and } 18,000 \text{ psi},$$

$$A = 0.1835 \text{ ft}^2 = \text{cross section area of gas flow at } T_{oc},$$

$$\sigma = \frac{8(1.2)(24.71^2)(6.73^2)}{0.545(0.1835^2)(\pi)} = 4,604,986 \text{ lb/ft}^2,$$

or

$$\sigma = 31,979 \text{ psi.}$$

In the same manner, the following stresses were calculated and are contained in the fifth column of Table N-2.

TABLE N-2. WIRE STRESS FOR VARIOUS TUNNEL CONDITIONS ( $T_{oc}$ )

$P_H$ psi	$P_S$ psi	$M$ $\frac{\text{Slug}}{\text{Sec}}$	$\rho$ $\frac{\text{Slug}}{\text{ft}^3}$	$\sigma$ psi
22,000	16,000	24.71	0.545	31,979
22,000	13,090	20.20	0.547	21,290
22,000	10,180	15.54	0.548	12,578
22,000	7,270	10.88	0.550	6,143
22,000	8,109	12.22	0.549	7,764

From the table above, the changeover point for thermocouple  $T_{oc}$  is 8109 psi. Since the thermocouple has a yield point of 8000 psi at 1500°F, find the value in the fifth column of the table above which is nearest to 8000 psi: this is found to be 8000 psi in the last row of the fifth column. Go across the last row to the  $P_S$  column and find 8109 psi as the changeover point. That is, below a  $P_S$  (nozzle supply pressure) of 8109 psi, use the unshielded thermocouple tube for  $T_{oc}$ . For pressures above 8109 psi, use the shielded thermocouple tube for  $T_{oc}$ .

Recapping the above calculations, the thermocouple tubes for  $T_{oa}$  and  $T_{ob}$  have a changeover pressure of 5500 psi. Thermocouple tube  $T_{oc}$  needs to be changed from shielded to unshielded when nozzle supply pressure is changed from more than 8109 psi to less than 8109 psi.

#### ERROR ANALYSIS OF THERMOCOUPLE AT GAS PRESSURE CHANGEOVER CONDITIONS

Calculations in this section cover conduction error, radiation error, and response time for thermocouples  $T_{oa}$ ,  $T_{ob}$  and  $T_{oc}$ . Since conditions at  $T_{oa}$  and  $T_{ob}$  are essentially the same, their calculations and error analysis are the same.

To calculate the conduction and radiation error for the shielded thermocouple configuration, calculate the convection heat transfer coefficient. Then use the coefficient to calculate thermocouple errors. Only shielded configurations are being addressed because, in general, they give the worst case.

#### Calculation of Heat Transfer Coefficient

The following is the calculation of the heat transfer coefficient  $h$  between thermocouple wires  $T_{oa}$ ,  $T_{ob}$  and tunnel gas at the changeover point condition of 5500 psi supply pressure, using an equation from Reference N-2.

$$h = \frac{K_f(0.0266)}{D} (R_{ed})^{0.805} (P_r)^{0.333} \quad (7)$$

where

$$R_{ed} = \frac{VD\rho}{\mu}$$

and

$$V = \frac{M}{2\rho A}$$

Substituting into Equation (7) gives the following.

$$h = \frac{K_f(0.0266)}{D} \left( \frac{MD}{2A\mu} \right)^{0.805} (P_r)^{0.333} \quad (8)$$

Calculate  $h$  by substituting the following values into Equation (8):

$M = 8.082$  slug/sec = tunnel mass flow rate,

$A = 0.1503$  ft<sup>2</sup> = nozzle inlet area,

$\mu = 6.47 \times 10^{-7}$  slug/ft·sec = viscosity of N<sub>2</sub> at 1500°F,

$D = 0.00125$  ft = diameter of thermocouple wire,

$K_f = 0.033$  Btu/hr(Ft)(°R) = conductivity of N<sub>2</sub> at 1500°F and 5500 psi,

$P_r = 0.703$

$$h = \frac{(0.033)(0.0266)}{(0.00125)} \left[ \frac{8.082(0.00125)}{2(0.1503)(6.47 \times 10^{-7})} \right]^{0.805} (0.703)^{0.333}$$

$$h = 3903 \text{ Btu/hr(ft}^2\text{)(}^\circ\text{R)} = 27.1 \text{ Btu/hr(in}^2\text{)(}^\circ\text{R)}.$$

### Thermocouple Conduction Error

The thermocouple conduction error (from an equation in Reference N-3) is calculated as follows:

$$\text{Error} = \frac{T_r - T_{\text{act}}}{\cosh m l} \quad (9)$$

where

$$m = \sqrt{\frac{4h}{KD}}$$

Substitute the following values into Equation (9) and calculate the thermocouple conduction error for  $T_{\text{Oa}}$  and  $T_{\text{Ob}}$  at changeover point conditions:

$K = 2.291 \text{ Btu/hr(in)(}^\circ\text{F)} = \text{conductivity of Alumel wire at } 1500^\circ\text{F,}$

$D = 0.015 \text{ in} = \text{diameter of wire,}$

$h = 27.1 \text{ Btu/hr(in}^2\text{)(}^\circ\text{F)} \text{ from the Equation (7) solution above,}$

$T_r = 70^\circ\text{F,}$

$T_{\text{act}} = 1500^\circ\text{F} = \text{actual temperature of } N_2 \text{ gas,}$

$$\text{Error} = \frac{70 - 1500}{\cosh \left[ \sqrt{\frac{(4)(27.1)}{(2.291)(0.015)}} (0.085) \right]} = -24.1^\circ\text{F .}$$

Conduction error for  $T_{\text{Oa}}$  and  $T_{\text{Ob}} = -9.5^\circ\text{F}$  when the nozzle pressure is 5500 psi.

### Thermocouple Radiation Error

The radiation error at  $T_{\text{Oa}}$  and  $T_{\text{Ob}}$ , when the nozzle pressure is 5500 psi, is calculated as follows (Reference N-3):

$$\text{Radiation Error} = \frac{0.174 \epsilon_p (T_w^4 - T_{ind}^4)}{h(10)^8} \quad (10)$$

Substitute the following values into Equation (10) to obtain the radiation error, using changeover point conditions:

$$h = 3903 \text{ Btu/hr(ft}^2\text{)(}^\circ\text{F)},$$

$$T_{ind} = 1960^\circ\text{R},$$

$$T_w = 610^\circ\text{R},$$

$$\epsilon_p = 0.5,$$

$$\text{Radiation Error} = \frac{(0.174)(0.5)(610^4 - 1960^4)}{3903(10)^8} = -3.2^\circ\text{F}.$$

Radiation Error =  $-3.2^\circ\text{F}$  for  $T_{oa}$  and  $T_{ob}$  operating with a nozzle supply pressure of 5500 psi.

#### Response Time for Thermocouples $T_{oa}$ and $T_{ob}$

Neglect heat losses due to radiation and conduction along the thermocouple wire, and apply conservation of energy to obtain  $hA(T_{act} - T_{ind})dt = mCdT_{ind}$ . Now take the LaPlace transform:

$$\frac{T_{ind}(s)}{T_{act}} = \frac{1}{(\tau s + 1)}$$

$$\tau = \frac{mC}{hA}$$

and

$$m = \frac{D^2 \pi \rho_a L}{4}$$

and

$$A = DL$$

Thus

$$\tau = \frac{D \rho_a C}{4h} . \quad (11)$$

Determine  $\tau$  by substituting the following values into Equation (11) and solving it:

$\rho_a = 0.289 \text{ lb/in}^3 = \text{density of Alumel},$

$D = 0.015 \text{ in} = \text{diameter of wire},$

$C = 0.107 \text{ Btu/sec(in}^2)(^\circ\text{F)},$

$h = 0.00752 \text{ Btu/sec(in}^2)(^\circ\text{F)},$

$$\tau = \frac{(0.015)(0.289)(0.107)}{4(0.00752)} = 0.0154 \text{ sec} = \text{response time for } T_{oa} \text{ and } T_{ob} \text{ when the nozzle supply pressure is 5500 psi.}$$

#### Heat Transfer Coefficient for Thermocouples $T_{oa}$ and $T_{ob}$

The following is the heat transfer coefficient  $h$  between thermocouple wires  $T_{oa}$  and  $T_{ob}$  and tunnel gas when the tunnel is operated with a 16,000 psi nozzle supply pressure. Substitute the following values into Equation (8) to calculate  $h$ :

$M = 24.71 \text{ slug/sec} = \text{tunnel mass flow rate},$

$A = 0.153 \text{ ft}^2 \text{ nozzle inlet area},$

$\mu = 1.209 \times 10^{-6} \text{ slug/ft(sec)},$

$D = 0.00125 \text{ ft},$

$K_f = 0.06996 \text{ Btu/hr(ft)}(^\circ\text{R}) = \text{conductivity of } N_2 \text{ gas at } 1500^\circ\text{F and } 16,000 \text{ psi},$

$P_r = 0.703,$

$$h = \frac{(0.06996)(0.0266)}{(0.00125)} \left[ \frac{(24.71)(0.00125)}{(2)(0.1503)(1.209 \times 10^{-6})} \right]^{0.805} (0.703)^{0.333} ,$$

$$h = 12,302 \text{ Btu/hr(ft}^2)(^\circ\text{F}) = 85.4 \text{ Btu/hr(in}^2)(^\circ\text{F}).$$



Thermocouple Conduction Error

Substitute the following values into Equation (9) to calculate the thermocouple conduction error for  $T_{oa}$  and  $T_{ob}$ :

$K = 2.291 \text{ Btu/hr(in}^2\text{)(}^\circ\text{F)} = \text{conductivity of Alumel wire at } 1500^\circ\text{F,}$

$D = 0.015 \text{ in} = \text{diameter of wire,}$

$h = 85.41 \text{ Btu/hr(in}^2\text{)(}^\circ\text{F)},$

$T_r = 70^\circ\text{F,}$

$T_{act} = 1500^\circ\text{F} = \text{actual temperature of } N_2 \text{ gas,}$

$$\text{Conduction Error} = \frac{70 - 1500}{\cosh \left[ \sqrt{\frac{(4)(85.4)}{2.291(0.015)} (0.085)} \right]} = 0.73^\circ\text{F.}$$

Conduction error =  $0.73^\circ\text{F}$  for thermocouples  $T_{oa}$  and  $T_{ob}$  when operating with a nozzle supply pressure of 16,000 psi.

Radiation Error for  $T_{oa}$  and  $T_{ob}$ 

To calculate the radiation error of  $T_{oa}$  and  $T_{ob}$ , when operating with a nozzle pressure of 16,000 psi, substitute the following numerical values into Equation (10):

$h = 12,300 \text{ Btu/hr(ft}^2\text{)(}^\circ\text{F)},$

$T_{ind} = 1960^\circ\text{R,}$

$T_w = 610^\circ\text{R,}$

$\epsilon_p = 0.5,$

$$\text{Radiation Error} = \frac{(0.174)(0.5)(610^4 - 1960^4)}{12300(10)^8} = -1.03^\circ\text{F.}$$

Radiation error =  $-1.03^\circ\text{F}$  for  $t_{oa}$  and  $T_{ob}$  when operating with a nozzle supply pressure of 16,000 psi.

Response Time of  $T_{oa}$  and  $T_{ob}$ 

Substitute the following values into Equation (11):

$\rho_a = 0.289 \text{ lb/in}^3,$

$$D = 0.015 \text{ in,}$$

$$C = 0.107 \text{ Btu/lb(}^\circ\text{F),}$$

$$h = 0.02372 \text{ Btu/sec(in}^2\text{)(}^\circ\text{F),}$$

$$\tau = \frac{(0.015)(0.289)(0.107)}{4(0.02372)} = 0.0049.$$

#### Heat Transfer Coefficient for Thermocouples $T_{oc}$

The following is the heat transfer coefficient  $h$  between thermocouple wires  $T_{oc}$  and tunnel gas when the tunnel is operated with a 8109 psi nozzle supply pressure. Substitute the following values into Equation (8) to calculate  $h$ :

$$\dot{M} = 12.22 \text{ slug/sec} = \text{tunnel mass flow rate,}$$

$$A = .1835 \text{ ft}^2 \text{ nozzle inlet area,}$$

$$\mu = 8.81 \times 10^{-7} \text{ slug/ft(sec),}$$

$$D = 0.00125 \text{ ft,}$$

$$K_f = 0.06996 \text{ Btu/hr(ft)(}^\circ\text{R)} = \text{conductivity of } N_2 \text{ gas at } 1500^\circ\text{F and } 18,500 \text{ psi,}$$

$$P_r = 0.703,$$

$$h = \frac{(0.06996)(0.0266)}{(0.00125)} \left[ \frac{(12.22)(0.00125)}{(2)(0.1835)(8.8 \times 10^{-7})} \right]^{0.805} (0.703)^{0.333},$$

$$h = 7675 \text{ Btu/hr(ft}^2\text{)(}^\circ\text{F)} = 53 \text{ Btu/hr(in}^2\text{)(}^\circ\text{F)}.$$

#### Thermocouple Conduction Error

Substitute the following values into Equation (9) to calculate the thermocouple conduction error for  $T_o$ :

$$K = 2.291 \text{ Btu/hr(in}^2\text{)(}^\circ\text{F)} = \text{conductivity of Alumel wire at } 1500^\circ\text{F,}$$

$$D = 0.015 \text{ in} = \text{diameter of wire,}$$

$$h = 53 \text{ Btu/hr(in}^2\text{)(}^\circ\text{F),}$$

$$T_r = 70^\circ\text{F,}$$

$$T_{act} = 1500^\circ\text{F} = \text{actual temperature of } N_2 \text{ gas,}$$

$$\text{Conduction Error} = \frac{70 - 1500}{\cosh \left[ \left( \frac{(4)(53)}{2.291(0.015)} \right)^{1/2} \right] 0.101} = -1.03^\circ\text{F.}$$

Conduction error =  $-1.03^{\circ}\text{F}$  for thermocouples  $T_{oc}$  operating with a nozzle supply pressure of 8109 psi.

#### Radiation Error for $T_{oc}$

To calculate the radiation error of  $T_{oa}$  and  $T_{ob}$ , when operating with a nozzle pressure of 8109 psi, substitute the following numerical values into Equation (10):

$$h = 7675 \text{ Btu/hr}(\text{ft}^2)(^{\circ}\text{F}),$$

$$T_{ind} = 1960^{\circ}\text{R},$$

$$T_w = 610^{\circ}\text{R},$$

$$\epsilon_p = 0.5,$$

$$\text{Radiation Error} = \frac{(0.174)(0.5)(610^4 - 1960^4)}{7675(10)^8} = -1.6^{\circ}\text{F}$$

Radiation error =  $-1.6^{\circ}\text{F}$  for  $t_{oc}$  when operating with a nozzle supply pressure of 8109 psi.

#### Response Time of $T_{oc}$

Substitute the following values into Equation (11):

$$\rho_a = 0.289 \text{ lb/in}^3,$$

$$D = 0.015 \text{ in},$$

$$C = 0.107 \text{ Btu/lb}(^{\circ}\text{F}),$$

$$h = 0.0148 \text{ Btu/sec}(\text{in}^2)(^{\circ}\text{F}),$$

$$\tau = \frac{(0.015)(0.289)(0.107)}{4(0.0148)} = 0.0079 \text{ for } T_{oc} \text{ when operating with a nozzle supply pressure of 8109 psi.}$$

#### Heat Transfer Coefficient for Thermocouples $T_{oc}$

The following is the heat transfer coefficient  $h$  between thermocouple wire  $T_{oc}$  and tunnel gas when the tunnel is operated with a 16,000 psi nozzle supply pressure. Substitute the following values into Equation (8) to calculate  $h$ :

$$\dot{M} = 24.7 \text{ slug/sec} = \text{tunnel mass flow rate},$$

$$A = 0.1835 \text{ ft}^2 \text{ flow restrict inlet linear area},$$

$$\mu = 1.29 \times 10^{-6} \text{ slug/ft(sec)},$$

$$D = 0.00125 \text{ ft},$$

$$K_f = 0.06996 \text{ Btu/hr(ft)}(^{\circ}\text{R}) = \text{conductivity of N}_2 \text{ gas at } 1500^{\circ}\text{F and } 18,500 \text{ psi},$$

$$P_r = 0.703,$$

$$h = \frac{(0.06996)(0.02666)}{(0.00125)} \left[ \frac{(24.71)(0.00125)}{(2)(0.1835)(1.29 \times 10^{-6})} \right]^{0.805} (0.703)^{0.333}$$

$$h = 9943 \text{ Btu/hr(ft)}^2(^{\circ}\text{F}) = 69 \text{ Btu/hr(in)}^2(^{\circ}\text{F}).$$

#### Thermocouple Conduction Error

Substitute the following values into Equation (9) to calculate the thermocouple conduction error for  $T_{oc}$ :

$$K = 2.291 \text{ Btu/Hr(in)}^2(^{\circ}\text{F}) = \text{conductivity of Alumel wire at } 1500^{\circ}\text{F},$$

$$D = 0.015 \text{ in} = \text{diameter of wire},$$

$$h = 69 \text{ Btu/hr(in)}^2(^{\circ}\text{F}),$$

$$T_r = 70^{\circ}\text{F},$$

$$T_{act} = 1500^{\circ}\text{F} = \text{actual temperature of N}_2 \text{ gas},$$

$$\text{Conduction Error} = \frac{70 - 1500}{\cosh \left[ \left( \frac{(4)(69)}{2.291(0.015)} \right)^{1/2} 0.101 \right]} = .335^{\circ}\text{F}.$$

Conduction Error =  $0.335^{\circ}\text{F}$  for thermocouples  $T_{oc}$  when operating with a nozzle supply pressure of 16,000 psi.

#### Radiation Error for $T_{oc}$

To calculate the radiation error of  $T_{oc}$  when operating with a nozzle pressure of 16,000 psi, substitute the following numerical values into Equation (10):

$$h = 9943 \text{ Btu/hr(ft)}^2(^{\circ}\text{F}),$$

$$T_{ind} = 1960^{\circ}\text{R},$$

$$T_w = 610^{\circ}\text{R},$$

$$\epsilon_p = 0.5,$$

$$\text{Radiation Error} = \frac{(0.174)(0.5)(610^4 - 1960^4)}{9943(10)^8} = -1.3^\circ\text{F}.$$

Radiation error =  $-1.3^\circ\text{F}$  for  $T_{oc}$  when operating with a nozzle supply pressure of 16,000 psi.

#### Response Time of $T_o$

Substitute the following values into Equation (11):

$$\rho_a = 0.289 \text{ lb/in}^3,$$

$$D = 0.015 \text{ in},$$

$$C = 0.107 \text{ Btu/lb}(\text{°F}),$$

$$h = 0.01918 \text{ Btu/sec}(\text{in}^2)(\text{°F}),$$

$$\tau = \frac{(0.015)(0.289)(0.107)}{4(0.01918)} = .00605 \text{ sec for } T_{oc} \text{ when operating with a nozzle supply pressure of 16,000 psi.}$$

SYMBOL DEFINITION

$A$  = Flow area  
 $C$  = Specific heat of thermocouple wire  
 $C_d$  = Drag coefficient perpendicular to a cylinder  
 $D$  = Diameter of thermocouple wire  
 $d_o$  = Outside diameter of thermocouple tube  
 $d_i$  = Inside diameter of thermocouple tube  
 $h$  = Convection heat transfer coefficient of thermocouple wire  
 $K$  = Conductivity of Alumel wire  
 $K_f$  = Conductivity of nitrogen gas  
 $l$  = Length of wire exposed to gas flow  
 $l_1$  = Figure 3 dimension showing length of negligible dynamic gas pressure on the thermocouple tube  
 $l_2$  = Figure 3 dimension showing the length of the thermocouple tube which is acted upon by dynamic gas pressure  
 $m$  = Mass of thermocouple wire  
 $M$  = Mass flow rate through the nozzle  
 $P_h$  = Heater pressure  
 $P_r$  = Prandtle number of nitrogen gas  
 $P_s$  = Nozzle supply pressure  
 $Re_d$  = Reynold's number  
 $t$  = Time  
 $T_{act}$  = Actual temperature of tunnel gas  
 $T_{ind}$  = Indicated temperature  
 $T_r$  = Room temperature  
 $T_w$  = Inside wall temperature  
 $V$  = Velocity of nitrogen flow past the thermocouple wire

SYMBOL DEFINITION (Cont.)

$V_{\infty}$  = Free stream velocity

$W$  = Thermocouple wire load per unit length

$\rho$  = Density of nitrogen gas at the thermocouple

$\rho_a$  = Density of thermocouple wire

$\sigma$  = Normal stress

$\tau_l$  = Shear stress

$\tau$  = Time constant

$\epsilon_p$  = Emittance of thermocouple wire

$\mu$  = Dynamic viscosity of nitrogen gas

## RESULTS OF DESIGN CALCULATIONS

Tables N-3 and N-4 contain a resume of design calculations for thermocouples  $T_{0a}$ ,  $T_{0b}$ , and  $T_{0c}$ . The rows titled "Wire Projection" identifies the longest length of wire which can protrude from the end of the shielded tube and into the flow of hot tunnel gas. Calculations of this length were made using Equation (N-3) of Enclosure (1) of this Appendix and gas loadings at high Reynold's number conditions (16,000 psi nozzle supply pressure). Different lengths are shown for  $T_{0a}$ ,  $T_{0b}$ , and  $T_{0c}$ . The different lengths are due to different dynamic gas pressures which impinge on the thermocouples at their respective locations in the wind tunnel. These are maximum wire lengths which can protrude beyond the thermocouple tube without the wires yielding during high Reynold's number operations.

The changeover points in Tables N-3 and N-4 specify the nozzle supply pressure below which the unshielded thermocouple should be used. The unshielded thermocouple gives more accurate temperature measurements. However, its wires will yield if they are used for pressures above the changeover point. The changeover point for  $T_{0a}$  and  $T_{0b}$  is 5,500 psi. The changeover point for  $T_{0c}$  is 8,109 psi. These differences are due to different dynamic gas pressure conditions which occur at the respective locations of the thermocouples. Calculations for changeover points were made using Equation (N-6) and Table N-1 of Enclosure (1) of this Appendix.

Finally, Tables N-3 and N-4 contain the conduction error and time constant of the thermocouples for wind tunnel supply pressures of 16,000, 8,109, and 5,500 psi (Equations (N-9), (N-10), and (N-11), respectively, in Enclosure (1) of this Appendix).

## CONCLUSIONS AND SUMMARY

The new thermocouple design assembly provides more structural integrity which enables it to withstand tunnel gas forces. It also gives faster thermocouple response, lower radiation error, and lower conduction error for more accurate measurements of changing tunnel gas temperatures.

The redesigned thermocouple tube provides better structural integrity and temperature measurement response time by the following means:

1. The tube is now made of thicker refractory (vice stainless steel) material to prevent bending or deformation when exposed to hot tunnel gases.
2. The design of the end of the shielded tube prevents hot tunnel gas damage to, or deformation of the thermocouple wire junction during high Reynold's number operations. This is accomplished by a backstop, or shield, located behind (downstream of) the thermocouple junction. The distance between the junction and its backstop is such that the tunnel gas velocity is reduced by about 50 percent in the area of the junction. This reduces tunnel gas forces on the wires and prevents their bending.



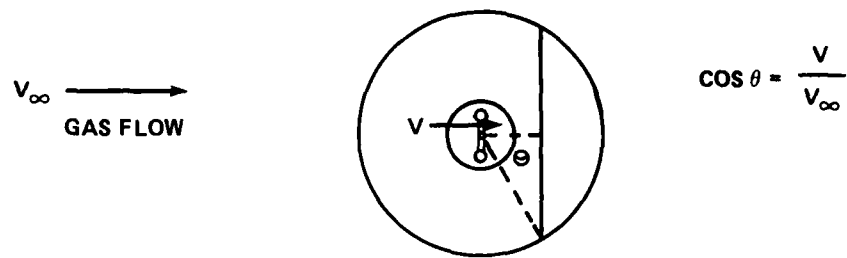


FIGURE N-1. TOP VIEW OF SHIELDED THERMOCOUPLE TUBE

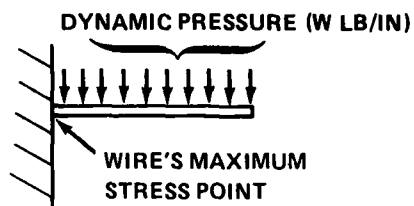


FIGURE N-2. WIRE MODEL

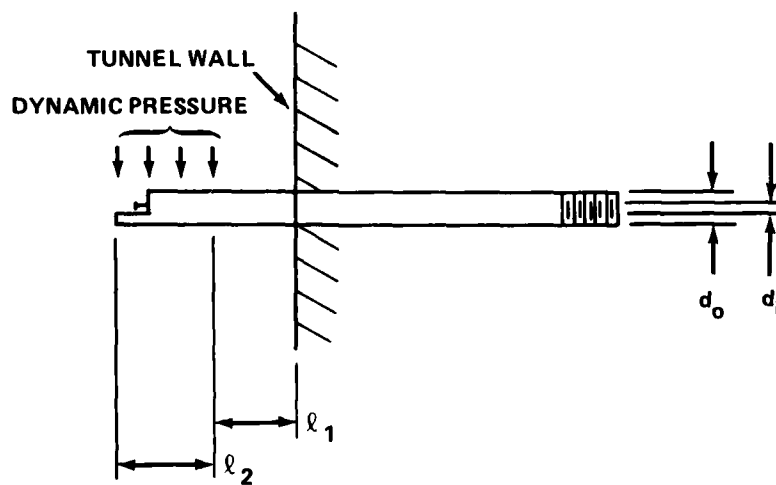


FIGURE N-3. SIDE VIEW OF SHIELDED THERMOCOUPLE TUBE

TABLE N-3. RESUME OF APPENDIX A CALCULATIONS FOR SHIELDED THERMOCOUPLE

	For Thermocouples $T_{0a}$ and $T_{0b}$		For Thermocouples $T_{0c}$	
Nozzle Supply Pressure (psi)	*5,500	16,000	*8,109	16,000
Wire Projection (inch)	0.083	0.083	0.101	0.101
Conduction Error (°F)	-24.1	-0.73	-1.03	-0.34
Radiation Error (°F)	-3.2	-1.03	-1.6	-1.3
Time Constant (sec)	0.0154	0.0049	0.0079	0.00607

\* = Thermocouple changeover point

TABLE N-4. RESUME OF CALCULATIONS FOR UNSHIELDED THERMOCOUPLE

	For Thermocouples $T_{0a}$ and $T_{0b}$	For Thermocouples $T_{0c}$
Nozzle Supply Pressure (psi)	*5,500	*8,109
Wire Projection (inch)	0.083	0.101
Conduction Error (°F)	-5.18	-0.077
Radiation Error (°F)	-1.86	-0.948
Time Constant (sec)	0.0088	0.0044

\* = Thermocouple changeover point

REFERENCES

- N-1. Melville, L., Theoretical Hydrodynamics, (New York: MacMillian, 1955).
- N-2. Holman, J. D., Heat Transfer, (New York: McGraw-Hill, 1976).
- N-3. Doebelin, E. O., Measurement Systems Application and Design, (New York: McGraw-Hill, 1975).

## APPENDIX O

## M-10 HIRE TOTAL TEMPERATURE PROBE DESIGN

## INTRODUCTION

In order to measure gas temperature in the test cell and confirm the accuracy of temperatures measured in the diaphragm area during M-10 HIRE testing, a total temperature probe was designed. Several problem areas existed in trying to measure temperatures accurately in the test cell at M-10 HIRE conditions. The first problem area was radiation error. Since considerable radiation error was present, a radiation shield was required in the probe design. A second problem area was response time. Due to the short tunnel run times experienced with M-10 HIRE testing, extremely fast thermocouple response time was required. Fast thermocouple response time dictated the use of very fine thermocouple wire and extremely thin radiation shielding. Lastly, the high operating temperatures required the use of materials and thermocouples having a high melting temperature.

## DESIGN APPROACH

Since a radiation shield was required for the probe, the gas flow had to be induced over the thermocouple wires. This was accomplished by venting the rear of the radiation shield to the tunnel. From previous wind tunnel experience it was determined that the open vent area required was approximately half of the radiation shield entrance area. Due to the high gas temperatures being measured, the shielding and vent area materials selected were stainless steel. A Chromel-Alumel type thermocouple with wire clad in stainless steel and magnesium oxide insulation was chosen for use in the design.

In order to obtain the desired response time and minimize error, it was determined that the radiation shield needed to be less than .003 inches thick and the thermocouple wire less than .004 inches thick. Analyses were performed to determine how small these components could be made and yet still withstand the expected loading conditions.

## STRUCTURAL ANALYSIS

Structural analyses were performed on particular design areas to ensure safe and reliable operation of the probe design. A working stagnation pressure of 55 psi and temperature of 1500°F were assumed for analysis purposes. From a structural analysis point of view the areas of interest are:

- a. Strength of the radiation shield,
- b. Flow restrictor plate thickness,
- c. Buckling of thermocouple wires,
- d. Bending of probe support wings.

The actual calculations performed on the design areas mentioned above are shown in the structural calculations section of this appendix. Some comments concerning the calculations made on the design areas are given below:

a. A .002 inch thick radiation shield was analyzed. Thermal stresses in the shield were shown to be high assuming the entire shield material rises to 1500°F. However, considering the material diffusivity and the short run duration, the shield will not see the full temperature differential and the actual thermal stresses will be considerably lower.

b. Due to the necessity of rather close spacing of the flow restrictor vent holes, the flow restrictor plate thickness was looked at. A plate thickness of .060 inch was chosen given a factor of safety of 20 in this area.

c. Since the thermocouple wires had to be very thin they were analyzed for a buckling mode of failure. In addition, bending of the thermocouple wire sheath was looked at. The analysis was performed using the dimensions of the smallest commercially available thermocouple wire (.0015 dia. wire, .010 dia. sheath). The analysis indicated no problems in using this wire in the probe design.

d. The total temperature probe was to be held in the tunnel flow by a probe holder. The probe holder wings and weldments were looked at for shear and bending forces imposed by the aero loads. Even though several worst-case assumptions were made, no problems were encountered in the probe holder design.

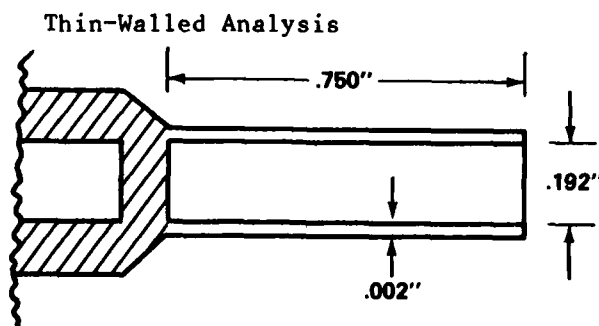
## STRUCTURAL CALCULATIONS

### Radiation Shield Strength

#### Hoop Stress

$$\frac{D}{t} = \frac{.192}{.002} = 96$$

$$\sigma_h = \frac{Pr}{t}$$



where

$$P = \Delta P_{\max} = 55 \text{ psi}$$

$$\sigma_h = \frac{(55)(.192)}{(.002)(2)} = 2,640 \text{ psi}$$

Yield strength for 17-4 PH S.S. at 1500°F =  $\sigma_y = 50,000 \text{ psi}$  (Ref. 0-1).

Collapse Pressure for a Cylinder

$$P = KE \left( \frac{t}{D} \right)^3 \quad (\text{Ref. 0-2})$$

where

$$E(1500^\circ\text{F}) = 22.8 \times 10^6 \text{ psi}$$

$$t = .002$$

$$P = .192$$

$$K = f \frac{L}{D} \text{ and } \frac{D}{t} \quad (\text{Figure 64 page 5-65 of Ref. 0-2})$$

$$\left. \begin{aligned} \frac{L}{D} &= \frac{.75}{.192} \approx 4 \\ \frac{D}{t} &= \frac{.192}{.002} = 96 \end{aligned} \right\} K = 21$$

$$P = (21)(22.8 \times 10^6) \left( \frac{.002}{.192} \right)^3 = 541 \text{ psi (compare to } \Delta P_{\max})$$

$$\Delta P_{\max} = 55 \text{ psi}$$

Thermal Stress

$$\sigma_{\text{Thermal}} = \frac{1.25 \alpha E \Delta T}{2(1-\nu)} \quad (\text{Ref. 0-3})$$

where

$$\alpha = 6.5 \times 10^{-6} \text{ in/in-}^\circ\text{F (Ref. O-1)}$$

$$E = 22.8 \times 10^6 \text{ psi}$$

$$\Delta T = \Delta T_{\max} = 1500 - T_{\text{amb}} = 1400^\circ\text{F}$$

$$\nu = .3$$

$$\sigma_{\text{H-Thermal}} = \frac{(1.25)(6.5 \times 10^{-6})(22.8 \times 10^6)(1400)}{2(1 - .3)} = 185,250 \text{ psi}$$

$\sigma_{\text{H-Thermal}} > \sigma_y$  - This rather high predicted thermal stress should not be a problem since the probe will be used for very short tunnel runs, thus the entire radiation shield material should not see a  $\Delta T$  of  $1400^\circ\text{F}$ .

#### FLOW RESTRICTOR PLATE

##### Ligament Shear

$$d = .005 \text{ in.}$$

Look at thickness (t) so that shearing of ligament area (d) will not be a problem.

Assume 1/2 the area of each .052 diameter hole is inside the .125 bolt circle.

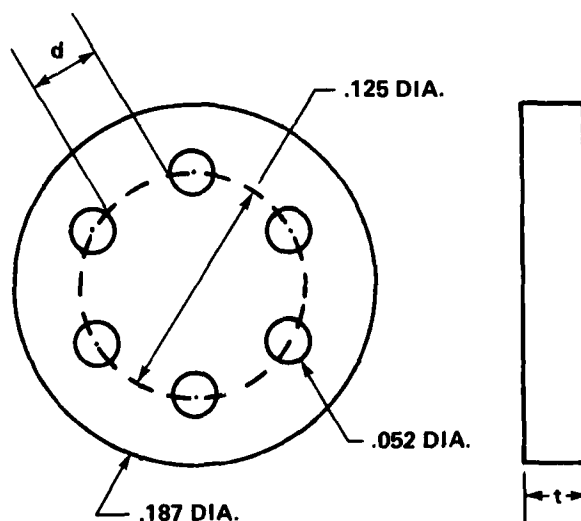
$$A_{\text{B.C.}} = A_{.125} - (.5)(6)A_{.052}$$

$$= \frac{\pi(.125)^2}{4} - (.5)(6) \frac{\pi(.052)^2}{4} = .006 \text{ in}^2$$

$$\text{Max } \Delta P \text{ across plate} = \Delta P_{\max} = 55 \text{ psi}$$

$$\text{Force on B.C. area} = \Delta P \times A = (55)(.006) = .33 \text{ lbs.}$$

$$\text{Shear area for 1 ligament} = (d)(t)$$



- Assume 1)  $d = .005$  in.,  
 2) 1 ligament bears the entire shear load (conservative).

$$\tau_y = \frac{\sigma_y}{2} = \frac{F}{A_s} = \frac{F}{td} \quad t = \frac{2F}{\sigma_y d} = \frac{(2)(.33)}{(50,000)(.005)} = .003 \text{ in.}$$

Flow restrictor plate thickness  $\geq .003$  in.

#### Entire Plate Shear

$$A_{\text{Plate}} = A_{.187} - 6A_{.052} = \frac{\pi(.187)^2}{4} - 6 \cdot \frac{\pi(.052)^2}{4} = .014 \text{ in}^2$$

$$\text{Force on plate} = \Delta P_{\text{max}} \times A_{\text{Plate}} = (55)(.014) = .77 \text{ lbs}$$

$$\tau_y = \frac{F}{A_s} = \frac{F}{Dt} \quad t = \frac{F}{\tau_y \pi D} = \frac{.77}{(25,000)(\pi)(.187)}$$

$$= 5.2 \times 10^{-5} \text{ in}$$

Thus, ligament shear consideration controls the selection of flow restrictor plate thickness ( $t$ ).

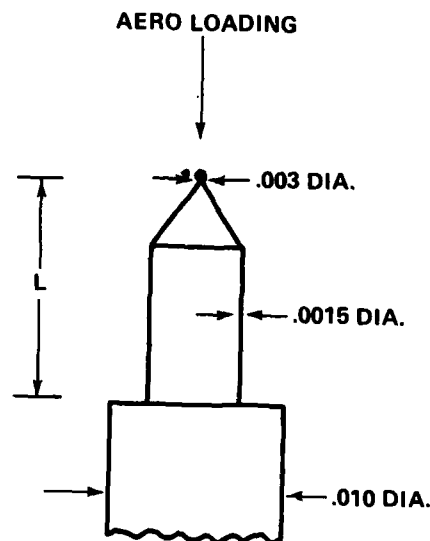
#### BUCKLING OF THERMOCOUPLE WIRE

Consider OMEGA brand "Omegaelad" type thermocouple wire. A schematic of the wire is shown at right. The wire is a Chromel-Alumel type wire.

Assume the thermocouple junction is a sphere of diameter .003 inches.

Drag load on sphere =

$$D = C_D A_x \frac{\rho}{P_o} P_{\text{max}} \quad (\text{Ref. O-4})$$





where

$$C_D = 1 \text{ for a sphere,}$$

$$A_x = \frac{\pi}{4} (.003)^2 = 7 \times 10^{-6} \text{ in}^2,$$

$$\frac{q}{P_o} = .0592 \text{ (Ref. O-4),}$$

$$\Delta P_{\max} = 55 \text{ psi,}$$

$$D = (7 \times 10^{-6})(.0592)(55) = 2.3 \times 10^{-5} \text{ lbs.}$$

Model the load on the thermocouple wire as an eccentrically loaded column. Would like to find acceptable values for the length (L) of the wire given the loading.

Using the secant formula for column stress due to eccentric loading:

$$\sigma_{\max} = \frac{P}{A} \left[ 1 + \frac{ec}{r_x^2} \sec \left( \frac{L^*}{2r_x} \sqrt{\frac{P}{EA}} \right) \right] \quad (\text{Ref. O-5})$$

where

$$P = \text{drag load} = 2.3 \times 10^{-5} \text{ lbs,}$$

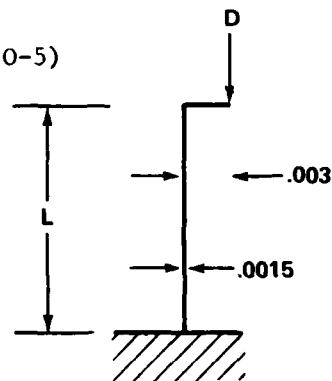
$$A = \text{column area} = \frac{\pi}{4} (.0015)^2 = 1.8 \times 10^{-6} \text{ in}^2,$$

$$C = \text{outer fiber dist.} = \frac{.0015}{2} = .00075 \text{ in.,}$$

$$r_x = \text{radius of gyration} = \frac{r}{2} = \frac{.0075}{2} = 3.7 \times 10^{-3} \text{ in.,}$$

$$L^* = 2L \text{ for a fixed end column,}$$

$$E = \text{modulus of elasticity for column (Chromel-Alumel).}$$



Chromel-Alumel Material Data (Ref. 0-6)Chromel

$$\sigma_T \text{ at } 1500^\circ\text{F} = 28,500 \text{ psi}$$

$$E \text{ at } 1500^\circ\text{F} = 11.0 \times 10^6 \text{ psi}$$

Alumel

$$\sigma_T \text{ at } 1500^\circ\text{F} = 25,000 \text{ psi}$$

$$E \text{ at } 1500^\circ\text{F} = 25,000 \text{ psi}$$

Since Alumel appears to be the weaker material I will use Alumel material data for design analyses.

$$\sigma_{\max} = \frac{2.3 \times 10^{-5}}{1.8 \times 10^{-6}} \left[ 1 + \frac{(.003)(.00075)}{(3.7 \times 10^{-3})^2} \text{ sec} \right. \\ \left. \left( \frac{2L}{(2)(3.7 \times 10^{-3})} \sqrt{\frac{2.3 \times 10^{-5}}{(9.3 \times 10^6)(1.8 \times 10^{-6})}} \right) \right] \\ = 12.7 \left[ 1 + \frac{.164}{\cos(.317L)} \right]$$

<u>L (inches)</u>	<u><math>\frac{L}{D}</math></u>	<u><math>\sigma_{\max}</math> (psi)</u>
.0375	25	1.48
.075	50	1.48
.150	100	1.48
.375	250	1.48

Since  $\sigma_y$  at  $1500^\circ\text{F} = 1/2 \sigma_T = 25000/2 = 12,500 \text{ psi}$ , buckling of the thermocouple wire should be not a problem.

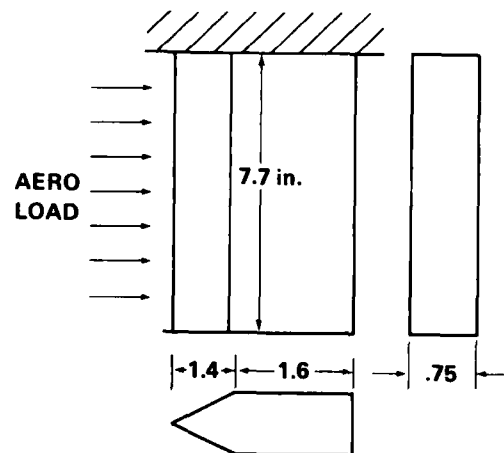
BENDING OF PROBE SUPPORT WINGSShear Stress

$$\text{Wing Frontal Area} = (7.7)(.75) = 5.78 \text{ in}^2$$

$$\Delta P_{\max} = 55 \text{ psi}$$

$$\text{Wing Load} = (5.78)(55) = 318 \text{ lbs}$$

$$\text{Shear Area} = (1.6)(.75) + 1/2(.75)(1.4) \\ = 1.725 \text{ in}^2$$



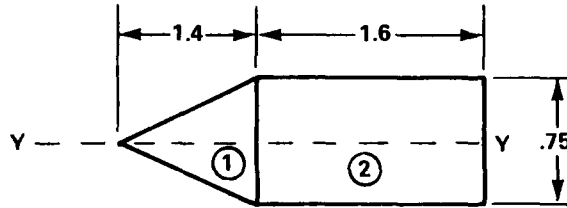
$$\text{Shear Stress} = \tau = \frac{318}{1.725} = 184 \text{ psi}$$

$$\text{Weld Shear (assuming 1/8 fillets)} = \frac{P}{.707hL} = \frac{318}{(.707)(.125)(2)(3)} = 600 \text{ psi}$$

Bending Stress

$$\sigma = \frac{Mc}{I}$$

$$I_{yy} = I_1 + I_2$$



$$I_1 = 2 \left[ \frac{bh^3}{36} + Ad^2 \right] = 2 \left[ \frac{(.375)(1.4)^3}{36} + (.5)(1.4)(.375)(.125)^2 \right] = .0642 \text{ in}^2$$

$$I_2 = \frac{bh^3}{12} = \frac{(1.6)(.75)^3}{12} = .056 \text{ in}^4$$

$$I_{yy} = .064 + .056 = .120 \text{ in}^4$$

M Force x Dist.

Force = Press. x Area

Area = (7.7)(3) = 23.1 in<sup>2</sup>

Pressure Max. = 15 psi (Ref. 0-7)

Force = (15)(23.1) = 347 lbs

$$M = (347)(7.7/2) = 1,336 \text{ in-lbs.}$$

$$\sigma = \frac{Mc}{I} = \frac{(1336)(.75/2)}{.120} = 4,175 \text{ psi}$$

Aluminum 2024-T351

$\sigma_y$  at room temperature = 42,000 psi

$\sigma_t$  at 1500°F = 20,000 psi

Aluminum 2024-Annealed

$\sigma_y$  at room temperature = 11,000 psi

$\sigma_y$  at 1500°F = 5,000 psi

Will use Aluminum 2024-T351 but due to welding and tunnel heating the aluminum may begin to approach the annealed condition. Even with these assumptions and a worst case pressure loading the bending stress is less than the yield strength.

Figure O-1 is an assembly drawing of the total temperature probe and probe holder. Note that in addition to the M-10 HIRE temperature probe two other probes are shown mounted on the probe holder. Of these other temperature probes, one was a commercially available probe; the other was built in-house for a previous test. The reason for mounting several probes was to compare structural capability, response time and error between the various probes. Figure O-2 is a detail drawing of the radiation shield.

#### CONCLUSION

A total temperature probe was designed and analyzed for use at high Reynolds numbers in Tunnel 9 Mach-10 applications. The probe was designed for test cell use at tunnel conditions up to 55 psia and 1500°F. The probe successfully withstood all operating conditions encountered in the demonstration test series.

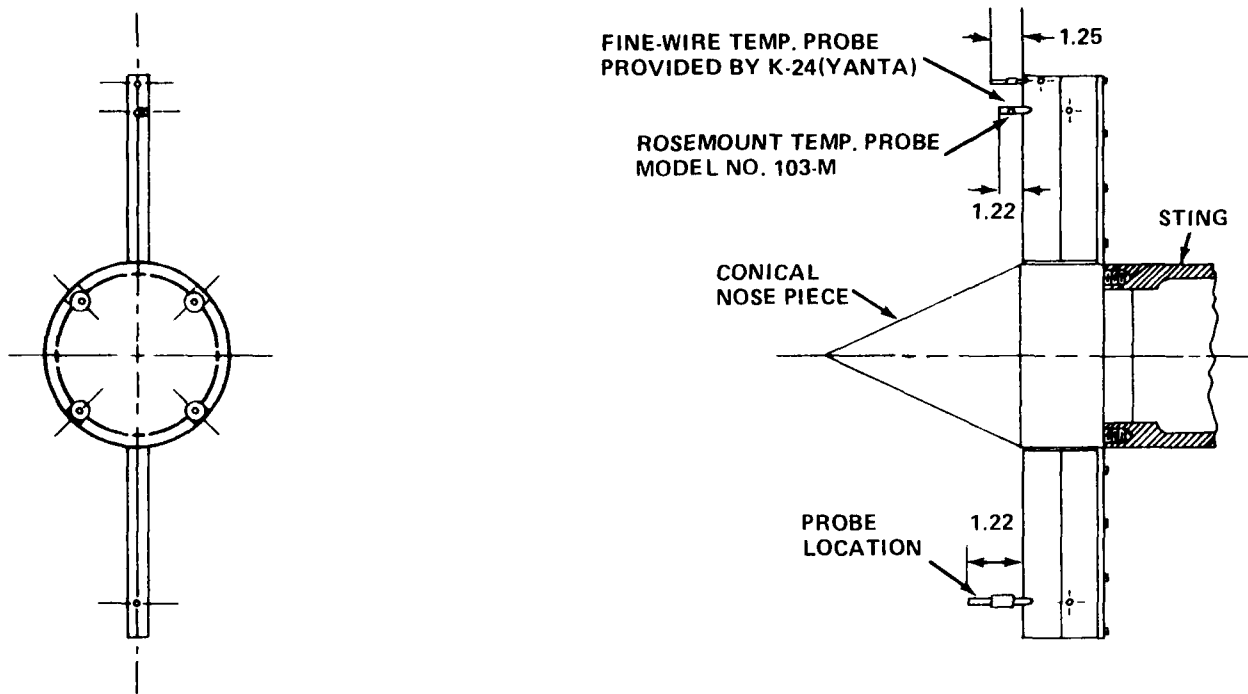


FIGURE O-1. PROBE MOUNT ASSEMBLY

NOTES:

1. MATERIAL - ST'NLESS ST'L TYPE 17-4 PH. COND. H-1100
2. ALL DIAMETERS CONCENTRIC WITHIN 0.001 T.I.R.
3. 125/ EXCEPT AS NOTED

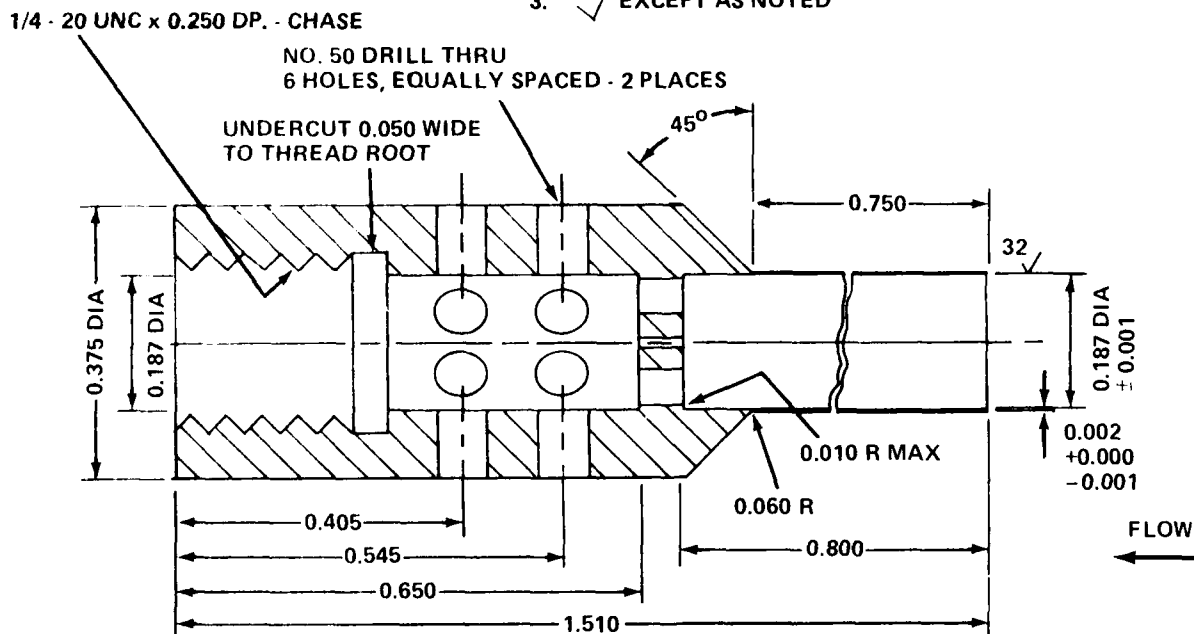


FIGURE O-2. DETAIL OF RADIATION SHIELD

REFERENCES

- O-1. "Precipitation-Hardenable Stainless Steels," Republic Steel Bulletin, 1975.
- O-2. Marks, Standard Handbook for Mechanical Engineers, (New York: McGraw-Hill, 1975).
- O-3. Timoshenko, S., Theory of Elasticity, (New York: McGraw-Hill, 1977).
- O-4. Streeter, V. L., Fluid Mechanics, Fifth Edition, (New York: McGraw-Hill, 1971).
- O-5. Higdon, Ohlsen, et al. Mechanics of Materials, (Wiley and Sons, 1976).
- O-6. "Chromel-Alumel Material Specifications," Haskins Manufacturing Bulletin, 1982.
- O-7. WA-40 Safety Committee, Safety Review of the Hypervelocity Facility Wind Tunnel No. 9, Navy JAG Report, Mar 1976.

## APPENDIX P

## HEATER ELEMENT BUFFETTING AND BAFFLE PLATE DESIGN

## BACKGROUND

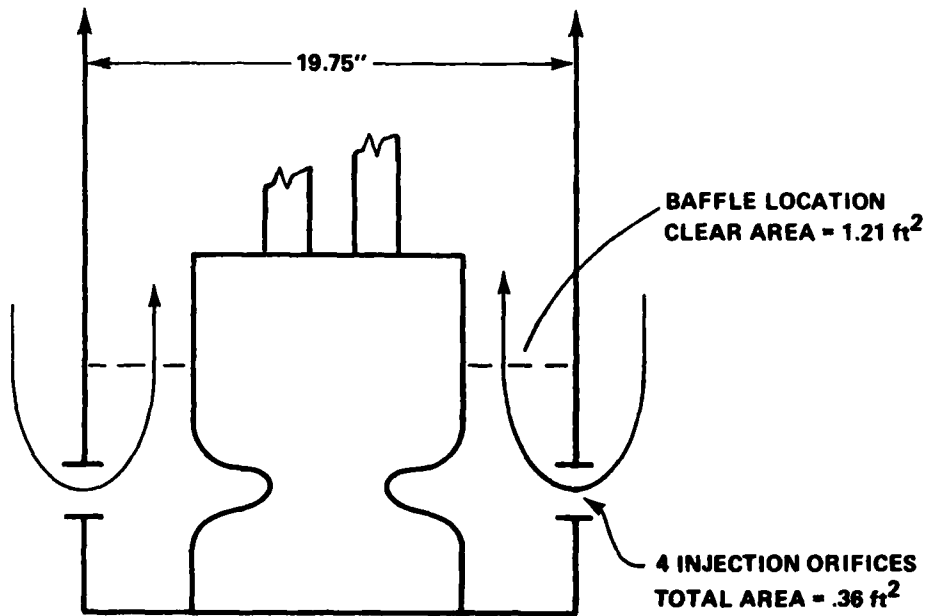
The reason for the failure of heater elements during the Mach-10 HIRE calibration test series was thought to be aerodynamic buffetting. The scenario was postulated as follows: the nitrogen driver gas enters the heater through four large (4" x 3-3/4") windows (Figure P-1), forming four large jets which are turned upward and impinge on the graphite heater base and the insulation can on the way up. The large fluctuations in the flow produced by these jets buffet the heater element, inducing a loading on the element severe enough to cause structural failure of the element.

Earlier Mach-10 HIRE ("cold shakedown") tests included instrumenting the graphite heater element with strain gages. Extrapolation of this data to calibration test conditions suggested that the buffetting was a very likely cause of the heater element failure.

A porous flow distributor or "inflow baffle plate" was proposed as a design fix which would break up the large jets and smooth out the flow, as shown in Figure P-2, thus greatly reduce aero-buffetting. A detailed engineering design for such a baffle device commenced and in approximately three months a baffle was ready to be installed in the Tunnel 9 vertical heater. The baffle design is shown in Figure P-3. The annular top plate, Figure P-4, and inner side wall are perforated with 1548 holes 1/4" in diameter. These perforations, as well as a 1/8" annular gap which exists between the solid outer side wall and heater can (Figure P-3) break up the large jets and distribute the flow evenly around the heater base.

BASELINE DESIGN

Consider the Geometry



Design Conditions

Initial  $P_H = 22,000$  psi.

$P_H$  after initial pressure decay = 19,000 psi.

$P_O = 16,000$  psi

where

$P_H$  = pressure in heater,

$P_O$  = nozzle supply pressure.

From Appendix L,  $\dot{m} = 780$  lb/sec,

Density in heater = 17.7 lb/ft<sup>3</sup>,



Volumetric flow = 44.1 ft<sup>3</sup>/sec,

Density of driver gas in heater at 500°K = 29.4 lb/ft<sup>3</sup>.

In the annulus between the heater can and the heater base element, without any baffle:

$$A = \frac{\pi}{4} ((19.75)^2 - (13.0)^2) \text{ in}^2 = 1.21 \text{ ft}^2$$

Velocity = 36.4 ft/sec,

$$\text{Dynamic pressure} = \frac{1/2 \rho V^2}{32.2} = 4.2 \text{ psi.}$$

Coming through the four ports at the bottom:

$$A = 4 \times 4 \times 3.25 \text{ in}^2 = .361 \text{ ft}^2,$$

Velocity = 122 ft/sec,

Dynamic pressure = 47.4 psi.

#### Baffle Design

To spread out the flow from the four inlet ports, the pressure drop across the baffle should be more than the inlet dynamic pressure.

Say,  $q(\text{baffle}) = 100 \text{ psi.}$

This means that the total force on the baffle is:

$$100 \times 144 \times 1.21 = 17,424 \text{ lbs}$$

and

$$1/2 \frac{\rho V^2}{g} = 100 \text{ psi, } V = 177 \text{ ft/sec}$$

If the discharge coefficient of the holes in the baffle is  $C_d = 0.6$ :

$$177 C_d A = 44.1 \text{ ft}^3/\text{sec},$$

$$A = 0.42 \text{ ft}^2 \text{ for } C_d = 0.6,$$

The porosity of the baffle is  $.42/1.21 = 0.34$ .

Now consider how big the holes should be. For smooth flow the jet velocity should decay to the mean velocity in the can in the distance between the baffle and the top of the heater base, say 6 inches. The mean velocity over the cross section of the heater can is:

$$44.1 / (\pi/4 \times (19.75)^2 / 144) = 20.7 \text{ ft/sec}.$$

$$\frac{u}{u_o} = \frac{6.4}{\frac{x}{d} + 0.6} = \frac{20.7}{177} = .12$$

$$\frac{x}{d} + 0.6 = \frac{6.4}{.12} = 54.7$$

Therefore

$$x/d_o = 54$$

and

$$d_o = 0.11 \text{ inches}.$$

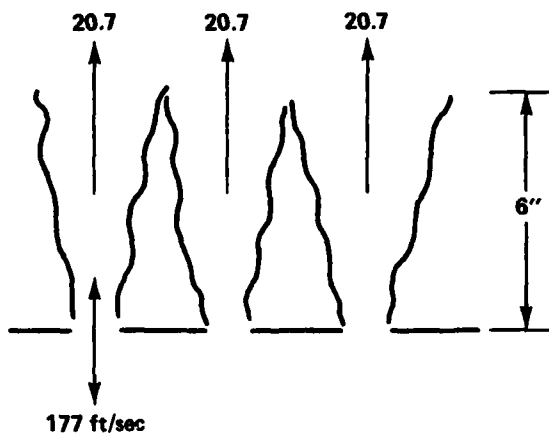
Say we use  $d = 0.125$  inches.

The number of holes is  $N$  where  $N \times \pi/4 \times (.125)^2 = 0.42 \times 144 = 60.5$ .

$$N \times 0.0123 = 60.5$$

$$N = 5000$$

This is the baseline aerodynamic design.



## CHANGE TO BASELINE DESIGN

After the baseline calculations were published it was determined that the heater can injection area could be increased to 127 in<sup>2</sup> by cutting 8 more smaller "windows." This larger injection area made it possible to reduce the required pressure drop across the baffle from 100 to only 50 psi which set the requirement for throttle area of the baffle to 83 in<sup>2</sup>. The baseline design called for a perforation hole diameter of 1/8 inch for 5000 holes. This diameter was increased to 1/4 inch and the number of holes reduced to 1548 both for structural reasons and to save time in drilling the perforations. The flow areas of importance for the final design are as follows:

- a) Heater can downflow area = 36.9 in<sup>2</sup>,
- b) Heater can injection area = 127.2 in<sup>2</sup>,
- c) Baffle inlet mouth area = 93.5 in<sup>2</sup>,
- d) Baffle throttle area = 83 in<sup>2</sup>,  
(1548 holes 1/4" diameter + 1/8" annular gap).

## STRUCTURAL ANALYSIS SUMMARY

The inflow baffle is designed to withstand a 50 psi operating pressure differential at a uniform material temperature of 500°F. Convection and radiation heat transfer calculations showed that the baffle temperature should not exceed 500°F at any time during the Mach-10 HIRE heat up cycle. The baffle is fabricated entirely of low carbon steel (either ASTM A36 or 1018 cold rolled). An E7018 electrode is specified for all welds. The following areas were included in the structural analysis:

- 1. Buckling of shroud due to pressure,
- 2. Hoop stress due to external pressure,
- 3. Radial thermal expansion,
- 4. Top area strength analysis,
- 5. Top plate strength analysis,
- 6. Outer side wall strength analysis,
- 7. Base flange strength analysis,
- 8. Welds analyses.

Nearly all safety factors in the analyses are comfortably high. For example, a calculation for buckling of the baffle shell due to a 50 psi pressure differential, for a 500°F uniform shell temperature, predicts a safety factor of 95. Safety factors for the perforated top plate were lowest in the analysis but

still acceptable. The annular top plate is divided by solid gussets into six equal sector-shaped panels, Figure P-4. Each panel is fixed at the gussets and at the inner and outer side walls by  $3/16$ " fillet welds. A 50 psi pressure differential across each of the panels will cause the panels to bulge upward at the center on the order of .0025 inches. Maximum plate bending stresses are developed at the center of each panel. The inner and outer edge welds are subjected to bending as well as shear. Safety factors for top plate and welds which were lowest in the analysis are given in Table P-1.

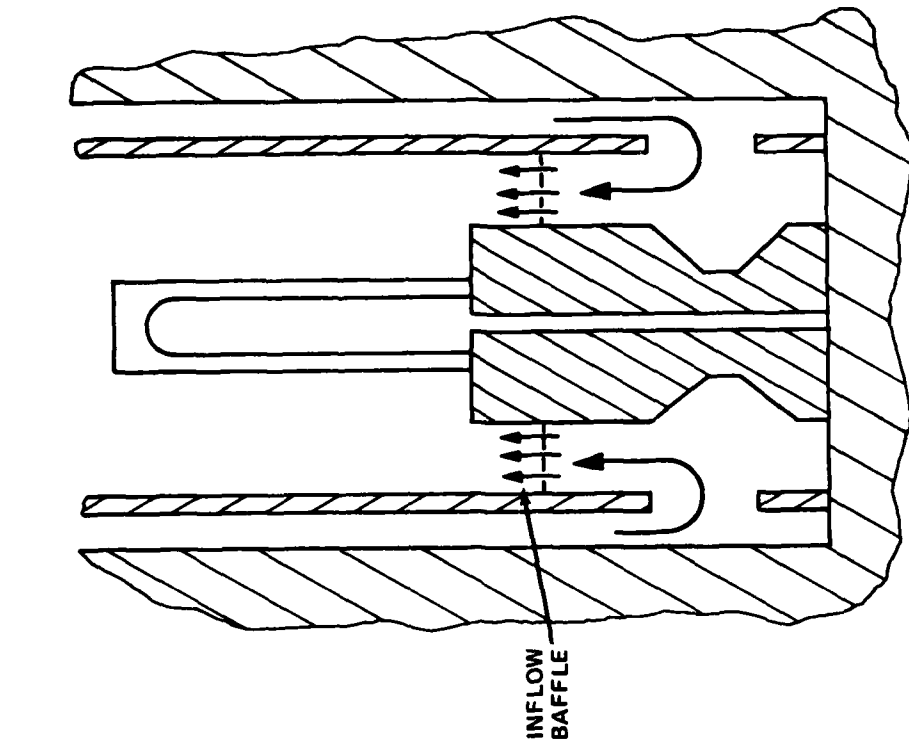


FIGURE P-2. POROUS FLOW DISTRIBUTOR CONCEPT

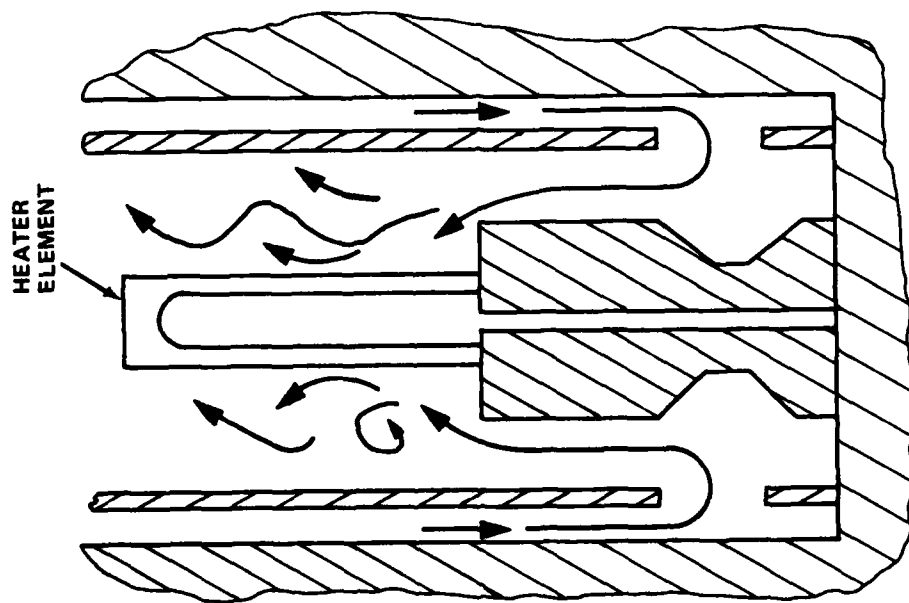


FIGURE P-1. BUFFETING OF VERTICAL HEATER ELEMENT

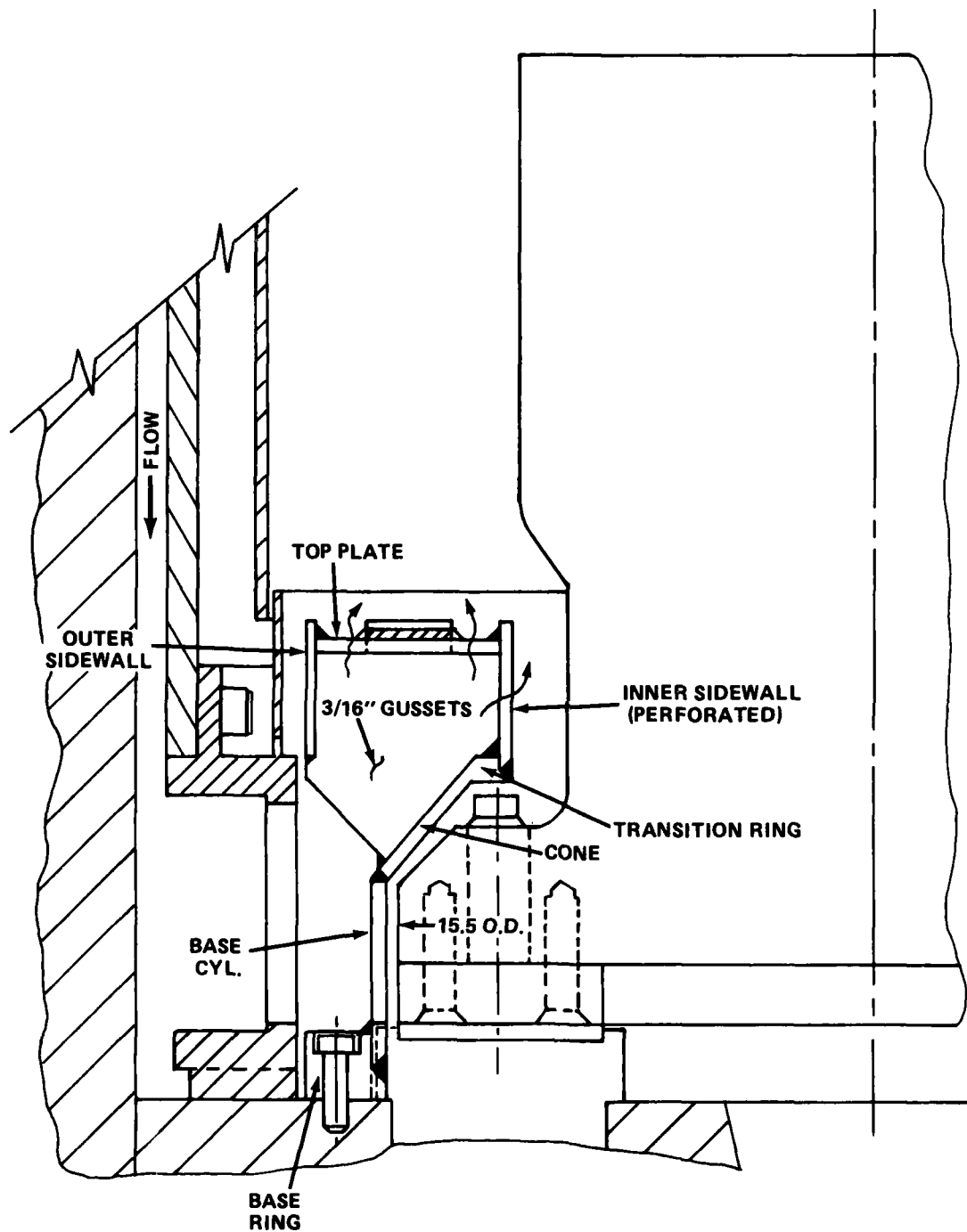


FIGURE P-3. MACH 10 VERTICAL HEATER INFLOW BAFFLE

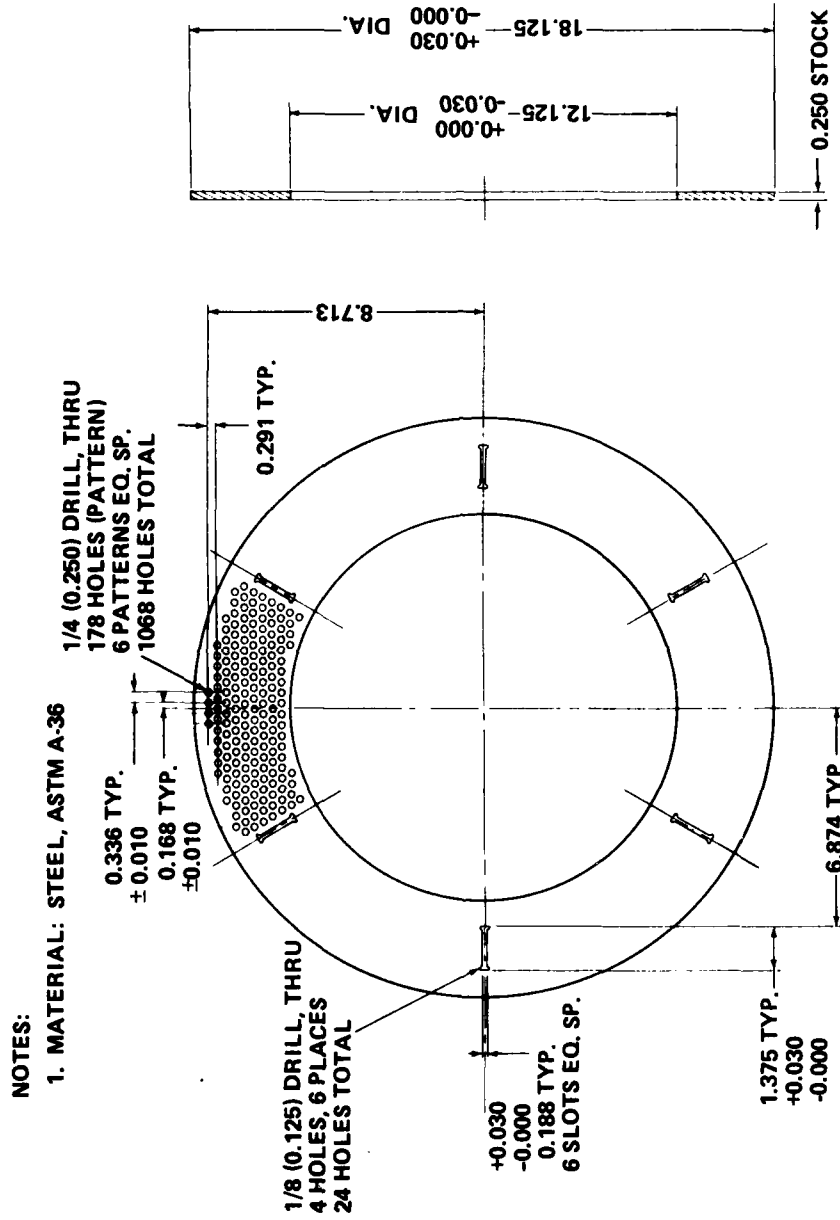


FIGURE P-4. TOP PLATE DETAIL

TABLE P-1. SAFETY FACTORS FOR TOP PLATE AND FILLET WELD

NO.	CASE DESCR.	SAFETY FACTOR DEFINITION	SAFETY FACTOR VALUE
1	AVERAGE BENDING STRESS @ CENTER OF TOP PLATE SECTOR PANEL, $\sigma_{BAVE}$	$\frac{\text{YIELD @ } 500^{\circ}\text{F}}{\text{COMPUTED } \sigma_{BAVE}}$	$\frac{28,800 \text{ PSI}}{9734 \text{ PSI}} = \boxed{2.95}$
2	MAX. LOCAL STRESS AT 1/4" HOLE EDGE STRESS CONCENTRATION	$\frac{\sigma_y @ 500^{\circ}\text{F}}{3 \times \sigma_{BAVE}}$	$\frac{28,800 \text{ PSI}}{29,202 \text{ PSI}} = \boxed{0.98} \text{ (NOTE 1)}$
3	3/16" FILLET WELD AT TOP PLATE/ INNER SIDE-WALL JUNCTION MAX. EFFECTIVE BENDING STRESS $\sigma_{bMAX}$	$\frac{\sigma_y @ 500^{\circ}\text{F}}{\sigma_{bMAX}}$	$\frac{48,000 \text{ PSI}}{14,685 \text{ PSI}} = \boxed{3.2}$

## NOTES:

1) RATIONALE FOR EXCEEDING 500°F YIELD STRESS:

- THE STRESS IS LOCAL AND THE MATERIAL IS DUCTILE HENCE THE STRESS CONCENTRATION MAY BE IGNORED IN THE STRENGTH ANALYSIS. (IT MUST BE INCLUDED IN A FATIGUE ANALYSIS)
- THE YIELDING SHOULD OCCUR ONLY ONCE ON 1ST LOAD APPLICATION AND DEVELOP A RESIDUAL COMPRESSIVE STRESS WHICH WILL PRECLUDE FURTHER YIELDING



## DISTRIBUTION

	<u>Copies</u>		<u>Copies</u>
Commander		Dorsey (K22)	1
Naval Sea Systems Command		Edwards (K22)	1
Attn: SEA 09G32	2	Etheridge (K22)	1
SEA 03B	1	Gorechlad (K22)	1
Washington, DC 20362		Jones (K22)	1
		Lopez (K22)	1
Office of Naval Research		McNutt (K22)	1
800 N. Quincy Street		Mentges (K22)	1
Arlington, VA 22217	2	Messick (K22)	1
		Morrison (K22)	1
Office of Chief of Naval		Opeka (K22)	1
Operations		Sheetz (K22)	1
Operation Evaluation Group		Rees (K22)	1
Washington, DC 20350	1	Regan (K22)	1
		Rowe (K22)	1
Library of Congress		Vamos (K22)	1
Attn: Gift and Exchange		Womble (K22)	1
Division	4	Yaney (K22)	1
Washington, DC 20540		Cornett (K23)	1
		Decesaris (K23)	1
Defense Nuclear Agency		Groome (K23)	1
Washington, DC 20301	2	Hackley (K23)	1
		Kavetsky (K23)	10
Headquarters		Ko (K23)	1
Air Force Special Communications		Marshall (K23)	1
Center		Metzger (K23)	1
USAFSS San Antonio, TX 78243	1	Mitchell (K23)	1
		Richards (K23)	1
Defense Technical Information		Richardson (K23)	1
Center		Roberts (K23)	1
Cameron Station		Rorabauch (K23)	1
Alexandria, VA 22314	12	Rozanski (K23)	1
		Schlegel (K23)	1
Internal Distribution:		Schlie (K23)	1
K	1	Smalley (K23)	1
K20	1	Truiit (K23)	1
Moore (K21)	1	Waser (K23)	1
Becker (K22)	1	Waldo (K23)	1
Bellamy (K22)	1	Aushman (K24)	1
Brown (K22)	1	Baltakis (K24)	1
Brunsvold (K22)	1	Bell (K24)	1

## DISTRIBUTION (Cont.)

	<u>Copies</u>		<u>Copies</u>
Cothran (K24)	1	Ragsdale (K24)	1
Driftmyer (K24)	1	Roberts (K24)	1
Dunn (K24)	1	Robertson (K24)	1
Falusi (K24)	1	Smith (K24)	1
Hedlund (K24)	1	Voisinet (K24)	1
Hill (K24)	1	Watts (K24)	1
Jobe (K24)	1	Westermeyer (K24)	1
Johnson (K24)	1	Yanta (K24)	1
King (K24)	1	Ratte (E342)	1
Knott (K24)	1	E431	9
Krumins (K24)	1	E432	3
Prats (K24)	1	E35	1